PFC/RR-88-13 DOE/ET-51013-256

Fast Wave Ion Cyclotron Resonance Heating Experiments on the Alcator C Tokamak

Thomas D. Shepard

Plasma Fusion Center
Massachusetts Institute of Technology
Cambridge, MA 02139

September 1988

This work was supported by the U. S. Department of Energy Contract No. DE-AC02-78ET51013. Reproduction, translation, publication, use and disposal, in whole or in part by or for the United States government is permitted.

Fast Wave Ion Cyclotron Resonance Heating Experiments on the Alcator C Tokamak

by

Thomas Donavon Shepard

Submitted to the Department of
Electrical Engineering and Computer Science
in partial fulfillment of the requirements for the degree of

Doctor of Science
at the
Massachusetts Institute of Technology

September, 1988

Signature of Author _____

Department of Electrical Engineering
and Computer Science
September 9, 1988

Certified by _____

Ronald R. Parker
Professor of Electrical Engineering
Thesis Supervisor

Accepted by _____

Professor Arthur C. Smith
Chairman, Committee on Graduate Students

Fast Wave Ion Cyclotron Resonance Heating Experiments on the Alcator C Tokamak

by

Thomas Donavon Shepard

Submitted to the Department of Electrical Engineering and Computer Science
on September 9, 1988 in partial fulfillment of the
requirements for the degree of Doctor of Science in
Electrical Engineering

Abstract

Minority regime fast wave ICRF heating experiments have been conducted on the Alcator C tokamak. The purpose of these experiments was to study ICRF heating in a compact high-field device at RF power levels sufficient to produce experimentally significant changes in plasma properties, and in particular to investigate the scaling to high density of the RF heating efficiency. Up to 450 kW of RF power at frequency $f = 180$ MHz, was injected into plasmas composed of deuterium majority and hydrogen minority ion species at magnetic field $B_0 = 12$ T, density $0.8 \leq \bar{n}_e \leq 5 \times 10^{20}\,\mathrm{m}^{-3}$, ion temperature $T_D(0) \sim 1$ keV, electron temperature $T_e(0) \sim 1.5$–2.5 keV, and minority concentration $0.25 \lesssim \eta_H \leq 8\%$.

Deuterium heating $\Delta T_D(0) = 400$ eV was observed at $\bar{n}_e = 1 \times 10^{20}\,\mathrm{m}^{-3}$, with smaller temperature increases at higher density. However, there was no significant change in electron temperature and the minority temperatures were insufficient to account for the launched RF power. Minority concentration scans indicated most efficient deuterium heating at the lowest possible concentration, in apparent contradiction with theory. Incremental heating $\tau_{\mathrm{inc}} \equiv \Delta W/\Delta P$ up to 5 ms was independent of density, in spite of theoretical predictions of favorable density scaling of RF absorption and in stark contrast to Ohmic confinement times $\tau_E \equiv W/P$ which increased from 5 ms at $\bar{n}_e = 0.5 \times 10^{20}\,\mathrm{m}^{-3}$ to 20 ms at $\bar{n}_e = 3 \times 10^{20}\,\mathrm{m}^{-3}$.

After accounting for mode conversion and minority losses due to toroidal field ripple, unconfined orbits, asymmetric drag, neoclassical and sawtooth transport, and charge-exchange, it was found that the losses as well as the net power deposition on deuterium do scale very favorably with density. Nevertheless, when the net RF and Ohmic powers deposited on deuterium are compared, they are found to be equally efficient at heating the deuterium. This result is attributed to the ion thermal conductivity, which becomes increasingly anomalous with increasing density on Alcator C. This anomaly has been previously observed on Alcator C and is believed responsible for the saturated confinement regime typical of high-density Alcator C plasmas. If this anomalous ion confinement can be eliminated in future high-density ICRF experiments, as has been done previously on Alcator C using pellet-fueled Ohmic discharges, then these future experiments are likely to be successful.

Thesis Supervisor: Dr. Ronald R. Parker
Title: Professor of Electrical Engineering

Acknowledgements

The success of this research project was dependent on the cooperation of many people. I would like to thank my thesis supervisor, Professor R. R. Parker, for giving me the opportunity to work on this interesting and important project, and the other members of my thesis committee: Professor M. Porkolab, RF group leader, for his practical advice regarding processing and presentation of the data, and Professor A. Bers for many revealing comments on the more theoretical aspects of this work. All three of the committee members took active roles in guiding the progress of this research.

Important diagnostic support was provided by other members of the Alcator C experimental team. Dr. C. L. Fiore was responsible for the charge-exchange neutral analyzer and neutron diagnostics. Mr. E. J. Rollins operated the Thomson scattering diagnostic, under the direction of Dr. R. L. Watterson. Dr. Y. Takase was responsible for the CO_2 laser scattering diagnostic. And Dr. S. M. Wolfe provided density measurements from the FIR interferometer, measurements of resistive loop voltage, OH power, and related raw and processed data. Dr. A. Wan provided edge density and temperature measurements from the work involved in his thesis.

Helpful consulting support was provided by Dr. M. Brambilla (IFP, Garching), Drs. P. L. Colestock, G. W. Hammett, and D. N. Smithe (PPPL), and Drs. S. M. Wolfe and P. T. Bonoli (MIT). I would like to thank Marco Brambilla for personalized instruction regarding the use of his 1D full-wave code, Pat Colestock for advice regarding the SHOOT code, Greg Hammett for extensive consulting on his FPPRF code, Dave Smith for the METS code, and Steve Wolfe for support on the ONETWO code. Pat, Dave, and Greg were always available for extensive consultation on a wide range of topics, for which I am very grateful. I would also like to thank Dr. A. Ram for his dispersion relation code.

Dr. J. D. Moody, a fellow graduate student in the RF group at the time, was a constant companion throughout my graduate tenure. We worked in close collaboration during both the experimental and analytical portions of our work. It seems that he and I always had two distinctly different viewpoints on any given subject, and that much insight was gained from bringing these views together.

I would like to thank David Griffin, Cees Holtjer, and Paul Telesmanic for operation of the RF power generation equipment, and William Byford and Jerry Gerolamo for technical support during operation of the experiment. These five people often devoted large amounts of overtime, often on weekends, to help with vacuum conditioning of the ICRF antennas. I also thank Robert Childs for directing the installation of the antennas and maintaining astonishing standards regarding ultra-high-vacuum technology. Finally, I thank Matt Besen for the mechanical design of the antennas, Norton Pierce for the design of the special limiters, and Carol Costa and Patricia Stewart for help with travel arrangements and other administrative details.

Contents

CHAPTER 1

Introduction

1.1: Introduction and Motivation

In order to produce thermonuclear fusion reactions, it is necessary to heat the reactants to a temperature at which the cross section for fusion reactions is significant. In order to achieve a net energy gain from the reaction, it is also necessary to limit the loss of energy from the system to a sufficiently low value.[1] In a tokamak, the reactants are in the form of a highly ionized gas (a plasma) confined inside a toroidal vacuum chamber by magnetic fields, and are heated resistively by driving a toroidal current through the plasma. The poloidal magnetic field associated with the induced toroidal current, as well as a separately imposed toroidal magnetic field, both play key roles in the confinement equilibrium and stability of the plasma.[2, 3] Thus, in a purely ohmically heated tokamak, the heating and confinement mechanisms are necessarily linked, and limitations involved with one of these mechanisms can indirectly affect the other.

There are several phenomena which limit the effectiveness of ohmically heating a magnetically confined plasma. Among the most basic of these is the nature of Coulomb collisions of unshielded charged particles. Since Ohmic heating involves Coulomb collisions, and since the cross section for Coulomb collisions decreases with increasing particle velocity, the electrical resistance of a plasma decreases as its temperature increases.[4] Thus, the effectiveness of Ohmic heating degrades at higher temperatures, in that a disproportionately larger increase in plasma current is needed in order to effect any certain temperature increase. In fact, the dependence of plasma temperature on current is complicated in many ways by the interactions between magnetic fields, currents, and thermal transport properties, a discussion of which would be quite lengthy and inappropriate to be included in this writing. Nevertheless, based on these simple considerations, it is valid to say that the effectiveness of Ohmic heating is limited by the linking between the Ohmic heating current and various stability and transport limitations. At the time of this writing, it is doubtful (although by no means certain) that a magnetically confined plasma can be brought to thermonuclear ignition by means of Ohmic heating alone.

These considerations motivate the exploration of alternative heating methods for magnetically confined plasmas, i.e., for techniques that allow the heating and confinement mechanisms to be decoupled. One possible strategy would be to give substantial kinetic energy to neutral atoms before injecting them into the tokamak. This technique of neutral beam injection (NBI) has been used successfully as an auxiliary heating mechanism for several tokamaks. In NBI, an energetic beam of neutral "reactant" gas is injected into a "target" plasma, where it is ionized while

giving its excess (suprathermal) energy to the plasma through collisional equilibration. It might be considered a disadvantage that while heating and magnetic confinement are no longer linked when using NBI, heating and fueling then become linked. A property of NBI which is more clearly a disadvantage is the necessity to inject the beam in the tangential direction, which imposes access requirements that interfere with the design of efficient magnetic field systems.

Another possible auxiliary heating technique is to inject power in the form of high-frequency electromagnetic waves, at frequencies and polarizations chosen to interact with natural modes of motion of the plasma particles. In the electron cyclotron range of frequencies (ECRF), the injected waves interact with the Larmor motion of the electrons. In the lower hybrid range of frequencies (LHRF), the interaction is with a resonant collective mode in which the ions and electrons oscillate out of phase with one another. In the ion cyclotron range of frequencies (ICRF), the interaction is with the Larmor motion of ions, and/or with the two-ion hybrid resonance — a mode in which two ion species oscillate out of phase with one another. It is also possible to heat the plasma with waves in the Alfvén wave frequency range.

At this point, it is worth clarifying my use of the word "confinement" in the preceding paragraphs. I am using this word to refer to the application of forces to balance the kinetic pressure of the plasma by imposing magnetic fields. The word "confinement" is also commonly used to describe the transport of energy (and loss thereof) in a plasma, i.e., "energy confinement". My reference to decoupling of heating and magnetic confinement, is not meant to apply to energy transport. In auxiliary heating experiments, energy confinement time is typically observed to degrade with the application of auxiliary heating power, even after accounting for all known loss mechanisms. At the time of this writing, it is not clear whether this degradation in energy confinement is a new effect introduced by the auxiliary heating (thus heating and energy confinement linked), or if it is an effect that is always present but is masked in purely Ohmic discharges due to the link between heating and magnetic confinement (which would then be considered to have been "unlinked" by the auxiliary heating). Due to the modesty of the heating results obtained in the Alcator C experiments, it will certainly not be possible to address this issue herein. In fact, after accounting for all known loss mechanisms in Alcator C, is will not even be possible to conclude that there was any degradation in energy confinement.

The work described in this thesis is concerned with heating in the ion cyclotron range of frequencies in the compact, high-magnetic-field tokamak Alcator C. ICRF heating has been successfully tested in the tokamaks TFR[5–10], ASDEX[11–22], PLT[23–33], JIPP T-II and JIPP T-IIU[34–36], Microtor and Macrotor[37, 38], JFT-2

and JFT-2M[39–43], JET[44–52], and TEXTOR[53–57]. Previous attempts at ICRF heating in Alcator A and Alcator C have been somewhat disappointing[58–60], although improved heating efficiency was observed during ion Bernstein wave heating experiments[61], which were conducted in parallel with the fast-wave experiments described herein.

The compact nature of the Alcator tokamak design imposes severe limitations on the design of the ICRF launcher, and the previous ICRF experiments on Alcator C were plagued by incessant electrical failures. One of the goals of the present work was to improve the design of the RF system, in order to allow injection of the total available ICRF power ($\sim$ 400 kW) for long pulse-lengths (100 ms or more) without electrical arcing in the antenna or transmission line, and thereby to eliminate launcher limitations as contributing factors to ICRF heating efficiency. By redesigning the ICRF antenna and employing an improved high-power RF vacuum feedthrough, which was designed by members of the PLT group[26], it was possible to produce ICRF heating efficiencies comparable to those in the previous Alcator C ICRF experiments, but to do so much more reliably.

Once the antenna design has been eliminated from consideration as a factor limiting heating performance, it is necessary to study the physics of wave propagation and absorption, and related energy transport in Alcator C. Unfortunately, because of the amount of time necessary to devote to antenna development, programmatic conflicts, and the limited port space on Alcator C, it was not possible to operate with the full set of plasma diagnostics that would be desirable during an RF heating experiment. These factors, coupled with the modest heating results obtained, make accurate data analysis impossible, so that it is difficult to speak unequivocally about the various physical processes that are involved. Nevertheless, by examining what data are available, both from the present experiments and from previous Alcator experiments, and by considering theoretical predictions based on numerical computations, it is possible to assemble a reasonably self-consistent explanation of the experimental results.

I will begin this thesis with an introductory review of the various theoretical topics related to ICRF heating, including a few detailed derivations of some elementary results. This will be followed by a review of some of the important experimental results from other machines. Then the design of the ICRF launcher will be presented in Chapter 2. The data collected from the available plasma diagnostics during the experiments will be summarized in Chapter 3, and an explanation of these results, based on theoretical computations, will be presented in Chapter 4. A brief overall summary and conclusions will be given in Chapter 5.

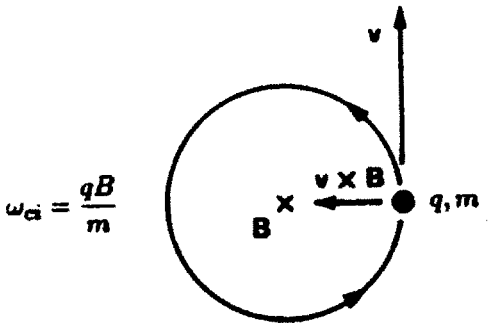

Figure 1.2.1: Cyclotron motion in a magnetic field—A positively charged ion gyrates in the left-hand sense with respect to a stationary observer looking along the magnetic field line.

1.2: Terminology and Units

In this section, I would like to establish a few conventions of terminology and introduce the system of electromagnetic units to be used in most of the discussions in this thesis.

The well-known gyromotion exhibited by a charged particle in a magnetic field is depicted in Fig. 1.2.1. The goal of an ICRF heating experiment is to transfer energy to the charged particle by an interaction between the particle and the electromagnetic fields of an imposed wave. The sense of rotation shown in Fig. 1.2.1 shall be referred to herein as the left-handed (LH) sense. Because the cyclotron motion of a positively charged ion is left-handed, it should not be surprising that the left-hand circularly polarized (LHCP) component of the wave electric field is an important quantity, and that the wave must have a significant LHCP component in order to heat efficiently. Therefore, regardless of the direction of wave propagation, the wave polarization is always defined in the plane perpendicular to the magnetic field, with respect to a stationary observer looking along **B**.

As will be shown later, when a fast wave is launched into a tokamak plasma at a frequency such that $\omega = \omega_{ci}$ at the plasma center, there is very little LHCP component of the electric field at the location of the cyclotron resonance. The reason why the fast wave is of interest for ICRF heating is that it is not practical to couple the slow wave (which is LHCP at $\omega = \omega_{ci}$) and there are ways to get around the limitation imposed by the polarization of the fast wave. One technique that can be used to heat effectively with the fast wave is to use a plasma composed of two (or more) ion species with different charge-to-mass ratios (and thus different cyclotron frequencies). If the species which is in cyclotron resonance is sufficiently dilute, then the wave polarization will be determined primarily by the majority ion species

and there will be a sufficient LHCP wave component to interact with the minority species. This technique is commonly referred to as the *minority ICRF heating regime*. At higher minority concentrations, cyclotron damping again becomes inefficient, but linear mode coupling to another plasma wave (the ion Bernstein wave[62]) becomes dominant. It is often possible for the ion Bernstein wave (IBW) to heat electrons via Landau damping and transit-time magnetic pumping. This technique is the *ICRF mode-conversion (MC) regime*. Landau damping and magnetic pumping can also be important for the fast wave in cases like the D-majority He^3-minority regime, where a majority cyclotron harmonic resonance is not degenerate with the main minority resonance.

Another technique by which it is possible to heat with the fast wave involves launching a wave at a frequency such that $\omega = 2\omega_{ci}$ at the plasma center. If one considers an ion gyrating at frequency ω_{ci} in the presence of a spatially uniform LHCP electric field at frequency $2\omega_{ci}$, then it is obvious that the forces acting on the ion will average to zero, and that no energy will be transferred. However, if the gyroradius of the ion orbit is significant compared to the wavelength of the electric field, then the electric field experienced by the particle will not be uniform and the forces will not average to zero. Incidentally, this same effect also allows the ion to absorb energy from a right-hand circularly polarized (RHCP) field, even at $\omega = \omega_{ci}$, but with less efficiency. Although the absorption from the RHCP component is less efficient than from the LHCP component and is often neglected in calculations, it can be important in situations where the RHCP component of the wave is large compared to the LHCP component.

Unfortunately the terminology used in the literature to refer to ICRF heating at $\omega = 2\omega_{ci}$ is inconsistent. The terms *first harmonic ICRF* and *second harmonic ICRF* are both used. As the reader can probably tell, I believe that the second term is preferable, for reasons that I am about to explain. I believe that the first expression originated from the misconception that the word "harmonic" is a "modifier" in the sense that it refers to a frequency other than the "fundamental" frequency. However, the term "harmonic" is commonly used by scientists to refer to motion that is sinusoidal in space and/or time. Any quantity whose motion is periodic with some "fundamental" frequency can be expressed as a Fourier series, often referred to as a sum of harmonics. In this respect, the fundamental is no less "harmonic" than any of the other frequency components. Thus, I consider the term "first harmonic" to be a synonym for the term "fundamental", and I will adhere to the convention in this thesis that ICRF heating at $\omega = 2\omega_{ci}$ is called the *second harmonic ICRF heating regime*. The reader is advised that when the word "harmonic" occurs in the ICRF literature, heating at $\omega = 2\omega_{ci}$ is usually (but not always!) what is being described, regardless of the ordinal number ascribed to it.

In Sec. 1.1, I have used the term "Ohmically heated tokamak" to refer to a tokamak in which the only source of plasma heating is the Ohmic dissipation of the current used to confine the plasma. Heating of the plasma from sources other than the confining current (such as RF or NBI) is often referred to as "auxiliary heating", and a tokamak which uses auxiliary heating is often referred to as an "auxiliary heated tokamak". The expressions "additional heating" and "additionally heated tokamak" are also used. Although it is difficult to argue that the latter expressions are grammatically incorrect, there usage in the English language is somewhat awkward. I suspect that they originated from a mistranslation into English from some other language. Because the word "auxiliary" explicitly refers to something that comes from an alternate source, I believe that the former expressions are preferable.

I have adopted what I call a rationalized dimensionless electromagnetic system of units for this thesis. In this system, the Maxwell equations are

$$\nabla \times \mathbf{E} = -\frac{\partial \mathbf{B}}{\partial t} \tag{1.2.1}$$

$$\nabla \times \mathbf{H} = \frac{\partial \mathbf{D}}{\partial \mathbf{t}} + \mathbf{J} \tag{1.2.2}$$

$$\nabla \cdot \mathbf{D} = \rho \tag{1.2.3}$$

$$\nabla \cdot \mathbf{B} = 0 \tag{1.2.4}$$

where the polarization and magnetization are given by

$$\mathbf{B} = \mathbf{H} + \mathbf{M} \tag{1.2.5}$$

$$\mathbf{D} = \mathbf{E} + \mathbf{P} \tag{1.2.6}$$

Here ρ represents the electric charge density and the other symbols are the usual electromagnetic fields. In plasma wave theory, all plasma currents are explicit, so $\mathbf{B} = \mathbf{H}$. Like conventional SI units, there are no constants like 4π present, and like cgs units, all electromagnetic field quantities have the same dimensions. This system can be thought of as a modification of the SI system, in which $\mu_0 = \epsilon_0 = c = 1$ and can be obtained rigorously be choosing to measure time and distance in the same units, as is often done in special and general relativity theory. But usually this kind of system is used in a "non-rigorous" fashion, by simply omitting the constants μ_0, ϵ_0, and c from the starting equations. It is usually very easy to see how to reintroduce them at the end of a derivation, but it is rarely necessary. In plasma wave physics this is particularly easy to do because most of the expressions used are written in terms of quantities like ω_{cj} and ω_{pj} and look the same no matter what system of units was used to derive them.

The advantage of using such a system is that one is spared alot of unnecessary writing when doing theoretical analyses, since the only quantities that have to be manipulated are those that are mathematically (and hence in some sense physically) relevant. I wholeheartedly disagree with anyone who believes that using dimensionless units obscures the underlying physics — in fact I believe that the opposite is true. I have even found this system of units convenient when making laboratory measurements. For example, the transmission line parameters R, L, and C of a strip line antenna are dimensionless quantities of order unity in RD units, and laboratory measurements of reflection coefficients and wavelengths lead more directly to the dimensionless parameters (which, incidentally, can be converted to conventional laboratory units simply by multiplying by η_0, μ_0, and ϵ_0 respectively).

The only quantities that appear in plasma wave physics calculations that are non-trivial to convert from RD to SI units are the Debye length λ_D, the Alfvén speed $c_A \equiv 1/N_A$, and the plasma frequency ω_p. Since $\omega_p \lambda_D = v_T$ and $N_A^2 = 1 + \omega_{pi}^2/\omega_{ci}^2$, it is only necessary to remember that the RD expression

$$\omega_p^2 = \frac{nq^2}{m} \tag{1.2.7}$$

translates into SI as

$$\omega_p^2 = \frac{nq^2}{\epsilon_0 m} \tag{1.2.8}$$

In this write-up, theoretical derivations will generally be given in RD units, while expressions used directly in arithmetic calculations will generally be given in SI units.

I also establish the following conventions regarding cyclotron frequencies and thermal velocities: The cyclotron frequency of a gyrating charged particle is denoted by

$$\Omega \equiv \frac{qB}{m} \tag{1.2.9}$$

where it is understood that q includes the algebraic sign of the electrical charge. If the sign of the electrical charge is to be ignored, then the notation is

$$\omega_c \equiv |\Omega| \tag{1.2.10}$$

The thermal velocity of a species which is characterized by a Maxwellian velocity distribution function is denoted by

$$v_{th} \equiv \sqrt{\frac{2T}{m}} \tag{1.2.11}$$

or by

$$v_T \equiv \sqrt{\frac{T}{m}} \tag{1.2.12}$$

and temperatures are always measured in energy units.

1.3: Elementary Cold-Plasma Wave Theory

In the remaining sections of this chapter, I will present a general review of ICRF heating theory starting from a fairly basic level, followed by a review of significant results from other ICRF heating experiments. I will assume that the reader's background includes a basic knowledge of plasma physics and applications to controlled thermonuclear fusion experiments, including a knowledge of plasma wave theory at a very basic level, but that he is unfamiliar with the issues related to RF heating experiments. That is, I am assuming that the reader has the same background that I had when I received this research assignment. I hope that by doing so, I can provide a useful guide through the bewildering array of ICRF-related literature, for future newcomers to this field. More knowledgeable readers may wish to skip part or all of the remainder of this chapter.

This section and the next will be concerned with elementary cold-plasma theory and hot-plasma theory, respectively. A good general review of these topics was given by Stix[63]. My presentation will be limited to topics directly relevant to ICRF heating. Detailed derivations will be given of some very basic plasma wave theory results, followed by a more abstract outline of the advanced topics treated in the literature.

The simplest possible model that can be applied to wave propagation in a plasma is the zero-temperature or "cold-plasma" limit, in which the plasma equilibrium consists of a state in which all particles are motionless. The only particle motion considered is motion that is directly associated with harmonic oscillations in the plasma. From the discussion in Sec. 1.1, it should be clear that it will not be possible to model second harmonic absorption in this limit. In fact, it is not possible to correctly model minority absorption or mode-conversion in this limit either. Also, the plasma will be considered to be infinite, spatially homogeneous, and immersed in a uniform, straight magnetic field. Difficulties associated with spatial gradients and magnetic shear will be discussed later. Nevertheless, cold-plasma theory is a useful approximation to determine, e.g., regions of propagation and cutoff in an inhomogeneous plasma. Cold-plasma theory provides an accurate estimate of the

wavelength and phase velocity of the fast wave in most regions of the plasma, but breaks down completely where mode conversion occurs and fails to predict cyclotron damping.

The analysis is begun by writing the Maxwell equations:

$$\nabla \times \mathbf{E} = -\frac{\partial \mathbf{B}}{\partial t} \tag{1.3.1}$$

$$\nabla \times \mathbf{B} = \frac{\partial \mathbf{E}}{\partial t} + \mathbf{J} \tag{1.3.2}$$

and seeking to express the electric current $\mathbf{J}$ in terms of the fields $\mathbf{E}$ and $\mathbf{B}$. This is easily accomplished by expressing the current in terms of the particle velocities $\mathbf{v}_j$ (j is the species index):

$$\mathbf{J} = \sum_j n_j q_j \mathbf{v}_j \tag{1.3.3}$$

and expressing the velocities in terms of the fields using the Lorentz force equation:

$$\frac{\partial \mathbf{v}_j}{\partial t} = \frac{q_j}{m_j}(\mathbf{E} + \mathbf{v}_j \times \mathbf{B}) \tag{1.3.4}$$

Note that, strictly speaking, the current is non-linearly related to the fields, due to the quadratic $\mathbf{v}_j \times \mathbf{B}$ term in Eq. 1.3.4. Thus, even in the cold-plasma limit, there is the possibility of nonlinear coupling between different plasma waves. If the wave equations are linearized, by considering small sinusoidal perturbations about equilibrium fields and dropping quadratic terms, then this nonlinear coupling is eliminated from the mathematical model. This is done by considering $\mathbf{B}$ in Eq. 1.3.4 to be the equilibrium magnetic field only.

Defining space and time Fourier transforms via

$$\nabla \rightarrow i\mathbf{k}, \qquad \frac{\partial}{\partial t} \rightarrow -i\omega, \qquad \mathbf{N} \equiv \frac{\mathbf{k}}{\omega} \tag{1.3.5}$$

where $\mathbf{N}$ is the vector refractive index, leads to the following algebraic wave equation:

$$\mathbf{N} \times (\mathbf{N} \times \mathbf{E}) + \mathbf{K} \cdot \mathbf{E} = \mathbf{0} \tag{1.3.6}$$

where

$$\mathbf{K} \cdot \mathbf{E} \equiv \mathbf{E} + \frac{i}{\omega}\mathbf{J} \tag{1.3.7}$$

There are only two distinguished directions in this problem: the direction of the equilibrium magnetic field $\mathbf{B}$ and the direction of wave propagation $\mathbf{N}$. Thus, it

is convenient to choose a Cartesian coordinate system in which the equilibrium magnetic field is in the z-direction ($\mathbf{B} = \hat{\mathbf{z}}B$) and the wave propagates in the xz-plane ($\mathbf{N} = \hat{\mathbf{x}}N_\perp + \hat{\mathbf{z}}N_\parallel$). In this case, one easily obtains an explicit expression for the matrix K:

$$\mathsf{K} = \begin{pmatrix} S & -iD & 0 \\ iD & S & 0 \\ 0 & 0 & P \end{pmatrix} \tag{1.3.8}$$

where the notation S, D, and P is due to Stix[63]:

$$S = \frac{R+L}{2} \tag{1.3.9}$$

$$D = \frac{R-L}{2} \tag{1.3.10}$$

$$R = 1 - \sum_j \frac{p_j}{1+g_j} \tag{1.3.11}$$

$$L = 1 - \sum_j \frac{p_j}{1-g_j} \tag{1.3.12}$$

$$P = 1 - \sum_j p_j \tag{1.3.13}$$

and I have introduced my own notation:

$$g_j \equiv \frac{\Omega_j}{\omega} \tag{1.3.14}$$

$$p_j \equiv \frac{\omega_{pj}^2}{\omega^2} \tag{1.3.15}$$

which I find significantly reduces the amount of algebraic tedium involved in wave-physics calculations. The cyclotron frequency of species j is

$$\Omega_j \equiv \frac{q_j B}{m_j} \tag{1.3.16}$$

where it is to be understood that q_j includes the algebraic sign of the charge, and the plasma frequency is given by

$$\omega_{pj}^2 = \frac{n_j q_j^2}{m_j} \tag{1.3.17}$$

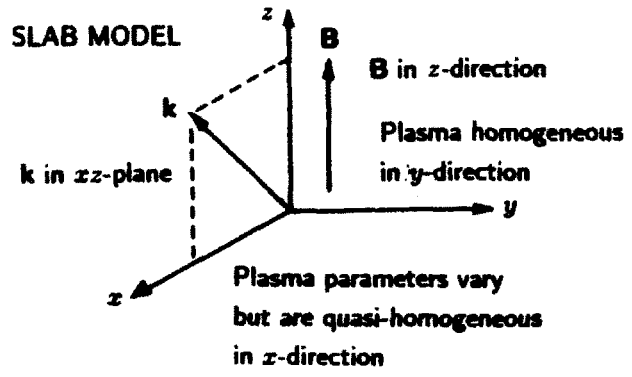

Figure 1.3.1: Slab Geometry—In this simplified slab geometry, the plasma parameters are assumed to vary only in the x-direction.

I also adopt the convention that

$$\omega_{cj} = |\Omega_j| \tag{1.3.18}$$

will be used to designate the cyclotron frequency without regard to the sign of the species charge. Writing the double cross product in matrix notation and adding to $\mathbf{K}$ puts the wave equation in the form

$$\mathbf{G}\cdot\mathbf{E} = \begin{pmatrix} S - N_{\|}^2 & -iD & N_{\perp}N_{\|} \\ iD & S - N^2 & 0 \\ N_{\perp}N_{\|} & 0 & P - N_{\perp}^2 \end{pmatrix} \begin{pmatrix} E_x \\ E_y \\ E_z \end{pmatrix} = 0 \tag{1.3.19}$$

The propagation of electromagnetic waves through the plasma can now be described by the dispersion relation

$$\det \mathbf{G} = 0 \tag{1.3.20}$$

Eq. 1.3.20 is formally a third order equation for N^2, but a simple calculation shows that the coefficients of N^6 exactly cancel one another, yielding only two solutions for N^2. The mode corresponding to the smaller value of N^2 is the fast wave and the other mode is the slow wave. If finite temperature effects are included in the analysis, the coefficient of N^6 is found to be nonzero. Thus, there is a third mode whose expansion in terms of temperature is singular, and whose refractive index is infinite in the cold plasma limit. This mode is the Bernstein wave. For frequencies in the ion cyclotron range, the mode is called the ion Bernstein wave (IBW).

In order to study the propagation characteristics of plasma waves, it is useful to evaluate the wave vector as a function of location throughout the plasma. Strictly

speaking, this type of analysis requires a wave equation to be derived which explicitly accounts for the effects of spatial gradients of the plasma parameters. However, one would expect the value of the homogeneous-plasma dielectric tensor (K) to have some physical relevance, provided the spatial gradients are sufficiently weak. Consider the simple slab geometry model illustrated in Fig. 1.3.1. One minor problem which immediately crops up is that there are now three distinguished directions in the plasma, including the direction of spatial inhomogeneity. Thus, one would like to extend the wave equation to include the effect of an N_y component of the wave vector. It turns out that the dimensions of a typical ICRF antenna (and particularly the Alcator C antenna) are such that nonzero N_y is not really very important. However, it is obviously not difficult to include it. A particularly elegant way to express the cold-plasma wave equation with arbitrary propagation direction is to resolve all vector components into parallel (to $\mathbf{B}$) and perpendicular components, and then to resolve the perpendicular components into right-hand and left-hand circularly polarized components (with respect to a stationary observer looking in the z-direction). Using the subscript $+$ to designate LHCP and $-$ to designate RHCP yields the following:

$$\mathbf{N} = N_{\|}\hat{\mathbf{z}} + \mathbf{N}_{\perp} \tag{1.3.21}$$

$$\mathbf{E} = E_{\|}\hat{\mathbf{z}} + \mathbf{E}_{\perp} \tag{1.3.22}$$

$$\mathbf{J} = J_{\|}\hat{\mathbf{z}} + \mathbf{J}_{\perp} \tag{1.3.23}$$

$$\mathbf{v}_j = v_{j\|}\hat{\mathbf{z}} + \mathbf{v}_{j\perp} \tag{1.3.24}$$

$$E_{\pm} \equiv \frac{E_x \pm iE_y}{2} \tag{1.3.25}$$

$$J_{\pm} \equiv \frac{J_x \pm iJ_y}{2} \tag{1.3.26}$$

$$v_{j\pm} \equiv \frac{v_{jx} \pm iv_{jy}}{2} \tag{1.3.27}$$

$$N_{\pm} \equiv \frac{N_x \pm iN_y}{2} \tag{1.3.28}$$

Using this notation, the relation between particle velocities and electric field is very simple:

$$v_{j\|} = \frac{iq_j}{m_j\omega}E_{\|} \tag{1.3.29}$$

$$v_{j+} = \frac{iq_j}{m_j\omega}\frac{E_+}{1-g_j} \tag{1.3.30}$$

$$v_{j-} = \frac{iq_j}{m_j\omega}\frac{E_-}{1+g_j} \tag{1.3.31}$$

and similarly for the current:

$$\frac{J_\parallel}{i\omega} = E_\parallel \sum_j p_j \tag{1.3.32}$$

$$\frac{J_+}{i\omega} = E_+ \sum_j \frac{p_j}{1-g_j} \tag{1.3.33}$$

$$\frac{J_-}{i\omega} = E_- \sum_j \frac{p_j}{1+g_j} \tag{1.3.34}$$

This yields a dielectric tensor which is diagonal:

$$\mathsf{K} = \begin{pmatrix} L & 0 & 0 \\ 0 & R & 0 \\ 0 & 0 & P \end{pmatrix} \tag{1.3.35}$$

and the wave equation becomes

$$\begin{pmatrix} L-\left(N_\parallel^2+\frac{1}{2}N_\perp^2\right) & 2N_+^2 & 2N_\parallel N_+ \\ 2N_-^2 & R-\left(N_\parallel^2+\frac{1}{2}N_\perp^2\right) & 2N_\parallel N_- \\ 2N_\parallel N_- & 2N_\parallel N_+ & 2(P-N_\perp^2) \end{pmatrix} \begin{pmatrix} E_+ \\ E_- \\ \frac{1}{2}E_\parallel \end{pmatrix} = 0 \tag{1.3.36}$$

For propagation parallel to the magnetic field, this reduces to

$$\begin{pmatrix} L-N_\parallel^2 & 0 & 0 \\ 0 & R-N_\parallel^2 & 0 \\ 0 & 0 & P \end{pmatrix} \begin{pmatrix} E_+ \\ E_- \\ E_\parallel \end{pmatrix} = 0 \tag{1.3.37}$$

and for propagation perpendicular to the magnetic field it becomes

$$\begin{pmatrix} L-\frac{1}{2}N_\perp^2 & 2N_+^2 & 0 \\ 2N_-^2 & R-\frac{1}{2}N_\perp^2 & 0 \\ 0 & 0 & P-N_\perp^2 \end{pmatrix} \begin{pmatrix} E_+ \\ E_- \\ E_\parallel \end{pmatrix} = 0 \tag{1.3.38}$$

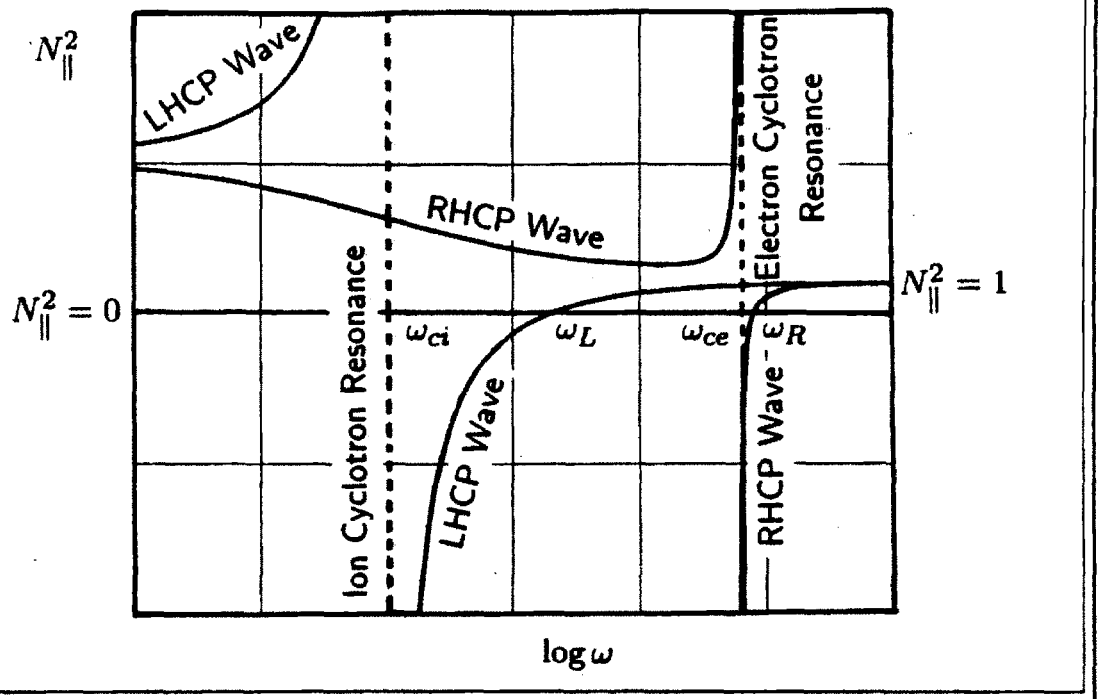

Figure 1.3.2: Propagation Parallel to the Magnetic Field—The dispersion relation is shown for a single-ion-species plasma and purely parallel propagation. In the ion cyclotron range of frequencies, the RHCP wave corresponds to the fast wave.

The dispersion relation ($N_\parallel^2$ as a function of ω) is shown in Fig. 1.3.2 for the case of propagation strictly parallel to the magnetic field in a single-ion-species plasma. As can be seen from Eq. 1.3.37, pure RHCP and LHCP waves propagate independently of one another. For each wave, resonance occurs at the frequency corresponding to the gyrofrequency of the species which gyrates in the same direction as the rotation of the electric field. The ICRF fast wave corresponds to the RHCP mode in this limit. Since the ICRF slow wave (LHCP) is resonant at ω_{ci}, this wave is useful for heating plasma in devices like mirrors or stellarators, in which the magnetic field is inhomogeneous in the parallel direction. The slow wave propagating parallel to the magnetic field is accessible to the ion cyclotron resonance if it is launched from a high-field region, where $\omega_{ci} > \omega$. The slow wave is not useful for heating tokamak plasmas at the ion cyclotron frequency due to poor accessibility. The slow wave propagates primarily along the magnetic field (must have large $N_\parallel$), particularly at high density, would have to be launched from the high-magnetic-field side of a tokamak, and would tend to be absorbed by Landau damping on electrons before it could propagate to the center.

The dispersion relation for the case of purely perpendicular propagation is shown in Fig. 1.3.3. From Eq. 1.3.38, the O-mode is seen to be linearly polarized with $\mathbf{E}||\mathbf{B}$

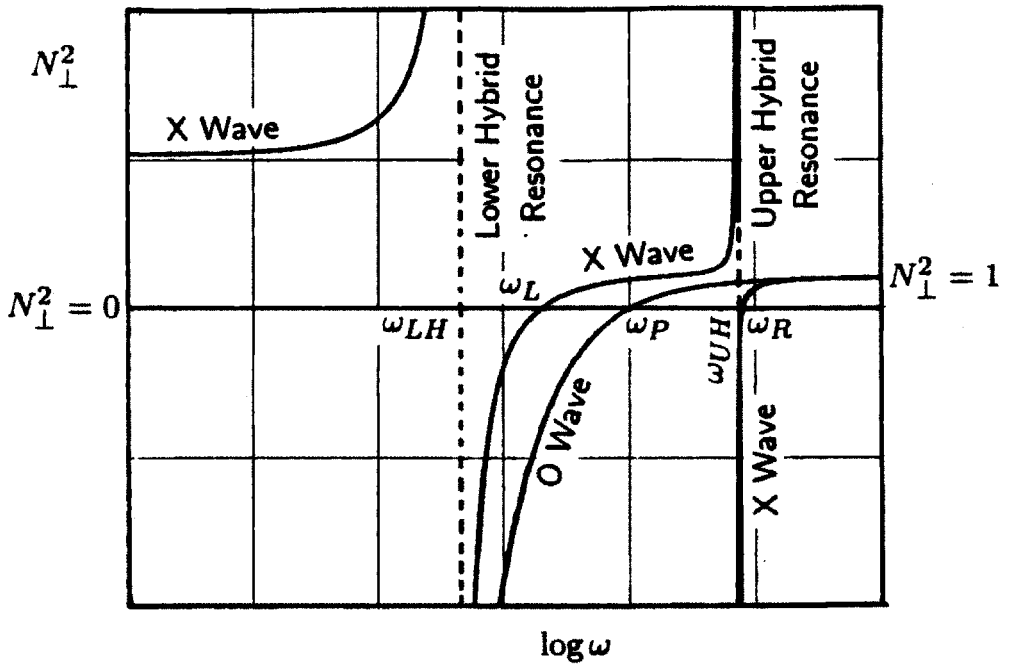

Figure 1.3.3: Propagation Perpendicular to the Magnetic Field—The dispersion relation is shown for a single-ion-species plasma and purely perpendicular propagation. For plasma parameters typical of tokamak plasmas, the ion cyclotron frequency is well below ω_{LH} except possibly near the wall of the vacuum chamber. Only the fast wave (which corresponds to the X-mode) can propagate with $N_\parallel = 0$ in this frequency range.

and has dispersion relation $N_\perp^2 = P$, which is the same as the dispersion relation for electromagnetic waves in a cold, unmagnetized plasma. Multiplying out the upper-left 2×2 determinant yields

$$N_\perp^2 = \frac{RL}{S} \tag{1.3.39}$$

as the dispersion relation for the X-mode. The X-mode has cut-offs at ω_R ($R = 0$) and ω_L ($L = 0$) and resonances at the hybrid resonant frequencies ω_{LH} and ω_{UH} ($S = 0$). For parameters typical of tokamak plasmas with only one ion species, the ion cyclotron frequency is well below ω_{LH} and ω_L, so that the ICRF fast wave propagates throughout most of the plasma, except in narrow low-density regions at the edge. Typically, the lower-hybrid resonance occurs very close to the wall in a tokamak, or else not at all (i.e., at a density lower than the density at the wall). But for finite $N_\parallel$, the left-hand cut-off will usually occur farther from the wall than the antenna, resulting in a layer of fast-wave evanescence at the plasma edge. Due

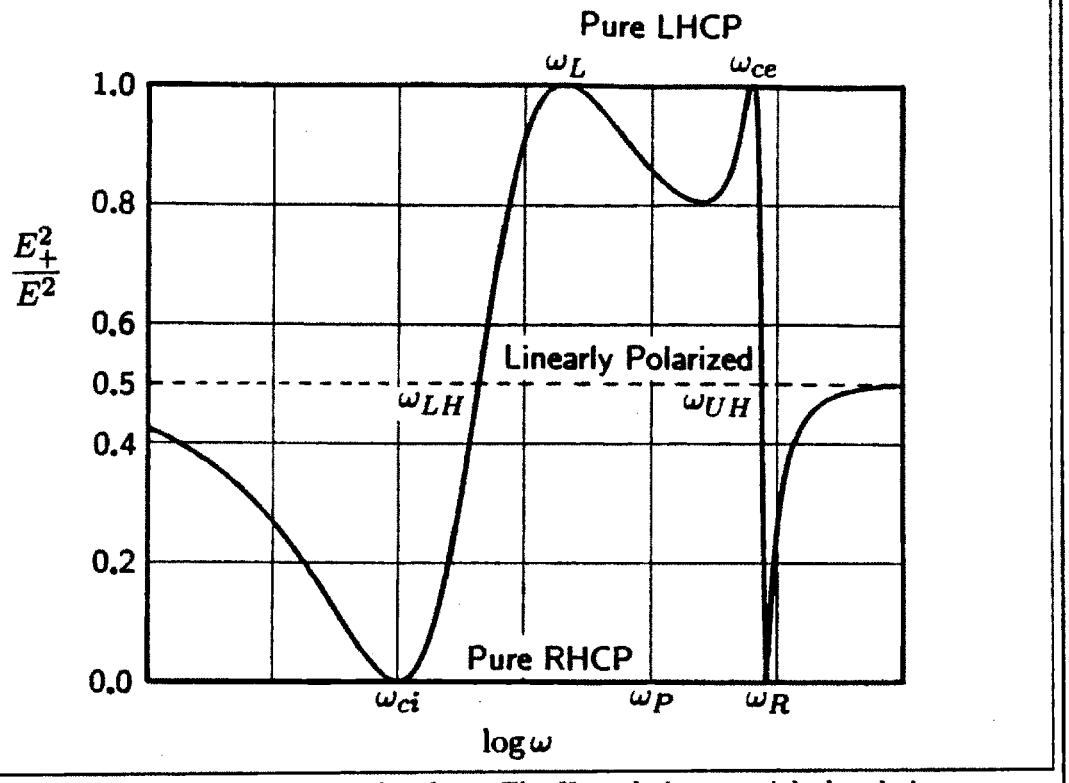

Figure 1.3.4: X-mode Polarization—The X-mode is pure right-hand circularly polarized at the ion cyclotron frequency and the right-hand cut-off, and is pure left-hand circularly polarized at the electron cyclotron frequency and the left-hand cut-off. The X-mode is linearly polarized at the hybrid resonances.

to the long wavelength of the fast wave, tunnelling through this layer will be very efficient, provided $N_{||}$ is not too large.

The electric field polarization of the X-mode is shown in Fig. 1.3.4. It is interesting to note that the sense of rotation of the electric field is opposite that of the ions at the ion cyclotron frequency, and is also opposite that of the electrons at the electron cyclotron frequency. Thus, in the cold-plasma limit, there is no way to transfer energy from the wave to ions (as mentioned in Sec. 1.2) or to electrons.

This phenomenon is analogous to the "shorting out" of $E_{||}$ which occurs as a result of the high electron mobility along the magnetic field. In order to maintain a constant applied $E_{||}$ field, electrons would be continuously accelerated to arbitrarily high velocities (unless limited by collisional and relativistic effects, both of which are ignored in this cold-plasma theory). This behavior is exhibited mathematically by Eq. 1.3.29. At zero frequency, $E_{||}$ must be zero in order for $v_{||}$ to be finite. Using Eqs. 1.3.29, 1.3.30, and 1.3.31 and taking the limit as $\omega \rightarrow 0$ yields

$$\frac{E_{||}}{E_\perp} \sim \frac{\omega}{\omega_c} \frac{v_{||}}{v_\perp} \tag{1.3.40}$$

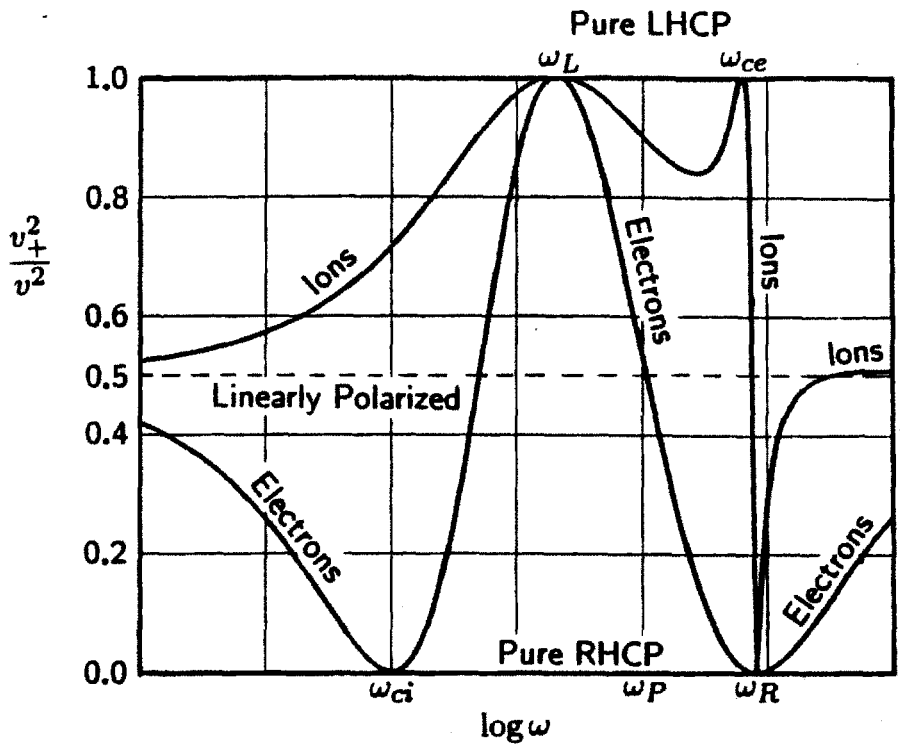

Figure 1.3.5: X-mode Perturbed Velocity Polarization—The electron velocity is pure RHCP at the ion cyclotron frequency, while the ion velocity is pure LHCP at the electron cyclotron frequency. Both species velocities are pure LHCP at the LH cut-off and pure RHCP at the RH cut-off.

from which it immediately follows that $E_\parallel \to 0$ as $\omega \to 0$ if $v_\parallel$ is finite.

The same kind of secular acceleration can take place in the perpendicular direction if the electric field rotates in synchronism with the particle at it's Larmor frequency. This "shorting" effect occurs for any electric field which would drive the particle along its unperturbed orbit. Using Eqs. 1.3.29, 1.3.30, and 1.3.31 again and taking the limit as $\omega \to \omega_c$ yields

$$\frac{E_\pm}{E_\parallel} \sim \frac{v_\pm}{v_\parallel}\left(1 \mp \frac{\omega}{\Omega}\right) \tag{1.3.41}$$

from which it follows that $E_+ \to 0$ as $\omega \to \omega_c$ for positively charged particles and $E_- \to 0$ as $\omega \to \omega_c$ for negatively charged particles. Thus, the ions "short out" the LHCP component of the electric field at $\omega = \omega_{ci}$ and the electrons "short out" the RHCP component of the electric field at $\omega = \omega_{ce}$.

Note also that the X-mode is pure LHCP at the left-hand cut-off (LHCO) and pure RHCP at the right-hand cut-off (RHCO), and is linearly polarized at the hybrid resonances.

The sense of rotation of the perturbed velocities for both electrons and ions is shown in Fig. 1.3.5. It is interesting to note that the electron velocity is pure RHCP at the ion cyclotron frequency, while the ion velocity is pure LHCP at the electron cyclotron frequency. This effect is clearly exhibited by Eqs. 1.3.30 and 1.3.31. Both species velocities are pure LHCP at the left-hand cut-off and pure RHCP at the right-hand cut-off, as is the electric field.

To understand how finite-temperature effects allow wave energy absorption to take place, note that the wave frequency will appear Doppler shifted in the reference frame of an ion with thermal motion parallel to the magnetic field. Then the condition for cyclotron resonance becomes

$$\omega - \omega_{ci} - k_{\|} v_{\|} = 0 \tag{1.3.42}$$

instead of $\omega - \omega_{ci} = 0$. Since resonance then occurs at a frequency that is slightly different than ω_{ci}, E_+ is not exactly zero anymore. However, this effect is relatively small because, since the wave is "fast" and propagates primarily in the perpendicular direction, $k_{\|}$ is "small" so that in order for the effect to be "significant", $v_{\|}$ must be "large", which means that the ions must be very "hot", unless other helpful physical mechanisms are present.

In order to study the case of finite $N_{\|}$ analytically, it is helpful to introduce an expansion in terms of the electron/ion mass ratio:

$$\epsilon \equiv \frac{m_e}{m_i} \ll 1 \tag{1.3.43}$$

and to seek solutions for the electric field in the form of a regular perturbation series:

$$E_{\pm} = E_{\pm 0} + \epsilon E_{\pm 1} + O(\epsilon^2) \tag{1.3.44}$$

and similarly for $E_{\|}$. For the case of a single ion species, one has

$$L = 1 - \frac{p_i}{g_i} \frac{1}{1 - g_i} + O(\epsilon) \tag{1.3.45}$$

$$R = 1 + \frac{p_i}{g_i} \frac{1}{1 + g_i} + O(\epsilon) \tag{1.3.46}$$

$$P = -\frac{1}{\epsilon} p_i + 1 - p_i + O(\epsilon) \tag{1.3.47}$$

Substituting this expansion into Eq. 1.3.36, the leading order equation has only one component

$$p_i E_{\|0} = 0 \tag{1.3.48}$$

which says that, since P is large ($O(m_i/m_e)$) compared to L and R, the parallel electric field must be small ($O(m_e/m_i)$) compared to $E_\perp$. This corresponds physically to the high parallel electron mobility. That is, since the electrons are free to move along the magnetic field, parallel conductivity is high and $E_\parallel$ is "shorted out". It is important to remember that $E_\parallel$ is only "shorted out" to zero order in m_e/m_i, and is nonzero if finite electron mass effects are important. It is also important to note that the fast and slow waves are decoupled in the limit $m_e/m_i \to 0$, so that linear mode conversion between the two waves cannot occur in this limit. Because $E_{\parallel 0} = 0$ the next order equation reduces to a 2×2 system:

$$\begin{pmatrix} L - \left(N_\parallel^2 + \frac{1}{2}N_\perp^2\right) & 2N_+^2 \\ 2N_-^2 & R - \left(N_\parallel^2 + \frac{1}{2}N_\perp^2\right) \end{pmatrix} \begin{pmatrix} E_+ \\ E_- \end{pmatrix} = \mathbf{0} \tag{1.3.49}$$

Going one order further yields a perturbative solution for the parallel electric field:

$$\frac{1}{2}E_\parallel = \epsilon N_\parallel \frac{N_- E_+ + N_+ E_-}{N_\perp^2 - (1 - p_i)} \tag{1.3.50}$$

This separation of the parallel and perpendicular equations in the limit of small m_e/m_i is also valid for multiple ion species, and for the wave equation including thermal effects, provided $N_\parallel$ is not too large. Multiplying out the determinant in Eq. 1.3.49 yields the dispersion relation for an arbitrary angle of propagation:

$$N_\perp^2 = \frac{(L - N_\parallel^2)(R - N_\parallel^2)}{S - N_\parallel^2} \tag{1.3.51}$$

Thus, for propagation at an arbitrary angle to the magnetic field, and to the extent that the small-electron-mass approximation is accurate, the equation for the left-hand cut-off becomes $N_\parallel^2 = L$, the equation for the right-hand cut-off becomes $N_\parallel^2 = R$, and the equation for the resonances becomes $N_\parallel^2 = S$.

Next, consider the situation where there is a direction of inhomogeneity in the plasma slab as illustrated in Fig. 1.3.1. For the case where the wave frequency is equal to the ion cyclotron frequency at the center of the plasma, the dispersion relation as a function of position in the plasma is shown in Fig. 1.3.6, and the corresponding electric field polarization is shown in Fig. 1.3.7. As has already been remarked, the absence of a LHCP component where $\omega = \omega_{ci}$ is cause for concern, and it is necessary to consider thermal effects in order to correctly model the cyclotron absorption process. Heating via thermal Doppler broadening is not

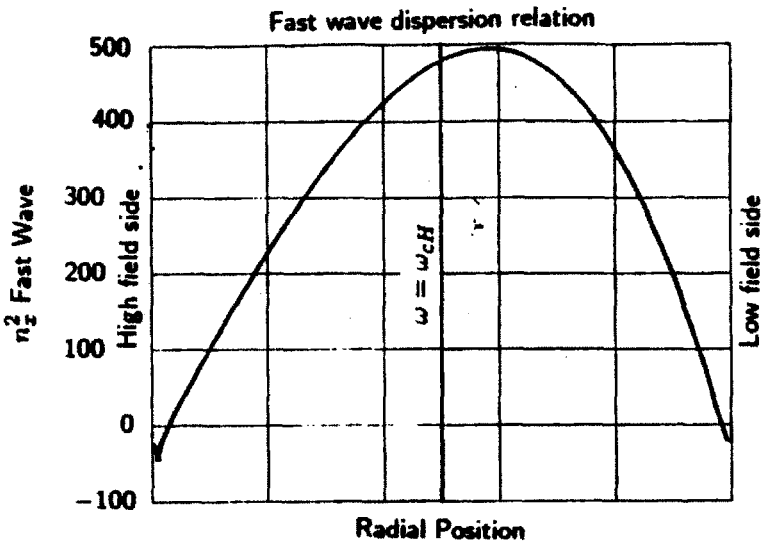

Figure 1.3.6: Fast Wave Dispersion Relation Near the Fundamental Ion Cyclotron Frequency—This is a plot of the $N_\perp^2$ as a function of distance into the plasma along the major radius. This plot and those that follow in this section were calculated using the following typical Alcator C parameters: (1) parabolic density profile with peak value of $4 \times 10^{20}\,\mathrm{m}^{-3}$, (2) inhomogeneous $1/R$ variation magnetic field profile with maximum at left side of graph, minimum at right, and an ion cyclotron frequency (or harmonic) at the center, (3) a wave frequency of $f_{RF} = 180$ MHz, (4) a fixed $N_\parallel = 5$. This calculation was done for a pure hydrogen plasma.

effective in this case because an enormous value of $v_\parallel$ would be required to produce resonant cyclotron absorption at the locations near the peaks in Fig. 1.3.7. This is the motivation for considering the second harmonic ICRF heating regime, in which the wave frequency is equal to the second harmonic $\omega = 2\omega_{ci}$ of the ion cyclotron frequency at the center of the plasma, and the minority ICRF heating regime, in which the wave frequency is equal to the fundamental (i.e. first harmonic) $\omega = \omega_{ci}$ of a very dilute minority ion species in a multiple-ion-species plasma.

Historically, attention was also drawn to the minority regime because of the existence of the two-ion hybrid resonance, which introduces wave damping even in the collisionless cold-plasma limit. In this case, the cold plasma wave equation has a singular turning point. Solution of the equation[65] shows that some of the wave energy is depleted when a fast wave is incident on the resonance layer from the low-field side, and that all of the wave energy is depleted for high-field incidence. However, cold plasma theory does not show what happens to the depleted energy. When thermal effects are included, it is found that the wave energy is actually coupled to the ion Bernstein wave. Under certain conditions the IBW can be strongly damped, resulting in efficient heating. It is also true that the effects of the hybrid

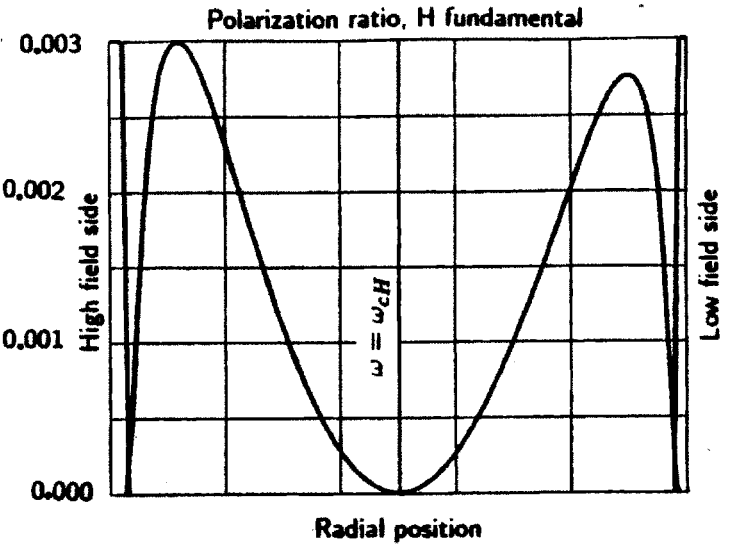

Figure 1.3.7: Fast Wave Polarization Near the Fundamental Ion Cyclotron Frequency—The quantity plotted here is E_+^2/E_-^2. As was seen in Fig. 1.3.4, the polarization is pure RHCP at the fundamental ion cyclotron frequency and at the right-hand cut-off, which occurs near the edge of the plasma.

resonance on the wavelength and polarization of the incident wave are such as to greatly enhance $k_\perp$ and E_+, leading to efficient cyclotron damping as well, provided the hybrid resonance layer is close enough to the cyclotron layer that the doppler broadened absorption region overlaps the hybrid resonance layer.

From Fig. 1.3.6, one can see that the fast wave propagates freely throughout the plasma, except for a small evanescent region at the edge. If $N_\parallel$ is not too large, tunneling through this layer is very efficient. In particular, the fast wave can easily be launched from the low-field side of the plasma. This is one reason why it is desirable to use the ICRF fast wave for plasma heating. In Fig. 1.3.7, one can see the problem with the fast wave polarization. The LHCP component is quite small throughout the central portion of the plasma, so that very strong Doppler broadening of the resonance would be necessary for wave absorption, which one might well expect to occur at the edge of the plasma. The location of the RHCO is also evident in Fig. 1.3.7 near the plasma edge where E_+ goes to zero. The sharp increase of E_+ just outside the RHCO is the effect of the lower hybrid resonance, where the electric field is linearly polarized and hence contains equal amounts of RHCP and LHCP components. This kind of behavior is typical whenever cold-plasma cut-offs and resonances are adjacent.

In the experiments on the Alcator C tokamak that are described in this thesis, heating was observed in the hydrogen minority regime in a two-ion-species plasma

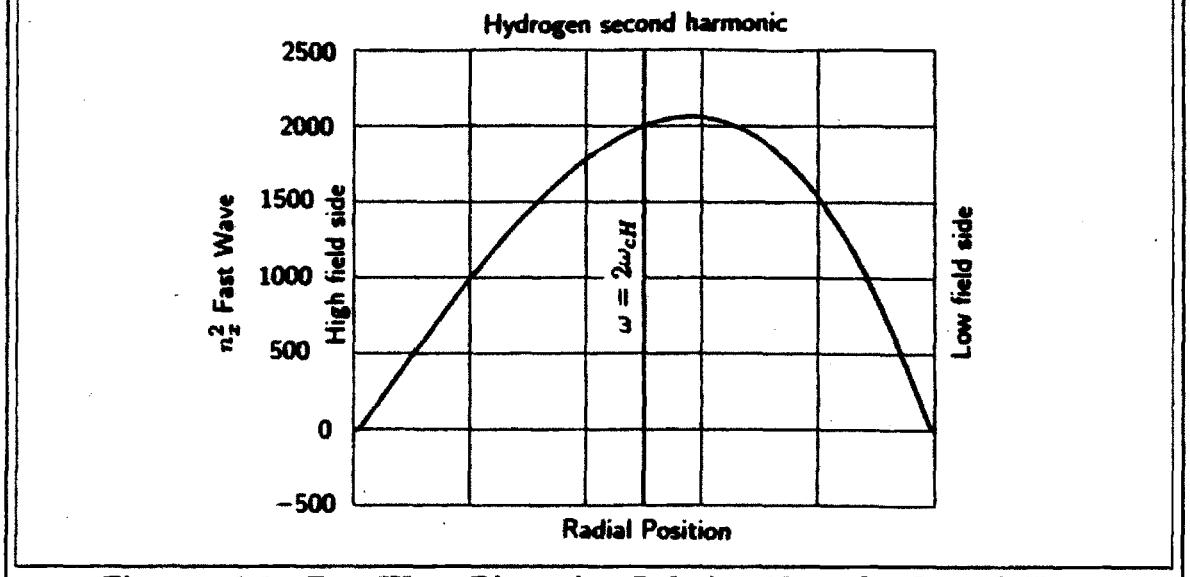

Figure 1.3.8: Fast Wave Dispersion Relation Near the Second Harmonic Ion Cyclotron Frequency—This calculation was done by changing the magnetic field to 6 T (as was done when hydrogen second harmonic heating was attempted in Alcator C). The result is a narrower cut-off layer at the edge and larger $N_\perp$.

with deuterium as the main species. Since $\omega_{cH} = 2\omega_{cD}$, the location in the plasma of the hydrogen fundamental cyclotron resonance is always the same as the location of the deuterium second harmonic resonance, and it is possible for both species to absorb power directly from the wave. There is evidence that this may have occurred in the Alcator C experiments, but the evidence is not nearly as conclusive and/or direct as it was in the case of PLT[64].

The dispersion relation for a second harmonic hydrogen regime at 6 T is shown in Fig. 1.3.8. The most noticeable effect in the cold-plasma model is simply that the refractive index increases. This can easily be understood by noting that the dispersion relation for the fast wave can be approximated by that of a compressional Alfvén wave ($N_\perp^2 \approx \omega_{pi}^2/\omega_{ci}^2$) and observing that ω_{ci} has been reduced by 1/2. The dispersion relation for pure deuterium at the second harmonic at 12 T is similar to the dispersion relation in Fig. 1.3.6.

Basically, the motivation for minority regime ICRF heating is to have the wave propagation and polarization determined predominantly by the nonresonant majority species, so that the minority species can absorb power by fundamental ion cyclotron damping. It is not really possible to show this using the cold plasma model. As shown in Fig. 1.3.9, there is indeed a nonzero LHCP component to the polarization for a pure deuterium plasma at the second harmonic of the ion cyclotron frequency. The effect on the cold-plasma dispersion relation of adding

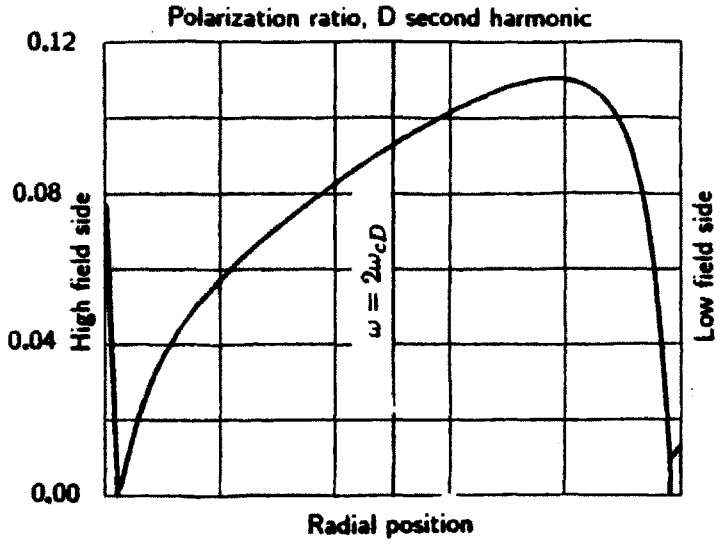

Figure 1.3.9: Fast Wave Polarization Near the Second Harmonic Ion Cyclotron Frequency—The cold-plasma model predicts a non-zero value of E_+^2/E_-^2 at the second harmonic of the ion cyclotron frequency.

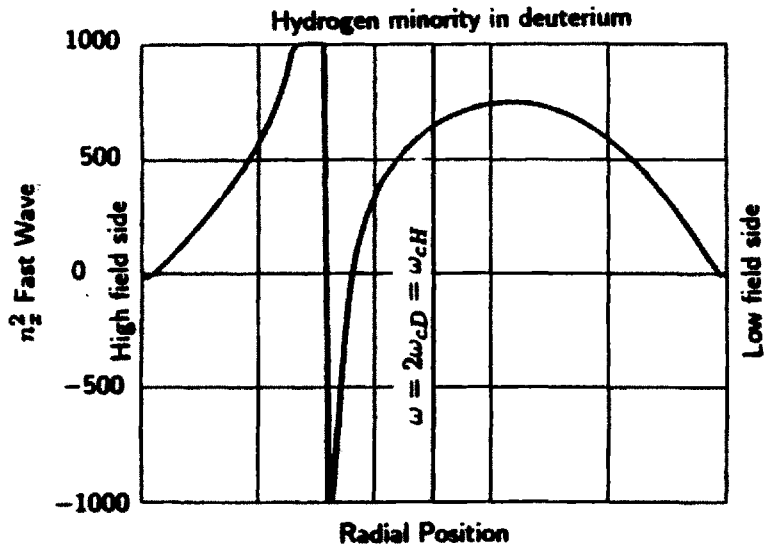

Figure 1.3.10: Fast Wave Dispersion Relation in a Two-Ion-Species Plasma—The cold-plasma model predicts an additional cutoff (given by $N_\parallel^2 = L$) and an additional resonance (given by $N_\parallel^2 = S$) when a second ion species is introduced. This calculation was done for a hydrogen minority concentration of 10%.

a small concentration of hydrogen is shown in Fig. 1.3.10, and is quite significant. The effect is to introduce a new cut-off, given by $N_\parallel^2 = L$, and a new resonance

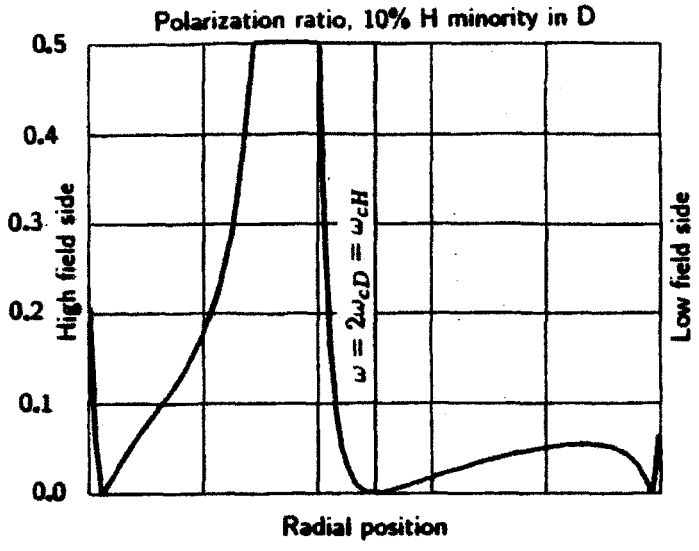

Figure 1.3.11: Fast Wave Polarization in a Two-Ion-Species Plasma—The polarization is always purely RHCP in the cold plasma model at the fundamental ion cyclotron resonance regardless of the concentration of the resonant species.

($N_{\|}^2 = S$). The effect on the polarization is shown in Fig. 1.3.11. The polarization is always pure RHCP at a (positively charged) ion fundamental cyclotron resonance, no matter how low the concentration. The polarization at the new cut-off is pure LHCP, as expected for a left-hand cut-off, and it is pure RHCP at the right-hand cut-offs at each edge of the plasma.

The dispersion relation in Figs. 1.3.10 and 1.3.11 was calculated for a 10% minority concentration, which is too high a concentration for efficient minority regime heating in Alcator C, but results in a plot in which the locations of the cyclotron resonance, LHCO and two-ion hybrid resonance are well separated and easy to see. In Fig. 1.3.12 the polarization is shown for the more realistic case of 1% minority concentration. In this case it is easy to see that the LHCP component is significantly enhanced by the presence of the majority species, even close to the position of $\omega = \omega_{cH}$, so that much less Doppler broadening is necessary for efficient absorption than would be the case in Fig. 1.3.7. Another beneficial effect is produced by the presence of the new two-ion hybrid resonance in the vicinity of the cyclotron absorption layer. Fig. 1.3.10 shows that $k_\perp$ is significantly enhanced near the resonance, while Fig. 1.3.12 shows that E_+ is also significantly enhanced. Both of these effects improve the efficiency of cyclotron absorption if the Doppler broadened cyclotron absorption region overlaps the hybrid resonance region.

The geometry of the cold-plasma cut-offs and resonances in the poloidal plane for tokamak geometry is shown in Fig. 1.3.13. The fast wave is evanescent in the

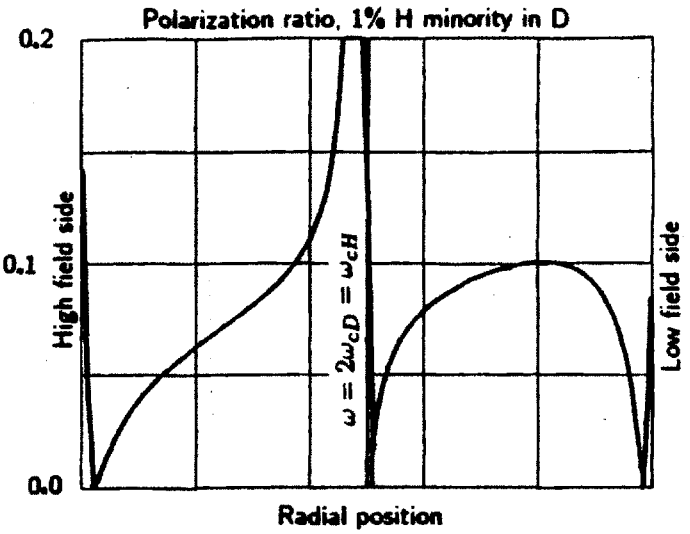

Figure 1.3.12: Fast Wave Polarization in a Two-Ion-Species Plasma—This is the same quantity as is shown in Fig. 1.3.11, except that it is calculated for a minority concentration of 1%, which is more typical of the concentration that would be used in a minority regime ICRF heating experiment.

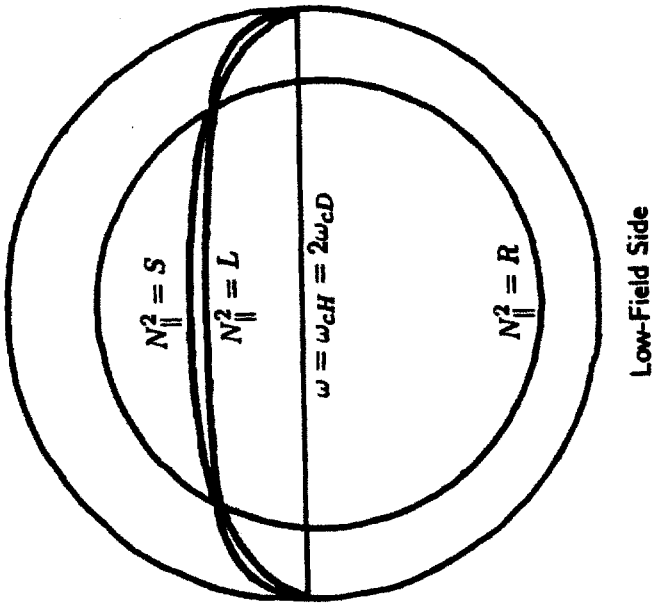

Figure 1.3.13: Cold-Plasma Dispersion Relation in 2D—The locations of the cold-plasma resonances and cut-offs are shown in the poloidal plane for tokamak geometry.

edge of the plasma (outside the RHCO), except for the thin crescent-shaped regions

near the top and the bottom. The fast wave propagates throughout the interior of the RHCO contour, except for the crescent shaped region between the LHCO and the two-ion hybrid resonance. This plot was done using the unrealistically high values $N_{||} = 12$ and 15% minority concentration in order to exaggerate the features.

It is nice that it is possible to say so much about cyclotron absorption in the context of simple cold-plasma theory. However, I must emphasize that cold-plasma theory is not valid in the region near the hybrid resonance layer, which was discussed in the preceding paragraph. For example, cold-plasma theory predicts the presence of a LH cutoff and the absence of any E_+ component, regardless of the minority concentration — no matter how small. This seems somewhat counter-intuitive. Also, a calculation of the energy flux associated with the plasma waves in the presence of a cold-plasma resonance, as was done by Budden[65], fails to show what happens to the depleted energy. It will be shown in the next section that the intuition developed in the preceding paragraph is approximately correct, except that the effects disappear gradually as minority concentration tends to zero. In hot-plasma theory E_+ is not exactly zero at $\omega = \omega_{cH}$ and approaches the value it would have in pure deuterium if the minority concentration is sufficiently low and the minority temperature is sufficiently high, and the LH cut-off disappears for low minority concentrations.

Another effect introduced by hot-plasma theory is the presence of waves which do not exist in the cold-plasma limit. In particular, the energy depleted from the fast wave at the two-ion hybrid resonance is accounted for. In hot-plasma theory the resonance is replaced by a linear mode-conversion layer, where energy can be coupled between the fast wave and the ion Bernstein wave.

Finally, it is worth mentioning that if finite electron mass effects are retained in cold-plasma theory, then the fast-wave resonance given by $N_{||}^2 = S$ is replaced by linear mode conversion to the slow wave, which then experiences a resonance at $S = 0$. This resonance is located just slightly further from the plasma center than the location where $N_{||}^2 = S$.

1.4: Elementary Hot-Plasma Wave Theory

The basic plan in hot-plasma theory is the same as in cold-plasma theory: Use the equations of motion to relate the perturbed electric current to the RF electromagnetic fields and substitute the result into the Maxwell equations to yield a linear wave equation. But the details are much more complicated. The essential difference is that the Lorentz force equation that related single-particle motion to the electromagnetic fields is replaced by the kinetic equation which describes a distribution function f of particles, and that an integration over f is necessary in order to relate the current to the fields. In the simplest approximation, the plasma is assumed to be spatially homogeneous as was done in Sec. 1.3, and collisions are neglected.

It is important to note that in the absence of collisions the plasma conductivity is nonlocal. That is, the velocity of a particle at a particular time and place depends on the entire time history of the forces experienced by the particle. And in the presence of thermal motion, the particle was at different locations at earlier times. This is in stark contrast to the well-known collision-dominated limit, in which the electric current is determined locally by balancing the electromagnetic forces against collisional drag. It is the randomizing effect of collisions that allows the plasma response to be determined locally in the collision-dominated limit. For plasmas of interest for fusion, the cyclotron frequency is large compared to the collision frequency, so that the RF plasma response is a nonlocal phenomenon. On the other hand, the plasma equilibrium is "zero frequency" and is therefore characterized by a local plasma resistivity.

Even though the plasma is collisionless on the RF time scale, it is often useful to do theoretical analysis based on a "local approximation." This is because the randomizing effect of even rare collisions limits the sensitivity of the plasma response to "old" and "distant" events. In other words, the plasma dynamics are nonlocal on the oscillatory time scale, but they are approximately local on the equilibrium and transport time scales. The same randomizing effect can be provided by plasma turbulence, which is neglected from the analysis when the equations are linearized. It turns out that, even when one is seeking a local approximation, proper formulation of the problem with regard to non-local effects is important in order to obtain a model with proper energy conservation properties.

In this section, I will present a standard derivation of the hot-plasma dielectric tensor for a spatially homogeneous plasma. This well-known derivation has been given before by several authors, including Stix[63] and Kennel and Engelmann[66]. It is important to realize that most of the steps given are valid, at least in principle, for the case of a non-uniform plasma. This derivation for the homogeneous plasma

case is usually given in Fourier transform space, by assuming wave-like variations of the form $e^{i(\mathbf{k}\cdot\mathbf{x}-\omega t)}$. The reader is encouraged to perform the derivation by explicitly carrying out the Fourier transformation of the wave equation, as this makes more clear the connection between the homogeneous and inhomogeneous-plasma derivations. My plan will be to show the details for the standard derivation in the homogeneous case, followed by a more rigorous and formal, but less explicit, treatment of the inhomogeneous case.

The kinetic equation neglecting Coulomb collisions is

$$\begin{aligned}\frac{df}{dt} &= \frac{\partial f}{\partial t} + \frac{d\mathbf{x}}{dt}\cdot\frac{\partial f}{\partial \mathbf{x}} + \frac{d\mathbf{v}}{dt}\cdot\frac{\partial f}{\partial \mathbf{v}} \\ &= \frac{\partial f}{\partial t} + \mathbf{v}\cdot\frac{\partial f}{\partial \mathbf{x}} + \frac{q}{m}(\mathbf{E}+\mathbf{v}\times\mathbf{B})\cdot\frac{\partial f}{\partial \mathbf{v}} = 0\end{aligned} \tag{1.4.1}$$

Linearization is accomplished by considering perturbations up to first order by defining

$$\begin{aligned} f &= f_0(\mathbf{v}) + f(\mathbf{x},\mathbf{v},t), && f \ll f_0 \\ \mathbf{E} &= \mathbf{0} + \mathbf{E}(\mathbf{x},t), && E(\mathbf{x},t) \sim O(f(\mathbf{x},\mathbf{v},t)) \\ \mathbf{B} &= \mathbf{B} + \mathbf{B}_1(\mathbf{x},t), && \mathbf{B}_1 \sim O(f(\mathbf{x},\mathbf{v},t)) \ll \mathbf{B} \sim O(f_0) \end{aligned} \tag{1.4.2}$$

The zero order equation is then

$$\mathbf{v}\times\mathbf{B}\cdot\frac{\partial f_0}{\partial \mathbf{v}} = 0 \tag{1.4.3}$$

and the first order equation is

$$\frac{\partial f}{\partial t} + \mathbf{v}\cdot\frac{\partial f}{\partial \mathbf{x}} + \mathbf{v}\times\boldsymbol{\Omega}\cdot\frac{\partial f}{\partial \mathbf{v}} = -\frac{q}{m}(\mathbf{E}+\mathbf{v}\times\mathbf{B}_1)\cdot\frac{\partial f_0}{\partial \mathbf{v}} \tag{1.4.4}$$

Defining cylindrical velocity space coordinates as

$$\mathbf{v} = (v_\perp, \alpha, v_\parallel) \tag{1.4.5}$$

where α is the gyrophase angle, the velocity space gradient operator takes the form

$$\frac{\partial f}{\partial \mathbf{v}} = \hat{\mathbf{v}}_\perp\frac{\partial f}{\partial v_\perp} + \frac{\hat{\boldsymbol{\alpha}}}{v_\perp}\frac{\partial f}{\partial \alpha} + \hat{\mathbf{z}}\frac{\partial f}{\partial v_\parallel} \tag{1.4.6}$$

so that the zero-order equation becomes

$$\mathbf{v}_\perp \times \hat{\mathbf{z}} \cdot \frac{\partial f_0}{\partial \mathbf{v}} = \frac{\partial f_0}{\partial \alpha} = 0 \tag{1.4.7}$$

This equation admits as solutions any arbitrary function of the constants of the particle gyromotion:

$$f_0(\mathbf{v}) = f_0(v_\perp^2, v_\parallel) \tag{1.4.8}$$

It is very well-known that if Coulomb collisions are introduced in the kinetic equation, then f_0 will relax to the form of an isotropic Maxwellian distribution function. It is only slightly less well-known that, in the presence of effects like a driven Ohmic or RF current, the resulting distribution function f_0 can be expanded in a series of the eigenfunctions of the collision operator, which can be written in terms of Legendre polynomials. The leading-order anisotropic effects can then be approximated by writing f_0 as a two-temperature Maxwellian distribution, with different temperatures in the parallel and perpendicular directions. Therefore, in the derivation that follows, the parallel and perpendicular velocity dependences of the equilibrium distribution function will be retained, and the form of the dielectric tensor for a two-temperature Maxwellian will be given. The leading-order nonthermal effects can be approximated by writing the distribution function as a sum of Maxwellians, each with different temperatures. Including this effect in the resulting dielectric tensor will be completely trivial. It is only necessary to separate each plasma species into two or more species, and assign different temperatures to each one.

The first-order equation can be solved by the method of characteristics, which is a standard mathematical technique. According to the method of characteristics, if one considers a so-called characteristic trajectory through phase space defined by

$$\frac{d\mathbf{x}}{dt} \equiv \mathbf{v} \tag{1.4.9}$$

$$\frac{d\mathbf{v}}{dt} \equiv \mathbf{v} \times \boldsymbol{\Omega} \tag{1.4.10}$$

then Eq. 1.4.4 says that the variation of f along that trajectory is given by the following one-dimensional equation:

$$\frac{df}{dt} = -\frac{q}{m}(\mathbf{E} + \mathbf{v} \times \mathbf{B}_1) \cdot \frac{\partial f_0}{\partial \mathbf{v}} \tag{1.4.11}$$

Eq. 1.4.4 says nothing at all about the variation of f in any direction other than along the characteristic trajectories.

The method of characteristics can be quite confusing to someone who has not seen it before, so I will embark on a brief conceptual discussion of it. Suppose the distribution function is known at some initial time to be given by $f(\mathbf{x}, \mathbf{v}, t_1) = F_1(\mathbf{x}, \mathbf{v})$,

and one desires to know the function at some later time $f(\mathbf{x},\mathbf{v},t_2)=F_2(\mathbf{x},\mathbf{v})$. Given some specific point $(\mathbf{x}_2,\mathbf{v}_2)$ at time t_2, Eq. 1.4.11 can be used to determine the corresponding value $F_2(\mathbf{x}_2,\mathbf{v}_2)$ in terms of one of the known values $F_1(\mathbf{x}_1,\mathbf{v}_1)$. To do this, one chooses the constants of integration when solving Eqs. 1.4.10 and 1.4.9 such that the solutions for the characteristic trajectories satisfy $\mathbf{x}(t_2)=\mathbf{x}_2$ and $\mathbf{v}(t_2)=\mathbf{v}_2$. This allows one to determine which particular value $F_1(\mathbf{x}_1,\mathbf{v}_1)$ is needed, i.e., the initial value used when solving Eq. 1.4.11 is given by $f(t_1)=F_1(\mathbf{x}(t_1),\mathbf{v}(t_1))$. Then Eq. 1.4.11 is converted to an explicitly one-dimensional equation by substituting the function $\mathbf{v}(t)$ for the variable $\mathbf{v}$ where it appears explicitly in Eq. 1.4.11, and in the v-dependence of $\frac{\partial f_0}{\partial \mathbf{v}}$ and by substituting the function $\mathbf{x}(t)$ where $\mathbf{x}$ appears in $\mathbf{E}(\mathbf{x},t)$ and $\mathbf{B}_1(\mathbf{x},t)$. Once this is accomplished, Eq. 1.4.11 can be integrated from $t=t_1$ to $t=t_2$ to determine the value $f(\mathbf{x}_2,\mathbf{v}_2,t_2)$. Repeating this procedure for every possible endpoint in phase space $(\mathbf{x}_2,\mathbf{v}_2)$ and every possible time t_2 completely determines the distribution function f.

Note that since the constants of integration of Eqs. 1.4.10 and 1.4.9 are functions of the endpoint $(\mathbf{x}_2,\mathbf{v}_2)$, the phase-space dependence of f comes from the explicit dependence of these integration constants on the chosen endpoint. For this reason, it is notationally convenient to choose un-subscripted variables to represent the endpoint. The notation that I will use in the following derivation is to use primed variables to represent the variations described by the kinetic equation and unprimed variables to represent the endpoint. The initial point will be chosen to be at time $t' \rightarrow -\infty$, and the contribution from the initial value at this infinitely remote past time will be neglected. Thus, representing f by an integration along the characteristic trajectory models the non-local behavior on the oscillatory time scale, but neglecting the initial value term is consistent with the local approximation on the equilibrium and transport time scales. In a driven system, this can be justified by invoking the randomizing effect of collisions or turbulence, no matter how small. In a freely oscillating system which may have been perturbed at $t'=-\infty$, this can be justified by first considering only unstable modes and then analytically continuing the results to the case of stable modes. To the extent that the dependence of f on the initial value term is "randomized", one can consider doing an ensemble average over all possible values of the initial value term.† Since the first-order perturbations are pure sinusoidal variations, the initial value term averages to zero.

Writing Eq. 1.4.11 using primed coordinates yields,

---

† Note that ignoring the initial value term will not be valid when treating phenomena such as plasma wave echoes, which only occur if the initial value term is significant.

$$\frac{df(\mathbf{x}'(t'),\mathbf{v}'(t'),t')}{dt'} = \frac{\partial f}{\partial t'} + \mathbf{v}'(t')\cdot\frac{\partial f}{\partial \mathbf{x}'} + \mathbf{v}'(t')\times\mathbf{\Omega}\cdot\frac{\partial f}{\partial \mathbf{v}'}$$
$$= -\frac{q}{m}[\mathbf{E}(\mathbf{x}'(t'),t') + \mathbf{v}'(t')\times\mathbf{B}_1(\mathbf{x}'(t'),t')]\cdot\frac{\partial f_0}{\partial \mathbf{v}'} \qquad (1.4.12)$$

and doing the same for the characteristic equations yields

$$\frac{d\mathbf{x}'(t')}{dt'} \equiv \mathbf{v}'(t') \qquad (1.4.13)$$

$$\frac{d\mathbf{v}'(t')}{dt'} \equiv \mathbf{v}'(t')\times\mathbf{\Omega} \qquad (1.4.14)$$

where $\mathbf{\Omega}$ is a constant for the case of a homogeneous plasma. Showing all variable dependences explicitly, Eq. 1.4.11 becomes

$$\frac{df(\mathbf{x}'(t'),\mathbf{v}'(t'),t')}{dt'} = -\frac{q}{m}[\mathbf{E}(\mathbf{x}'(t'),t') + \mathbf{v}'(t')\times\mathbf{B}_1(\mathbf{x}'(t'),t')]\cdot\frac{\partial f_0([v'_\perp(t')]^2, v'_\parallel(t'))}{\partial \mathbf{v}'} \qquad (1.4.15)$$

and the characteristics are vector functions of the single variable t', which depend parametrically on the endpoint $(t,\mathbf{v},\mathbf{x})$:

$$\mathbf{v}'(t') = \mathbf{v}'(t';t,\mathbf{v}) \qquad (1.4.16)$$

$$\mathbf{x}'(t') = \mathbf{x}'(t';t,\mathbf{v},\mathbf{x}) \qquad (1.4.17)$$

Inverting Eq. 1.4.11 yields the following expression:

$$f(\mathbf{x},\mathbf{v},t) = \int_{-\infty}^{t}\frac{df(\mathbf{x}'(t';t,\mathbf{v},\mathbf{x}),\mathbf{v}'(t';t,\mathbf{v}),t')}{dt'}\,dt' + f(\mathbf{x}_{-\infty},\mathbf{v}_{-\infty},-\infty)$$
$$= -\int_{-\infty}^{t}\frac{q}{m}[\mathbf{E}(\mathbf{x}'(t';t,\mathbf{v},\mathbf{x}),t') + \mathbf{v}'(t';t,\mathbf{v})\times\mathbf{B}_1(\mathbf{x}'(t';t,\mathbf{v},\mathbf{x}),t')]$$
$$\cdot\frac{\partial f_0([v'_\perp(t';t,\mathbf{v})]^2, v'_\parallel(t';t,\mathbf{v}))}{\partial \mathbf{v}'}\,dt' + f(\mathbf{x}_{-\infty},\mathbf{v}_{-\infty},-\infty) \qquad (1.4.18)$$

For a spatially homogeneous plasma, the solutions for the characteristic trajectories are

$$v'_x = v_\perp\cos(\Omega\tau+\alpha) \qquad (1.4.19)$$

$$v'_y = v_\perp\sin(\Omega\tau+\alpha) \qquad (1.4.20)$$

$$v'_z = v_\parallel = \text{const} \qquad (1.4.21)$$

and

$$x' = x - \frac{v_\perp}{\Omega}[\sin(\Omega\tau + \alpha) - \sin\alpha] \tag{1.4.22}$$

$$y' = y + \frac{v_\perp}{\Omega}[\cos(\Omega\tau + \alpha) - \cos\alpha] \tag{1.4.23}$$

$$z' = z - v_\parallel \tau \tag{1.4.24}$$

where the integration constants $\mathbf{v}$ and $\mathbf{x}$ are expressed in cylindrical $(v_\perp, \alpha, v_\parallel)$ and Cartesian (x, y, z) coordinates respectively, and $\tau \equiv t - t'$. It is a general property of the method of characteristics that there is one more integration constant than is necessary to match the boundary conditions (t in this case), and that its value reflects an arbitrary choice of the origin of the variable that measures "distance" along the characteristic trajectory (t' in this case).

Once the equations for the characteristics have been obtained and the initial value term has been dropped, the next step is to substitute the expressions for the characteristics into the equation

$$f(\mathbf{x}, \mathbf{v}, t) = -\frac{q}{m}\int_0^\infty [\mathbf{E}(\mathbf{x}', t') + \mathbf{v}'(t') \times \mathbf{B}_1(\mathbf{x}', t')] \cdot \frac{\partial f_0}{\partial \mathbf{v}'}\, d\tau \tag{1.4.25}$$

A problem arises at this point, because the explicit forms of $\mathbf{E}(\mathbf{x}, t)$ and $\mathbf{B}_1(\mathbf{x}, t)$ are not known. Indeed, these expressions are formally obtained by integrations over the distribution function f, which is the function that we are trying to calculate. Of course this problem can immediately be overcome by expressing the functions f, $\mathbf{E}$, and $\mathbf{B}_1$ in terms of Fourier transforms. In this case the $\mathbf{x}$ and t dependences are explicit, and the problem reduces to determining $\mathbf{k}$ and ω dependences instead. In the case of a spatially homogeneous plasma, the $\mathbf{k}$ and ω dependences are purely algebraic when Eq. 1.4.25 is transformed to Fourier space, and it is sufficient to make the simple substitutions

$$f_j(\mathbf{x}, \mathbf{v}, t) = f_j(\mathbf{k}, \mathbf{v}, \omega) e^{i(\mathbf{k}\cdot\mathbf{x} - \omega t)} \tag{1.4.26}$$

$$\mathbf{E}(\mathbf{x}, t) = (\hat{\mathbf{x}} E_x + \hat{\mathbf{y}} E_y + \hat{\mathbf{z}} E_z) e^{i(\mathbf{k}\cdot\mathbf{x} - \omega t)} \tag{1.4.27}$$

and similarly for $\mathbf{B}_1$ which, from Eq. 1.3.1, is given by

$$\mathbf{B}_1 = \mathbf{N} \times \mathbf{E} \tag{1.4.28}$$

where

$$\mathbf{N} = \hat{\mathbf{x}} N_\perp + \hat{\mathbf{z}} N_\parallel \tag{1.4.29}$$

Making all these substitutions yields

$$\begin{aligned}\mathbf{k}\cdot(\mathbf{x}'-\mathbf{x}) &= k_\perp(y'-y)+k_\parallel(z'-z)\\ &= \lambda[\cos(\Omega\tau+\alpha)-\cos\alpha]-k_\parallel v_\parallel\tau\end{aligned} \tag{1.4.30}$$

where

$$\lambda \equiv \frac{k_\perp v_\perp}{\Omega} = \frac{N_\perp v_\perp}{g} \tag{1.4.31}$$

and

$$f(\mathbf{v}) = -\frac{q}{m}\int_0^\infty e^{-i\{\lambda[\sin(\Omega\tau+\alpha)-\sin\alpha]-(\omega-k_\parallel v_\parallel)\tau\}}[\mathbf{E}+\mathbf{v}'\times(\mathbf{N}\times\mathbf{E})]\cdot\frac{\partial f_0}{\partial \mathbf{v}'}\,d\tau \tag{1.4.32}$$

Now a major simplification occurs if one observes that, directly from Eqs. 1.4.19, 1.4.20, and 1.4.21 for the characteristics, and transforming $\mathbf{v}'$ from Cartesian to cylindrical coordinates, one obtains

$$v_\parallel' = v_\parallel \tag{1.4.33}$$

$$v_\perp'^{\,2} = v_\perp^2 \tag{1.4.34}$$

In this case, the equilibrium distribution function becomes

$$f_0(\mathbf{v}') = f_0(v_\perp'^{\,2}, v_\parallel') = f_0(v_\perp^2, v_\parallel) \tag{1.4.35}$$

and its velocity-space gradient can be written as

$$\hat{\mathbf{x}}\cdot\frac{\partial f_0(\mathbf{v}')}{\partial \mathbf{v}'} = 2v_x'\frac{\partial f_0(\mathbf{v})}{\partial v_\perp^2} \tag{1.4.36}$$

$$\hat{\mathbf{y}}\cdot\frac{\partial f_0(\mathbf{v}')}{\partial \mathbf{v}'} = 2v_y'\frac{\partial f_0(\mathbf{v})}{\partial v_\perp^2} \tag{1.4.37}$$

$$\hat{\mathbf{z}}\cdot\frac{\partial f_0(\mathbf{v}')}{\partial \mathbf{v}'} = \frac{\partial f_0(\mathbf{v})}{\partial v_\parallel} \tag{1.4.38}$$

and all quantities in which primed velocity variables were replaced by unprimed velocity variables may be taken outside the integration in Eq. 1.4.32. The physical significance of this is that $v_\perp^2$ and $v_\parallel$ are constants of the motion and, since the integration in Eq. 1.4.32 is over an actual particle trajectory in phase space, constants of the motion are independent of the integration variable. Re-writing the integrand to exploit the constants of the motion is done by writing

$$[\mathbf{E}+\mathbf{v}'\times(\mathbf{N}\times\mathbf{E})]\cdot\frac{\partial f_0(\mathbf{v}')}{\partial \mathbf{v}'}=A_1v_x'+A_2v_y'+A_3 \tag{1.4.39}$$

where

$$A_1\equiv 2\left[v_\parallel(N_\parallel E_x-N_\perp E_z)\left(\frac{\partial f_0(\mathbf{v})}{\partial v_\parallel^2}-\frac{\partial f_0(\mathbf{v})}{\partial v_\perp^2}\right)+E_x\frac{\partial f_0(\mathbf{v})}{\partial v_\perp^2}\right] \tag{1.4.40}$$

$$A_2\equiv 2\left[N_\parallel v_\parallel E_y\left(\frac{\partial f_0(\mathbf{v})}{\partial v_\parallel^2}-\frac{\partial f_0(\mathbf{v})}{\partial v_\perp^2}\right)+E_y\frac{\partial f_0(\mathbf{v})}{\partial v_\perp^2}\right] \tag{1.4.41}$$

$$A_3\equiv 2E_z\frac{\partial f_0(\mathbf{v})}{\partial v_\parallel^2} \tag{1.4.42}$$

Then Eq. 1.4.32 reduces to

$$f(\mathbf{v})=-\frac{q}{m}e^{i\lambda\sin\alpha}\left(A_1v_\perp\frac{i}{\lambda}\frac{\partial}{\partial\alpha}+iA_2v_\perp\frac{\partial}{\partial\lambda}+A_3v_\parallel\right)I \tag{1.4.43}$$

where the integral I is defined as

$$I=\int_0^\infty e^{-i[\lambda\sin(\Omega\tau+\alpha)-(\omega-k_\parallel v_\parallel)\tau]}\,d\tau \tag{1.4.44}$$

Further progress can be made using the Bessel function identities

$$e^{i\lambda\cos(\Omega\tau+\alpha)}=\sum_{l=-\infty}^{\infty}e^{il(\pi/2-\Omega\tau-\alpha)}J_l(\lambda) \tag{1.4.45}$$

and

$$e^{-i\lambda\cos\alpha}=\sum_{l'=-\infty}^{\infty}e^{-il'(\pi/2-\alpha)}J_{l'}(\lambda) \tag{1.4.46}$$

which allows explicit integration over τ, yielding

$$f(\mathbf{v})=-\frac{q}{m\omega}\sum_l\sum_{l'}\frac{e^{-i(l-l')\alpha}}{1-lg-N_\parallel v_\parallel}\left[i\left(\frac{lg}{N_\perp}A_1+A_3v_\parallel\right)J_l(\lambda)J_{l'}(\lambda)-A_2v_\perp J_l(\lambda)J_{l'}'(\lambda)\right] \tag{1.4.47}$$

An expression for the electric current can now be obtained:

$$\mathbf{J} = \sum_j n_j q_j \int d^3v\, \mathbf{v} f_j(\mathbf{v}) \tag{1.4.48}$$

One of the summations can be performed and the result further simplified using the identities

$$\int_0^{2\pi} d\alpha\, e^{i(l-l')\alpha} = 2\pi\delta_{ll'} \tag{1.4.49}$$

$$\int_0^{2\pi} d\alpha\, \cos\alpha\, e^{i(l-l')\alpha} = \pi(\delta_{l-1,l'} + \delta_{l+1,l'}) \tag{1.4.50}$$

$$\int_0^{2\pi} d\alpha\, \sin\alpha\, e^{i(l-l')\alpha} = i\pi(\delta_{l-1,l'} - \delta_{l+1,l'}) \tag{1.4.51}$$

$$J_{l+1}(\lambda) + J_{l-1}(\lambda) = \frac{2l}{\lambda} J_l(\lambda) \tag{1.4.52}$$

$$J_{l+1}(\lambda) - J_{l-1}(\lambda) = -2J_l'(\lambda) \tag{1.4.53}$$

yielding a wave equation of the form

$$\mathbf{N} \times (\mathbf{N} \times \mathbf{E}) + \mathbf{K} \cdot \mathbf{E} = \mathbf{0} \tag{1.4.54}$$

where the dielectric tensor $\mathbf{K}$ is defined by

$$\mathbf{K} \cdot \mathbf{E} \equiv \mathbf{E} + \frac{i}{\omega}\mathbf{J} \tag{1.4.55}$$

and is given explicitly by

$$\mathbf{K} = \mathbf{I} + 2\pi \sum_j \sum_{l=-\infty}^{\infty} p_j \int_0^{\infty} 2v_\perp\, dv_\perp \int_{-\infty}^{\infty} dv_\parallel \frac{1}{1 - lg_j - N_\parallel v_\parallel} \times \begin{pmatrix} \left(\frac{lg_j}{N_\perp}\right)^2 J_l^2 P_j & i\frac{lg_j}{N_\perp} v_\perp J_l J_l' P_j & \frac{lg_j}{N_\perp} v_\parallel J_l^2 Q_{lj} \\ -i\frac{lg_j}{N_\perp} v_\perp J_l J_l' P_j & (v_\perp J_l')^2 P_j & -iv_\perp v_\parallel J_l J_l' Q_{lj} \\ \frac{lg_j}{N_\perp} v_\parallel J_l^2 P_j & iv_\perp v_\parallel J_l J_l' P_j & (v_\parallel J_l)^2 Q_{lj} \end{pmatrix} \tag{1.4.56}$$

where

$$P_j \equiv \frac{\partial f_{0j}}{\partial v_\perp^2} + N_\parallel v_\parallel \left(\frac{\partial f_{0j}}{\partial v_\parallel^2} - \frac{\partial f_{0j}}{\partial v_\perp^2} \right) \tag{1.4.57}$$

$$Q_{lj} \equiv \frac{\partial f_{0j}}{\partial v_\parallel^2} - l g_j \left(\frac{\partial f_{0j}}{\partial v_\parallel^2} - \frac{\partial f_{0j}}{\partial v_\perp^2} \right) \tag{1.4.58}$$

$$J_l \equiv J_l(\lambda_j) \tag{1.4.59}$$

$$\lambda_j \equiv \frac{N_\perp v_\perp}{g_j} \tag{1.4.60}$$

It is useful to obtain an expression for the dielectric tensor in the case of isotropic Maxwellian equilibrium distribution functions:

$$f_{0j}(\mathbf{v}) = \frac{1}{\pi^{3/2} v_{th_j}^3} e^{-v^2/v_{th_j}^2} \tag{1.4.61}$$

Using the Bessel function identities

$$\int_0^\infty e^{-x} J_l^2(2\beta\sqrt{x})\, dx = I_l(2\beta^2) e^{-2\beta^2} \tag{1.4.62}$$

and

$$\sum_{l=-\infty}^{\infty} I_n(b) e^{-b} = 1 \tag{1.4.63}$$

yields

$$\mathbf{K} = \mathbf{I} + \sum_j \sum_{l=-\infty}^{\infty} p_j\, \zeta_{0j}\, e^{-b_j} \times \begin{pmatrix} \frac{l^2}{b_j} I_l Z & -il(I_l - I_l')Z & -\frac{l g_j}{N_\perp v_{th_j}} I_l Z' \\ il(I_l - I_l')Z & \left[\frac{l^2}{b_j} I_l + 2b_j(I_l - I_l')\right] Z & -i\frac{N_\perp v_{th_j}}{2g_j}(I_l - I_l')Z' \\ -\frac{l g_j}{N_\perp v_{th_j}} I_l Z' & i\frac{N_\perp v_{th_j}}{2g_j}(I_l - I_l')Z' & -I_l \zeta_{lj} Z' \end{pmatrix} \tag{1.4.64}$$

where

$$Z \equiv Z(\zeta_{lj}) \tag{1.4.65}$$

$$I_l \equiv I_l(b_j) \tag{1.4.66}$$

are the plasma dispersion function and modified Bessel function, respectively, and

$$b_j \equiv \frac{k_\perp^2 v_{Tj}^2}{\Omega_j^2} = \frac{N_\perp^2 v_{Tj}^2}{g_j^2} \tag{1.4.67}$$

is the argument of the modified Bessel function, and

$$\zeta_{lj} \equiv \frac{\omega - l\Omega_j}{k_\parallel v_{thj}} = \frac{1 - lg_j}{N_\parallel v_{thj}} \tag{1.4.68}$$

is the argument of the plasma dispersion function, defined as

$$Z(\zeta) = \frac{1}{\sqrt{\pi}} \int_{-\infty}^{\infty} dz \frac{e^{-z^2}}{z - \zeta} \tag{1.4.69}$$

This dielectric tensor can be expanded in terms of a finite-Larmor-radius (FLR) expansion. Using the asymptotic approximations of the plasma dispersion function $Z = Z_r + iZ_i$ given by

$$Z_r(\zeta) \sim \begin{cases} -2\zeta\left(1 - \frac{2}{3}\zeta^2 + \frac{4}{15}\zeta^4 + \cdots\right) & |\zeta| \ll 1 \\ -\frac{1}{\zeta}\left(1 + \frac{1}{2\zeta^2} + \frac{3}{4\zeta^4} + \cdots\right) & |\zeta| \gg 1 \end{cases} \tag{1.4.70}$$

$$Z_i(\zeta) = \sqrt{\pi}\,\mathrm{sgn}(k_z) e^{-\zeta^2} \tag{1.4.71}$$

and the modified Bessel function given by

$$\left.\begin{aligned} e^{-b} I_0(b) &\sim 1 - b + \frac{3}{4}b^2 \\ e^{-b} I_1(b) &\sim \frac{1}{2}b - \frac{1}{2}b^2 \\ e^{-b} I_2(b) &\sim \frac{1}{8}b^2 \end{aligned}\right\}, \qquad b \ll 1 \tag{1.4.72}$$

$$e^{-b} I_l(b) \sim \frac{1}{\sqrt{2\pi b}}\left[1 - \frac{4l^2 - 1}{8b} + \frac{(4l^2 - 1)(4l^2 - 9)}{2!(8b)^2}\right], \quad b \gg 1 \tag{1.4.73}$$

and

$$I_l(b) = I_{-l}(b) \tag{1.4.74}$$

yields

$$\mathbf{K} = \mathbf{K}_C + \mathbf{K}_1(k_\parallel) + \mathbf{K}_H(k_\perp^2(, k_\parallel)) + \mathbf{K}_2(\mathbf{k}) \tag{1.4.75}$$

where $\mathbf{K}_C$ is the cold-plasma dielectric tensor

$$\mathbf{K}_C = \begin{pmatrix} S & -iD & 0 \\ iD & S & 0 \\ 0 & 0 & P \end{pmatrix} \tag{1.4.76}$$

$\mathbf{K}_1$ contains the leading order contributions from Landau damping and fundamental cyclotron damping

$$\mathbf{K}_1 = \sum_j \begin{pmatrix} iL_{1j}^+ & -L_{1j}^- & 0 \\ L_{1j}^- & iL_{1j}^+ & 0 \\ 0 & 0 & -\frac{1}{2}iL_{0j}' \end{pmatrix} \tag{1.4.77}$$

$\mathbf{K}_H$ contains the leading order contributions from hot-plasma waves

$$\mathbf{K}_H = \begin{pmatrix} K_{xx}^H & K_{xy}^H & K_{xz}^H \\ -K_{xy}^H & K_{yy}^H & K_{yz}^H \\ -K_{xz}^H & -K_{yz}^H & K_{zz}^H \end{pmatrix} \tag{1.4.78}$$

where

$$K_{xx}^H = \sum_j b_j p_j \left[\frac{1}{1-g_j^2} - \frac{1}{1-4g_j^2} - \frac{N_\parallel^2}{N_\perp^2} g_j^2 \frac{1+3g_j^2}{(1-g_j^2)^3} \right] \tag{1.4.79}$$

$$K_{xy}^H = i \sum_j 2 b_j p_j g_j \left[\frac{1}{1-g_j^2} - \frac{1}{1-4g_j^2} - \frac{N_\parallel^2}{2N_\perp^2} g_j^2 \frac{3+g_j^2}{(1-g_j^2)^3} \right] \tag{1.4.80}$$

$$K_{xz}^H = -2 \frac{N_\parallel}{N_\perp} \sum_j b_j p_j \frac{g_j^2}{(1-g_j^2)^2} \tag{1.4.81}$$

$$K_{yy}^H = \sum_j b_j p_j \left[\frac{1+2g_j^2}{1-g_j^2} - \frac{1}{1-4g_j^2} - \frac{N_\parallel^2}{N_\perp^2} g_j^2 \frac{1+3g_j^2}{(1-g_j^2)^3} \right] \tag{1.4.82}$$

$$K_{yz}^H = -i \frac{N_\parallel}{N_\perp} \sum_j b_j p_j g_j \left[1 - \frac{1+g_j^2}{(1-g_j^2)^2} \right] \tag{1.4.83}$$

$$K_{zz}^H = -\sum_j b_j p_j g_j^2 \left(3 \frac{N_\parallel^2}{N_\perp^2} + \frac{1}{1-g_j^2} \right) \tag{1.4.84}$$

and $\mathbf{K}_2$ contains the leading order contributions from second harmonic cyclotron damping

$$\mathbf{K}_2 = \sum_j b_j \begin{pmatrix} i(L_{2j}^+ - L_{1j}^+) & -(L_{2j}^- - 2L_{1j}^-) & -i\frac{g_j}{N_\perp v_{thj}} L_{1j}^{-\prime} \\ (L_{2j}^- - 2L_{1j}^-) & i(2L_{0j} + L_{1j}^+ + L_{2j}^+) & -\frac{g_j}{N_\perp v_{thj}}(L_{1j}^{+\prime} - L_{0j}^{\prime}) \\ i\frac{g_j}{N_\perp v_{thj}} L_{1j}^{-\prime} & \frac{g_j}{N_\perp v_{thj}}(L_{1j}^{+\prime} - L_{0j}^{\prime}) & -\frac{1}{2}i(L_{1j}^{+\prime} - L_{0j}^{\prime}) \end{pmatrix} \tag{1.4.85}$$

where

$$L_{lj}^{\pm} = \frac{\sqrt{\pi}}{2} p_j \zeta_{0j} (e^{-\zeta_{lj}^2} \pm e^{-\zeta_{-lj}^2}) \tag{1.4.86}$$

$$L_{lj}^{\pm\prime} = -\sqrt{\pi} p_j \zeta_{0j} (\zeta_{lj} e^{-\zeta_{lj}^2} \pm \zeta_{-lj} e^{-\zeta_{-lj}^2}) \tag{1.4.87}$$

Note that $\mathbf{K}_C$ is completely independent of the wave vector $\mathbf{k}$. This indicates that in the cold-plasma limit, the response is local, without the need for further approximation. $\mathbf{K}_1$ depends only on $k_\parallel$ and is exponentially small except near a Landau or fundamental cyclotron resonance. $\mathbf{K}_H$ depends primarily on $k_\perp$, and the weak $k_\parallel$ dependence is often neglected in calculations. Similarly, for the second-harmonic contribution in $\mathbf{K}_2$, only the $k_\perp^2$ dependence through b_j is usually kept, along with the $k_\parallel$ dependence from the Landau and cyclotron damping terms. Also note that $\mathbf{K}_C$ and $\mathbf{K}_1$ are leading order in the FLR expansion while $\mathbf{K}_H$ and $\mathbf{K}_2$ are first order.

A calculation of the hot-plasma dispersion relation as a function of position for a pure deuterium plasma is shown in Fig. 1.4.1. The deuterium second harmonic cyclotron resonance occurs at the plasma center ($x = 0$). The dispersion relation for the fast wave is similar to the cold-plasma case, except that some absorption is evident from the small imaginary part of N_x, and there is a slight perturbation of the fast wave polarization near the cyclotron resonance. Note the correspondence between the slight enhancement of the polarization and the asymmetry of the absorption region. The ion Bernstein wave, which is not predicted by cold-plasma theory, is present and propagates only on the high-field side of the cyclotron resonance. (In general, the IBW actually has regions of propagation between all harmonics of the cyclotron frequency.[62]) There is the possibility of mode conversion between the IBW and the FW at the point where the curves cross in the first plot. Mode conversion is relatively weak in the case of a pure deuterium plasma, compared with the following two-ion-species cases. The polarization of the IBW is linear, except for a slight perturbation near the center of the plasma. This indicates that the IBW is predominately electrostatic in nature.

The same calculation for the case of a 1% concentration of hydrogen is shown in Fig. 1.4.2. There is now a nonzero E_+ component of the FW at the position of the

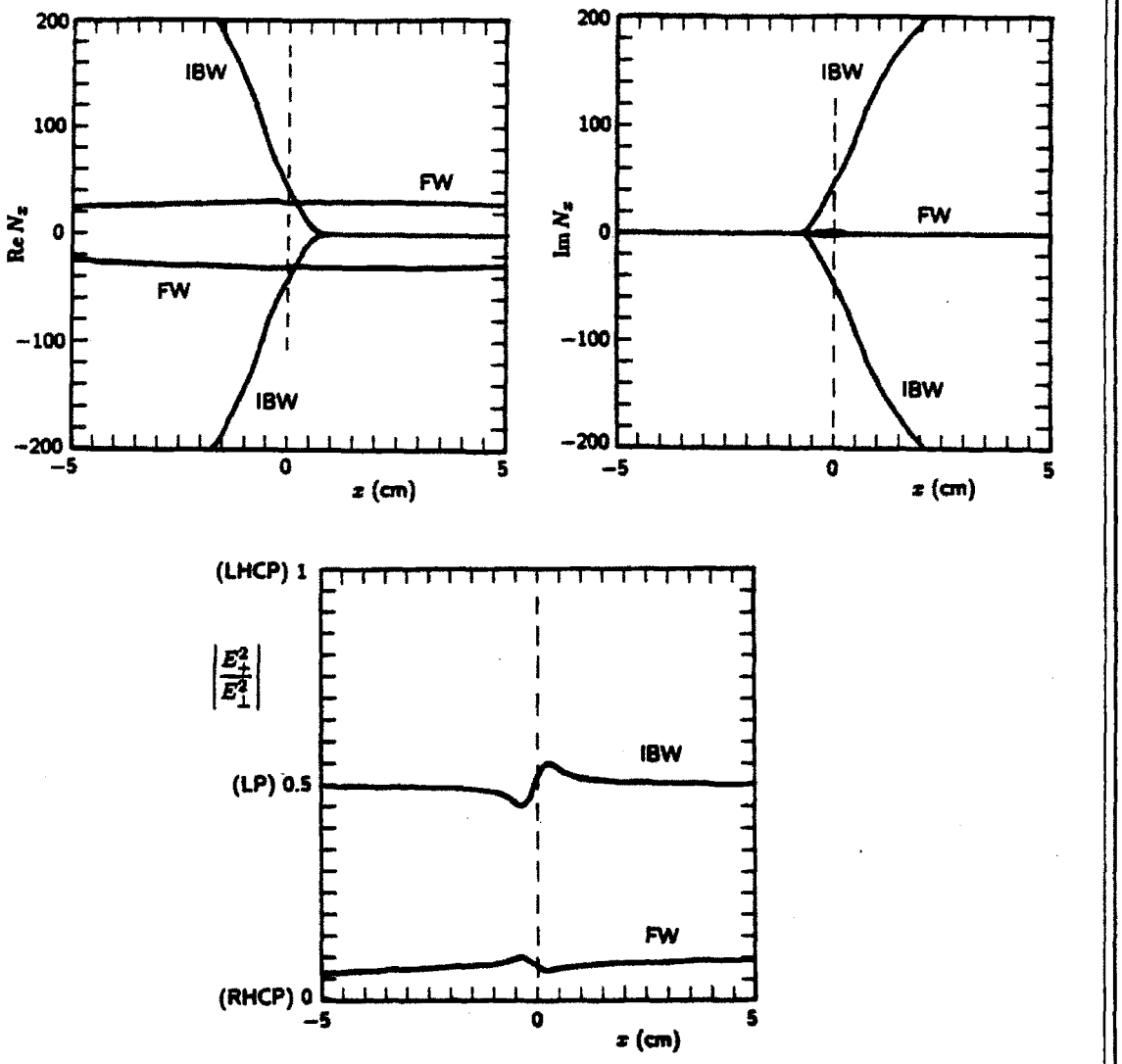

Figure 1.4.1: Hot Plasma Dispersion Relation for Deuterium Second Harmonic—The real and imaginary parts of N_z and the wave polarization are shown for a pure deuterium plasma with Alcator C parameters. The cyclotron resonance $\omega = 2\omega_{cD}$ $(= \omega_{cH})$ is at $z = 0$ and the high magnetic field side is at the left on these plots. The plasma parameters for this plot and those that follow are the same as for the corresponding cold-plasma dispersion relation plots in Sec. 1.3, except that all ion species have a central temperature of 1 keV and the electron central temperature is 1.8 keV. The temperatures have a parabolic squared profile shape. Peak electron density is $n_{e0} = 4 \times 10^{20}\,\mathrm{m}^{-3}$ and a single plane wave at $N_\parallel = 5$ is assumed. Only the central 5 cm is shown for a plasma with minor radius $a = 12.5$ cm. (Dispersion relation code courtesy of Dr. A. Ram of MIT.)

cyclotron resonance, and there is significant enhancement of both N_z and E_+ at the position of the cold-plasma two ion hybrid resonance layer. The corresponding

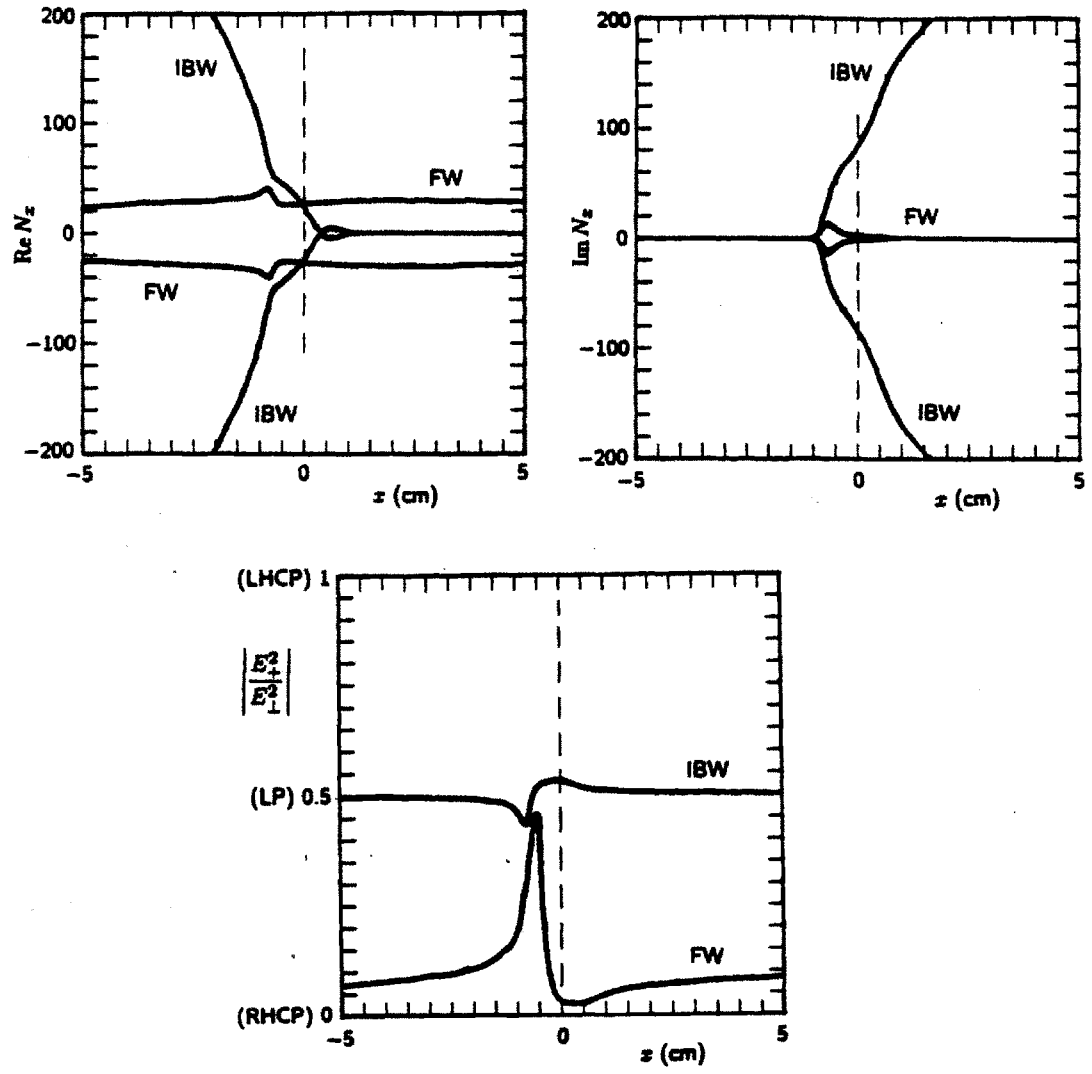

Figure 1.4.2: Hot Plasma Dispersion Relation for 1% Hydrogen Minority in Deuterium—With a very small minority concentration, N_x and E_+ are both enhanced in the vicinity of the cold-plasma two-ion hybrid resonance and the "shorting out" effect of E_+ is suppressed at the center, where the minority species is at fundamental cyclotron resonance. The left-hand cut-off is completely absent.

effect in Im N_x for the FW is suggestive of enhanced absorption, an effect caused by the overlap of the Doppler-shifted cyclotron absorption region and the hybrid resonance layer. The IBW is still predominately electrostatic in nature.

The effect of raising the minority concentration to 2.5% is shown in Fig. 1.4.3. In this case, there is a mode-conversion (MC) region in which N_x is the same for both waves, and strong mode conversion is to be expected. There is still no left-hand

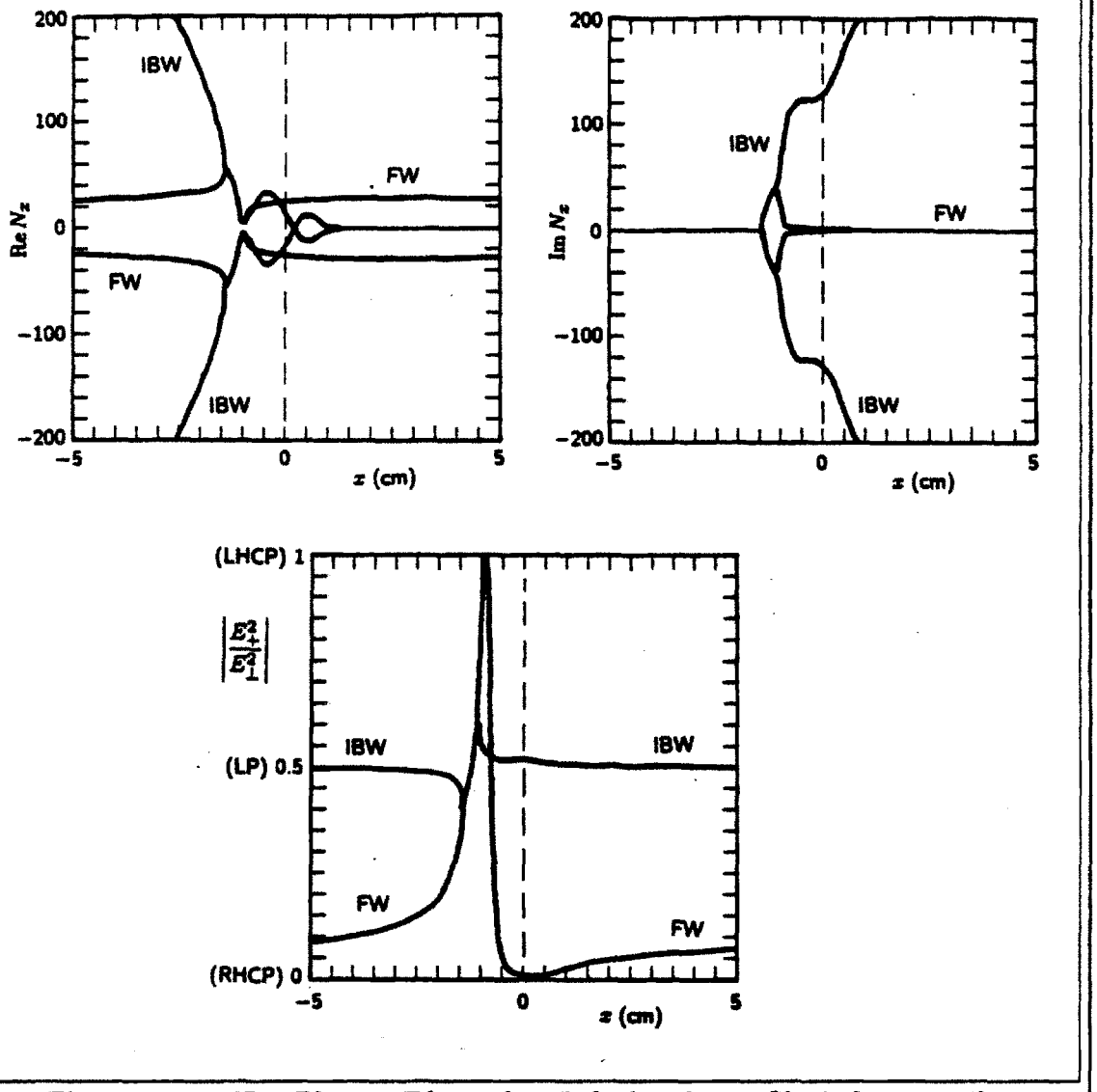

Figure 1.4.3: Hot Plasma Dispersion Relation for 2.5% Hydrogen Minority in Deuterium—As the minority concentration is increased, the dispersion relation exhibits coupling between the IBW and FW modes, but there is still no left-hand cut-off of the fast wave.

cut-off of the FW. The effect on the wave polarization is quite pronounced. There is even a point where the polarization becomes pure LHCP, which is suggestive of the slow electromagnetic cold-plasma wave. As was mentioned in Sec. 1.3, the cold-plasma fast wave mode-converts to the cold-plasma slow wave at this point ($N_{\|}^2 = S$) and the slow wave then exhibits a resonance at $S = 0$. In hot plasma theory, the identification of the modes becomes ambiguous. If one wishes, one can think of this process as mode conversion of the fast wave to the slow cold-plasma wave, followed

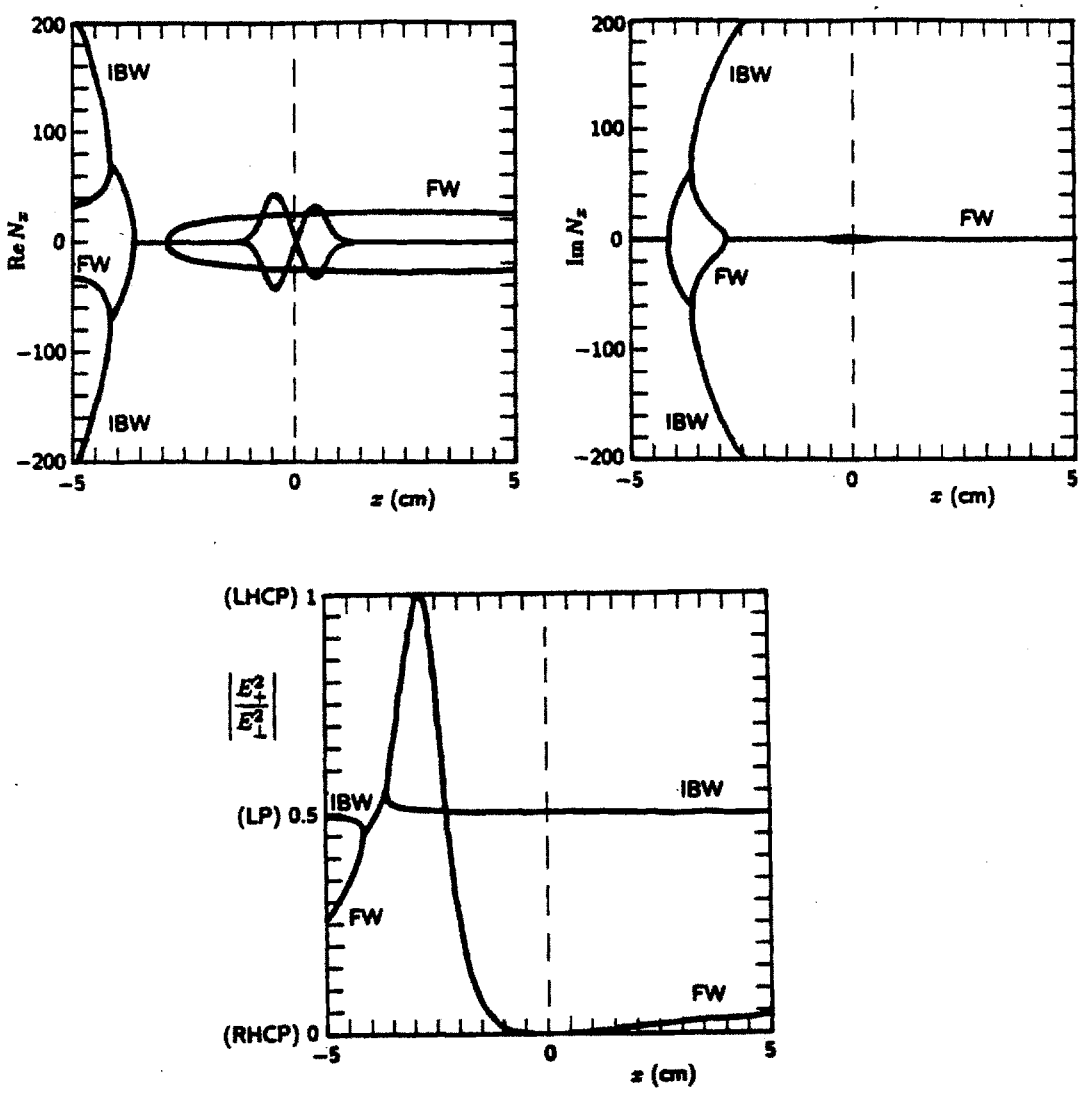

Figure 1.4.4: Hot Plasma Dispersion Relation for 10% Hydrogen Minority in Deuterium—At high minority concentration, E_+ is again "shorted out" at the position of the cyclotron resonance, and the left-hand cut-off is present.

by transformation of the slow wave to the IBW. In this case, the wave would be considered to be the slow wave where the polarization is LHCP and the IBW where the polarization is linear. Some authors prefer not to distinguish between the cold-plasma slow wave and the IBW, and instead speak of "electromagnetic corrections" to the IBW dispersion relation.

The hot-plasma dispersion relation for the case of 10% minority concentration is shown in Fig. 1.4.4. In this case, the behavior of the FW near the cyclotron resonance layer is similar to the cold-plasma case. The FW is pure RHCP at

the cyclotron resonance and there is a left-hand cut-off. In this regime, a FW launched from the low-field side would be expected to be predominately reflected, with relatively little absorption or mode-conversion. A FW launched from the high-field side would be efficiently mode-converted.

A simple and very useful expression for estimating the distribution of RF power between hydrogen fundamental cyclotron absorption and deuterium second harmonic cyclotron absorption can be easily obtained analytically from the hot plasma dielectric tensor. The procedure to be followed is to calculate the absorbed power density in slab geometry using the expression

$$Q = -\frac{1}{4} i\omega \mathbf{E}^* \cdot \mathbf{K} \cdot \mathbf{E} + \text{c.c.} \tag{1.4.88}$$

retaining only terms involving E_+ and keeping terms from hydrogen fundamental and deuterium second harmonic absorption separate. Making the small-electron-mass approximation, so that only the upper left 2×2 submatrix of $\mathbf{K}$ is involved, the terms involving E_+ are

$$\mathbf{E}^* \cdot \mathbf{K} \cdot \mathbf{E} = (K_{xx} + 2K_{xy} + K_{yy})|E_+|^2 \tag{1.4.89}$$

Expanding the Bessel functions J_1 and J_2 to leading order in the FLR expansion and performing the velocity integrations assuming Maxwellian distribution functions for both species, one readily obtains

$$Q_H = \frac{\omega}{2} \frac{p\eta_H}{\sqrt{\pi}} \frac{|E_+|^2}{N_\parallel v_{thH}} \exp\left[-\left(\frac{1-g}{N_\parallel v_{thH}}\right)^2\right] \tag{1.4.90}$$

$$Q_D = \frac{\omega}{2} \frac{p\beta_D}{\sqrt{\pi}} \frac{|E_+|^2}{N_\parallel v_{thD}} \exp\left[-\left(\frac{1-g}{N_\parallel v_{thD}}\right)^2\right] \tag{1.4.91}$$

where

$$p \equiv \frac{ne^2}{m_H \omega^2} \tag{1.4.92}$$

$$g \equiv \frac{eB}{m_H \omega} \tag{1.4.93}$$

$$\eta_H \equiv \frac{n_H}{n_D} \tag{1.4.94}$$

$$\beta_D \equiv \frac{n_D T_D}{\frac{1}{2}B^2} \tag{1.4.95}$$

And the fast-wave dispersion relation was approximated by that of a compressional Alfvén wave in order to evaluate $k_\perp^2$. Next, since $g = \Omega_H/\omega = B/B_0 = R_0/R$, one has $1 - g \approx r/R_0$, yielding an expression for the e-folding width, due to Doppler broadening, of the absorption layer

$$\delta = R_0 N_\parallel v_{th} \tag{1.4.96}$$

Now treating all quantities except $1 - g$ as constants and integrating across the absorption layer yields

$$P_H = A \int_{-\infty}^{\infty} Q_H(r)\, dr = \frac{\omega}{2} p \eta_H |E_+|^2 R_0 A \tag{1.4.97}$$

$$P_D = A \int_{-\infty}^{\infty} Q_H(r)\, dr = \frac{\omega}{2} p \beta_D |E_+|^2 R_0 A \tag{1.4.98}$$

where A is the cross-sectional area of the plasma slab, and taking the ratio between these two equations yields simply

$$\frac{P_D}{P_H} = \frac{\beta_D}{\eta_H} \tag{1.4.99}$$

As long as the distribution functions for both species remain approximately Maxwellian, and as long as the contribution to absorption from E_+ dominates, Eq. 1.4.99 provides a very useful way to estimate the importance of direct deuterium second harmonic absorption in an ICRF experiment.

1.5: Inhomogeneous Plasma Wave Theory

In this section, a more careful treatment of the mathematical implications of plasma spatial inhomogeneity will be given. The details of this derivation in its most rigorously correct form are much too complicated to be given here, so I will instead adopt a more formal and abstract approach than I have used so far. The purpose here is not to cloud the mind with myriads of detailed mathematical expressions, but rather to develop an understanding of the structure of the analysis.

The last expression written in Sec. 1.4 that was valid in general for a spatially inhomogeneous plasma was the phase integral, given by

$$f(\mathbf{x}, \mathbf{v}, t) = -\frac{q}{m} \int_0^{\infty} [\mathbf{E}(\mathbf{x}', t') + \mathbf{v}'(t') \times \mathbf{B}_1(\mathbf{x}', t')] \cdot \frac{\partial f_0}{\partial \mathbf{v}'}\, d\tau \tag{1.5.1}$$

At this point, it is to be understood that f_0 is no longer a function only of $\mathbf{v}$, but depends on space too. For example, in general the zero-order distribution function would be of the form $f_0(\mathbf{x}, \mathbf{v})$, in slab geometry the form would be $f_0(x, \mathbf{v})$, and in toroidal geometry the form would be $f_0(\psi, \mathbf{v})$. Now consider the velocity dependence more closely. In Sec. 1.4 it was found to be very useful to write the velocity dependence in terms of the constants of the motion for the unperturbed particle orbits. For an inhomogeneous plasma, these constants are no longer $(v_\perp^2, v_\parallel)$, but are now (E, μ) where $E = mv^2/2$ is the particle kinetic energy,† and $\mu = mv_\perp^2/(2B)$ is the magnetic moment.

Consider next what will happen when Fourier transformation is used in Eq. 1.5.1. This transformation is defined by

$$f(\mathbf{x}, \mathbf{v}, t) = \int_{-\infty}^{\infty} \frac{d^3k}{(2\pi)^3} \int_{-\infty}^{\infty} \frac{d\omega}{2\pi} e^{i(\mathbf{k}\cdot\mathbf{x} - \omega t)} f(\mathbf{k}, \mathbf{v}, \omega) \tag{1.5.2}$$

$$f(\mathbf{k}, \mathbf{v}, \omega) = \int_{-\infty}^{\infty} d^3x \int_{-\infty}^{\infty} dt\, e^{-i(\mathbf{k}\cdot\mathbf{x} - \omega t)} f(\mathbf{x}, \mathbf{v}, t) \tag{1.5.3}$$

and similarly for the quantities $\mathbf{E}$, $\mathbf{B}_1$, f_0, and also, in principle, $\mathbf{v}'$. Fourier transformation is useful here because when expressing $\mathbf{B}_1$ in terms of $\mathbf{E}$, the differential curl operator is replaced by a simpler algebraic cross product. When quantities are expressed in terms of their transforms in Eq. 1.5.1, the product of $\mathbf{E}$ and $\frac{\partial f_0}{\partial \mathbf{v}'}$ will lead to a convolution integral, which introduces some complication into the analysis. Additional complication is introduced because in general $\mathbf{v}'$ also depends on $\mathbf{x}$, which will lead to a double convolution integral. Simplifying approximations are often made in which some complication is avoided by retaining spatial variation in f_0, but neglecting spatial variation in $\mathbf{B}_0$ ($\boldsymbol{\Omega}$) or treating magnetic field gradients in an approximate way by including ∇B-driven particle drifts when calculating the unperturbed orbits, but assuming that both $\boldsymbol{\Omega}$ and the particle drifts are spatially homogeneous. To see how this kind of approximation affects the analysis, note that the magnetic field is the only driving term in the equations for the characteristic trajectories:

$$\frac{d\mathbf{x}'(t')}{dt'} \equiv \mathbf{v}'(t') \tag{1.5.4}$$

$$\frac{d\mathbf{v}'(t')}{dt'} \equiv \mathbf{v}'(t') \times \boldsymbol{\Omega} \tag{1.5.5}$$

† Note that the symbol E is being overloaded. In the literature it is fairly common to see E used to represent kinetic energy and $\mathbf{E}$ used to represent the electric field, with surprisingly little confusion as a result.

As shown explicitly in Sec. 1.4, if $\mathbf{\Omega}$ is not a function of $\mathbf{x}$, then the solution of Eq. 1.5.5 is of the form $\mathbf{v}'(t';t,\mathbf{v})$, and the only $\mathbf{x}$-dependence in the solution of Eq. 1.5.4 comes from a simple integration constant. However, if $\mathbf{\Omega}=\mathbf{\Omega}(\mathbf{x})$, then the solution of Eq. 1.5.5 will be of the form $\mathbf{v}'(t';t,\mathbf{v},\mathbf{x})$ so that the solution to Eq. 1.5.4 then becomes

$$\mathbf{x}' = \mathbf{x} - \int_{t'}^{t} \mathbf{v}'(s;t,\mathbf{v},\mathbf{x})\,ds \equiv \mathbf{x} - \mathbf{X}(t';t,\mathbf{v},\mathbf{x}) \tag{1.5.6}$$

In addition to the double convolution integral that results from the $\mathbf{x}$-dependence of $\mathbf{v}'$, complication is also introduced by the $\mathbf{x}$-dependence of $\mathbf{X}$. Thus, it is tempting to ignore either nonuniform particle drifts or nonuniform magnetic field when calculating the particle trajectories. This approximation can be justified physically by again invoking the randomizing effects of collisions or turbulence, so that only the portion of the particle trajectory in the vicinity of $\mathbf{x}$ is important.

In the following simplified presentation, consider neglecting the $\mathbf{x}$-dependences of both $\mathbf{v}'$ and $\mathbf{X}$, in which case Eq. 1.5.1 can be written formally as follows:

$$f(\mathbf{x},\mathbf{v},t) = -\int_0^\infty \mathbf{F}(\mathbf{x}',\mathbf{v}',t')\cdot\frac{\partial}{\partial\mathbf{v}'}f_0(\mathbf{v}',\mathbf{x}')\,d\tau \tag{1.5.7}$$

Writing each spatially dependent quantity in terms of its Fourier transform, and then inverse transforming both sides of this equation yields

$$f(\mathbf{k},\mathbf{v},\omega) = -\int d^3x \int_{-\infty}^{\infty} dt\, e^{-i(\mathbf{k}\cdot\mathbf{x}-\omega t)} \int_0^\infty d\tau \int \frac{d^3k''}{(2\pi)^3}\int_{-\infty}^{\infty}\frac{d\omega''}{2\pi}\times$$
$$\mathbf{F}(\mathbf{k}'',\mathbf{v}',\omega'')e^{i(\mathbf{k}''\cdot\mathbf{x}'-\omega''t')}\cdot\frac{\partial}{\partial\mathbf{v}'}\int\frac{d^3k'}{(2\pi)^3}f_0(\mathbf{v}',\mathbf{k}')e^{i\mathbf{k}'\cdot\mathbf{x}'} \tag{1.5.8}$$

At this point, one exploits the fact that f_0 depends only on the constants of the unperturbed motion. By doing this, one can eliminate the τ-dependence of f_0 which comes from the τ-dependence of $\mathbf{v}'$. In general, the constants of the motion Q' are functions of both $\mathbf{x}'$ and $\mathbf{v}'$, but for simplicity I will assume only $\mathbf{v}'$ dependence. Thus, if the constants of the motion are denoted by $Q'_m(\mathbf{v}')$, then one can write

$$\frac{\partial}{\partial\mathbf{v}'}f_0(\mathbf{v}') = \sum_m \frac{\partial Q'_m(\mathbf{v}')}{\partial\mathbf{v}'}\frac{\partial f_0(\mathbf{v})}{\partial Q_m(\mathbf{v})} \tag{1.5.9}$$

Rearranging the integrations, making use of $\mathbf{x}'=\mathbf{x}-\mathbf{X}$ and $t'=t-\tau$, and taking advantage of the assumption that $\mathbf{X}$ is not a function of $\mathbf{x}$, yields

$$f(\mathbf{k},\mathbf{v},\omega) = -\int_0^\infty d\tau \int d^3k'' \int_{-\infty}^\infty d\omega'' \int \frac{d^3k'}{(2\pi)^3} \underbrace{\int \frac{d^3x}{(2\pi)^3} e^{i\mathbf{x}\cdot[\mathbf{k}''-(\mathbf{k}-\mathbf{k}')]}}_{\delta(\mathbf{k}''-[\mathbf{k}-\mathbf{k}'])} \underbrace{\int \frac{dt}{2\pi} e^{it(\omega-\omega'')}}_{\delta(\omega-\omega'')}$$

$$\times e^{-i(\mathbf{k}''\cdot\mathbf{X}-\omega''\tau)} e^{-i\mathbf{k}'\cdot\mathbf{X}} \mathbf{F}(\mathbf{k}'',\mathbf{v}',\omega'') \cdot \sum_m \frac{\partial Q_m'}{\partial \mathbf{v}'} \frac{\partial f_0(Q_m,\mathbf{k}')}{\partial Q_m}$$

$$= \int \frac{d^3k'}{(2\pi)^3} \int_0^\infty d\tau\, e^{-i(\mathbf{k}\cdot\mathbf{X}-\omega\tau)} \mathbf{F}(\mathbf{k}-\mathbf{k}',\mathbf{v}',\omega) \cdot \sum_m \frac{\partial Q_m}{\partial \mathbf{v}'} \frac{\partial f_0(Q_m,\mathbf{k}')}{\partial Q_m} \tag{1.5.10}$$

The current $\mathbf{J}$ can now be written as

$$\mathbf{J}(\mathbf{k},\omega) = \sum_j n_j q_j \int d^3v\, \mathbf{v} f_j(\mathbf{k},\mathbf{v},\omega)$$

$$\equiv i\omega \left[\mathbf{E}(\mathbf{k},\omega) - \int \frac{d^3k'}{(2\pi)^3} \mathbf{K}(\mathbf{k},\mathbf{k}',\omega)\cdot\mathbf{E}(\mathbf{k}',\omega)\right] \tag{1.5.11}$$

where $\mathbf{K}$ is often referred to as the *dielectric kernel*, and the wave equation can be written as

$$\nabla\times(\nabla\times\mathbf{E}) - \omega^2 \int d^3x'\, \mathbf{K}(\mathbf{x},\mathbf{x}')\cdot\mathbf{E}(\mathbf{x}') = 0 \tag{1.5.12}$$

or as

$$\mathbf{k}\times(\mathbf{k}\times\mathbf{E}) + \omega^2 \int \frac{d^3k'}{(2\pi)^3} \mathbf{K}(\mathbf{k},\mathbf{k}')\cdot\mathbf{E}(\mathbf{k}') = 0 \tag{1.5.13}$$

where $\mathbf{K}(\mathbf{k},\mathbf{k}')$ is the double Fourier transform of $\mathbf{K}(\mathbf{x},\mathbf{x}')$. Thus, for a spatially inhomogeneous plasma, the wave equation is no longer a differential equation. Eq. 1.5.12 is a Fredholm integro-differential equation. As suggested here, the best way to solve Eq. 1.5.12 is to stay in Fourier transform space, in which case the differential part of the equation becomes algebraic, and one is left with Eq. 1.5.13, which is a Fredholm integral equation of the second kind.

Straightforward discretization reduces Eq. 1.5.13 to an algebraic matrix equation. However, rather than directly discretizing Eq. 1.5.13, there may be advantages in first making use of conventional Hilbert-Schmidt theory. In this method, solutions for eigenfunctions and corresponding eigenvalues of a simple integral eigenvalue problem are first obtained. Then, the dielectric tensor is written in terms of these eigenvalues and eigenfunctions via a Hilbert-Schmidt expansion. Eq. 1.5.13 would then be used to express the desired solutions in terms of the previously determined eigenvalues and eigenfunctions. The advantage of the Hilbert-Schmidt expansion is

that the dielectric kernel is expressed as a sum of products of functions of $\mathbf{k}$ only and functions of $\mathbf{k}'$ only. This reduces the integral equation to a matrix equation without the need (in principle) for numerical discretization and therefore could conceivably yield approximate analytic solutions. To the best of my knowledge, this technique has not yet been applied to this problem.

A very elegant technique for solving Eq. 1.5.13 is via an FLR expansion, which allows the integro-differential equation (Eq. 1.5.12) to be approximated by a differential equation. This is done by transforming from real space to Fourier space and then back again, using a variational formulation as described by Colestock and Kashuba[68]. This variational method was developed by Berk, *et al.*[69] The variational form of Eq. 1.5.12 is

$$\int d^3x\, \mathbf{E}^\dagger(\mathbf{x}) \cdot \left\{ -\boldsymbol{\nabla} \times [\boldsymbol{\nabla} \times \mathbf{E}(\mathbf{x})] + \omega^2 \int d^3x'\, \mathbf{K}(\mathbf{x},\mathbf{x}') \cdot \mathbf{E}(\mathbf{x}') \right\} = 0 \qquad (1.5.14)$$

where $\mathbf{E}^\dagger$ is the solution of the adjoint of Eq. 1.5.12. Eq. 1.5.14 can be rewritten in terms of transformed quantities as

$$\int \frac{d^3k}{(2\pi)^3} \mathbf{E}^\dagger(-\mathbf{k}) \cdot \left\{ \mathbf{k} \times [\mathbf{k} \times \mathbf{E}(\mathbf{k})] + \omega^2 \int \frac{d^3k'}{(2\pi)^3} \mathbf{K}(\mathbf{k},\mathbf{k}') \cdot \mathbf{E}(\mathbf{k}') \right\} = 0 \qquad (1.5.15)$$

The FLR expansion of the dielectric kernel (written in one dimension to avoid a notational nightmare) is of the form

$$K(k,k') = \sum_{n,m}^{N} K^{(n,m)}(0,0) k^n k'^m \qquad (1.5.16)$$

where the dielectric tensor has been Taylor expanded about $k = 0$, $k' = 0$. When Eq. 1.5.16 is substituted into Eq. 1.5.15, the powers of k are brought outside the k'-integration and instead grouped with the $\mathbf{E}^\dagger(k)$. When the resulting equation is transformed back into x-space, derivatives of $\mathbf{E}^\dagger(x)$ are introduced via

$$\int \frac{dk}{2\pi} k^m E(k) e^{ikx} = (-i)^m \frac{d^m E}{dx^m} \qquad (1.5.17)$$

and, similarly, the powers of k' introduce derivatives of $\mathbf{E}$. Partial integration is used to eliminate the derivatives of $\mathbf{E}^\dagger$, which can then be factored out of each term, resulting in a differential equation of the form

$$\frac{\partial}{\partial x} \mathbf{G}(x) \frac{\partial}{\partial x} \cdot \mathbf{E}(x) + \mathbf{F}(x) \cdot \frac{\partial}{\partial x} \mathbf{E}(x) + \mathbf{H}(x) \cdot \mathbf{E}(x) = 0 \qquad (1.5.18)$$

This method resolves an ambiguity which arises when one attempts to construct a wave differential equation directly from the homogeneous plasma dispersion relation. It is important to keep in mind that this derivation is based on an FLR expansion, and therefore can yield inaccurate results for short-wavelength modes, such as the IBW. Note also that the number of terms N kept in the Taylor series expansion of the dielectric kernel is an arbitrary choice which influences the order of the resulting differential equation. If more terms are kept in the expansion, nonphysical wave modes are introduced, which must be dealt with during calculations. That is, one must make certain that higher order derivatives result in small corrections to solutions that would be obtained with the lower order equations, and not in introduction of new solutions. These nonphysical solutions would have very short wavelengths, and the FLR expansion would not be valid for them. This problem is quite analogous to what happens when one attempts to solve the transcendental equation $e^x = 0$ by approximating it by an algebraic equation obtained by truncating the Taylor series expansion of e^x.

Note also that the key to the success of the FLR expansion in the variational expression is that the dielectric tensor $\mathbf{K}$ is written as a sum of products of functions of $\mathbf{k}$ and of $\mathbf{k}'$. This again suggests that a method based on a Hilbert-Schmidt expansion might be useful, perhaps in situations where the IBW wavelength is too short to allow accurate solutions with the FLR expansion.

Results from the plasma wave code METS for typical high-density Alcator C parameters are shown in Fig. 1.5.1. METS is a computer program which was written by D. Smithe of the Princeton Plasma Physics Laboratory, and solves the one-dimensional version of Eq. 1.5.18 using slab geometry. Explicit expressions for the coefficients used in Eq. 1.5.18 are given by Eqs. 10 and A24 in Ref. 68. The code described in Ref. 68 uses a Runge-Kutta numerical integration technique which is very sensitive to contamination by the evanescent IBW on the low-field side of the absorption layer. In METS, this problem is eliminated by using a spectral method instead. The METS code is a so-called single-pass code, in which a particular wave mode (the fast wave in these calculations) is assumed incident at the center of the plasma, coming from either the high-field side or the low-field side. When the wave reaches the absorption layer at the center of the plasma, it is partially absorbed, partially reflected, partially transmitted to the other side, and partially mode-converted to the IBW. Outgoing waves are assumed to propagate away without being reflected from walls.

No physics relevant to antenna coupling is included in this calculation. Instead, for each chosen value of $k_{\|}$, a calculation is performed as if all the power was concentrated at that particular value of $k_{\|}$, i.e., separate calculations are done for

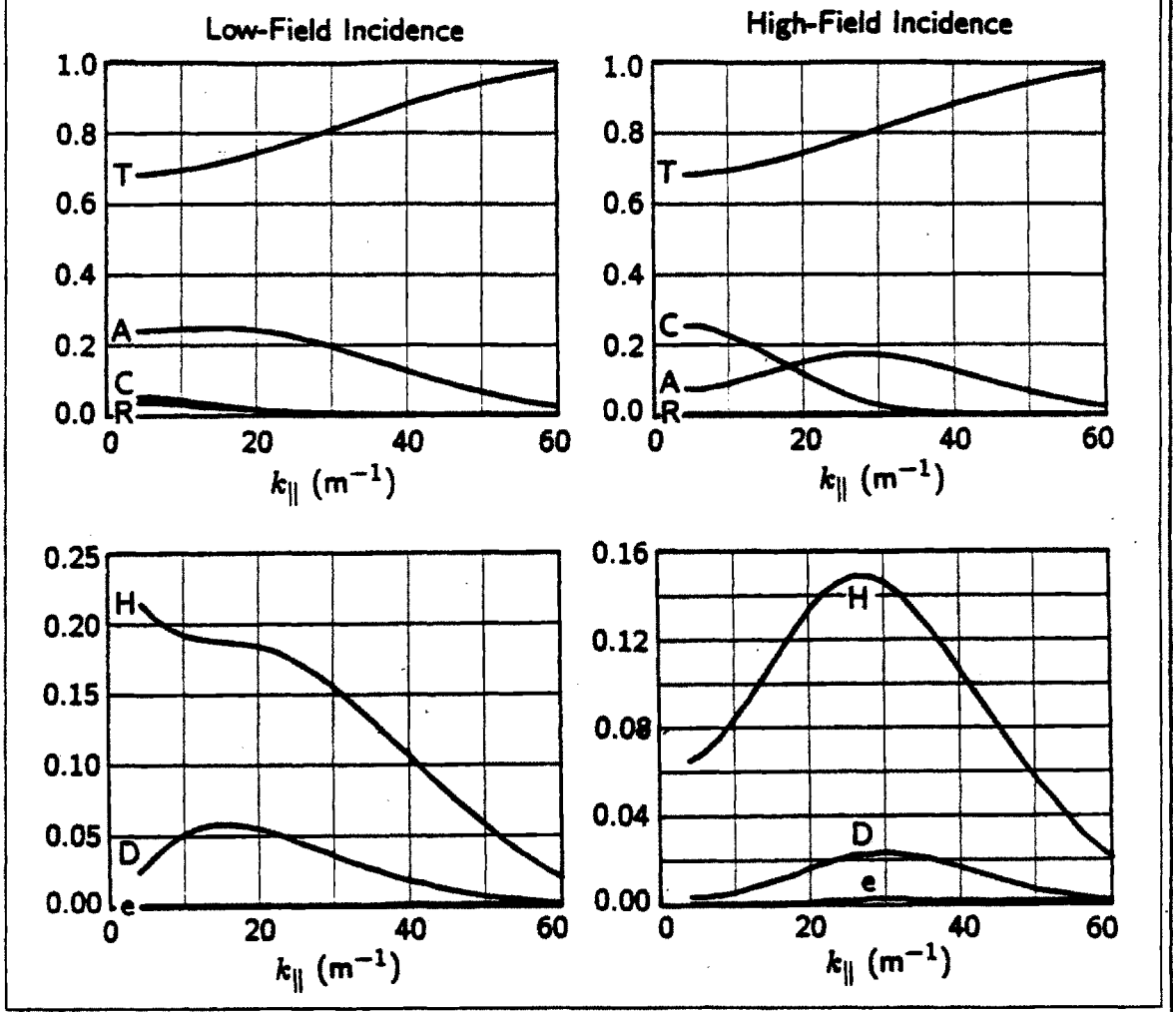

Figure 1.5.1: METS Calculation for High Density—METS calculation for density $n_e = 4 \times 10^{20}\,\mathrm{m}^{-3}$, electron temperature $T_e = 1.5$ keV, deuterium temperature $T_D = 1.15$ keV, minority concentration $\eta_H = 0.5\%$, and minority temperature $T_H = 1.15$ keV.

plane waves incident from various angles. To determine which values of $k_{\|}$ are actually launched by the antenna, it is necessary to include the antenna current and vacuum chamber walls as boundary conditions. This is done in the Brambilla code calculations shown in Chapter 4 of this thesis. From the Brambilla code, it is found that most of the launched power is concentrated near $15 \lesssim k_{\|} \lesssim 20\,\mathrm{m}^{-1}$.

The quantities plotted in Fig. 1.5.1 are the fraction of incident power which is transmitted (T), absorbed (A), mode-converted (C), and reflected (R). Also shown are the individual fractions of power absorbed on the hydrogen minority (H), the deuterium majority (D), and the electrons (e). One can see that Alcator C is characterized by very low single-pass absorption, with most of the power being

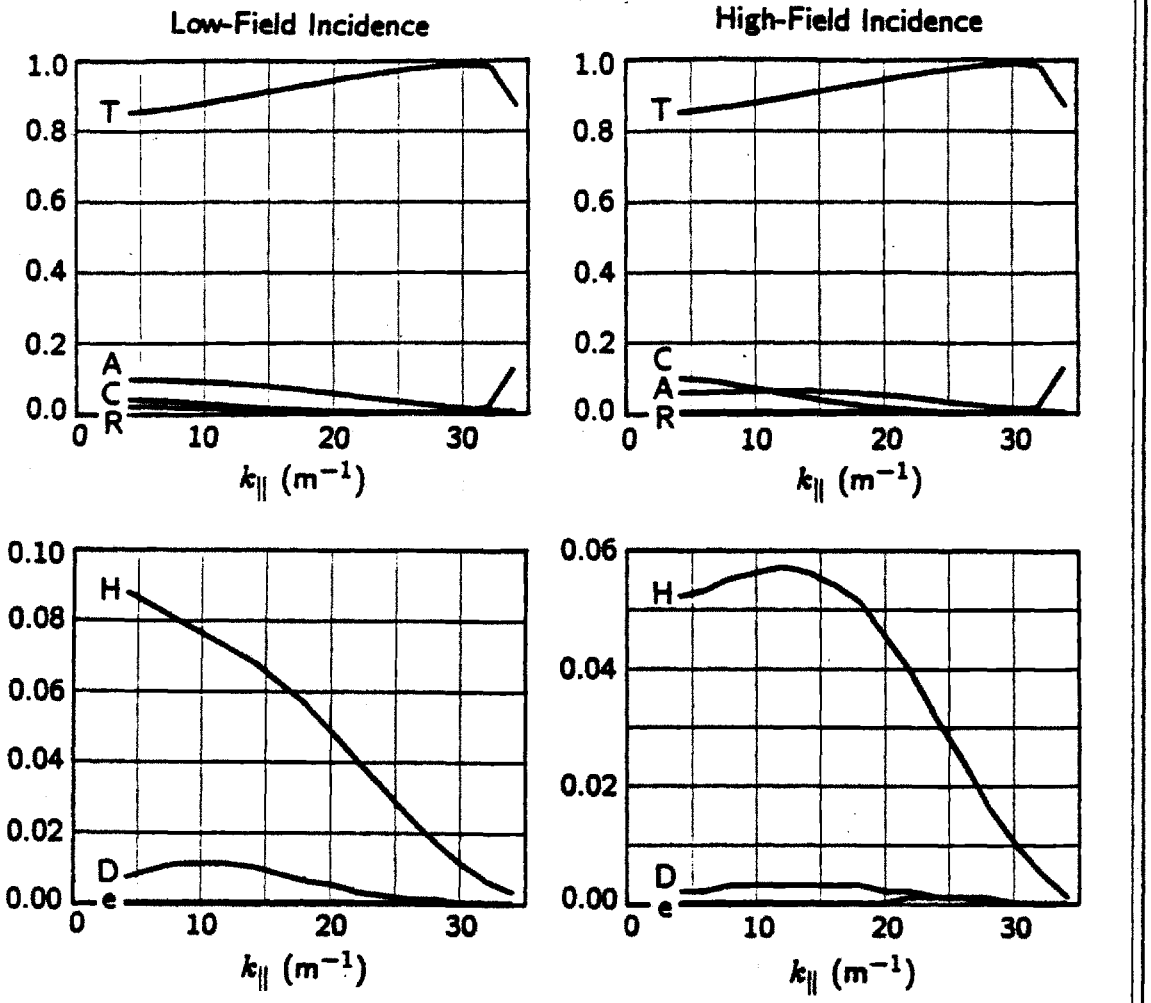

Figure 1.5.2: METS Calculation for Low Density, Low Concentration, and No Elevated Minority Tail—METS calculation for density $n_e = 1 \times 10^{20}\,\mathrm{m}^{-3}$, electron temperature $T_e = 2$ keV, deuterium temperature $T_D = 1.2$ keV, minority concentration $\eta_H = 0.5\%$, and minority temperature $T_H = 1.2$ keV.

transmitted. Absorption by electrons (via Landau damping) is also quite weak. It is important to note that it is possible for the mode-converted IBW to Landau-damp efficiently on electrons if the value of $k_{\|}$ changes as the wave propagates. This is an effect that can be caused by parallel gradients (which are non-zero due to the presence of the poloidal field) of the plasma parameters[70] and is not included in this version of the code. Transit-time magnetic pumping is another effect that can lead to absorption by electrons, and which is not included in METS.

Another METS calculation is shown in Fig. 1.5.2 for a low-density low-minority-concentration case typical of the Ohmic target plasma in Alcator C, before the minority temperature increases. Single-pass absorption is seen to be extremely weak

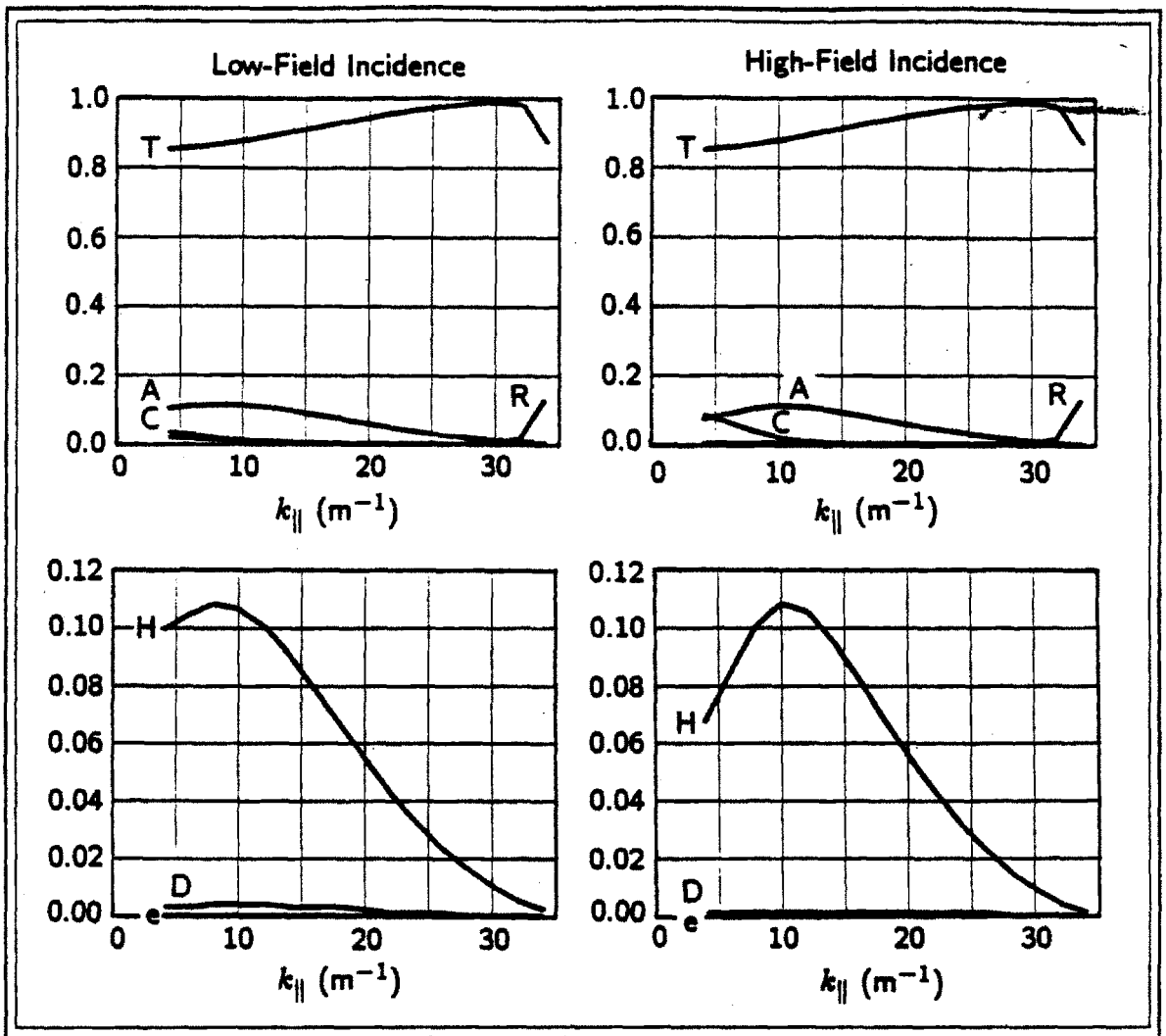

Figure 1.5.3: METS Calculation for Low Density, Low Concentration, with Elevated Minority Tail—METS calculation for density $n_e = 1 \times 10^{20}\,\mathrm{m}^{-3}$, electron temperature $T_e = 2$ keV, deuterium temperature $T_D = 1.2$ keV, minority concentration $\eta_H = 0.5\%$, and minority temperature $T_H = 10$ keV.

in this case — significantly weaker than for the high-density case. Mode conversion and reflection are also quite weak, and it is clear that it will be necessary to treat the metallic wall surrounding the plasma as well at the boundary condition at the antenna current in order to model absorption in any reasonable way in Alcator C. The codes that will be used to do detailed simulations and analyses in Chapter 4 of this thesis were selected with this in mind.

The effect of raising the minority temperature to 10 keV, is shown in Fig. 1.5.3. The effect is a very slight enhancement of the absorption and a decrease in mode conversion. The effect of Doppler broadening is evident in the behavior of the absorption coefficient as a function of $k_{\|}$. Although these changes appear to be

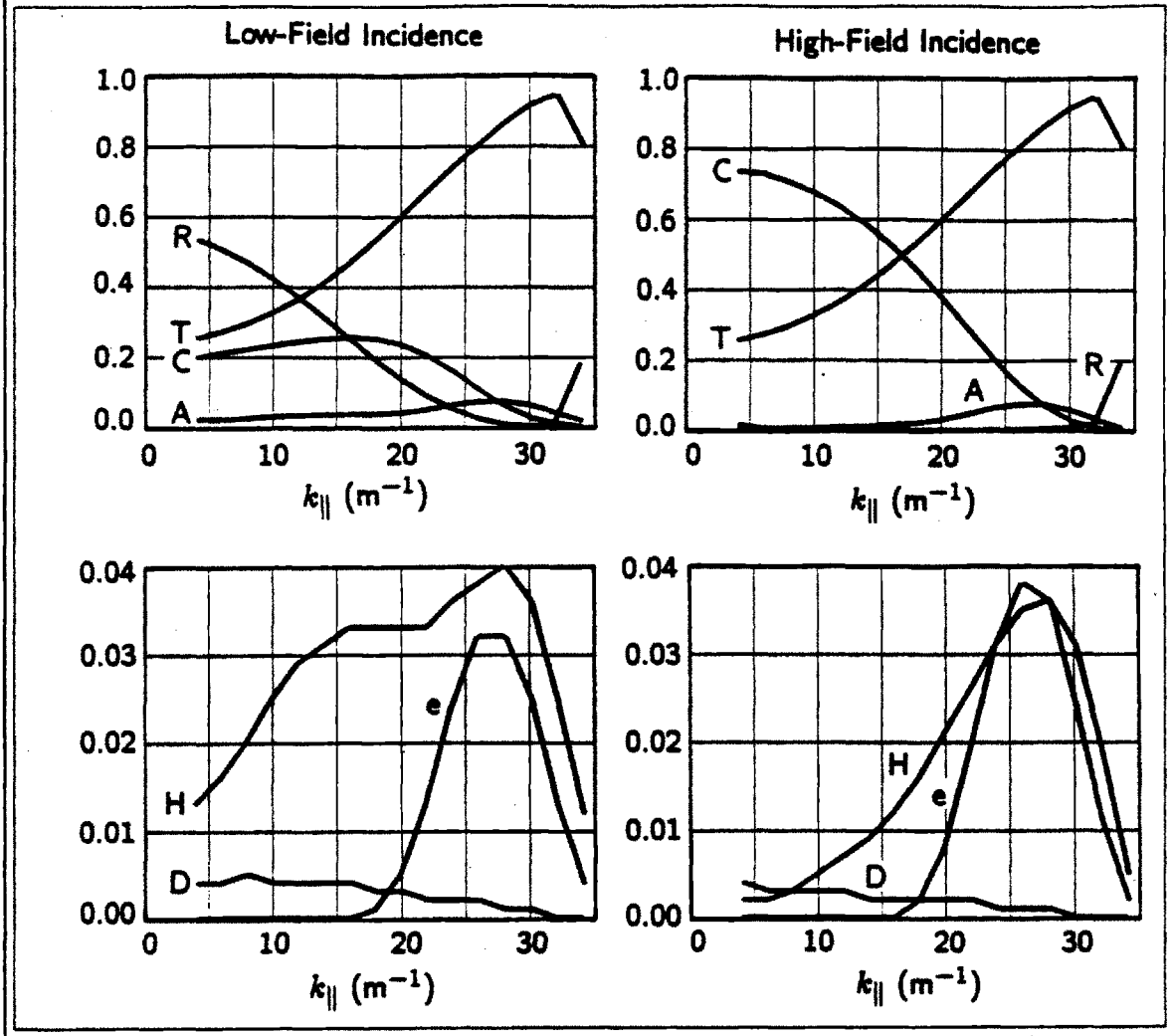

Figure 1.5.4: METS Calculation for Low Density, High Concentration, no Elevated Minority Tail—METS calculation for density $n_e = 1 \times 10^{20}\,\mathrm{m}^{-3}$, electron temperature $T_e = 2$ keV, deuterium temperature $T_D = 1.2$ keV, minority concentration $\eta_H = 5\%$, and minority temperature $T_H = 1.2$ keV.

quite small, note that the decrease in mode conversion is significant when compared to the magnitude of the absorption. The electron absorption is still quite small.

The effect of raising the minority concentration to 5% is shown in Fig. 1.5.4. At this concentration, large increases in minority tail temperature were not observed, and so were not included in this calculation. Note that mode conversion is greatly increased in this case, and absorption is markedly reduced compared to the other cases. There is also significantly increased reflection. Significant electron absorption is indicated at high $k_{\|}$, but the results of the Brambilla code calculations to be presented in Chapter 4 indicate that these values of $k_{\|}$ are not launched by the antenna except at high density.

This treatment with the METS code lends important supporting evidence to the conclusions reached using other codes in Chapter 4.

Before concluding this section, there are a few other treatments of wave propagation in an inhomogeneous plasma that are worth mentioning. I will just present a brief introduction to these treatments, referring the reader to the appropriate references for the actual implementations and applications.

Beginning prior to the variational treatment of the wave equation by Colestock and Kashuba, an important body of work was accomplished by Swanson, Perkins, *et al.*[71–80] In these works, one-dimensional wave equations were usually derived by inverse Fourier transformation of homogeneous-plasma dispersion relations. This technique results in an ambiguity involving derivatives of terms exhibiting explicit spatial dependence. This ambiguity was expected to be unimportant so long as gradients of the wave fields were large compared to gradients of the plasma properties. However, it was possible to resolve this ambiguity by deriving the wave equation directly from the Vlasov equation[77], using a suitable extension of the method shown in Sec. 1.4 of this thesis.

The derivation of such an equation, for the case of normal incidence ($k_\parallel = k_y = 0$) including mode conversion without damping, is given by Swanson in Ref. 72, and the solution of that equation is discussed in painstaking detail by Ngan and Swanson in Ref. 73. This derivation begins with a fourth-order linear dispersion relation including leading order thermal effects describing propagation of the IBW, but excluding damping terms arising from the imaginary parts of the plasma dispersion function. Two ion species are considered. The only spatially varying quantity considered is the equilibrium magnetic field. This is reasonable, since the density and temperature profiles are locally flat at the center of the plasma, while the magnetic field is not. Spatial dependences are expanded to leading (linear) order in Taylor series, and the following notation is defined:

$$\rho \equiv r/R \tag{1.5.19}$$

$$\lambda \equiv k_\perp^2 \rho_{Li}^2 \tag{1.5.20}$$

$$\alpha \equiv n_2/n_1 \tag{1.5.21}$$

$$\mu \equiv m_2/m_1 \tag{1.5.22}$$

$$\delta \equiv \frac{4\mu(1+\alpha)(1+\mu\alpha)}{\alpha(\mu-1)^2(\mu+1)} \tag{1.5.23}$$

$$g \equiv \frac{(\mu+1)[4-\mu f+\alpha\mu(4\mu-f)]}{(4\mu-f)(4-\mu f)} \tag{1.5.24}$$

$$f \equiv \frac{1+\mu\alpha}{\mu+\alpha} \tag{1.5.25}$$

$$A \equiv \frac{2(\mu+\alpha)(1+\mu\alpha)}{\alpha(\mu^2-1)(\mu-1)(1+g)} \tag{1.5.26}$$

$$B \equiv \beta_1 \frac{\mu+\alpha}{2\mu(\mu+1)(1+g)} \tag{1.5.27}$$

This results in the following expression for the dispersion relation:

$$\lambda_1^2 + A\rho\lambda_1 + B(1-\delta\rho) = 0 \tag{1.5.28}$$

Fourier transformation is then accomplished via $k_\perp^2 R_0^2 \rightarrow -d^2/d\rho^2$ and a new independent variable is defined by $z = -\kappa\rho$, along with the following additional notation:

$$\kappa \equiv \omega_{p1} R_0 \sqrt{\frac{2(1+\alpha)}{1+\mu}} \tag{1.5.29}$$

$$\gamma \equiv \frac{(\mu+\alpha)(1+\mu)}{2\mu(1+g)(1+\alpha)^2\beta_1} \tag{1.5.30}$$

$$\lambda^2 \equiv \frac{2(\mu+\alpha)(1+\mu\alpha)}{\kappa\alpha(1+\alpha)(1+g)(\mu-1)^2\beta_1} \tag{1.5.31}$$

This leads to the so-called "fourth-order mode conversion-tunneling" differential equation, given by

$$y^{iv} + \lambda^2 z y'' + (\lambda^2 z + \gamma) y = 0 \tag{1.5.32}$$

This equation was solved by Ngan and Swanson[73] using two different methods. One method is a straightforward asymptotic method in which solutions are first obtained for small z, and then again for large z. These solutions are then connected by means of standard asymptotic matching in an intermediate convergence region. In the other solution method, called the Laplace method, the solution y is represented as a Laplace transform

$$y = \int_\Gamma e^{pz} Y(p)\, dp \tag{1.5.33}$$

where Γ is a suitable Laplace inversion contour in the complex p-plane. This method is fruitful because the coefficients in Eq. 1.5.32, have only constant and linear terms. When Eq. 1.5.32 is Laplace transformed, the constant coefficients become algebraic functions of p while the linear terms introduce first order derivatives with respect to p. Thus, Laplace transformation reduces a fourth-order differential equation to a first-order differential equation. Four independent solutions are obtained by suitable

selection of the inversion contour Γ. Laplace transformation of Eq. 1.5.32 yields

$$\frac{d\ln y}{dp} = \frac{p^4 - 2\lambda^2 p + \gamma}{\lambda^2(1+p^2)} \tag{1.5.34}$$

which has solution

$$Y(p) = \frac{1}{1+p^2}\exp\left\{\frac{1}{\lambda^2}\left[\frac{p^3}{3} - p + (1+\gamma)\tan^{-1}p\right]\right\} \tag{1.5.35}$$

Inverse Laplace transforming and introducing a new integration variable $u \equiv \tan^{-1} p$ yields

$$y(z) = \int_\Gamma du \exp\left[\frac{\tan^3 u}{3\lambda^2} + \left(z - \frac{1}{\lambda^2}\right)\tan u + \frac{1+\gamma}{\lambda^2}u\right] \tag{1.5.36}$$

Equation 1.5.36 is then solved by the method of steepest descents. Transmission, reflection, and mode-conversion coefficients are then derived from these solutions. Selection of the appropriate contours corresponding to individual wave modes and propagation directions is non-straightforward, unless one is armed with the solutions obtained from the method of matched asymptotic expansions. The results of this analysis are that reflection and transmission coefficients for high-field incidence are given by

$$R = 0 \tag{1.5.37}$$

$$T = \theta e^{-\eta} \tag{1.5.38}$$

and for low-field incidence are given by

$$R = 1 - \theta e^{-2\eta} \tag{1.5.39}$$

$$T = e^{-\eta} \tag{1.5.40}$$

where

$$\eta = \pi(\gamma+1)/2\lambda^2 \tag{1.5.41}$$

θ is a complex phase-shift factor, and the mode conversion is given by $C = 1 - R - T$.

This method has been extended to include treatment of nonzero $k_\parallel$ and the presence of absorption[75, 76]. New terms in Eq. 1.5.32 which represent absorption and cannot be approximated as linear in the vicinity of the mode-conversion layer are written on the right-hand side, yielding an equation of the form

$$y^{iv} + \lambda^2 z y'' + (\lambda^2 z + \gamma)y = g(y,z) \tag{1.5.42}$$

where $g(y,z)$ is written as if it were an inhomogeneous term. Keep in mind that $g(y,z)$ depends on y as well as z. Once solutions for Eq. 1.5.32 are obtained, it is possible to construct a Green function $G(z,z')$. Eq. 1.5.42 can then be inverted to yield a Fredholm integral equation of the second kind:

$$y(z) = \int_{-\infty}^{\infty} G(z,z')g(y(z'),z')\,dz' \tag{1.5.43}$$

Whether Eq. 1.5.43 is ultimately homogeneous or not depends on the particular problem to which it is applied. Because $g(y,z)$ is a spatially localized quantity, one is assured that the kernel of Eq. 1.5.43 is square-integrable, and that a solution by simple iteration will converge.

The treatment of the mode-conversion problem using the fourth order equation can be very tedious. It is actually possible to treat processes like wave coupling, tunneling, and reflection using lower order equations. This involves techniques where the modes of interest (e.g., an incident fast wave and transmitted IBW) are modeled using differential operators while other modes (e.g., reflected fast wave and evanescent IBW) are modeled using wave vectors. These theories were developed by Cairns, Lashmore-Davies, Fuchs, Bers, *et al.*[81–86]

As an example of the theory of Cairns and Lashmore-Davies[81, 82], consider two wave modes which, in the uncoupled approximation, have dispersion relations of the form

$$\omega^2 = \omega_1^2(k,x) \tag{1.5.44}$$

$$\omega^2 = \omega_2^2(k,x) \tag{1.5.45}$$

In the presence of mode coupling, these waves will come from a more general dispersion relation of the form

$$(\omega^2 - \omega_1^2)(\omega^2 - \omega_2^2) = \mu \tag{1.5.46}$$

which, for the sake of example, can be considered to be fourth order in k, (e.g., $\omega_1 = c_1 k$, $\omega_2 = c_2 k$). The right-hand side quantity μ is a small coupling term, which is usually negligible, except when both factors on the left-hand side are also small. Suppose one is only interested in the waves corresponding to $\omega = +\omega_1$ and $\omega = +\omega_2$. This could correspond to the case where a fast wave is incident from the high-field side and one is only interested in the returning mode-converted IBW. The other two modes that are not of interest would then be the evanescent IBW and the reflected fast wave. (It is commonly known that reflection is zero in this particular case, but that is not important for this example.) In this case, Eq. 1.5.46 can be

divided by $(\omega + \omega_1)(\omega + \omega_2)$. Then, since the right-hand side is only important when $\omega = \omega_1 = \omega_2$, Eq. 1.5.46 can be well approximated by

$$(\omega - \omega_1)(\omega - \omega_2) = \eta \tag{1.5.47}$$

where $\eta \equiv \mu/(4\omega^2)$. Eq. 1.5.47 now describes only the two modes of interest. Coupling between the two modes occurs in the vicinity of the point $k = k_0$, $x = x_0$, defined by

$$\omega = \omega_1(k_0, x_0) = \omega_2(k_0, x_0) \tag{1.5.48}$$

Taylor expanding the individual dispersion functions about this point yields

$$\omega_1 \sim \omega + a\delta + b\xi \tag{1.5.49}$$

$$\omega_2 \sim \omega + f\delta + g\xi \tag{1.5.50}$$

where $k = k_0 + \delta$, and $x = x_0 + \xi$. Treating $\eta = \eta_0$ as a constant at the value corresponding to x_0 and k_0 yields

$$(ak - ak_0 + b\xi)(fk - fk_0 + g\xi) = \eta_0 \tag{1.5.51}$$

This is then converted into a pair of differential equations by the replacement $k \to -id/d\xi$, yielding

$$\frac{d\phi_1}{d\xi} - i\left(k_0 - \frac{b}{a}\xi\right)\phi_1 = i\lambda\phi_2 \tag{1.5.52}$$

$$\frac{d\phi_2}{d\xi} - i\left(k_0 - \frac{g}{g}\xi\right)\phi_2 = i\lambda\phi_1 \tag{1.5.53}$$

where

$$\lambda \equiv \sqrt{\frac{\eta_0}{af}} \tag{1.5.54}$$

This reduced second-order system is much easier to solve analytically than the fourth order equation, Eq. 1.5.32.

A more general order reduction theory was developed by Fuchs, Ko, Bers, and Harten[83]. In this theory, one begins with a general high-order dispersion relation of the form

$$D(\omega; k, z) = 0 \tag{1.5.55}$$

and it is not necessary to factor the dispersion relation into a form similar to Eq. 1.5.46. This theory implicitly assumes that the system is driven at some fixed frequency ω, and does a local analysis in k and z, where the spatial coordinate z is

generalized to allow complex values. With z and k both complex, the general dispersion function of the form $k = k(z)$ is a multi-valued surface with branch points at the junctions of the various surfaces. Each surface corresponds to a different wave mode, and each branch point corresponds to a coupling event. The branch points $z = z_b$ and corresponding $k = k_s$ are determined from simultaneous solution of Eq. 1.5.55 and

$$\frac{\partial D}{\partial k} \equiv D_k = 0 \tag{1.5.56}$$

A particular coupling event involves only two modes if

$$D_{kk} \neq 0 \tag{1.5.57}$$

at (k_s, z_b). Expanding the dispersion function about this point then yields

$$D(k_b) + \frac{1}{2}(k - k_b)^2 D_{kk}(k_b) = 0 \tag{1.5.58}$$

(It is not necessary to also expand in z, in which case $k_b = k_b(z)$.) A second order equation describing the coupling event is then obtained via

$$y''(z) + Q(z)y(z) = 0 \tag{1.5.59}$$

where

$$Q(z) \equiv -2 \left. \frac{D}{D_{kk}} \right|_{k_b(z)} \tag{1.5.60}$$

Applications of these techniques to the general problem of determining coupling coefficients and to specific physical problems can be found in the references cited above and references contained therein.

A more exact method of order reduction, analogous to the treatment of Cairns and Lashmore-Davies, has recently been given by Swanson[87]. Instead of expressing the dispersion relation as a product of two lower-order dispersion relations set equal to a localized coupling term, Swanson performs the same kind of factoring on the differential operator in the wave equation. That is, starting with a fourth-order wave equation of the form

$$y^{iv} + b(x)y'' + a(x)y = 0 \tag{1.5.61}$$

Swanson rewrites this in the form

$$D_+ D_- y = g(x, y) \tag{1.5.62}$$

where

$$D_+ = \frac{d^2}{dx^2} + k_+^2(x) \tag{1.5.63}$$

$$D_- = \frac{d^2}{dx^2} + k_-^2(x) \tag{1.5.64}$$

$$k_\pm^2 = \frac{1}{2}(b \pm \sqrt{b^2 - 4a}) \tag{1.5.65}$$

$$g = 2(k_-^2)'y' + (k_-^2)''y \tag{1.5.66}$$

and g is the spatially localized coupling term. It is then possible to construct a Green function from the four solutions to the two separate second-order equations

$$D_+ y = 0 \tag{1.5.67}$$

$$D_- y = 0 \tag{1.5.68}$$

This then leads to an inhomogeneous Fredholm integral equation of the second kind, from which the exact solutions may be obtained numerically.

1.6: Integration of Wave Theory and Kinetic Theory

So far, derivations have been given of equations which describe the propagation of plasma waves, and the (linear) absorption and mode conversion of power from wave to plasma and from one wave mode to another. What is needed now is a treatment of the effects (hopefully heating) that this has on the plasma. Perhaps the simplest approach one can take is to use the absorbed power calculated from a solution of the wave equation as an input heating power in a calculation in which the plasma is modeled as a fluid, with transport properties derived by assuming Maxwellian distribution functions for all species. This is essentially what is done in the ONETWO code analyses of deuterium heating to be presented in Chapter 4 of this thesis. The present section, however, is concerned with exactly how the RF wave fields appear in the kinetic equation that determines the particle distribution functions.

The treatment in this section is going to be extremely abstract, even more so than the treatment in Sec. 1.5. Again, the details of the derivations are too complicated to be included here, and they can be found in the references. One particularly well-known explicit version of the steps outlined in this section was given by Kennel and Engelmann[66], for the infinite homogeneous hot-plasma case.

All of the steps illustrated abstractly in this section are done explicitly in Ref. 66, except that the infinite homogeneous plasma derivation requires a limit to be taken as the plasma volume tends to infinity, which is not required in bounded geometry. When comparing my abstract notation with that of Kennel and Engelmann, note that at my presentation does not necessarily involve Fourier transforms.

I will introduce my abstract notation by using it to describe the derivation of the plasma wave equation in a very concise manner. The fundamental starting equation is the kinetic equation in which the Vlasov operator, denoted herein as D, is balanced against the Coulomb collision operator, denoted by C:

$$Df = Cf \tag{1.6.1}$$

The linear wave equation is obtained by linearization, in which the distribution function is separated into an equilibrium part and a small perturbation which oscillates at the wave frequency: $f = f_0 + f_1$. The Vlasov operator is also linearized: $D = D_0 + D_1$. Note the omission of higher order nonlinear quantities composed of other wave harmonics. (I use the expression "harmonics" in this section to refer to oscillatory behavior either in space or in time.) The treatment here is "quasilinear" — a term which means basically that the only higher-order nonlinear terms which are retained in the treatment are those with zero beat-frequency and zero spatial average which arise from the nonlinear interaction of two first-order terms. These terms are extracted from the second order equation by averaging over the velocity gyrophase angle. Thus, second-order terms like $D_1 f_1$ have non-zero gyrophase average, but terms like $D_0 f_2$ do not. Physically, this kind of "quasilinear truncation" of the small perturbation expansion corresponds to dropping nonlinear coupling between different wave modes while retaining nonlinear coupling between the wave and the plasma, which is exactly what we want. Note that, since all first order terms oscillate at the wave frequency and average to zero, the leading order contribution from the collision operator must be treated as a second-order effect, to be balanced against the gyrophase-averaged effect of the RF wave fields, (unless one wants collisions to be dominant). The zero-order equilibrium problem is then denoted by

$$D_0 f_0 = 0 \tag{1.6.2}$$

Once f_0 is known, it can be treated as a driving term in the first-order equation

$$D_0 f_1 = -D_1 f_0 \tag{1.6.3}$$

whose solution,

$$f_1 = -D_0^{-1} D_1 f_0 \tag{1.6.4}$$

has been the primary subject of this chapter.

The next step is to allow slow, second-order evolution of the equilibrium solution f_0 to occur. This could be done by introducing a quantity f_2 as a second order quantity. However, conventional notational usage would be that f_2 is oscillatory, and only the time and space-averaged part is wanted. This is usually done by considering the quantity denoted by f_0 to be a "slowly varying equilibrium quantity" and requiring that the gyrophase average of f_2 be zero. Formally, one does a multiple-time-scales analysis in which the fast time scale is oscillatory, via

$$\frac{\partial f}{\partial t} = \frac{\partial f_0}{\partial t} - i\omega f_1 \tag{1.6.5}$$

where the ordering is such that

$$\frac{\partial f_0}{\partial t} \sim C f_0 \ll f_1 \ll f_0 \tag{1.6.6}$$

or, more generally

$$D_0 f = D_0 f_0 + D_0 f_1 \tag{1.6.7}$$

where

$$D_0 f_0 \sim C f_0 \ll D_0 f_1 \sim f_1 \ll f_0 \tag{1.6.8}$$

Going to second order and gyrophase-averaging in order to eliminate oscillatory contributions yields

$$\langle D_0 \rangle f_0 - \underbrace{\left\langle D_1 D_0^{-1} D_1 \right\rangle}_{\equiv Q} f_0 = \langle C \rangle f_0 \tag{1.6.9}$$

The quantity Q is the quasilinear diffusion operator. Note that, since D_1 contains the first-order wave fields, a solution of the linear wave equation is required in order to evaluate Q. Eq. 1.6.9 is the well-known drift kinetic equation, with an added quasilinear diffusion term to represent the RF absorption:

$$\left(\frac{\partial}{\partial t} + \mathbf{v}_{D\perp} \cdot \frac{\partial}{\partial \mathbf{x}_\perp} + v_\parallel \frac{\partial}{\partial l} \right) f_0 = C f_0 + Q f_0 \tag{1.6.10}$$

where $\mathbf{v}_{D\perp}$ represents the particle guiding-center drifts and $v_\parallel$ is the velocity along the particle drift orbit. The angle bracket notation $\langle\rangle$ has been dropped for convenience, so that it may be used again later to represent the bounce-averaging operation.

For the case of an infinite homogeneous plasma, the general form for the quasi-linear diffusion operator from Ref. 66 is

$$Q = \frac{\partial}{\partial \mathbf{v}} \cdot \mathbf{D} \cdot \frac{\partial}{\partial \mathbf{v}} \tag{1.6.11}$$

where

$$\mathbf{D} = \lim_{V\to\infty} \frac{q^2}{m^2} \sum_n \frac{1}{V} \int \frac{d^3k}{(2\pi)^3} \frac{i}{\omega - k_\parallel v_\parallel - n\Omega} \mathbf{a}^* \mathbf{a} \tag{1.6.12}$$

$$\mathbf{a} = \mathcal{E} \frac{k_\parallel}{\omega} \left[\left(\frac{\omega}{k_\parallel} - v_\parallel \right) \hat{\mathbf{v}}_\perp + v_\perp \hat{\mathbf{z}} \right] + E_\parallel J_n \left[\hat{\mathbf{z}} + \frac{n\Omega}{v_\perp \omega} (v_\parallel \hat{\mathbf{v}}_\perp - v_\perp \hat{\mathbf{v}}_\parallel) \right] \tag{1.6.13}$$

$$\mathcal{E} = \frac{E_+ e^{i\psi} J_{n+1} + E_- e^{-i\psi} J_{n-1}}{\sqrt{2}} \tag{1.6.14}$$

$$J = J(k_\perp v_\perp / \omega) \tag{1.6.15}$$

where, in carrying out the k-integration, it is to be understood that ω is a function of $\mathbf{k}$ according to the dispersion relation. The angle ψ represents a rotation that allows one to introduce nonzero k_y, and is usually taken to be zero.

The first analytic and semi-analytic calculations of ICRF minority distribution functions obtained by balancing RF-driven quasilinear diffusion against collisions were done by Stix[88]. In Stix's analysis, as is usually done for RF quasilinear calculations, the non-resonant wave-particle interactions are neglected, and the quasi-linear diffusion operator takes the form

$$Qf = \lim_{V\to\infty} \sum_n \frac{\pi q^2}{m^2} \frac{1}{V} \int \frac{d^3k}{(2\pi)^3} \mathrm{L} v_\perp \delta(\omega - k_\parallel v_\parallel - n\Omega) |\Theta|^2 v_\perp \mathrm{L} f \tag{1.6.16}$$

where

$$\mathrm{L} \equiv \left(1 - \frac{k_\parallel v_\parallel}{\omega} \right) \frac{1}{v_\perp} \frac{\partial}{\partial v_\perp} + \frac{k_\parallel}{\omega} \frac{\partial}{\partial v_\parallel} \tag{1.6.17}$$

$$\Theta = E_- e^{i\psi} J_{n+1} + E_+ e^{-i\psi} J_{n-1} + \frac{v_\parallel}{v_\perp} E_\parallel J_n \tag{1.6.18}$$

Stix neglects parallel velocity diffusion and terms containing E_- and $E_\parallel$ and uses $\psi = 0$ to obtain

$$Qf = \frac{\pi q^2}{2m^2}\frac{|E_+|^2}{|k_\parallel|}\sum_n \frac{1}{v_\perp}\frac{\partial}{\partial v_\perp}v_\perp^2\left|J_{n-1}\left(\frac{k_\perp v_\perp}{\Omega}\right)\right|^2 \delta\left[v_\parallel - \frac{(\omega - n\Omega)}{k_\parallel}\right]\frac{1}{v_\perp}\frac{\partial f}{\partial v_\perp} \tag{1.6.19}$$

Among many other useful analytical results, Stix derives an analytic expression for the minority distribution function using an isotropic approximation for f (leading order in Legendre polynomial expansion), a uniformly asymptotically matched analytic approximation for the Coulomb collision coefficients, and a flux-surface-averaged quasilinear diffusion operator. This yields an expression for the "effective temperature", i.e., the negative of the reciprocal of the slope of the log of the distribution function:

$$T_{\text{eff}} \equiv -\left[\frac{d\ln f}{dE}\right]^{-1} \tag{1.6.20}$$

where

$$\frac{1}{T_{\text{eff}}(E)} \equiv -\frac{d\ln f(E)}{dE} \tag{1.6.21}$$

$$= \frac{1}{T_e(1+\xi)}\left[1 + \frac{R_D(T_e - T_D + \xi T_e)}{T_D(1+R_D+\xi)}\frac{1}{1+(E/E_D)^{3/2}}\right] \tag{1.6.22}$$

where

$$\xi = \frac{1}{8\sqrt{\pi}}\left(\frac{4\pi\epsilon_0}{e^2}\right)^2 \frac{m\langle P\rangle}{\eta_H n_e^2 \ln\Lambda}\sqrt{\frac{2T_e}{m_e}} \tag{1.6.23}$$

$$R_D = \sqrt{\frac{m_D}{m_e}\frac{T_e}{T_D}} \tag{1.6.24}$$

$$E_D(\xi) = \frac{m_H T_D}{m_D}\left[\frac{3\sqrt{\pi}}{4}\frac{1+R_D+\xi}{1+\xi}\right]^{2/3} \tag{1.6.25}$$

The quantity $\langle P\rangle$ is the flux-surface average of the ICRF power density absorbed by the hydrogen.

This analysis has been further refined in recent years by other authors. A more detailed analytic treatment of the anisotropic effects and the extension to second harmonic regime ICRF was done by Anderson, *et al.*[89]. The flux surface averaging done by Stix does not accurately model the contribution from banana-trapped particles, although it can be shown to be correct in the limit of centrally peaked absorption. A better way to do this average is to weight the average according to the amount of time a particle spends at each point on the flux surface. Note

that trapped particles spend zero time at certain locations on the flux surface. The correct treatment of trapped (as well as passing) particles is thus accomplished by replacing the flux-surface average by a "bounce average", also done by Anderson, *et al.*[90]. It was also pointed out by Anderson *et al.* that knowledge the high energy distribution function itself is only an intermediate result used to obtain important quantities such as collisional deposition to the other species and fusion reactivity, and approximate expressions for those secondary quantities were worked out and compared with numerical calculations[91–93].

One problem that can occur when combining wave physics and Fokker-Planck calculations is inconsistency that results if the absorption is calculated assuming Maxwellian distribution functions while the kinetic effects result in highly non-Maxwellian components. As was mentioned earlier in this Chapter, a non-Maxwellian tail in the minority regime ICRF can be well approximated by splitting the ion species up into "bulk" and "tail" species of different temperatures. This technique was used by Morishita *et al.*[94] in a one-dimensional slab-geometry numerical treatment. Four parameters, bulk and tail densities and temperatures, were determined by fitting to the low and high-energy parts of the distribution function determined from a Fokker-Planck calculation. These parameters were then used in a wave equation calculation to determine how the power deposition profile evolves. The two calculations were iterated in order to determine the time evolution of this heating process.

A crucial point discussed by various authors (e.g., Stix) is that the motion of the ion must be decorrelated by the effects of collisions between transits of the absorption region in order for quasilinear theory to be applicable. It was mentioned earlier in this Chapter that this decorrelation could also be provided by the effects of turbulence. A rigorous formulation of quasilinear theory in which this turbulent decorrelation was employed was carried out by Yasseen and Vaclavik[95]. They also include the full quasilinear diffusion operator — both resonant and non-resonant parts.

1.7: Comparison With Other Experiments

A number of tokamak ICRF heating experiments predated the experiments discussed in this thesis, and met with varying degrees of success. In this section, some of the important previous experimental results will be described briefly and compared with the present results from Alcator C.

Results from several of these earlier experiments are summarized in Table 1.7.1. Some of the early TFR results are quite comparable to the Alcator C results. In the early TFR minority regime D(H) experiments, the antenna used was similar to the Alcator C antenna, except that a current maximum existed only on the high-field side (HFS), from which most of the power can be assumed to be launched. However, for the low-η_H minority regime, single-pass absorption is small, so the RF field pattern in the plasma would not be expected to be much different regardless of the launching direction. The electron density for this experiment is similar to the low-density range explored in Alcator C and the Ohmic target temperatures are only slightly lower. (The ion temperatures are more important than the electron temperatures for this comparison.) Although the magnetic field was lower in TFR (hence lower RF frequency and longer wavelength), the machine dimensions were larger so that the plasma dimensions were comparable in terms of electrical wavelengths. Also, no carbonization was used in either experiment. However, global energy confinement times are larger for TFR than for Alcator C (in this density range), and the electrons and ions are more strongly collisionally coupled (due to the larger plasma size). The deuterium heating per kW of ICRF power is approximately the same for these two experiments. A small amount of electron heating is shown for TFR, while no electron heating is claimed for Alcator C. However, it would be impossible to detect an electron temperature change this small (65 eV) with the Alcator C Thomson scattering diagnostic and, again, the collisional coupling between electrons and ions is stronger in TFR.

Also shown are some ICRF mode-conversion regime results from TFR. For the same power as in the minority regime experiments, significantly more electron heating and less deuterium heating is observed, and the increase in impurity radiation is smaller. Mode-conversion regime experiments at higher power exhibit significant electron heating as well as ion heating. In Alcator C it is not possible to operate at an RF frequency low enough, or a magnetic field high enough, to perform mode-conversion regime experiments.

Early attempts at minority regime ICRF using a low-field-side (LFS) antenna in TFR were not very successful. It was not possible to operate at $P_{RF} > 150$ kW due to severe high-Z impurity production. However, significantly improved heating

Experiment	B_0	$\bar{n}_e$	n_{e0}	I_P	T_{e0}	T_{i0}	η	P_{OH}	P_{RF}	ΔP_{OH}	ΔT_e	ΔT_i	ΔP_{rad}	Reference	Comment
TFR, HFS, D(H), minority	4.0		1.5–2.0	200–270	1.0	0.8	2		420	100	65	460	220	5	no carbonization
TFR, HFS, D(H), mode-conversion	4.5						20		440	90	260	185	80	5	no carbonization
TFR, Hi P_{RF}, HFS, D(H), MC	4.5						20		1150	30	400	630	450	5	no carbonization
TFR, Hi P_{RF}, HFS, D(H), MC	4.9						40		1250	200	710	570		5	no carbonization
TFR, LFS, D(H), minority?	4.0						20		150			75		5	P_{RF} limited by impurities
TFR, HFS, D(H), carbonization									750		900			7	reduced metal impurities
TFR, LFS, D(H), carbonization	4.0		1.2	200	1.2–1.5	0.8	5		600		0	800		8	no heating in MC regime
Asdex, $2\omega_{cH}$	2.2	0.4		380	0.6	0.5		450	700		300	500		12,13,17,18	impurities reduced by carbonization
PLT, Lo P_{RF}, D(H)		0.1	0.2	230	1.4	0.4	3		35		140	80		23	
PLT, Hi P_{RF}, D(H)	2.8	0.4				0.7			1400			1000		25	
PLT, $2\omega_{cH}$	1.4	0.38		400		0.5			1600			1800		25	
PLT, D(^{3}He)	2.5	0.32			1.0	0.6	10		1200		1000	2200		25	
JIPP T-II, D(H)	2.7		0.2–0.5	90	0.78	0.27	4	100	260		320	300		34	
JIPP T-IIU, HFS, D(H), SS limiter	2.9	0.25		170	0.7	0.4	10	680	500		400	700		36	
JIPP T-IIU, HFS, D(H), C limiter	2.9	0.35		240	1.1	0.4	10	600	250		700	400		36	
JFT-2, D(H), MC	1.2	0.4		140	0.6	0.4	20		500		300	400		39	
JET, D(H)	2.0			2000	1.8	1.7	4		3000		1200	800		45	severe carbon impurities
Textor, D(H), MC	2.0	0.3		340	0.7	0.6			1000		700	175		53	rising density
Alcator C, D(H)	12	1.4	2.1	154	1.8	0.9	0.5	230	300	100	0	400		herein	rising density
Alcator C, D(H)	12	1.0	1.3	160	2.0	1.0	0.5	240	220	50	0	220		herein	steady density
Alcator C, D(H)	12	4.5	6.0	400	1.6	1.0	0.5	800	175	50	0	50		herein	steady density

Table 1.7.1: Comparison of Various ICRF Heating Experiments—Results are shown for several significant ICRF heating experiments as of 1986. More recent results from ongoing experiments on Asdex and Jet are not included in this table. Experimental parameters in this table are listed for B_0 in T, $\bar{n}_e$ and n_{e0} in 10^{20} m^{-3}, I_P in kA, T_{e0} and T_{i0} (for the Ohmic target plasma) in keV, η (minority concentration) in %, P_{OH}, P_{RF}, ΔP_{OH}, and ΔP_{rad} in kW, and ΔT_e and ΔT_i (of the majority species) in eV.

efficiency was observed in TFR both in the mode-conversion and minority regimes after wall carbonization and replacement of the limiters by carbon limiters.

Efficient hydrogen second harmonic regime heating was observed during experiments carried out on the Asdex tokamak. Significant reduction in metal impurities when operating in a carbon environment was also reported. (All data reported were taken with carbonization.) In other experiments (discussed in the references but not included in Table 1.7.1) efficient D(H) minority fundamental and D(H) minority second harmonic regime heating was reported. Also, when a neutral-beam preheated target plasma was used, ICRF heating efficiency was improved to a level comparable to the Ohmic heating efficiency.

On the PLT tokamak, successful heating experiments were performed in the D(H), $2\omega_{cH}$, and D(^{3}He) regimes — all at RF power levels significantly exceeding 1 MW. The most efficient heating regime was found to be the D(^{3}He) regime. While the wave absorption is weaker in this regime than in the D(H) regime (due to the frequency being closer to the majority fundamental cyclotron frequency), the minority species is more strongly coupled to the bulk plasma, particularly to the ions ($E_{\rm crit}$ is larger). Thus, a less energetic minority tail is required to couple the RF power to the bulk plasma, and this minority tail is easier to confine. This appears to be the reason for the improved heating efficiency.

A direct comparison between heating results with and without carbon limiters was made during experiments on the JIPP T-IIU tokamak. When one considers the difference in target plasma density and RF power in the data shown in Table 1.7.1, a dramatic improvement in heating efficiency is evident. This improved heating efficiency is due to the fact that low-Z impurities are fully ionized at the center of the plasma, and hence do not emit line radiation. On the other hand, partially-stripped high-Z impurities are highly radiative and can cool the plasma center, resulting in decreased heating efficiency and possible disruption of the discharge.

Although appreciable heating was observed, early high-power ICRF heating experiments on JET (always with carbonization) were plagued by severe carbon impurities, with values of $Z_{\rm eff}$ often exceeding 3. Under these circumstances, depletion of the majority ion species and direct cyclotron absorption by the carbon becomes an issue. However, in more recent experiments on JET (not included in Table 1.7.1) the impurity problem has been corrected and efficient heating at even higher RF power has been achieved.

The Alcator C ICRF heating experiments described in this thesis were performed at unprecedented high densities and magnetic fields. When one considers the high densities and relatively low RF powers involved, these results compare favorably with the other experiments listed in Table 1.7.1. However, like most of the

ICRF heating experiments, the RF heating efficiency is degraded when compared with the Ohmic heating efficiency.

A revealing way to compare RF and Ohmic heating efficiencies is to compare the incremental energy confinement time with the Ohmic confinement time. The Ohmic confinement time (assuming steady state) is the ratio of the total plasma thermal energy to the total plasma heating power during the Ohmic portion of the discharge. The incremental confinement time is the ratio $\Delta W/\Delta P$ where ΔW is the change in total thermal energy content of the plasma during the RF and ΔP is the change in total heating power. For Alcator C, the Ohmic confinement time increases linearly with density over the range $0.5 \lesssim \bar{n}_e \lesssim 3 \times 10^{20}\,\mathrm{m}^{-3}$ from ~ 5 ms up to ~ 20 ms and remains constant for higher densities (the saturated confinement regime). The incremental confinement time exhibits a great deal of scatter, but is essentially independent of density, with a maximum value of ~ 5 ms at any density up to $\bar{n}_e \sim 6 \times 10^{20}\,\mathrm{m}^{-3}$. However, even this apparently unfavorable scaling does not tell the whole story. Since there was no electron heating in Alcator C, it makes more sense to compare the heating of the deuterium caused by collisional exchange power from electrons in the Ohmic discharge with the heating due to collisional exchange plus RF deposition during the RF heated portion of the discharge. Also, the efficiency of the deposition of RF power to the deuterium is a strongly increasing function of density. When this is accounted for, it is found that both the Ohmic (from collisional exchange) and RF heating efficiencies of the deuterium are equal and scale unfavorably with density. The data and calculations on which this conclusion is based are presented in detail in the following chapters of this thesis.

CHAPTER 2

Antenna Design

2.1: Introduction

The antenna design used in these experiments evolved directly from the antenna design used in previous Alcator C ICRF experiments conducted by B. D. Blackwell. This previous design consisted of a toroidal array of two conventional loop antennas similar to the high-field-side launcher used in early ICRF experiments on TFR[5–7], except that the Alcator antenna had current maxima on both high and low-field sides, and hence is considered a "two-side" launcher. The antenna conductor was fed by a coaxial transmission line at the low-field side and shorted to the backplane on the high field side. An unusual Faraday shield, designed to minimize the diamagnetic eddy currents in the shields, was used. This shield design was motivated by the work of Faulconer[96]. The electrical design of all of the Alcator C antennas was dominated by the physical constraints imposed by the compact dimensions of the tokamak. In particular, since the largest access port on the tokamak is a 4 cm wide slot, no part of the antenna can be wider than 4 cm unless one is willing to assemble parts inside the vacuum chamber. In the previous attempts at fast wave ICRF heating in Alcator C, there were recurring problems with electrical breakdown. This breakdown was believed to occur at the vacuum feedthrough, and/or in the section of the power feed line within the 4 cm wide port. In order to reduce the electric field strength within the feed line, a self-resonant loop antenna design was developed. This design allows the antenna to present a matched load to the feed line, and has the added benefit of increasing the bandwidth of the system as viewed by the RF generator.

2.2: Antenna Construction

Three different fast-wave antennas were used during the experiments described in this thesis. The first antenna that was constructed is illustrated in Fig. 2.2.1. This antenna has a single radiating conductor, shorted to the backplane at each end, with the feed tapped in near one end. This antenna is in a sense not well-matched to the plasma because the toroidal spectrum of the antenna current is much wider than the spectrum of accessible $N_{||}$ for Alcator-type plasmas. However, this antenna is very easy to install and remove. This feature was very important in the early stages of the experiment, when it was necessary to make several trial-and-error adjustments to the antenna in order to achieve a matched load.

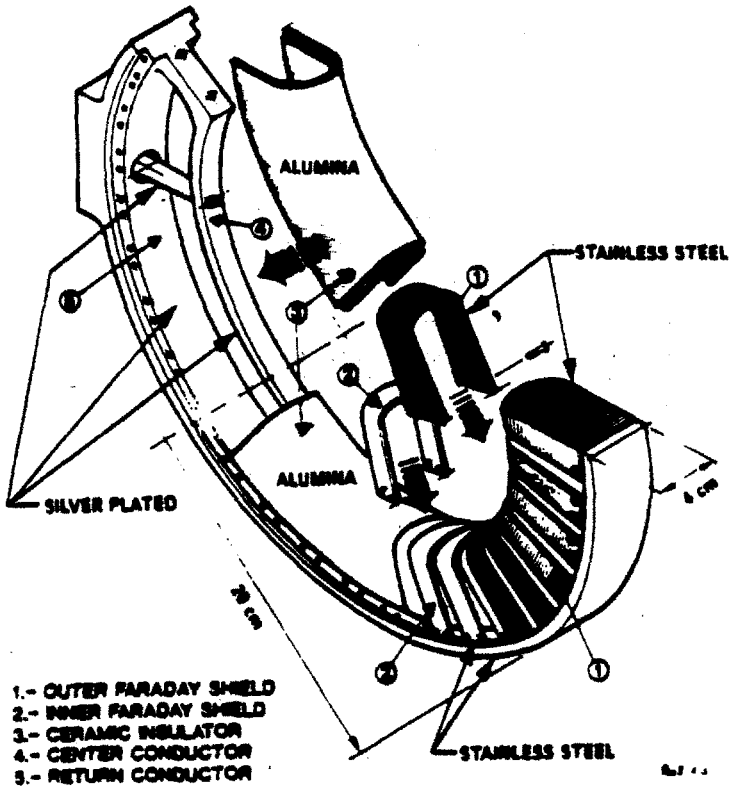

Figure 2.2.1: Single-Element Antenna—The basic antenna design consists of a half-wave resonant loop, shorted at each end, with the feed tapped in near one end.

The radiating conductor and backplane were machined from a single piece of stainless steel. The center conductor of a coaxial transmission line enters through a hole in the backplane and is threaded into a tapped hole in the radiating element. A double-layer stainless steel Faraday shield is attached by screws to the backplane, with a five-section ceramic shell between the antenna conductor and the Faraday shield. The ceramic shell is made of alumina (Al_2O_3) and is held in place by the inner Faraday shields, by clamping against the backplane. The ceramic shell does not contact the antenna conductor.

The antenna is installed through a side port, as illustrated in Fig. 2.2.2, and held in place by the attached coaxial feed and by a threaded rod inserted through the bottom port. Since the current pattern on this antenna is at a maximum at each end, power is launched from both the high and low-field sides of the plasma. The Faraday shield structure is replaced by a continuous conducting cover at the center of the antenna, where the current is small.

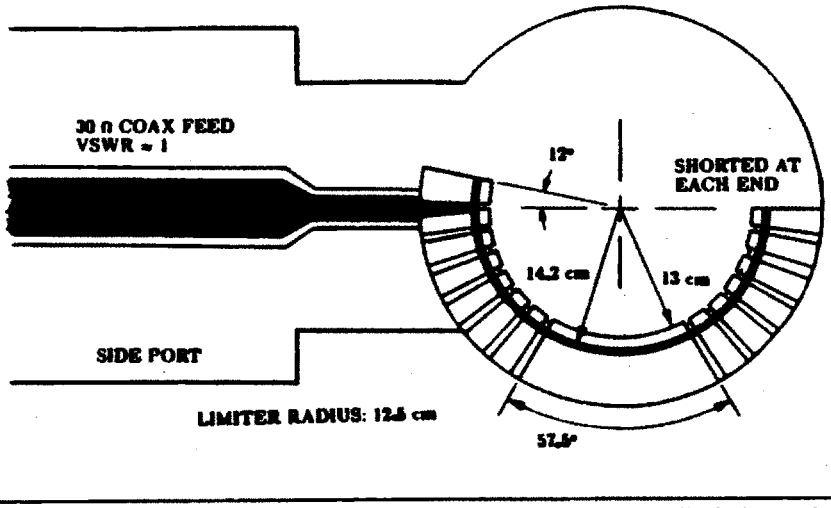

Figure 2.2.2: Antenna Installation—The antenna is installed through a side port and rests on the bottom of the vacuum chamber.

Conceptually, it is necessary to adjust two physical parameters of the antenna in order to achieve a matched load at the desired frequency. For example, the resonant frequency can be controlled by varying the length of the antenna while the input impedance can be controlled by varying the feed tap position. Designing and constructing an antenna with remotely movable shorts was judged to be too ambitious an undertaking, given the limited resources available for the project. Also, the analysis presented later in this chapter suggests that an antenna with fixed tap positions can match a fairly wide variety of plasma loads. The actual adjustments of the antenna were made after collecting data from bench tests and the preliminary plasma runs. To make adjustment possible, the shorting ends were made thick enough that metal could be machined off later. Adjustment was also possible by varying the number of ceramic pieces in the antenna and by varying the number of inner Faraday shield elements used to hold the center ceramic piece in the enclosed portion of the antenna.

Most of the heating data presented in this thesis were obtained using the double element antennas shown in Figs. 2.2.3 and 2.2.4. In addition to providing a better match to propagating modes in the plasma, the radiated power flux is spread out over a larger antenna surface. The electrical design of the two-side launch antenna was based on data obtained from the original single-element antenna (with suitable corrections for cross-coupling between the two elements and improved loading due to the modified spectrum). When this antenna was first used in the tokamak with plasma, it was found to be well matched to the feed at the desired operating frequency. The antenna in Fig. 2.2.4 was constructed to provide a pure low-field

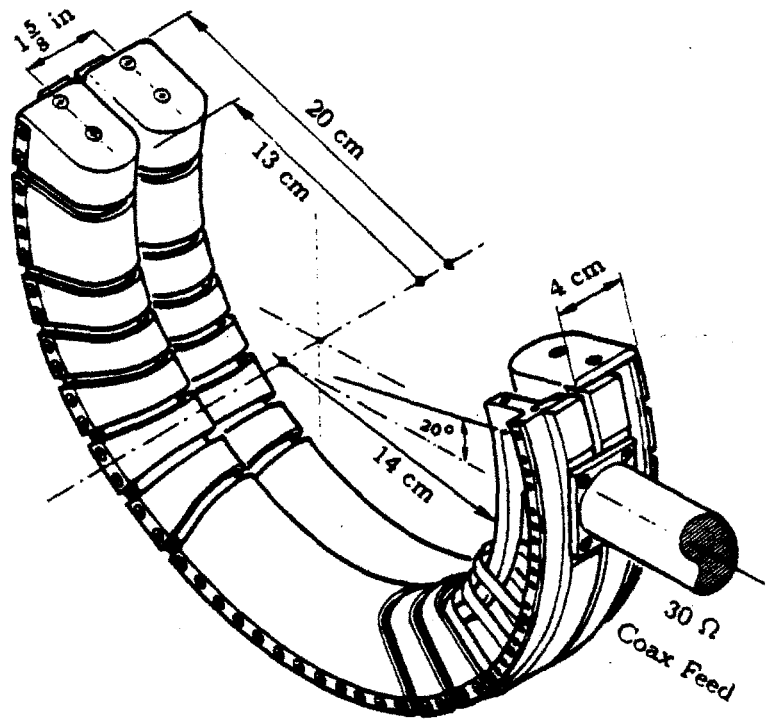

Figure 2.2.3: Two-Side Launch Antenna—This antenna is similar in design to the basic design shown in Fig. 2.2.1, except that two elements are connected in parallel, resulting in a more favorable current spectrum.

side launch; however, it was not possible to achieve a self-resonant loop with this structure.

Installation of these antennas was extremely difficult. It was necessary to insert each half of an antenna individually into the torus. The first half that was inserted had to be pushed toroidally out of the way in order to insert the second half. Then both halves were physically manipulated into position using specially designed tools. Support rods were then connected through the bottom port for the two-side launch antenna, and through both top and bottom ports for the outside launch antenna. After clamping the antenna into place, the coaxial feed was connected. Since it was impossible to view the connection to the inner coaxial connector, it was necessary to verify connection from electrical measurements.

In order to make room for the antennas inside the vacuum chamber, it was necessary to reduce the minor radius of the plasma from the fairly standard 16.5 cm to 12.5 cm by installing special limiters. Unfortunately, this resulted in degraded plasma confinement and stability properties.

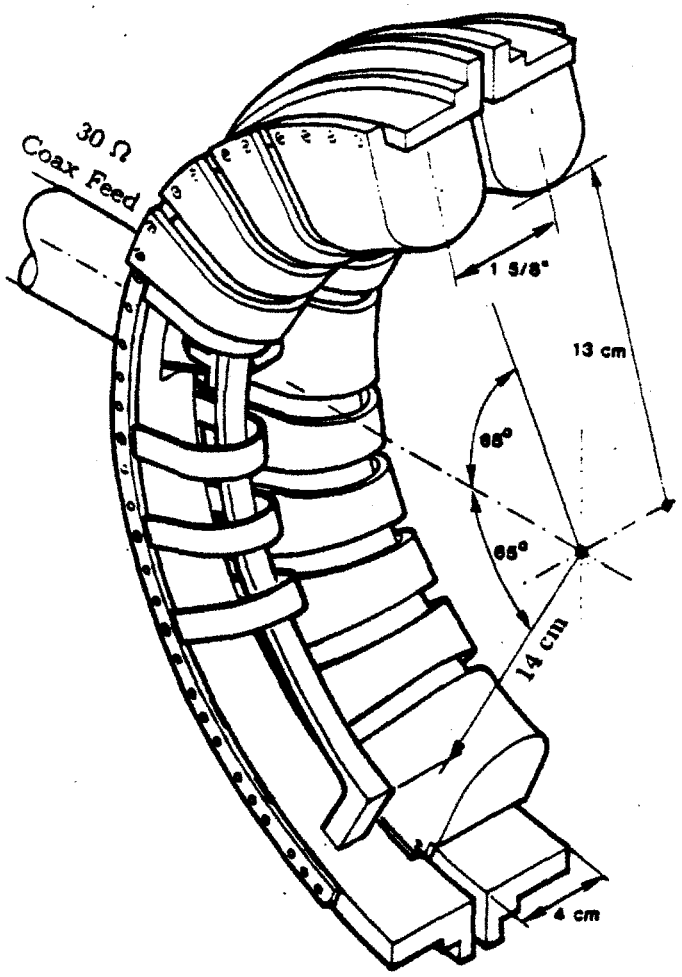

Figure 2.2.4: Outside Launch Antenna—This antenna is non-resonant, and launches power only from the low-field side of the plasma.

As previously mentioned, the Faraday shields were fabricated from stainless steel. Significant melting of the shields was observed in preliminary experiments. After this problem was discovered, new Faraday shields were fabricated, with a 0.020 inch coating of molybdenum on each outer surface. No melting of the molybdenum-coated shields was subsequently observed.

2.3: Electrical Modeling

A simple and useful way to model the electrical behavior of an ICRF loop antenna is to treat the antenna as a section of lossy transmission line, characterized by a specific (i.e., per unit length) capacitance C, a specific inductance L, and a specific resistance R. An interesting work in which the validity of this model is apparent was done by Fortgang and Hwang[97, 98] for the PLT ICRF antenna. Ideally, the specific capacitance C is determined by solving a 2D electrostatics boundary-value problem in which the Faraday shield is assumed to be an enclosed structure, while the specific inductance L is determined by solving a 2D magnetostatics boundary value problem in which the Faraday shield is ignored and the plasma can be assumed to be a perfectly conducting surface. In a more refined model, the plasma can be treated as an imperfectly conducting boundary with surface impedance obtained from a solution of the appropriate wave equation inside the plasma, in which case a value for R would also be obtained. The justification for this model is that the antenna is highly reactive (large circulating power) so that the field configuration will be approximately TEM, as in an enclosed line, and the coupling to the plasma is through the magnetic field. One function of the Faraday shield is to shield out the electrostatic components of the wave fields, thus ensuring that the coupling is through the magnetic field. Thus, the loading experienced by the antenna is determined by the antenna current, and not by the voltage on the antenna. This is why the model contains a specific resistance R but no specific conductance G.

Since the antenna design for these experiments was somewhat similar to the design of an antenna that had already been operated in Alcator C, and from which coupling data were already available, sophisticated modeling of the present design was not attempted. Several of the antenna codes that were available at the time were run for Alcator C parameters, but they were unable to predict the antenna loading that was observed on the previous antenna. It was therefore decided to construct a bench prototype of the new antenna design and to use data from the previous antenna for guidance (specifically, for an estimate of the expected plasma loading R).

The simple lossy-line model used in the design of the Alcator C antenna will be described below, and measurements from the bench tests will be summarized. I will depart slightly from conventional lossy-line notation and define the line characteristic impedance and wavenumber to be the purely real quantities given by $Z_0 \equiv \sqrt{L/C}$ and $k \equiv \omega\sqrt{LC}$. The effect of the nonzero specific resistance will be expressed explicitly in terms of the small dissipation parameter defined by $\epsilon \equiv R/\omega L$. The antenna input impedance will be denoted by $Z_i = R_i + jX_i = Z_0 z_i$, where

$z_i = r_i + jx_i$ and $j \equiv \sqrt{-1}$ is used instead of i for time variations $\sim e^{+j\omega t}$. The phase velocity on the antenna is also defined to be purely real by $v \equiv 1/\sqrt{LC}$.

In terms of this notation, the input impedance of a lossy line of length l is

$$z_i = j\sqrt{1-j\epsilon}\,\tan(\sqrt{1-j\epsilon}\,\theta) \tag{2.3.1}$$

where $\theta \equiv kl$ is the electrical length of the line. From this expression, the relation between the characteristic resistance R and the lumped radiation resistance R_L of the previous antenna (which had electrical length π) is found to be

$$R_L = \frac{R\lambda}{4} \tag{2.3.2}$$

i.e., half the length of the antenna times the specific resistance. The new resonant antenna has electrical length $\alpha \approx \pi$ and has the feed line tapped in at an electrical length θ away from one end. Considering this to be two lossy lines connected in parallel yields

$$\frac{z_i}{\sqrt{1-j\epsilon}} = j\frac{\tan(\sqrt{1-j\epsilon}\,\theta)\tan[\sqrt{1-j\epsilon}\,(\alpha-\theta)]}{\tan(\sqrt{1-j\epsilon}\,\theta)+\tan[\sqrt{1-j\epsilon}\,(\alpha-\theta)]} \tag{2.3.3}$$

As long as α does not deviate too much from π and ϵ is not too large, this expression can be approximated by

$$z_i = \frac{\sin^2\theta}{\pi\epsilon} \tag{2.3.4}$$

If it is desired to match the antenna to a feed line of impedance Z (purely real), then one selects the tap point from

$$\frac{Z}{Z_0} \equiv z = \frac{\sin^2\theta}{\pi\epsilon} \tag{2.3.5}$$

From more detailed study of Eq. 2.3.3, one finds that a slight deviation of α from the value π is necessary for the input impedance to be purely real.

Before presenting the measured values of the lossy-line parameters, I will discuss qualitatively some of the non-ideal effects that can be introduced by the Faraday shield. Ideally, the Faraday shield should have no effect on the coupling to the plasma. That is, as far as the electrical characteristics of the antenna are concerned, the geometry of the Faraday shield determines the specific capacitance C in the lossy line model but has no effect on L or R. How well an actual shield approximates the ideal case depends on both the geometry and electrical properties of the material from which the shield is fabricated. Obviously, the shield elements should be parallel

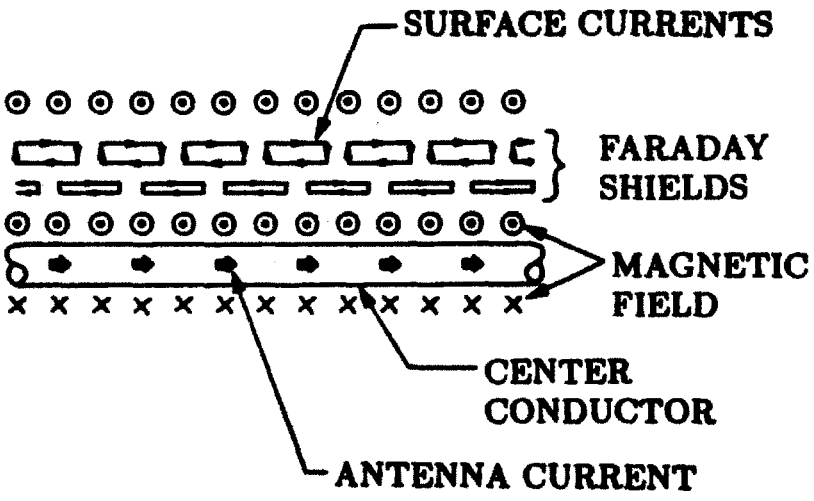

Figure 2.3.1: Faraday Shield Surface Currents—An RF magnetic field tangent to the surface of the Faraday shield will induce a surface current in the shield. This will have no effect on the magnetic field outside the shields but will cause a decrease in the antenna specific inductance proportional to the magnetic flux excluded by the shield.

to the confining magnetic field in order to avoid suppressing coupling to the fast wave and the shield should have low resistivity in order to avoid absorbing significant amounts of RF power.

Another important issue concerning Faraday shield geometry is the angle between the surface of the shields and the RF magnetic field. This effect is discussed in detail by Faulconer[96]. Consider the situation depicted schematically in Fig. 2.3.1. This illustration represents the geometry of the fields in the region nearest the plasma surface. In this region the RF magnetic field is tangent to the surface of the Faraday shields. Under these circumstances, a surface current will circulate around the edges of the shields as shown. If the shields are small compared to the wavelength of the antenna field pattern, then this surface current will be uniform in magnitude and electric charge will not build up at any point. In this case the magnitude of the RF magnetic field outside the Faraday shields will be exactly the same as it would be in the absence of Faraday shields, and there will be no effect on coupling to the fast wave in the plasma. However, there will be an effect on the electrical characteristics of the antenna — the specific inductance L will be decreased because of the flux excluded from the interior of the Faraday shields. Obviously, this effect can be made small if the Faraday shields are sufficiently thin.

The situation where the RF magnetic field is not tangent to the Faraday shield is illustrated in Fig. 2.3.2. For the Alcator C ICRF antennas, this occurs on the

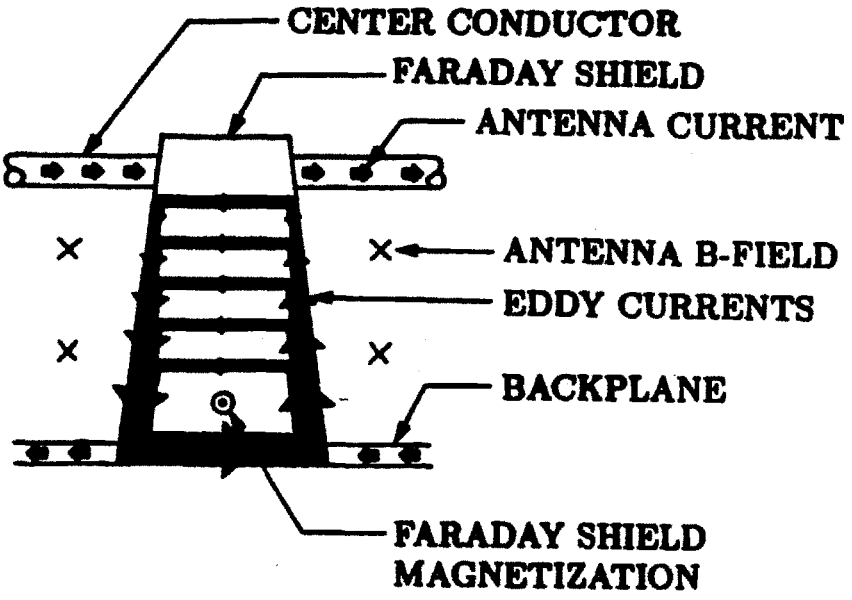

Figure 2.3.2: Faraday Shield Eddy Currents—An RF magnetic field normal to the surface of the Faraday shield will induce diamagnetic eddy currents. This will reduce the magnetic flux that reaches the plasma as well as reducing the antenna specific inductance.

sides of the Faraday shields. In this case, diamagnetic eddy currents are induced in the shields which reduce both the flux linked by the antenna radiating conductor and the flux which would couple to the fast wave in the plasma. It is intuitively obvious that this effect is more significant than the effect illustrated in Fig. 2.3.1. In principle, this effect could be eliminated by designing a Faraday shield that is everywhere tangent to the RF magnetic field, as was done for the ICRF antenna used by Blackwell in previous Alcator C ICRF experiments. However, the Blackwell design results in an open space near the backplane, and it was suspected that arcing in that region was caused by plasma and/or neutrals present in that region. In the present design, the Faraday shield is closed to the backplane in an effort to reduce the amount of plasma present there.

A simple electric circuit model for the Faraday shield flux excluding effect is shown in Fig. 2.3.3. In this model, I_1 represents the current in the antenna conductor at some point along its length and I_2 represents the surface and eddy currents in the Faraday shields. Resistance of the antenna conductor, plasma loading, and resistance of the Faraday shield are neglected in this model. The flux that links L_1 is the flux between the antenna conductor and backplane. Thus L_1 is the specific inductance of the antenna with no Faraday shields. The flux that links L_2 is the

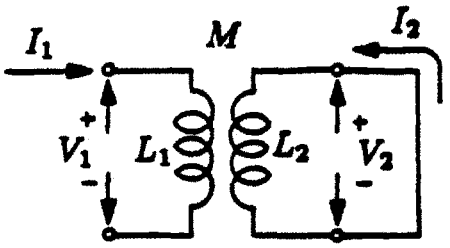

Figure 2.3.3: Electrical Model for Lossless Faraday Shield—The flux-excluding effect of the Faraday shields can be modeled by treating the shield as a transformer with the secondary winding shorted.

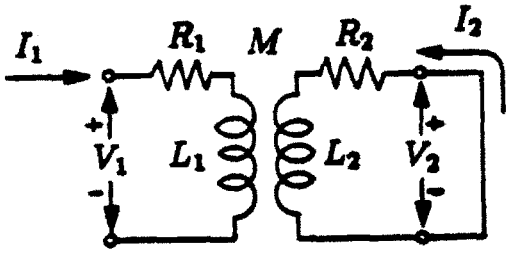

Figure 2.3.4: Electrical Model for Lossy Faraday Shield—Loss in the antenna is modeled by the resistance R_1 and loss in the Faraday Shield is modeled by R_2.

total flux excluded by the Faraday shield. Thus L_2 is the inductance associated with the surface currents and diamagnetic eddy currents (easy to estimate for the surface currents, not so easy to estimate for the eddy currents). Once L_1 and L_2 are known, the coupling between them, represented by M, is easily determined by requiring that all the flux that links L_2 also links L_1. This implies that $M = L_2$. The actual specific inductance L of the antenna with Faraday shields would then be the input inductance of the circuit in Fig. 2.3.3, which is found to be

$$L_{\text{in}} = L_1 - L_2 = L_1 - M \tag{2.3.6}$$

Here L_{in} is the specific inductance of the antenna with Faraday shields.

If dissipative effects are included in the model, one is lead to the circuit shown in Fig. 2.3.4. In this case, R_1 represents the sum of antenna conductor resistance and plasma loading in the absence of Faraday shields, while R_2 represents the resistance of the Faraday shields. The actual specific resistance and inductance of the antenna with Faraday shields would then be the input resistance and inductance respectively of the circuit in Fig. 2.3.4. This is calculated to be $Z_{\text{in}} = R_{\text{in}} + j\omega L_{\text{in}}$, where

Parameter	No Shields	Inner	Outer	Both	Ceramic
L/μ_0	0.486	0.422	0.408	0.340	0.340
M/μ_0	0.0	0.064	0.078	0.146	0.146
C/ϵ_0	2.57	7.95	6.08	6.11	13.0
v/c	0.895	0.546	0.635	0.694	0.5
Z_0 (Ω)	164.0	86.9	97.7	88.9	60.0
R (Ω/m)	2.06	0.208	0.486	0.218	0.218

Table 2.3.1: Parameters for Lossy-Line Antenna Model—These parameters were determined from bench test measurements on copper and brass antenna prototype antennas. The antenna was unloaded during these tests.

$$R_{\text{in}} = R_1 + \frac{R_2}{1+d^2} \tag{2.3.7}$$

$$L_{\text{in}} = L_1 - \frac{M}{1+d^2} \tag{2.3.8}$$

and $d \equiv R_2/\omega M$. This corresponds physically to the resistive magnetic diffusion that allows a finite amount of magnetic flux to penetrate the surface of the Faraday shield. This results in less eddy-current generation, so that the increase in loading and decrease in inductance is slightly less than proportional to the shield resistivity.

Lossy-line model parameters determined during bench tests are shown in Table 2.3.1. Parameters were measured with shields absent, with only the inner layer, only the outer layer, with both shield layers, and finally with all shields plus the ceramic cap present. The inductance L was measured by open-circuiting one end of the antenna and applying a signal at a frequency of 1 kHz to the open end of the antenna conductor, and then measuring the resulting lumped inductive reactance. The measurement was then repeated at increasingly higher frequencies to eliminate possible errors due to internal inductance and resistance of the antenna conductor. The frequency was increased until distributed field effects appeared at frequencies of a few MHz. The next step was to replace the short at the end of the conductor and measure the fundamental resonant frequency of the antenna, from which the phase velocity v was determined. The specific capacitance was then calculated from $v = 1/\sqrt{LC}$. The loading R was inferred from the feed tap position for matching.

The effect of flux exclusion by eddy currents is readily apparent in the measurements of L, which is progressively reduced as additional shielding is added. The corresponding values of M were inferred by subtracting the measurements of L from the measurement in the case with no shields. The value of M for the case with both

shield layers is nearly equal to the sum of the values for each shield layer alone, reflecting the fact that the shields are staggered with only slight overlap. From a simple cylindrical approximation of the antenna geometry, one can estimate that the effect illustrated in Fig. 2.3.1 will contribute a value $M \sim 0.035$ so that the eddy current effect illustrated in Fig. 2.3.2 is dominating. The value of L was reduced significantly to $L = 0.18$ for the double-element antennas due to coupling between the elements.

The measured values of C may seem somewhat counterintuitive at first. It is reasonable to expect C to increase significantly as shields are added, and it is reasonable to expect C to be larger for the inner shields alone than for the outer shields alone. However, the relative increase in C for the inner shields alone compared to that for the outer shields alone is larger than one would expect based on a cylindrical approximation to the antenna geometry, and C for the case with both shield layers is smaller than with the inner layer alone. It is possible to argue that these values are plausible by considering more carefully the geometry of the shields. The inner shields were fabricated from ~ 1 mm sheet metal, while the outer shields were 1/8 inch thick with rounded corners. Thus, it is reasonable to expect significant fringing fields to occur near the sharp corners of the inner shields. This would result in more capacitance than one would expect if fringing were neglected. This fringing effect would be expected to be less significant with the more rounded edges of the outer shields. Moreover, when both shield layers are present, it is reasonable to expect that the outer shields would function as "corona shields" by relaxing the field lines that were previously concentrating on the sharp surfaces of the inner shields.

Of the various parameters in the lossy-line model, the quantity which is the least accurately known and most likely to vary during the experiment is the specific resistance R. The physical antenna parameter that is most sensitive to R is the location of the feed tap point. Since it is not possible to adjust the antenna once it is installed, it is essential to determine how sensitive the antenna matching will be to variations in R. In order to explore this issue, the feed-line VSWR calculated from the lossy-line model is plotted in Fig. 2.3.5 as a function of tap position for various values of loading R. If one is interested in maintaining the feed line VSWR below 2, for example, then for any particular loading R, the range of acceptable tap positions can be determined from the intersections of the curves with the top of the graph. One can also see that the accuracy of the tap position is less critical for larger loadings.

The specific resistance observed during the Blackwell experiments was typically 15 Ω/m. Assuming a loading of $R = 15\,\Omega$/m, a tap position of 3.2 cm would seem to be an appropriate choice. Once this choice is made, the behavior of the feed-line

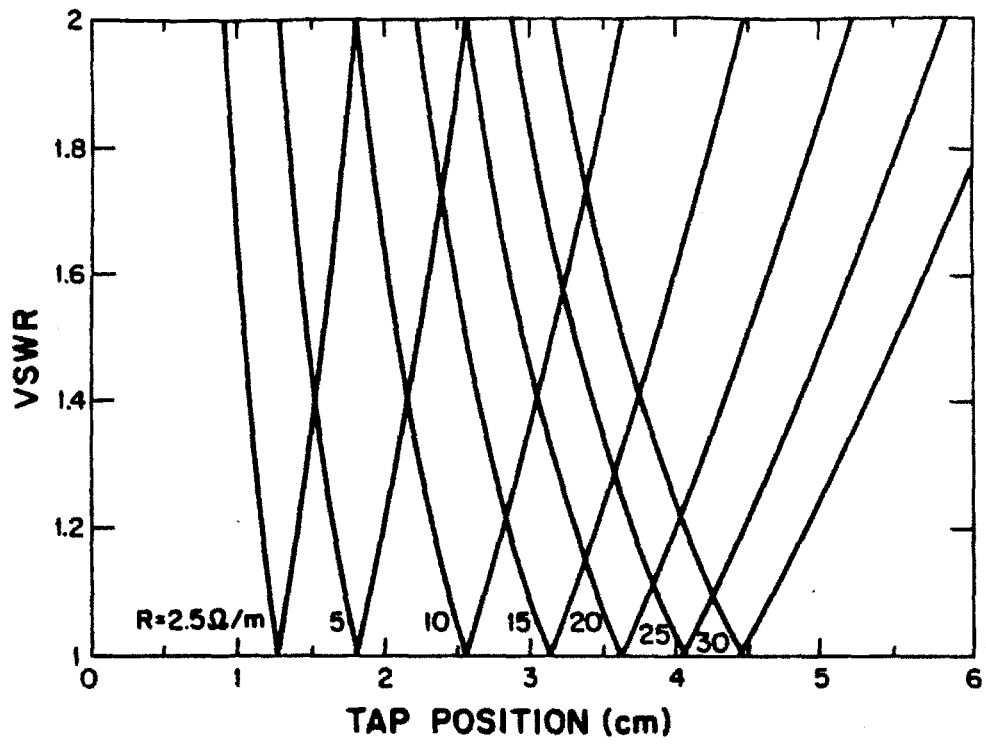

Figure 2.3.5: VSWR Versus Tap Position and Specific Resistance—The lossy-line model is used to calculate the expected voltage standing wave ratio in the antenna feed line. The dependence of the matching tap position on loading is shown here. For each loading (R), the range of tap positions over which the VSWR would be less than 2 can be seen from intersections of the curves with the top of the graph.

VSWR can be seen in Fig. 2.3.6. It can be seen that this antenna should be able to provide a reasonable match to a wide variety of loads.

The RF source used to power the antenna during the experiments can operate only within a fairly limited frequency range. The behavior of the feed-line VSWR over this frequency range is shown in Fig. 2.3.7. It is clear that the antenna is sufficiently broadband to operate at any frequency within the available range.

For sufficiently low values of antenna loading, such as during vacuum conditioning, the lossy-line model provides an estimate of the value of R. During vacuum conditioning, the feed line VSWR was measured at several different frequencies. The results are plotted in Fig. 2.3.8. Conditioning was begun at 175.5 MHz. At each frequency, the loading was observed to decrease over time, and then to return to a relatively high value when the frequency was changed. Conditioning at the two highest frequencies was not continued long enough for the VSWR to stabilize, due to lack of patience. By fitting a curve from the lossy-line model to these points, a value of $R \sim 3\,\Omega/\mathrm{m}$ is estimated. Fortunately, this value is significantly lower than

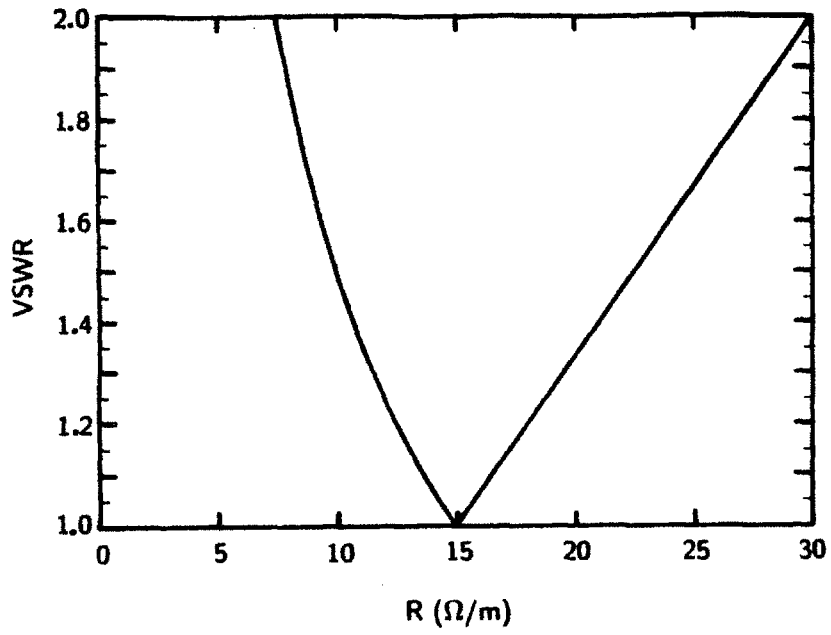

Figure 2.3.6: VSWR Versus Loading—The lossy-line model is used to calculate the variation of reflection with loading for the tap point that was chosen for the antenna.

the loading observed during the experiment, but it is also significantly higher than the loading determined during bench tests. I would speculate that this loading is produced by effects such as ionization of the residual gas in the vacuum chamber by the antenna fields and multipactoring.

One might be tempted to assume that this loading is a measure of the "background" loading during the experiment, and to conclude that 20% would be a reasonable estimate for the fraction of the RF power lost before coupling to the fast wave. However, there is no reason to believe that the parasitic loading would be similar at the much higher pressures and plasma loading involved during the experiment. Nevertheless, numbers obtained this way are often used as an estimate of the parasitic power lost during experiments. It is worth mentioning that the specific resistance of the actual service antenna was measured during a bench test in which the antenna was tightly wrapped with aluminum foil, in an effort to eliminate all coupling to "vacuum". It was not physically possible to place a short circuit close enough to the feed point to obtain a match, and the inductance of the shorting device was probably significant. It is estimated from this measurement that the resistive loading of the antenna is less than 0.7 Ω/m. In order to account for the behavior of the heating results in these experiments, it will be necessary to look for much more severe loss mechanisms than this.

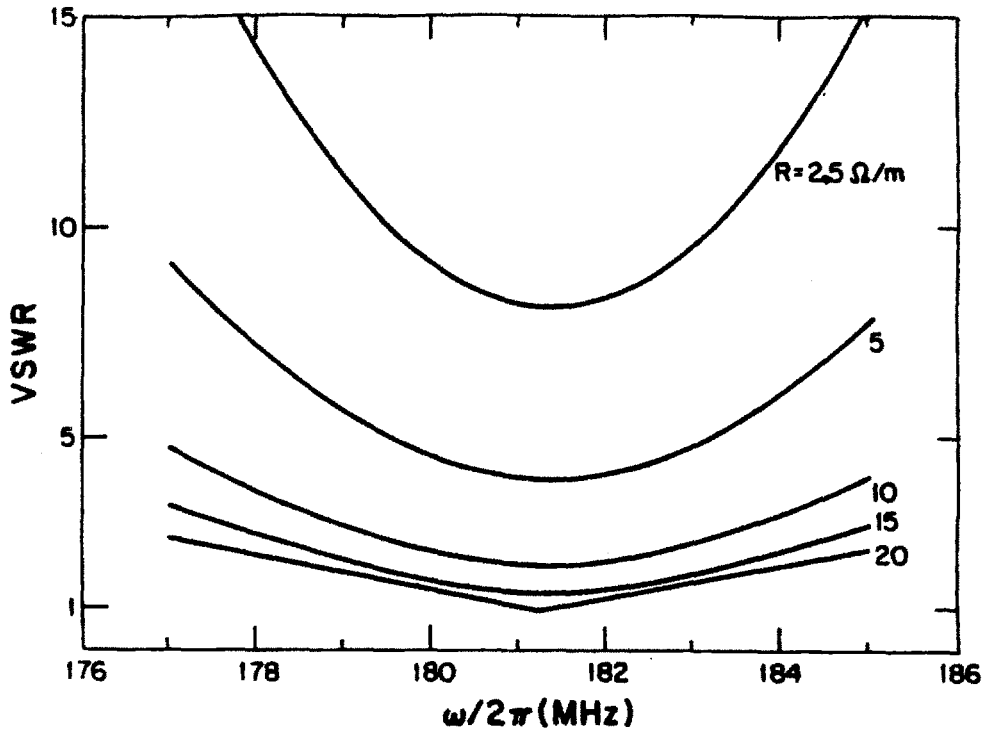

Figure 2.3.7: VSWR Versus Frequency—The lossy-line model is used to calculate the VSWR as frequency is swept for various loadings.

2.4: Summary

Antenna designs have been developed which are capable of coupling the fast wave reasonably well to the Alcator C target plasma while delivering the full available ICRF power. This design was accomplished without the need to resort to extensive numerical modeling by using a previous design as a starting point and taking advantage of loading data obtained during experiments carried out with the previous design. The power-handling capability of the system was significantly improved compared to the system used with the earlier antenna, so that electrical failures were reduced to a tolerable level.

The resonant (matched) and non-resonant (unmatched) antennas had quite similar power handling capabilities. The antennas were the only part of the system that ever exhibited physical evidence of electrical breakdown (such as arc tracks). It therefore appears that the improved vacuum feedthrough design is primarily responsible for the improved power handling capability.

Although the antennas were capable of handling the full ($\sim$ 450 kW) available ICRF power, the power handling capability was observed to degrade at high density.

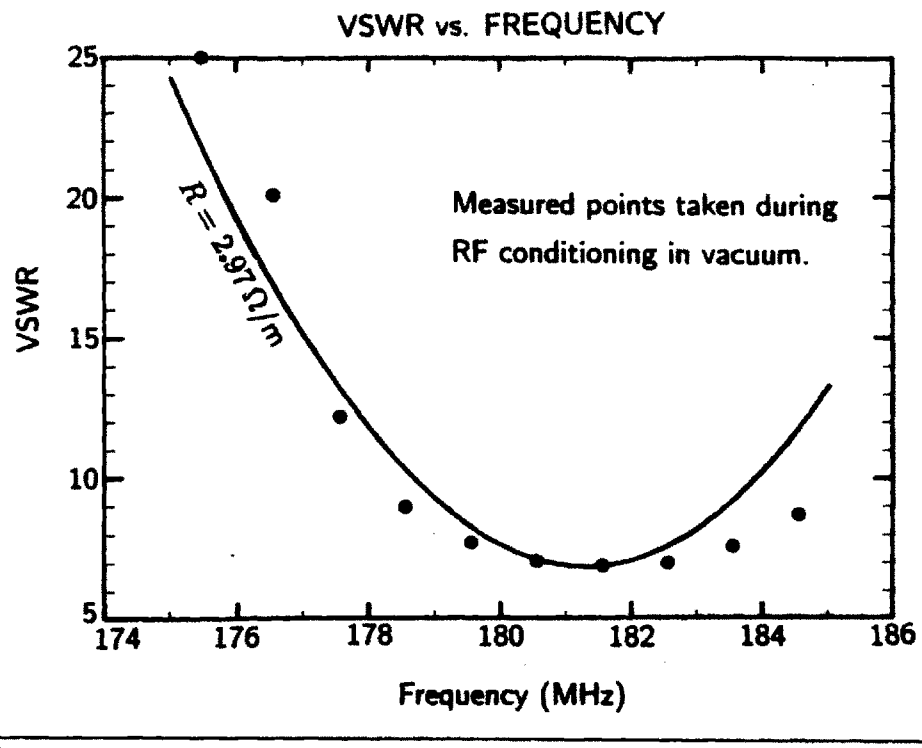

Figure 2.3.8: VSWR During Vacuum Conditioning—By fitting a curve from the lossy-line model to experimentally measured points, an estimate of the parasitic loading of the antenna during vacuum conditioning is obtained.

It therefore seems reasonable to presume that it would not have been possible to handle significantly higher power at any density if more power had been available. However, considering the space limitations, the power flux density at the antenna surface was comparable to that which would be required for next-generation experiments, with improved port access. From the results presented in the next chapter, and from the analysis presented in Chapter 4, it is concluded that antenna power-handling limitations are not the cause of the discouraging heating results observed during the Alcator C ICRF heating experiments.

CHAPTER 3

Experimental Results

Parameter	Alcator	ICRF
R_0 (cm)	64	64
a (cm)	16.5	12.5
B_0 (T)	5–13	12
I_P (kA)	50–800	140–410
$\bar{n}_e$ (10^{20} m^{-3})	0.3–20	0.8–5
T_e (keV)	1–3	1.5–2.5
T_i (keV)	0.5–1.5	1–1.3
τ_E (ms)	5–50	5–25
P_{OH} (MW)	0.1–1.5	0.2–1

Table 3.1.1: Experimental Parameters—Typical experimental parameters for Alcator C in general, and for the target plasmas during ICRF fast-wave experiments are shown.

3.1: Introduction

Results of fast wave ICRF minority regime heating experiments carried out on the Alcator C tokamak are presented in this chapter. The majority ion species in these experiments was always deuterium and the minority species was always hydrogen, resulting in a required toroidal field magnitude of 12 T for the available generator frequency of 180 MHz.

Typical plasma parameters are shown in Table 3.1.1, both for Alcator C in general, and for the ICRF fast wave experiments in particular. It was necessary to reduce the minor radius of the plasma, by installing special limiters, in order to make room for the antennas inside the vacuum chamber. This may have been responsible for some tokamak operational difficulties encountered. The toroidal field of 12 T places the cyclotron resonance layer within 1 cm of the plasma center. This toroidal field was used for most of the shots, except when conditioning the antenna. Operation at lower field when bringing the antenna up to power required less time between shots (to wait for the toroidal field magnet to cool down). The toroidal field was also scanned downwards from 12 T during a controlled experiment, in which the hydrogen tail formation was monitored. It is not possible to operate Alcator C at toroidal field magnitudes significantly greater than 12 T.

It was not possible to vary the plasma parameters independently of one another in an arbitrary manner during the ICRF experiments. The plasma current I_P = 140 kA corresponded to the lowest plasma density, and the plasma current I_P = 410 kA corresponded to the highest plasma density. With very few exceptions,

Major Radius :	R_0
Minor Radius :	a
Central Toroidal Magnetic Field :	B_0
Toroidal Plasma Current :	I_P
Resistive Loop Voltage :	V_R
Line-Average Electron Density :	$\bar{n}_e$
Central Electron Density :	n_{e0}
Central Electron Temperature :	T_e
Central Ion Temperature :	T_i
Central Deuterium Temperature :	T_D
Central Hydrogen Temperature :	T_H
Global Energy Confinement Time :	τ_E
Gross ICRF Power :	$P_{\rm RF}$
Ohmic Heating Power :	$P_{\rm OH} = I_P V_R$
Hydrogen Minority Concentration :	$\eta_H = n_H/(n_H + n_D)$
Global Effective Z :	$Z_{\rm eff} = \sum_i \frac{n_i Z_i^2}{n_e}$
Edge Safety Factor :	$q_a = 2\pi \frac{a^2 B_0}{\mu_0 R_0 I_P}$

Table 3.1.2: Notation—Definition of symbols used in this chapter to represent experimental quantities.

the variation of plasma current for intermediate densities was approximately linear between these two values. The electron temperature was ~ 2.5 keV at low density and decreased to ~ 1.5 keV at high density, while the deuterium ion temperature was ~ 1 keV at low density, increasing to ~ 1.3 keV at high density. The Ohmic heating power increased from ~ 200 kW to ~ 1 MW as density increased.

The notation used in this chapter to refer to various plasma parameters is shown in Table 3.1.2. Most of these symbols are standard. The "gross ICRF power" is the net forward power (i.e., forward minus reflected) measured in the antenna feed line, without correcting for any losses that may be present. The line-average electron density was averaged over a vertical chord through the center of the plasma (i.e., at $R = R_0 = 64$ cm).

Significant changes in target-plasma density were often observed when the ICRF was applied. When a significant density increase appears to be correlated with the RF, the shot is termed a "rising-density shot". Data from such a shot, along with introductory descriptions of the experimental diagnostics, are presented in

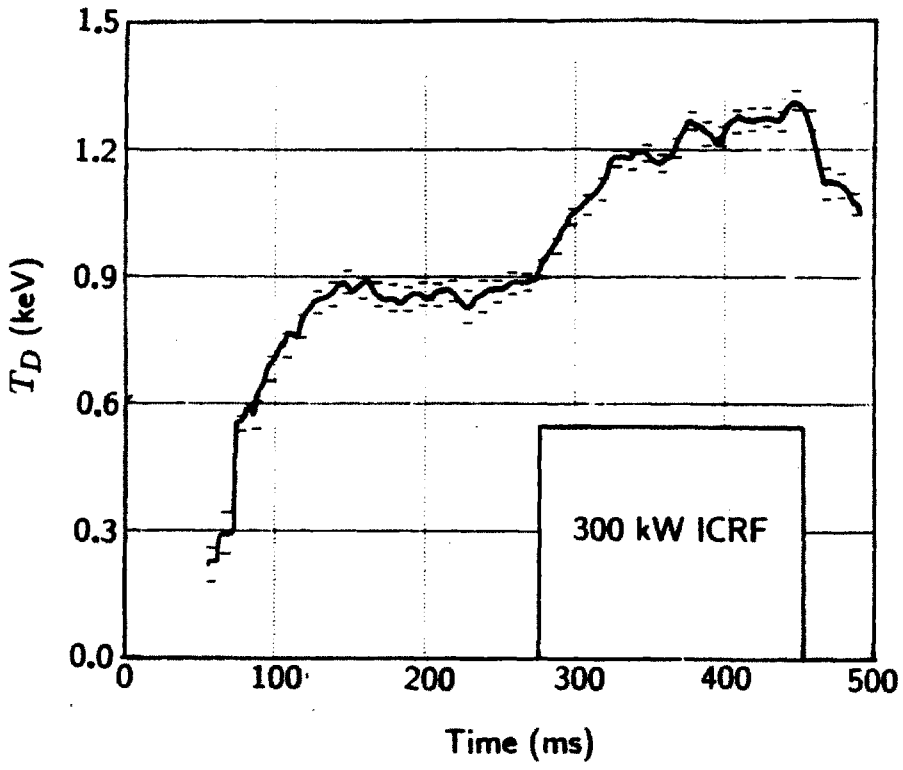

Figure 3.2.1: Deuterium Temperature for Rising-Density Shot—Application of 300 kW of ICRF power for 175 ms produced a 400 eV increase in deuterium temperature. This temperature measurement was derived from the deuterium charge-exchange spectrum.

the next section. A "steady-density shot" is shown in the following section for comparison. When there is a significant density change during the RF, some heating can be caused by changes in collisional coupling between electrons and ions, and it is necessary to perform careful power balance analysis in order to evaluate the effectiveness of the RF heating. Such analyses are performed using the ONETWO transport code and are presented in Chapter 4.

3.2: Rising-Density Shot

The largest observed increase in deuterium temperature occurred during a rising-density shot. The deuterium temperature for this shot determined from the charge-exchange diagnostic is shown in Fig. 3.2.1. This measurement was obtained from

Parameter	Ohmic	RF
T_D	900 eV	1300 eV
I_P	154 kA	154 kA
q_a	9.5	9.5
V_R	1.5 V	2.15 V
$P_{\rm OH}$	230 kW	330 kW
$P_{\rm RF}$	0 kW	300 kW
$\bar{n}_e$	0.84×10^{20} m^{-3}	1.35×10^{20} m^{-3}
n_{e0}	1.0×10^{20} m^{-3}	2.0×10^{20} m^{-3}
η_H	$\sim 0.5\%$	—
$Z_{\rm eff}$	2.2	3.5
τ_E	7.7 ms	5.2 ms*

* Assumes 100% RF absorption.

Table 3.2.1: Parameters for Rising-Density Shot—Equilibrium data are listed before and during the RF pulse for the shot in Fig. 3.2.1.

a horizontally and perpendicularly viewing charge-exchange neutral energy analyzer[99]. The operation of this diagnostic and processing of the raw data was performed by Dr. C. L. Fiore. By fitting a Maxwellian to the high-energy channels, a measurement of the central ion temperature is obtained (assuming the ion temperature to be centrally peaked). This analyzer can measure either hydrogen or deuterium, but not both on the same shot. It can, however, be switched from one ion species to another on a shot-to-shot basis. There is no tangential viewing access in Alcator C, so it is not possible to scan the analyzer in the horizontal direction. However, it is possible to obtain radial temperature profile information out to $r \sim 7$ cm by scanning the viewing chord in the vertical direction. The central deuterium temperature measurement from this diagnostic is typically accurate to within ± 50 eV.

For this shot, 300 kW of ICRF power was applied for 175 ms, yielding a 400 eV increase in deuterium temperature. The target plasma was a fairly low-density, low-current shot, with $\bar{n}_e = 0.84 \times 10^{20}$ m^{-3} and $I_P = 154$ kA. Some other plasma parameters for this shot are shown in Table 3.2.1. The global energy confinement time was calculated as the ratio of the total thermal energy content of the plasma to the total heating power, where the total heating power was the sum of $P_{\rm OH}$ and $P_{\rm RF}$ without correcting for any RF loss mechanisms.

Deuterium temperature measurements are also available from the neutron diagnostic operated by Dr. C. L. Fiore during these experiments. The deuterium

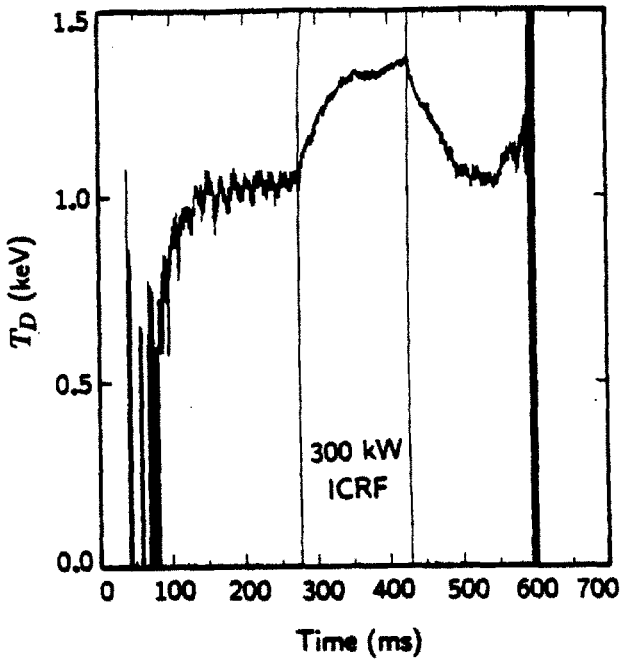

Figure 3.2.2: Deuterium Temperature from Neutron Measurement for Rising-Density Shot—There was generally good agreement between deuterium temperatures deduced from neutron measurements and charge-exchange spectra. This measurement was from a rising-density shot similar to the one in Fig. 3.2.1.

temperature deduced from neutron measurements for a shot similar to the one in Fig. 3.2.1 is shown in Fig. 3.2.2.† Normally, the accuracy of the deuterium temperature measurement from the neutron diagnostic is ±50 eV — the same as for the charge-exchange diagnostic. However, under certain circumstances which were common during the ICRF experiments, the uncertainty can be greater. The rate of production of thermonuclear neutrons from the D + D $\longrightarrow$ He^3 + n reaction depends globally on the deuterium temperature and density. When the data analysis is performed, a power-law approximation is used for the reaction cross-section, yielding

$$R \propto n_{D0}^2 T_{D0}^{5.611} \times P \tag{3.2.1}$$

where P represents an integration over the entire plasma volume, and thus contains all the profile information. The power-law approximation is not a source of significant error. The greatest source of uncertainty is from the measurement of the bulk neutron production rate R, which is accurate to within ±25%. This

† The charge-exchange analyzer can only analyze one ion species per shot and was measuring hydrogen during the shot in Fig. 3.2.2. These two shots were produced consecutively.

alone accounts for ±40 eV of uncertainty in the inferred T_{D0}. Assuming no error in the profile shape P, the uncertainty in n_{D0} brings the uncertainty in T_{D0} up to ±50 eV. The central deuterium density is inferred from the central electron density and the central Z_{eff}. In these experiments, carbonization was not used, so deuterium depletion from impurities was not serious. However, there was often significant density profile peaking during the RF, usually for shots in which the line-averaged density was increasing. The software which analyses the neutron data determines the central density by inputting the measured line-averaged density and assuming a time-independent density profile shape. Ordinarily, this does not introduce serious errors in the measurement. However, since the indicated deuterium heating in these experiments was often extremely modest, this density peaking effect is cause for concern. For most of the shots during which there was density profile peaking, the central-to-line average density ratio increased by less than 10%. A simple calculation shows that if P is held fixed a 10% change in n_{D0} changes R by the same amount as a 30 eV change in T_{D0}. Thus, density peaking increases the experimental uncertainty to ±80 eV. Because the plasma becomes excessively opaque to neutrals at high density, the charge-exchange diagnostic is only useful for determining ion temperatures for the lower-density shots. Because of this and the need to use the charge-exchange analyzer to measure the hydrogen tail, it was necessary to rely heavily on the neutron diagnostic for deuterium temperature measurements. Fortunately, density peaking tended to occur only for low-density shots, for which it was possible to cross-check many of the neutron measurements with charge-exchange measurements.

In Chapter 4 a more accurate analysis will be done using 44 of the shots from the database by running the ONETWO transport code. The ONETWO code includes a more accurate calculation of the ion temperature from measured neutron rates and can self-consistently include the effects of time-dependent temperature and density profiles as well as depletion of deuterium density, using Z_{eff} inferred from the resistive loop voltage. However, use of ONETWO for data analysis is extremely tedious and time consuming, so analysis of the entire data base was not feasible. Nevertheless, the analysis of 44 shots to be presented in Chapter 4 shows no serious discrepancy between the deuterium temperatures determined from ONETWO and from the Alcator C diagnostic. ONETWO also provides detailed power balance and energy transport information from analysis of measured data, but this analysis must be deferred until after the RF power deposition calculations, which are also presented in Chapter 4.

Electron density measurements during the experiment were obtained by Dr. S. M. Wolfe from a five-chord far-infrared laser interferometer[100]. Interferometer data for the shot in Fig. 3.2.1 are shown in Fig. 3.2.3. When the smaller 12.5 cm

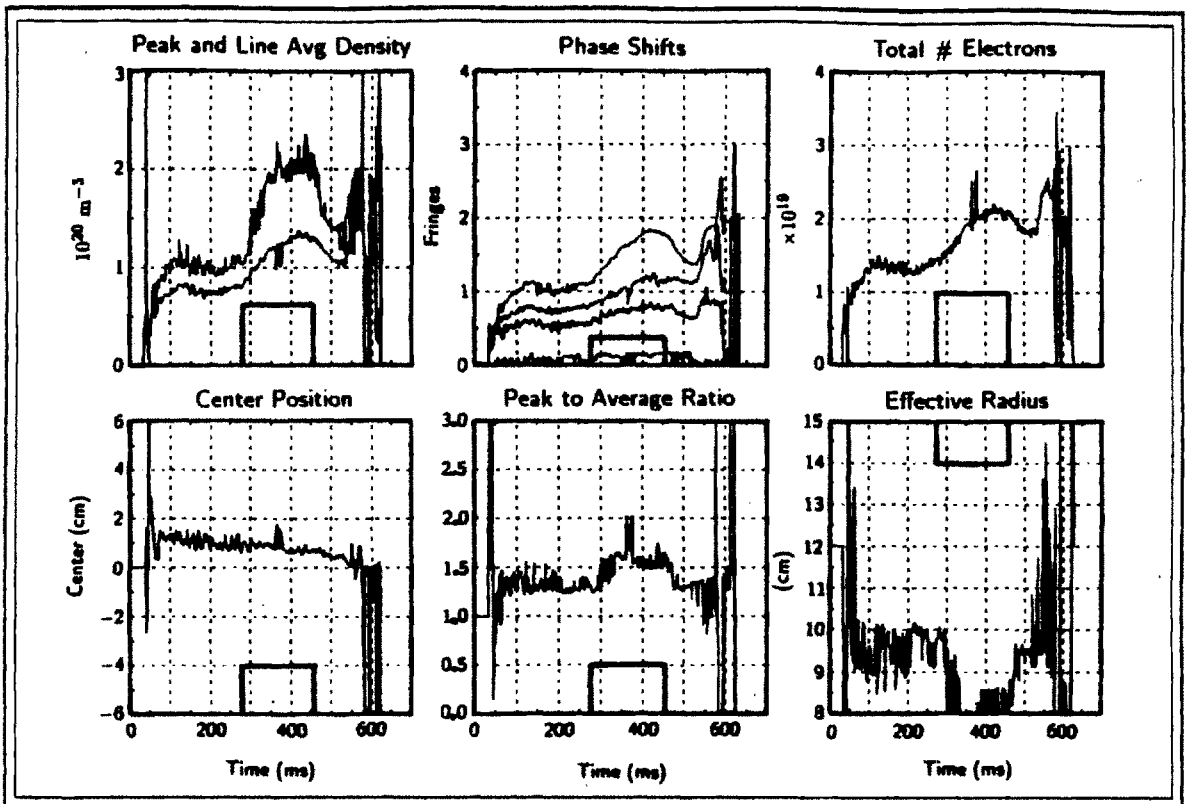

Figure 3.2.3: Density Profile Data for the Rising-Density Shot—There was significant peaking of the density profile for the rising-density shot. Although the deuterium temperature increments were indeed higher for this type of shot compared to steady-density shots, the density profile peaking would tend to exaggerate estimates of incremental energy confinement time which assume unvarying profile shapes. The quantity called "effective radius" is $\frac{1}{n_0}\int_0^a n_e(r)\,dr$.

limiter is installed, one of the chords is completely outside the plasma, while another of the chords barely grazes the limiter radius. Thus the radial profile information in Fig. 3.2.3 represents only a "3 1/2-point fit". The measurement of line-averaged density is accurate to $\pm 5\%$ or $\pm 0.1 \times 10^{20}\,\mathrm{m}^{-3}$, whichever is greater, but the inferred peak density will be somewhat more uncertain. Since the local neutron production rate is $\propto n^2 T_D^{5.611}$, the neutron temperature diagnostic is far less sensitive to the actual profile shapes than to the peak temperatures. Thus, a direct measurement of the peak density would be preferred. Such a measurement is available from the Alcator C Thomson scattering diagnostic[101], which was operated by E. J. Rollins under the direction of Dr. R. L. Watterson. This diagnostic provides central electron density measurements of accuracy equal to that of the line-average electron density measurement from the interferometer. The Thomson scattering diagnostic also provides electron temperature measurements which are usually accurate to within ± 100 eV. These data will be used in the ONETWO analysis to infer a density profile by fitting a parabolic shape to the measured peak and line-average densities.

Both a substantial density increase as well as a significant profile peaking effect are exhibited by the data in Fig. 3.2.3. Because the deuterium heating was substantial for this shot, the uncertainty in the neutron-derived ion temperature is not a problem. However, there is significant ambiguity introduced in evaluating the efficiency of the RF heating because a density increase also increases the collisional coupling between electrons and ions, increases the ohmic power, and alters the transport properties of the plasma. This ambiguity is obvious if one considers the time scale exhibited by the measurements shown in Figs. 3.2.1 and 3.2.2. If the heating was caused only by an increase in the heating power to the deuterium, with all other plasma parameters constant, then the time scale for the deuterium temperature to reach equilibrium during the RF should be on the order of the deuterium energy confinement time, which is ~ 10 ms for this shot. However, the heating seen on this shot seems to take place on a much longer time scale. This time scale is in fact the same as the time scale for the change in density during the RF, suggesting that there is indeed a significant change in collisional exchange power during this shot. These effects can be carefully considered when doing analysis with the ONETWO transport code, but for the simpler analyses in this chapter it is best to concentrate on shots without large changes in density during the RF.

The hydrogen charge-exchange energy spectrum for the shot in Fig. 3.2.2 is shown in Fig. 3.2.4. The observed tail temperatures were generally quite modest, ranging from a few keV to a few tens of keV. Charge-exchange spectra, both during the ohmic phase and the RF, are always depleted for energies above ~9–15 keV. This behavior is not unique to the RF experiments and has been attributed to the effects of toroidal-field ripple-trapping of high energy ions. A second region of depletion is sometimes observed for energies localized around 2 keV. This depletion at lower energy is observed only during the RF. Radial charge-exchange scans indicate that this depletion takes place primarily in the outer ($r \gtrsim 7$ cm) portions of the plasma. This lower-energy depletion might also be caused by ripple-trapping. The ripple amplitude in Alcator C increases rapidly with r in the outer portions of the plasma, so that depletion at these lower energies might be expected if 2 keV hydrogen ions were present near the edge. This would be expected for low-density shots. These features of the hydrogen energy spectrum are not unique to rising-density shots.

It appears that this ripple-trapping phenomenon is a very serious problem for the ICRF heating experiments on Alcator C. A significant amount of literature has been written on this topic[102–119]. This effect is caused by imperfect toroidal axisymmetry in the confining magnetic field. Normally particles are confined to move on drift surfaces which are either circular toroids slightly displaced from the magnetic flux surfaces (passing particles) or "banana-shaped" toroids (banana-trapped particles). If the toroidal field is not perfectly axisymmetric, this causes the drift

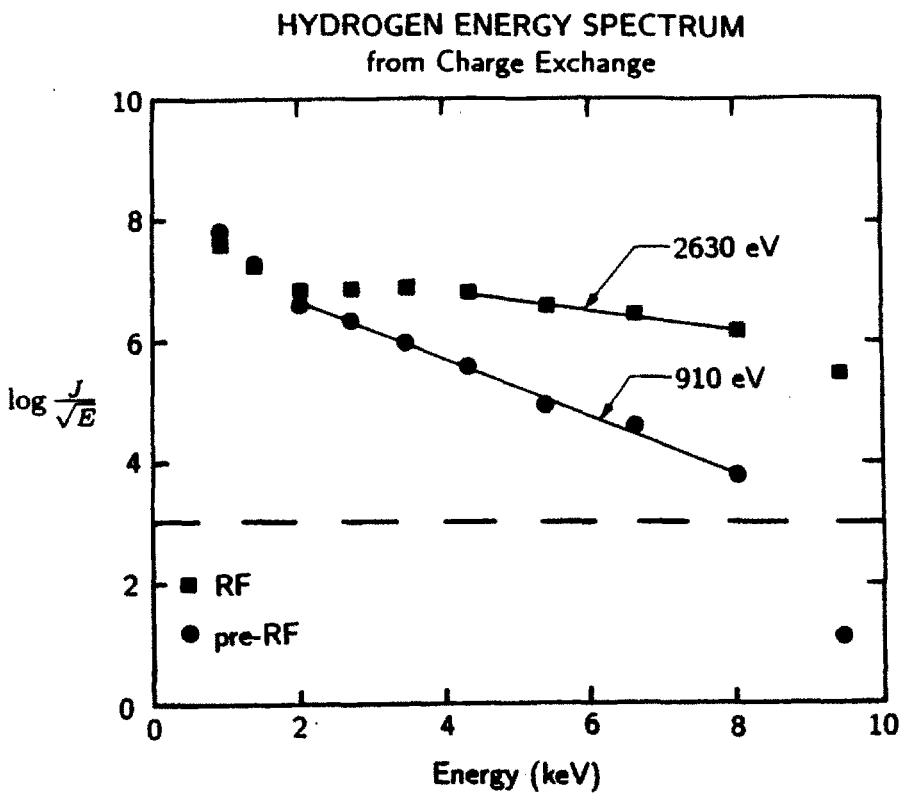

Figure 3.2.4: Hydrogen Charge-Exchange Spectrum—The hydrogen spectrum typically showed modest tail formation and depletion for energies above ~9–15 keV. Depletion at 2 keV was not always observed.

surfaces to become slightly irregular, so that the orbits no longer close on themselves. The result is a process known as *ripple diffusion*, in which the particles gradually wander away from the original drift surfaces. Ripple diffusion occurs for both trapped and passing particles, but is more severe for trapped particles, when the tip of the banana orbit is in the magnetic ripple well. It is also possible for orbits to be profoundly changed if a particle becomes mirror-trapped in the magnetic ripple well — a phenomenon called *ripple trapping*. A particle can become ripple trapped either by pitch-angle scattering into the ripple "loss cone" or by drifting into a region of higher ripple magnitude near the banana tip due to the finite width of the banana orbit (because ripple magnitude generally increases rapidly with minor radius). Once in the ripple well, the particle reflects back and forth at the mirror points and simultaneously drifts vertically out of the plasma due to the $\mathbf{B} \times \nabla B$ drift. The particle can then either escape from the plasma or pitch-angle scatter out of the loss-cone, back onto a confined orbit.

In complete analogy with neoclassical transport, this process has a collisional regime in which particles scatter out of the loss-cone faster than the time between

mirror bounces, a collisionless regime in which particles mirror-bounce many times before pitch-angle scattering, and a plateau regime in between. In the literature, it is the ripple plateau regime that receives the most attention, because most experiments fall in that regime. However, because the ripple magnitude is so large on Alcator C[118], Alcator C falls in the collisionless regime. Since this regime is not well treated in the literature, it will be difficult to accurately treat the ripple-trapping when analyzing the ICRF data. For this reason, the treatment of ripple losses in this thesis will be somewhat ad hoc. It is difficult to justify spending time to analyze this regime theoretically, since it is obvious that this regime should be avoided in any experiment. Another disturbing fact concerning the toroidal-field ripple in Alcator C is that there is a nonzero ripple well throughout the plasma cross-section, including the location of the cyclotron absorption layer. Thus trapped particles with banana tips in the resonance layer, which absorb most of the RF power, are also most susceptible to ripple trapping. This interaction between the effects of resonance localization and ripple trapping has also not been treated in the literature, and again there is no strong motivation to study it. This is because it is not necessary to have zero magnetic ripple in order to avoid a well in the resonance layer. For any finite ripple magnitude, it is possible to "wash out" the ripple well if the poloidal field is sufficiently strong. This effect occurs when the variation in toroidal field strength due to motion of the particle in the major-radial direction is greater than the variation of the toroidal ripple due to motion of the particle in the toroidal direction. In Alcator C the ripple is too great for this to happen for the plasma currents used in the ICRF experiments.

A simplified treatment of ripple-trapping in Alcator was given by Greenwald, Schuss, and Cope[114]. They find that, to a good approximation, the effect of ripple-trapping is that the distribution function is truncated at an energy $E_{\rm tr}$ given by

$$E_{\rm tr} = \left[\frac{8\pi}{2^{7/2}}\left(\frac{e^2}{4\pi\epsilon_0}\right)^2 \frac{n\lambda\sqrt{m}\,aR_0\omega_c}{\delta}\right]^{2/5} \tag{3.2.2}$$

and has a Maxwellian shape for $E < E_{\rm tr}$. In Eq. 3.2.2, λ is the Coulomb logarithm and δ is the magnitude of the ripple well depth normalized to the magnitude of the applied toroidal field. The magnitude of the toroidal field ripple in Alcator C was documented by Schissel[118]. Using values of δ from Ref. 118 and plasma parameters typical of the ICRF experiments yields values of $E_{\rm tr}$ ranging from $\sim$ 10 keV at $\bar{n}_e = 1 \times 10^{20}\,{\rm m}^{-3}$ up to $\sim$ 20 keV at $\bar{n}_e = 4 \times 10^{20}\,{\rm m}^{-3}$.

The time evolution of the hydrogen tail temperature, shown in Fig. 3.2.5, shows a significant increase throughout the RF pulse, even though the RF power is held

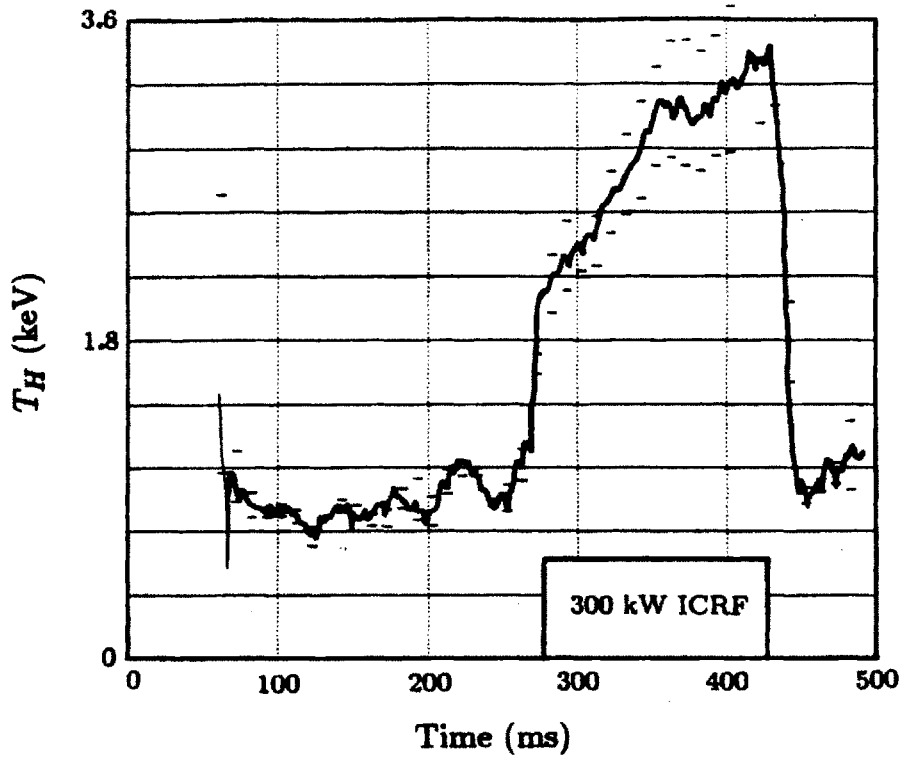

Figure 3.2.5: Time Evolution of Hydrogen Tail Temperature—The hydrogen tail is generated rapidly at the beginning of the pulse and equilibrates rapidly at the end of the pulse. The gradual increase in the tail temperature throughout the pulse suggests that the hydrogen may be seriously depleted by losses during the RF.

constant during the pulse. This could indicate that the hydrogen concentration is being depleted due to strong losses. If the concentration was decreasing during the pulse, while collisional-exchange power was constant, then the hydrogen tail temperature would have to increase. If this was true, then the amount of power absorbed by deuterium second harmonic cyclotron resonance would be expected to increase. In the next chapter, it will be shown that the hydrogen minority tail is subject to severe losses. Thus a net increase in the fraction of power absorbed directly by the deuterium would increase the heating efficiency. This could explain the long time scale for the increase in deuterium temperature shown in Figs. 3.2.1 and 3.2.2. However, as has already been mentioned, this effect (for the deuterium) could also be caused by an increase in the collisional exchange power from electrons to deuterium. An alternate hypothesis is that the loss mechanism from toroidal field ripple trapping was gradually improving. It is known that the toroidal field

ripple in Alcator C decreases in time as the current in the toroidal field windings relaxes[118]. It is not possible to test either of these hypotheses using the available experimental data.

It is possible to do a simple, rough analysis to estimate the importance of hydrogen tail loss for this shot. Using the isotropic analytic approximation from Stix[88], the slope of the hydrogen energy spectrum is given by

$$\frac{1}{T_{\rm eff}(E)} \equiv -\frac{d\ln f(E)}{dE} \tag{3.2.3}$$

$$= \frac{1}{T_e(1+\xi)}\left[1+\frac{R_D(T_e-T_D+\xi T_e)}{T_D(1+R_D+\xi)}\frac{1}{1+(E/E_D)^{3/2}}\right] \tag{3.2.4}$$

where

$$\xi = \frac{1}{8\sqrt{\pi}}\left(\frac{4\pi\epsilon_0}{e^2}\right)^2 \frac{m\langle P\rangle}{\eta_H n_e^2 \ln\Lambda}\sqrt{\frac{2T_e}{m_e}} \tag{3.2.5}$$

$$R_D = \sqrt{\frac{m_D}{m_e}\frac{T_e}{T_D}} \tag{3.2.6}$$

$$E_D(\xi) = \frac{m_H T_D}{m_D}\left[\frac{3\sqrt{\pi}}{4}\frac{1+R_D+\xi}{1+\xi}\right]^{2/3} \tag{3.2.7}$$

The quantity $\langle P\rangle$ represents the flux-surface average of the ICRF power density absorbed by the hydrogen (and therefore is a function of r). There is no way to directly determine this power deposition profile from experimentally measured data. For an extremely rough estimate, one can assume that the power deposition profile is uniform, and estimate $\langle P\rangle$ as follows:

$$\langle P\rangle = \frac{P_{\rm RF}}{2\pi^2 R_0 a^2} \tag{3.2.8}$$

Clearly, if the power deposition profile is peaked in the center, then this will significantly underestimate the power density at the center as well as the calculated tail temperature. Keeping this in mind, and using the data from Table 3.2.1, I obtain $\langle P\rangle = 1.5\,\mathrm{MW/m^3}$, $\xi = 26.4$, $R_D = 85.7$, $E_D(\xi) = 2$ keV, and

$$T_{\rm eff}(E) = \frac{49\ \mathrm{keV}}{1+\frac{28}{1+(E/2)^{3/2}}} \tag{3.2.9}$$

where $E = E_H$ is in keV. This predicts that there would be a minority tail temperature of $T_H = T_{\rm eff}(\infty) = 49$ keV. In order to measure this tail, one would

have to measure particles from the distribution function with energies such that $1 + (E/2)^{3/2} \gg 28$ (i.e., where $T_{\rm eff}(E)$ is linear), which yields $E \gg E_c \equiv 18$ keV.

It is now clear that the truncation of the minority distribution function caused by ripple trapping should have a very profound effect on the RF heating effectiveness. If this tail was really present, but for some reason the charge-exchange flux above 10 keV was too weak to measure, then (ignoring the apparent depletion between 8 and 10 keV) the minority tail temperature expected to be shown by the charge-exchange diagnostic would be $T_H = T_{\rm eff}(8) = 12$ keV. Thus, even with the pessimistic assumption that the power deposition profile is uniform, one would expect much higher minority tail temperatures than were observed.

Before going on, it should be emphasized that the interpretation of the hydrogen charge exchange spectrum is extremely ambiguous. Normally, if loss mechanisms are not present, the hydrogen distribution function would approach the shape of a high-energy Maxwellian (i.e., $T_{\rm eff} \to T_\infty$, independent of E) for energies $E \gg E_c \approx 10T_e$. There is also another condition that must be satisfied in a practical measurement derived from a charge-exchange neutral analyzer. Even if the energy range that is being sampled is high enough that the *central* $T_{\rm eff}$ approaches T_∞, the charge-exchange diagnostic actually samples data from a chord through the plasma cross-section. Thus, the actual neutral flux will contain contributions from all minor radii, at which there are varying values of $T_{\rm eff}(r)$ (as well as $T_\infty(r)$). Assuming the minority temperature to be centrally peaked, then one must measure the charge-exchange flux in an energy range that contains contributions only from the central part of the plasma in order to obtain an accurate measurement. The energy range involved will then depend on the actual temperature and density profiles of the ions and the background neutrals. In general, this requires that the charge-exchange spectrum be measured in the range $E \gg 3$–$10T_\infty$.[120]

In the Alcator C experiments, there are no high-energy particles in that energy range, so instead a fit was made in a much lower energy range. It is not at all clear that the charge-exchange spectrum comes from a sufficiently localized part of the sightline for this fitted temperature to be the same as the fit that would be obtained if one could make a strictly localized measurement at the plasma center. It has been impossible to correlate hydrogen temperatures determined in this manner in any way with any other data, except for when minority concentration was scanned to higher values, where the indicated hydrogen temperature approached the value of the deuterium temperature. For the shot shown in this section, the indicated hydrogen temperature is far too low to result in enough collisional deposition on deuterium to account for the observed heating. A calculation of this collisional exchange power based on the inferred $T_H(r)$ taken during a radial charge-exchange

scan appears later in this chapter. In that case the indicated $T_H(0)$ was much higher: 15 keV. The density was also higher. But the calculated collisional exchange power was only 8 kW. If the charge-exchange spectrum in the energy range fitted is not dominated by particles coming from the center of the plasma, then one would expect the inferred temperature to underestimate the actual central temperature. On the other hand, if the indicated temperature is greater than the estimated ripple-trapping truncation energy, then it must overestimate the energy in the central distribution function; i.e., the central distribution function must be truncated below its thermal energy.

Based on the preceding considerations, I believe that there are only two things that can be reliably said about the minority distribution function at low concentration and low density: (a) there are energetic particles for $E < E_{\rm tr} \sim 10$ keV, and (b) there are no energetic particles for $E > E_{\rm tr}$. I will therefore take the following attitude: In this chapter, I will present the data exactly as obtained from the diagnostics, but in subsequent analysis done in Chapter 4, I will assume that the minority temperature for the low-density, low-concentration case is 10 keV. Presenting the data exactly as obtained from the diagnostics will help emphasize the ambiguity in the data interpretation. A 10 keV Maxwellian distribution function has an e-folding width equal to the assumed truncation energy and is acceptable input to any of the numerical codes used in the next chapter. As suggested by the discussion in the introduction to this chapter, the uncertainty in the treatment of the minority distribution function is not enough to alter the conclusions that will ultimately be reached. For example, this will not alter the conclusion that a significant contribution from deuterium second harmonic absorption is necessary to explain the results. The behavior of mode conversion versus minority temperature as determined by the Brambilla code begins to saturate at temperatures below 10 keV. The split between slowing down of hydrogen on deuterium versus on electrons is not seriously affected by approximating a truncated distribution function by a Maxwellian with $T = E_{\rm tr}$. What really matters here is not whether the tail temperature is 2.5 keV or 10 keV or 15 keV, but that it is not the 62 keV that will be predicted by the FPPRF code in Chapter 4.

Some other data for the rising-density shot are shown plotted in Fig. 3.2.6. A rapid increase in the resistive loop voltage is always observed when the RF turns on, indicating a prompt influx of impurities. The gas puffing was programmed to maintain a steady density of $\bar{n}_e = 1.0 \times 10^{20}\ {\rm m}^{-3}$ in the absence of the RF. Unfortunately, the timing of the RF was such as to obscure this fact. Shots without RF taken in the same series as this rising density shot exhibited density behavior similar to the behavior of the steady-density shot shown in the next section. That steady-density shot immediately preceeded the shot in Fig. 3.2.2.

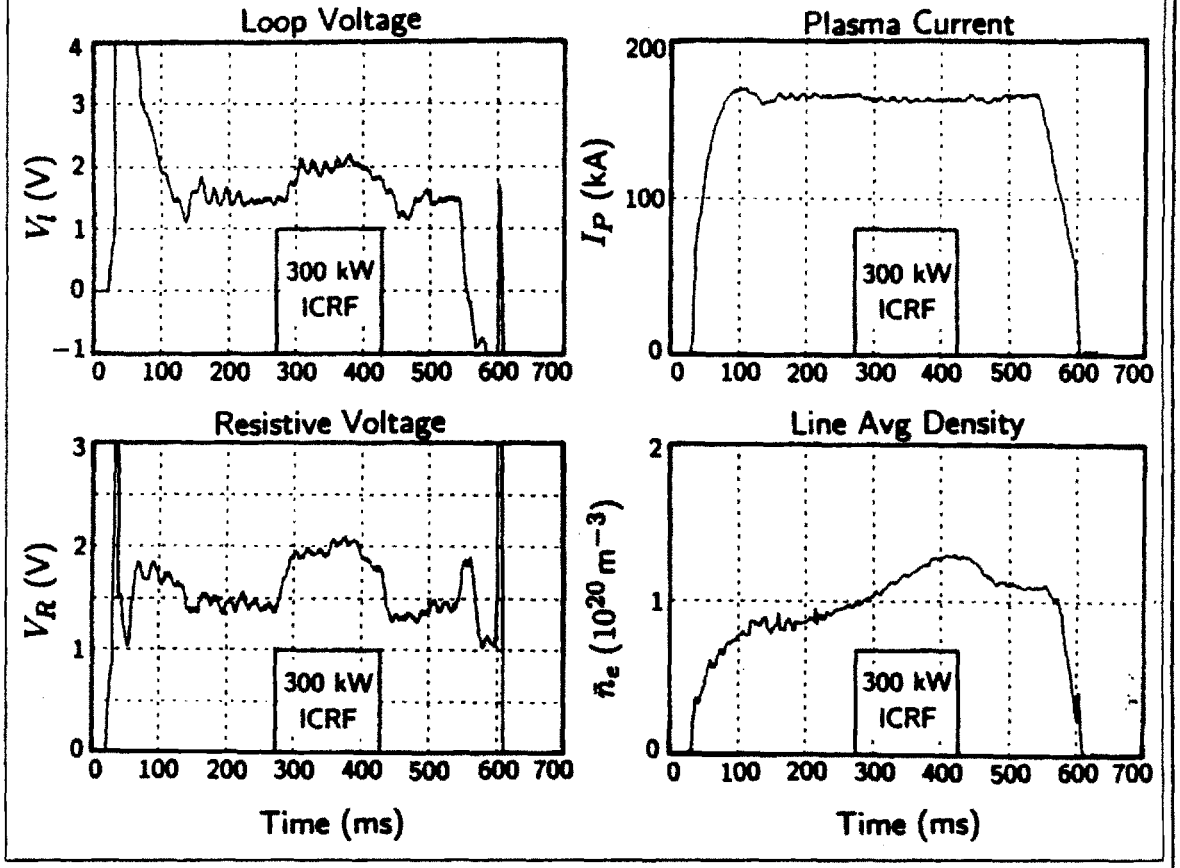

Figure 3.2.6: Plasma Evolution During Rising-Density Shot—Time evolution of total loop voltage, resistive loop voltage, plasma toroidal current, and line-averaged electron density are shown for the rising-density shot.

3.3: Steady-Density Shot

The deuterium temperature for a steady-density shot is shown in Fig. 3.3.1. In this case, 220 kW of ICRF power was injected for 150 ms, producing a 175 eV increase in deuterium temperature. After an initial rapid increase in deuterium temperature when the RF turns on, there is a gradual further increase in temperature throughout the remainder of the RF pulse. As for the rising-density shot, this could be related to a possible gradual drop in the minority concentration during the RF or to a gradual decrease in the toroidal field ripple magnitude. However, in this case it is less likely that the effect is caused by a change in collisional coupling between the deuterium and the electrons. In fact, as long as the density is constant in time, the collisional exchange power must decrease as the deuterium heats. Note that the heating exhibited in Fig. 3.3.1 shows two distinct time scales. The initial rapid time scale is comparable to the deuterium energy confinement time, while the second slower time scale is comparable to the time scale exhibited in Fig. 3.2.5.

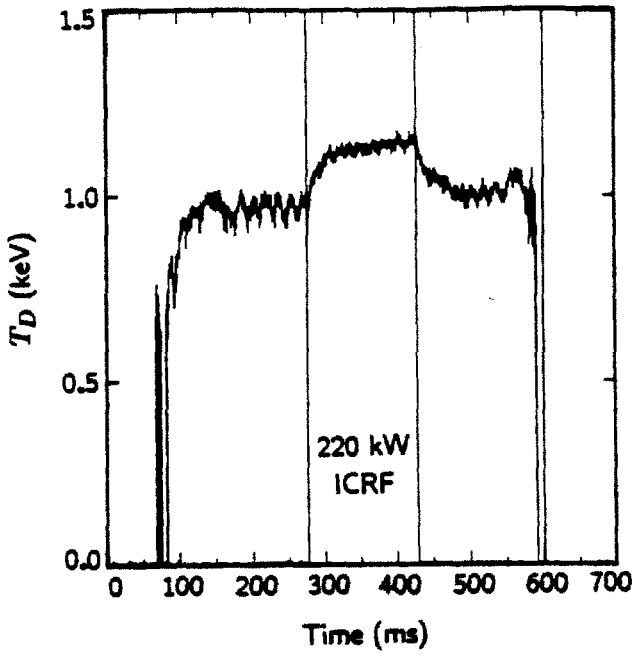

Figure 3.3.1: Deuterium Temperature for Steady-Density Shot—Application of 220 kW of ICRF power for 150 ms produced a 175 eV increase in deuterium temperature.

Interferometer data for this shot are shown in Fig. 3.3.2. For this shot there was a slight movement of the plasma position and a slight increase in the density throughout the shot, but these effects were due to imperfections in the adjustment of the plasma controls and not caused by the RF. In particular, note that there was no measurable change in the density profile shape. Although shots like this one, in which the density was not quite constant but had no changes that correlated with the RF, were classified as "steady-density shots", the small changes were included when the data were analyzed. Shots with large density changes that were due to poor plasma control were discarded.

In Fig. 3.3.3, one can again see a sudden increase in loop voltage when the RF turns on. Other plasma parameters for this shot are shown in Table 3.3.1. For this shot, the increase in ohmic heating power during the RF was only 50 kW, compared with 100 kW for the rising-density shot. The change in loop voltage was also smaller, as were both the $Z_{\rm eff}$ of the target plasma and the increase in $Z_{\rm eff}$ during the RF.

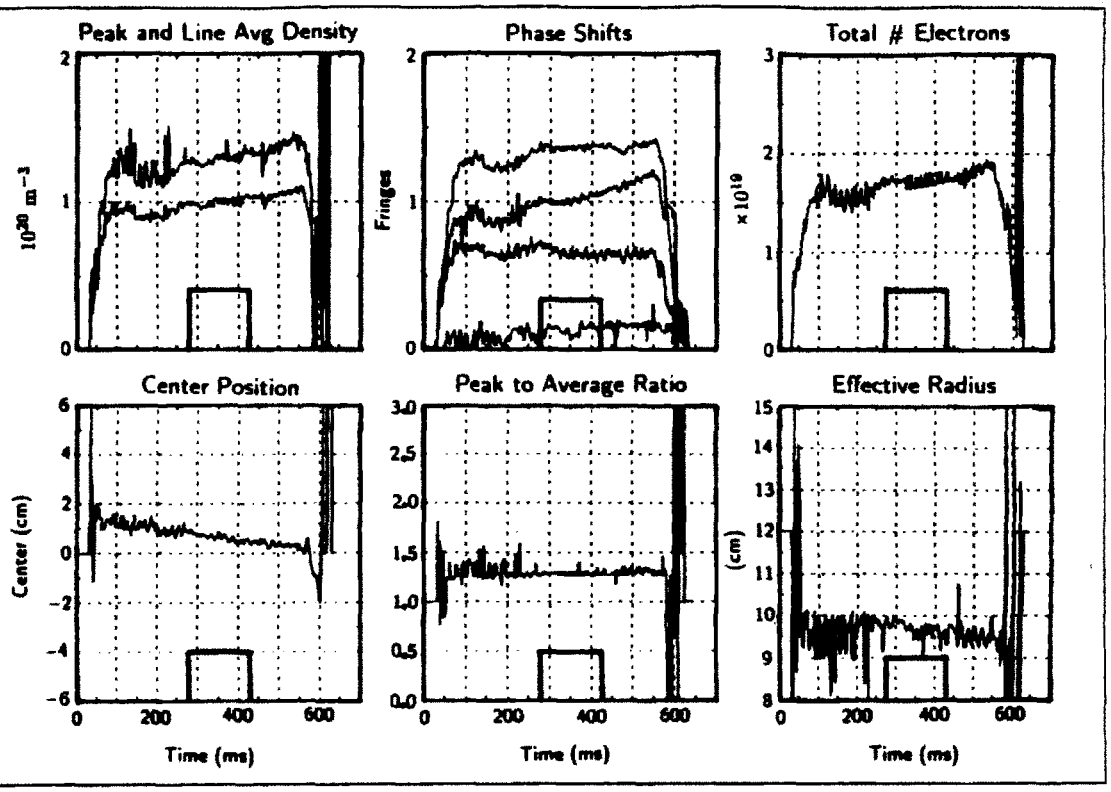

Figure 3.3.2: Density Profile Data for the Steady-Density Shot—Although the plasma position was occasionally observed to move during the shot (not caused by the RF), the density profile shape tended to be constant during steady-density shots.

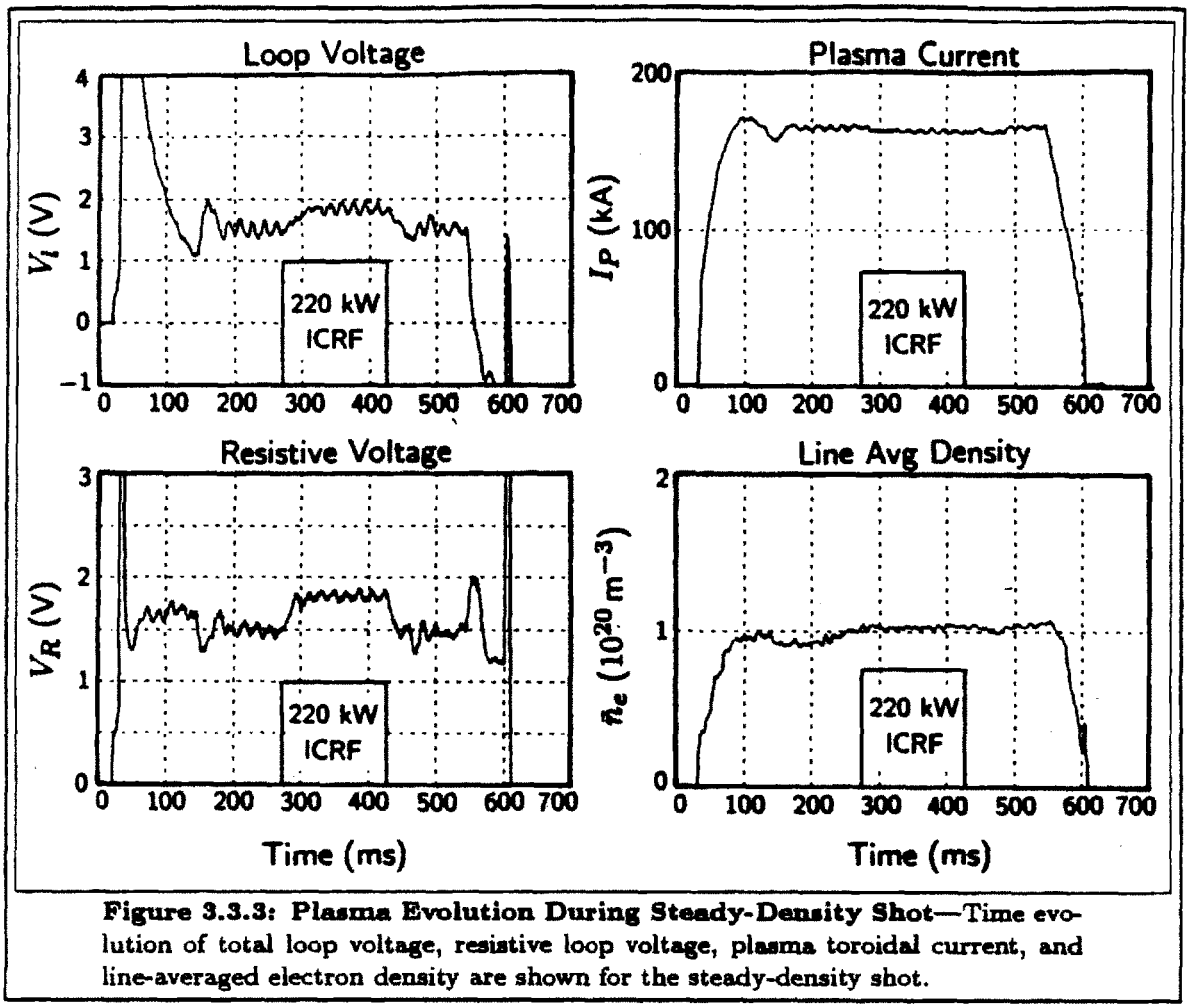

Figure 3.3.3: Plasma Evolution During Steady-Density Shot—Time evolution of total loop voltage, resistive loop voltage, plasma toroidal current, and line-averaged electron density are shown for the steady-density shot.

Parameter	Ohmic	RF
T_D	970 eV	1145 eV
I_P	160 kA	160 kA
q_a	9.25	9.25
V_R	1.5 V	1.8 V
P_{OH}	240 kW	290 kW
P_{RF}	0 kW	220 kW
$\bar{n}_e$	$1.0 \times 10^{20}\ \mathrm{m}^{-3}$	$1.0 \times 10^{20}\ \mathrm{m}^{-3}$
n_{e0}	$1.3 \times 10^{20}\ \mathrm{m}^{-3}$	$1.3 \times 10^{20}\ \mathrm{m}^{-3}$
η_H	$\sim 0.5\%$	—
Z_{eff}	1.9	2.6
τ_E	8.6 ms	4.3 ms*

* Assumes 100% RF absorption.

Table 3.3.1: Parameters for Steady-Density Shot—Equilibrium data are listed before and during the RF pulse for the shot in Fig. 3.3.1.

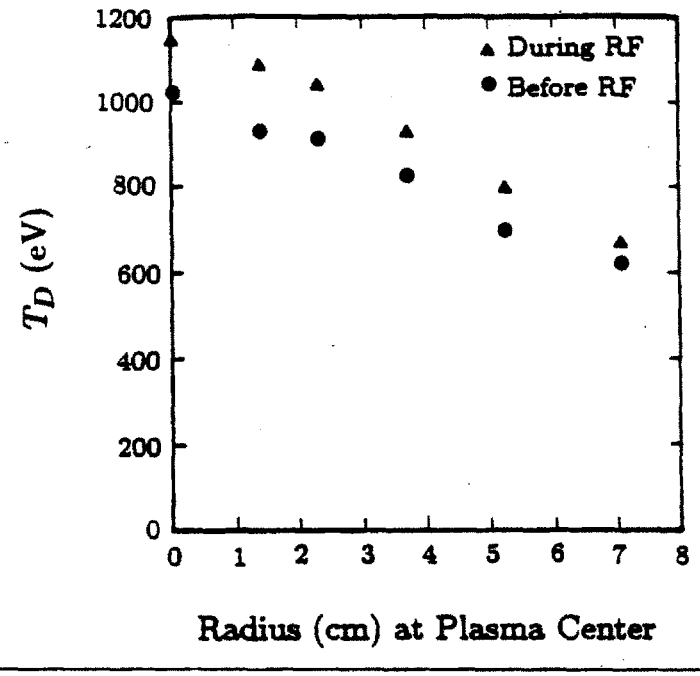

Figure 3.4.1: Deuterium Temperature Radial Profile—No significant change in deuterium temperature radial profile shape is evident from this radial charge-exchange scan. It is not possible to obtain accurate temperature measurements from the charge-exchange diagnostic for $r \gtrsim 7$ cm.

3.4: Radial Charge-Exchange Scan

The radial profile of the deuterium temperature, determined from charge-exchange measurements, is shown in Fig. 3.4.1, and the radial profile of the hydrogen minority tail temperature is shown in Fig. 3.4.2. These data were taken by producing a series of similar shots, and varying the viewing angle of the charge-exchange analyzer. These shots were similar to the steady-density shot of Fig. 3.3.1, except that the density of the target plasma was somewhat higher, and the density actually dropped slightly during the RF. Due to wall reflections, it is not possible to obtain accurate charge-exchange measurements beyond $r \gtrsim 7$ cm. Some other plasma parameters for this series of shots are shown in Table 3.4.1.

It is possible to estimate the collisional exchange power between hydrogen and deuterium from these data. By treating both species as having Maxwellian distribution functions at the indicated temperatures, the collisional exchange power is found to be roughly uniformly distributed from $r = 0$ to $r = 7$ cm, and the total collisional exchange power is found to be ~ 8 kW. Even though measurements are not available for $r > 7$ cm, it certainly seems safe to say that there is a big discrepancy between this power and the ~ 250 kW of RF power that was launched. In fact, it

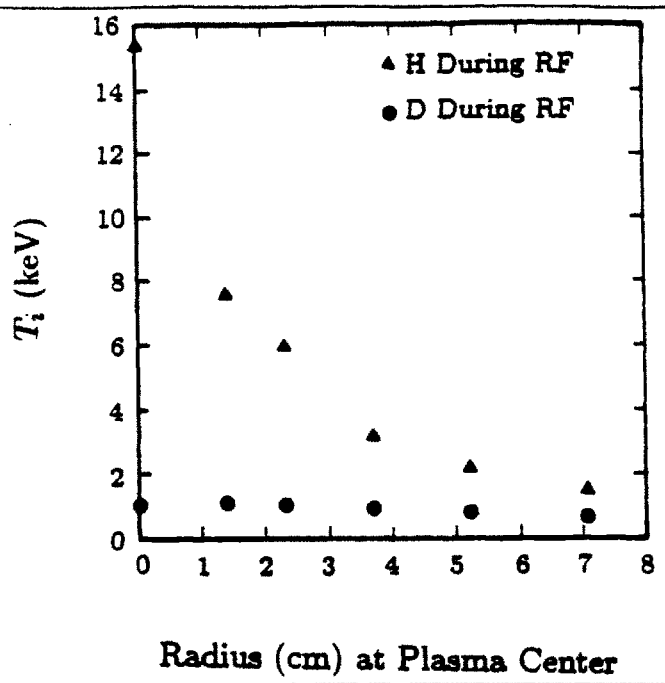

Figure 3.4.2: Hydrogen Tail Radial Profile—The hydrogen tail was fairly localized in the plasma center. The deuterium data points are the same points plotted with triangles in Fig. 3.4.1.

Parameter	Ohmic	RF
T_D	1100 eV	1240 ± 15 eV
I_P	165 kA	165 kA
q_a	8.9	8.9
V_R	1.6 V	1.9 ± 0.3 V
P_{OH}	265 ± 5 kW	320 ± 60 kW
P_{RF}	0 kW	250 ± 40 kW
$\bar{n}_e$	1.4×10^{20} m^{-3}	1.2×10^{20} m^{-3}
τ_E	12.5 ± 2.5 ms	6 ± 3 ms*

* Assumes 100% RF absorption.

Table 3.4.1: Parameters for Radial CX Scan—Equilibrium data are listed for the series of shots in Figs. 3.4.1 and 3.4.2. Entries shown as a range of values indicate extent of shot-to-shot variation during the scan.

seems doubtful that this power is sufficient to account for the observed deuterium heating. A more careful analysis using the ONETWO transport code shows that it is necessary to include the contribution from deuterium second harmonic absorption

in order to account for the observed heating. Thus, I have reached the surprising conclusion that a major portion of the heating is caused by the contribution from direct deuterium second harmonic absorption.

This conclusion may seem objectionable at first, because one normally expects to see a strong non-thermal tail in the deuterium distribution function when second harmonic heating occurs. Such tails were not observed in the charge-exchange data collected during these experiments. However, since it is evident that only a small portion of the RF power actually contributes to heating, and since severe ripple trapping is known to occur, it is conceivable that the distribution function of deuterium might not deviate far enough from a Maxwellian to exhibit a tail. To investigate this, one can do an isotropic analytic approximation by extending the treatment in Ref. 88 to the case of second harmonic absorption. This useful analytic calculation was done by Hammett[120], who obtains

$$T(E) = \frac{E^{3/2} T_{\text{tail}} + E_c^{3/2} T_0}{E^{3/2} + E_c^{3/2}} \tag{3.4.1}$$

where

$$T_{\text{tail}} = T_e + \frac{2E}{5T_0} \frac{P_D}{3n_D} \tau_s \tag{3.4.2}$$

$$E_c = 18.65\, T_e \tag{3.4.3}$$

τ_s is the classical slowing-down time for a fast deuterium test particle on the electrons, T_0 is the "bulk" deuterium temperature (i.e., from fitting a Maxwellian to the distribution function in the limit as $E \to 0$), and E_c is the energy at which the drag forces experienced by the deuterium test particle on the electrons and on the bulk are equal. The critical energy E_c is larger in the case of second harmonic than for the minority regime because the ratio of the masses of the test and field particles is unity in the present case. The fast deuterium ion is more strongly collisionally coupled to the bulk deuterium and less strongly coupled to the electrons than was the fast hydrogen ion in the case of minority heating. Thus, it is already obvious that the energy at which $T \sim T_{\text{tail}}$ will be higher than in the case of minority heating, and well above the ripple truncation energy.

Now to actually carry out the calculation requires knowledge of the power density P_D of absorption by the deuterium. At this point, I cannot play the same trick I used before of assuming a uniform power deposition profile, because I want to show that the tail is small instead of large. Looking ahead to the next chapter, it is found that the ratio P_D/n^2 is largest for the low-density shots with $n \sim 1 \times 10^{20}\,\text{m}^{-3}$.

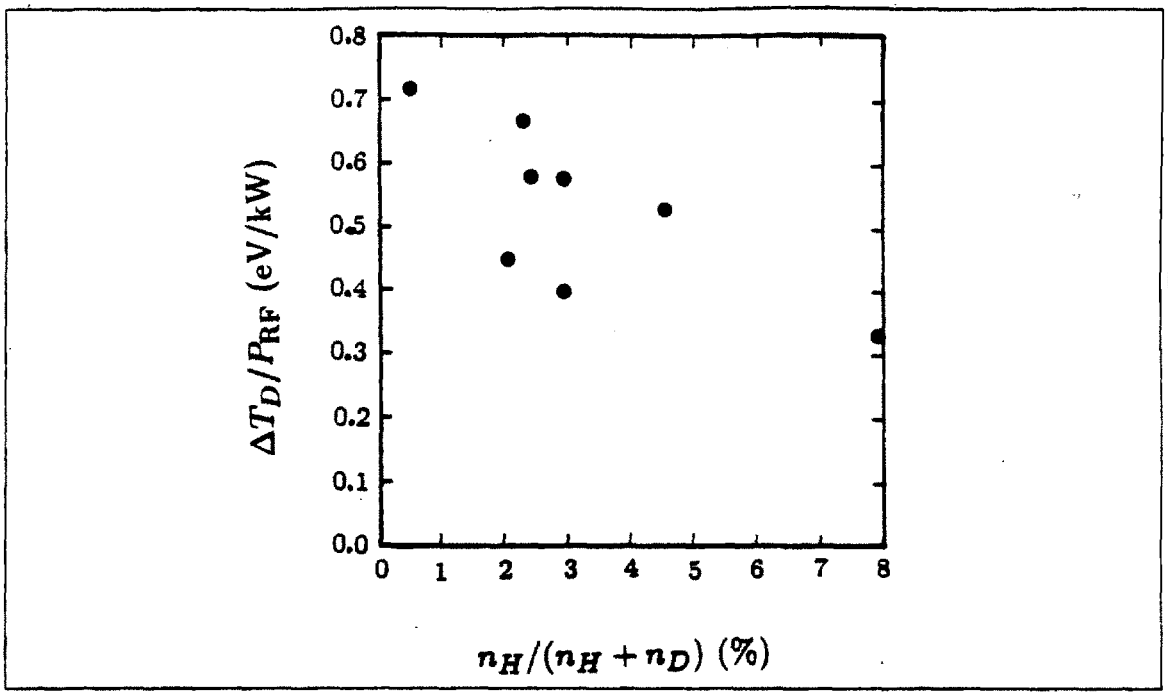

Figure 3.5.1: Deuterium Heating as a Function of Minority Concentration—The heating improved as concentration decreased. This trend continued to the lowest concentrations measurable using the charge-exchange flux.

(n appears squared here because of the n_e in the denominator of the expression for τ_s.) For $P_{RF} = 220$ kW (launched), P_D is estimated to be 0.25 W/cm^3, and with $n = 1 \times 10^{20}$ m^{-3}, $T_e = 2$ keV, $T_0 = 1$ keV, I obtain $T(E) = 1.005$ keV for $E = 1$ keV, $T = 1.065$ keV for $E = 5$ keV, and $T = 1.179$ keV for $E = 10$ keV. These parameters are similar to those for the steady-density shot in Sec. 3.3, for which a 175 eV increase in deuterium temperature was measured. It is therefore not surprising that no non-thermal deuterium tail was observed.

3.5: Minority Concentration Scan

The behavior of the deuterium and hydrogen temperatures as functions of minority concentration are shown in Figs. 3.5.1 and 3.5.2, respectively. These data were obtained from charge-exchange measurements by producing two or more similar shots at each concentration, because the charge-exchange diagnostic can only measure one ion species per shot. Due to difficulties controlling the RF power, it is necessary to normalize the measurements by dividing by the RF power. The deuterium temperature shows a steady trend towards better heating as concentration

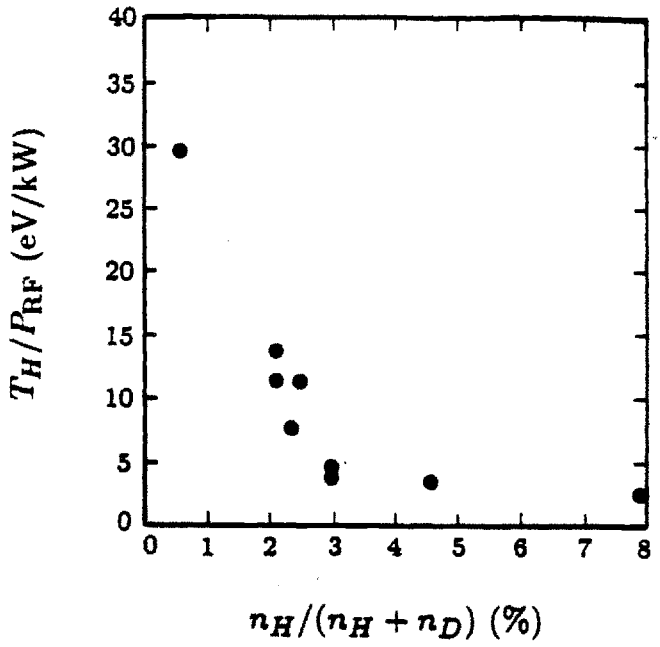

Figure 3.5.2: Hydrogen Tail Temperature as a Function of Minority Concentration—The hydrogen tail temperature was significantly greater than the deuterium tail temperature at concentrations $\eta_H < 3\%$; however, at higher concentrations the hydrogen was essentially thermal at the same temperature as the deuterium.

Parameter	Ohmic	RF
T_D	1250 ± 50 eV	—
I_P	200 kA	200 kA
q_a	7.5	7.5
V_R	1.65 ± 0.05 V	2.15 ± 0.15 V
P_{OH}	330 ± 10 kW	430 ± 30 kW
P_{RF}	0 kW	290 ± 80 kW
$\bar{n}_e$	1.25×10^{20} m^{-3}	1.45×10^{20} m^{-3}
τ_E	14 ± 3 ms	8 ± 1 ms*

* Assumes 100% RF absorption.

Table 3.5.1: Parameters for Hydrogen Minority Concentration Scan—Equilibrium data are listed for the series of shots in Figs. 3.5.1 and 3.5.2. Entries shown as a range of values indicate extent of shot-to-shot variation during the scan.

is lowered which continues to the lowest concentration obtainable. The hydrogen

tail temperature also increases as concentration is lowered, as one would expect. For concentrations $\eta_H \gtrsim 3\%$, the hydrogen is essentially thermal at a temperature comparable to that of the deuterium. Other plasma parameters for this scan are summarized in Table 3.5.1.

Stix gives a simple criterion for determining the optimum minority concentration in Ref. 88. Since the quantity E_+^2/E_-^2 decreases as η_H increases, there should be some nontrivial concentration at which the power absorbed by hydrogen, which is proportional to $n_H|E_+|^2$, attains a maximum. Maximizing this quantity leads to an expression for the optimum minority concentration:

$$\eta_H^{\rm opt} = \frac{4}{3}\frac{N_\parallel\sqrt{T_H}}{1215}\left[1+\frac{1}{87.6}\frac{N_\parallel^2}{n}\right] \tag{3.5.1}$$

where T_H is measured in keV and n is the deuterium density in units of $10^{20}\,{\rm m}^{-3}$. From the Brambilla code analysis in the next chapter, the $N_\parallel$ spectrum for these shots is strongly peaked at $N_\parallel = 4$. In this case, Eq. 3.5.1 leads to an optimum minority concentration of ~ 2 %. Again, there is a contradiction with the experimental results, which could be a result of incorrectly assuming that all of the RF power is delivered to the deuterium through absorption on hydrogen followed by collisional exchange. This is another piece of evidence that suggests that the hydrogen tail losses are so extreme that it is necessary to consider the contribution from deuterium second harmonic absorption in order to explain the experimental results. If that were the case, then it would not be surprising that heating efficiency continues to improve at the lowest measurable minority concentrations, since the fraction of power absorbed by deuterium second harmonic cyclotron absorption is inversely proportional to minority concentration.

3.6: Toroidal Magnetic Field Scan

The hydrogen minority tail temperature is plotted as a function of toroidal field in Fig. 3.6.1. Again, the rapid degradation in hydrogen tail temperature is indicative of poor confinement of high-energy minority ions, which could be a result of the toroidal field ripple trapping. This is also good supporting evidence that the minority tail is really being produced in the center of the plasma by cyclotron damping, and not by some other parasitic effect. As the toroidal field is scanned below 12 T, the cyclotron absorption layer moves away from the center of the plasma

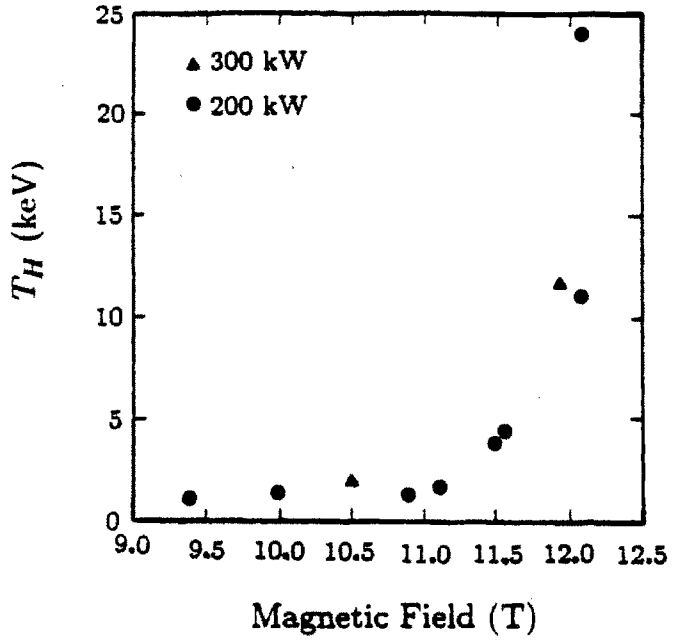

Figure 3.6.1: Hydrogen Tail Temperature as a Function of Toroidal Field—The hydrogen tail formation degrades very rapidly as the absorption layer is moved away from the center.

Parameter	Ohmic	RF
T_D	1110 ± 90 eV	—
I_P	160 ± 5 kA	160 ± 5 kA
q_a	8 ± 1	8 ± 1
V_R	1.6 ± 0.1 V	2.5 ± 0.5 V
P_{OH}	255 ± 25 kW	400 ± 100 kW
P_{RF}	0 kW	250 ± 50 kW
$\bar{n}_e$	$1.15 \pm 0.15 \times 10^{20}$ m^{-3}	$1.2 \pm 0.2 \times 10^{20}$ m^{-3}
τ_E	10 ± 3 ms	5 ± 2 ms*

* Assumes 100% RF absorption.

Table 3.6.1: Parameters for Toroidal Magnetic Field Scan—Equilibrium data are listed for the series of shots in Fig. 3.6.1. Entries shown as a range of values indicate extent of shot-to-shot variation during the scan.

into regions where the toroidal field ripple magnitude is larger. Other effects which could contribute to this result are that the banana orbit width increases with r and that the power is being deposited further from the plasma center and is therefore

not as well "insulated" from the edge of the plasma. Other plasma parameters for this scan are summarized in Table 3.6.1.

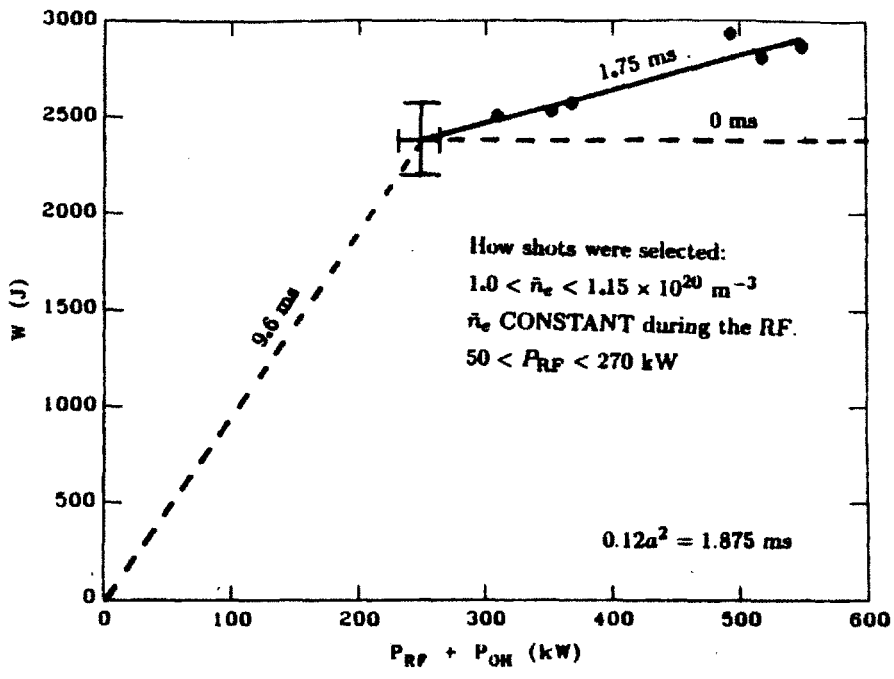

Figure 3.7.1: Thermal Energy as a Function of Heating Power—In a well-controlled power scan, the increase in thermal energy with RF power is consistent with constant incremental confinement time.

3.7: ICRF Power Scan

Analysis of incremental energy confinement for a controlled power scan is shown in Fig. 3.7.1. In this scan, the incremental ohmic heating power was always less than 50 kW, so that the variations along the horizontal axis are primarily due to the RF heating power. The solid line in Fig. 3.7.1 represents a linear least squares fit to the six data points, and its slope is the incremental confinement time $\tau_{inc} = 1.75$ ms. The ohmic energy confinement time for these shots was $\tau_E = 9.6$ ms, the slope of the dashed line. The shot-to-shot variation of the ohmic points is indicated by the error bars. If there was no heating at all during the RF, then the data points would lie along the horizontal dashed line, labeled 0 ms, and the incremental confinement time would be 0. On the other hand, if the heating was as efficient as ohmic heating, then the data points would lie along the extension of the dashed line. Thus, there was significant heating due to the RF, but the efficiency was degraded from the ohmic value. The important question now is whether this can be accounted for in terms of power loss mechanisms, or whether there is actually a real decrease in the energy confinement time of the plasma. This question will be addressed in the next chapter.

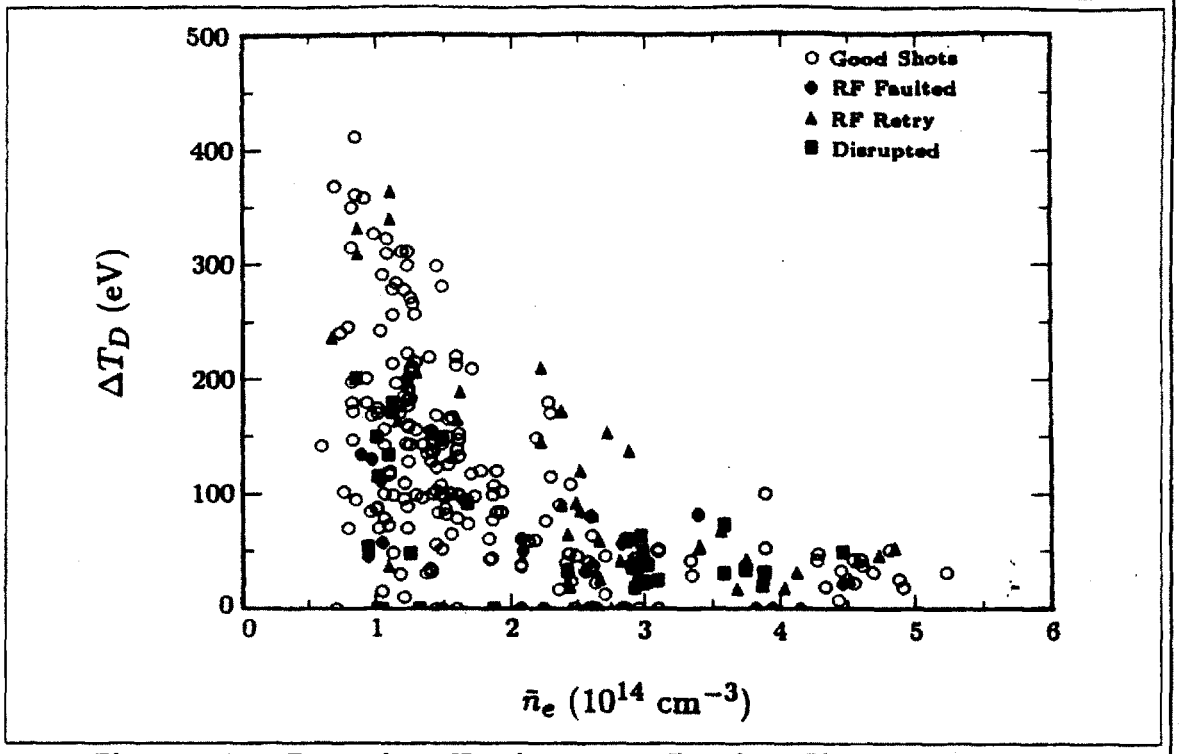

Figure 3.8.1: Deuterium Heating versus Density—The measured ΔT_D is shown versus line-averaged electron density for every shot in the database compiled with the two double-element antennas.

3.8: Density Scans

The most important issue to investigate during these experiments is the scaling of heating efficiency with increasing density. To present an overall view of the raw heating results, the observed deuterium temperature change is plotted against line-averaged electron density for every 12 Tesla shot in the database. The results are shown in Fig. 3.8.1. The maximum observed ΔT_D decreases as density increases. This behavior is not surprising, not only because there are more particles in the plasma at higher density, but also because the power handling capability of the antennas degraded somewhat at higher density. The maximum power delivered to the antennas at low density was limited only by the capability of the RF generator to $\sim$ 400 kW. Power handling capability degraded linearly for $\bar{n}_e \gtrsim 3 \times 10^{20}\,\mathrm{m}^{-3}$, dropping to 100 kW at the highest density. Power was scanned from 0 kW up to the maximum achievable at each density. Therefore, it is not surprising that data points are scattered all the way down to the horizontal axis. However, one might reasonably expect that this scatter would be eliminated by plotting a quantity like incremental stored energy normalized to RF power. This turns out not to be the case. As shown below, this kind of simple-minded analysis yields a heating

efficiency plot with data uniformly scattered between 0 and some maximum (which is independent of density).

The shots depicted in Fig. 3.8.1 are grouped according to operational status. The RF generation and transmission system is protected by a fault detection circuit. If the reflected power in the transmission line exceeds a certain preset value, the generator is automatically shut off. The reflected power in the line can change suddenly if there is electrical breakdown somewhere in the system or if the plasma loading changes suddenly. Shots in which this occurred are shown with solid circles in Fig. 3.8.1. When the RF is shut off due to an electrical fault, it will attempt to re-energize after a 10 ms delay. If unsuccessful (fault still present), the RF will try again after another 10 ms. This will continue up to a maximum of four tries, unless the time programmed for the RF pulse elapses first. Shots in which the RF faulted but retried successfully are indicated with solid triangles in Fig. 3.8.1. Shots which disrupted during the RF pulse, but which were stable long enough during the pulse to show some heating are shown as solid squares. All other shots are shown as open circles. In the case of disruptive shots, the value of ΔT_D plotted is the maximum achieved during the RF pulse. In shots which disrupted but subsequently recovered during the RF, the deuterium temperature at the end of the pulse was usually lower than before the RF, but the temperature plotted in Fig. 3.8.1 is the maximum achieved before the disruption. Including these "defective" shots adds nothing useful to further analysis, so all further analysis will be done using only the "good" shots.

The deuterium heating data from Fig. 3.8.1 are plotted again in Fig. 3.8.2, grouped according to whether there was a density increase or decrease that appeared to be caused by the RF. The separation of the data into this grouping was sometimes somewhat subjective. Shots for which the line-average density shows an obvious change that was correlated with the RF pulse were classified according to that change. Shots which had a significant change in line-average density that was not correlated with the RF (due to poor plasma control) were discarded. All other shots were classified as steady-density shots. Rising-density shots tended to occur primarily for the lower density target plasmas and tended to exhibit more deuterium heating than steady-density shots. As has already been mentioned, this rising-density behavior renders the evaluation of the RF heating efficiency somewhat ambiguous. The more sophisticated analysis in Chapter 4 using the ONETWO transport code is able to resolve this ambiguity.

The electron and ion temperatures for the ohmic target plasmas are shown plotted against line-average density in Fig. 3.8.3. Unfortunately, the only electron temperature diagnostic available during the experiments was the Thomson scattering diagnostic. This diagnostic yields a reasonably accurate measurement of the

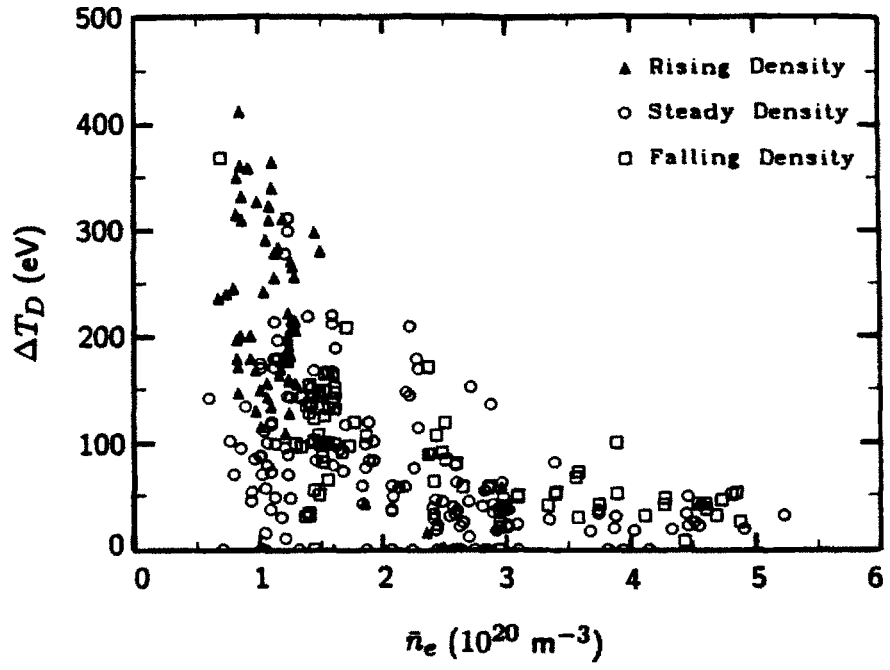

Figure 3.8.2: Deuterium Heating versus Density—The data from Fig. 3.8.1 are re-plotted, grouped according to the behavior of the density as correlated to the timing of the RF.

central electron temperature, but with limited time resolution — only one point every ~ 20 ms. Thus, it is not possible to observe sawtooth behavior in the electron temperature, which might have yielded useful information about the electron power balance. Even more unfortunate is the complete lack of electron temperature data for the highest densities. This severely limits the amount of analysis that can be done for the highest-density shots. In the next chapter, it will be possible to model RF deposition and loss mechanisms for these high densities by assuming a value for the electron temperature, but the transport and power-balance analyses using the ONETWO code are too sensitive to electron temperature to allow this.

In general, the electron temperature showed no trend to either increase or decrease during the RF, but often exhibited random fluctuations of magnitude $\sim \pm 200$ eV during the RF. Data from the Thomson scattering diagnostic showing this effect for a typical RF heated discharge are shown in Fig. 3.8.4. There were no diagnostics available during the experiment from which total radiated power or impurity line radiation power could be obtained. Since the limiters and Faraday shields were fabricated from molybdenum and carbonization was not applied to the walls of the vacuum chamber, a reasonable hypothesis would be that high-Z impurity radiation was responsible for the lack of electron heating. During the earlier ICRF heating experiments performed on Alcator C by Blackwell, a study of

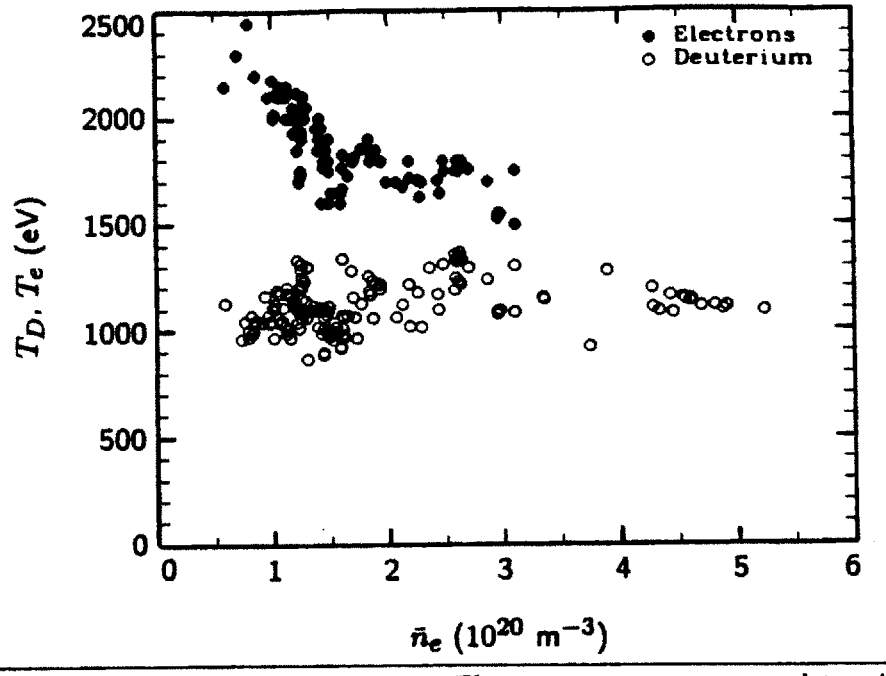

Figure 3.8.3: Ohmic Temperatures—Electron temperatures were determined from the Thomson scattering diagnostic and ion temperatures were determined by both charge-exchange and neutron measurements.

impurity generation and radiation was carried out by Manning *et al.*[59] In these experiments, the plasma was limited by a 12.5 cm graphite limiter, but the antenna Faraday shields and the vacuum chamber wall were stainless steel. Also, the normal 16.5 cm molybdenum limiters were left installed in the torus during the experiment. During the ohmic portions of the discharges, the primary impurity component was carbon, and the impurity radiation was greatly reduced compared to operation with molybdenum limiters. However, when the RF was applied, the impurities were again dominated by high-Z elements (mainly iron and chromium). The sources of these impurities were identified as the antenna Faraday shields, the vacuum chamber wall, and the 16.5 cm limiter. Electron heating was not observed in those experiments, as in the present experiments. In the Blackwell experiments, T_e usually remained constant during the RF, but often was observed to decrease by ~ 175 eV.

In addition to ohmic heating and impurity radiation power, the electron power balance is also affected by collisional exchange with the ions (both majority and minority) and possible absorption of power from the mode-converted IBW via electron Landau damping and magnetic pumping. Because of the truncation of the minority distribution which was indicated by the charge-exchange diagnostic and hypothesized to be caused by ripple-trapping, electron heating via collisional exchange with

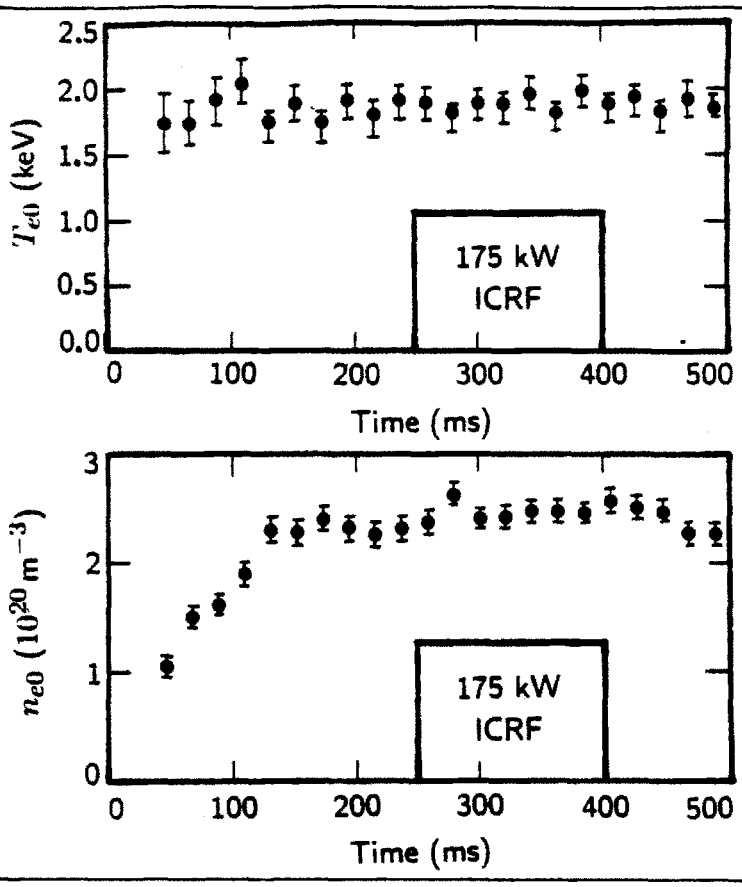

Figure 3.8.4: No Electron Heating—Data from the Alcator C Thomson scattering diagnostic are shown for a steady-density shot with $\bar{n}_e = 1.45 \times 10^{20}\,\mathrm{m}^{-3}$, $I_P = 210$ kA, $T_{D0} = 1070$ eV (Ohmic), and $\Delta T_{D0} = 100$ eV.

the minority tail will not be expected. Although the analysis to be presented in the next chapter does not predict significant electron Landau damping of the IBW, the models used do not include all the relevant physics for this effect and cannot rule this out. However, the amount of power in question is not sufficient to dominate the electron power balance. Because of the lack of diagnostic information necessary to study the electron power balance, and considering the lack of significant electron heating, it will turn out that the most rewarding way to analyze the data will be to concentrate on analyzing the deuterium power balance, treating both the RF and the electrons as known sources of power. This is the method of analysis that will be pursued in Chapter 4 using the RF deposition model to be developed in Chapter 4 and the ONETWO transport code.

While reading this thesis, it is worth remembering that the deuterium temperature never equals or exceeds the electron temperature during the RF.

Once the densities and temperatures are known, it is trivial to calculate the heating efficiency figure of merit $\bar{n}_e \Delta T_D / P_{\mathrm{RF}}$. This quantity is shown in Fig. 3.8.5.

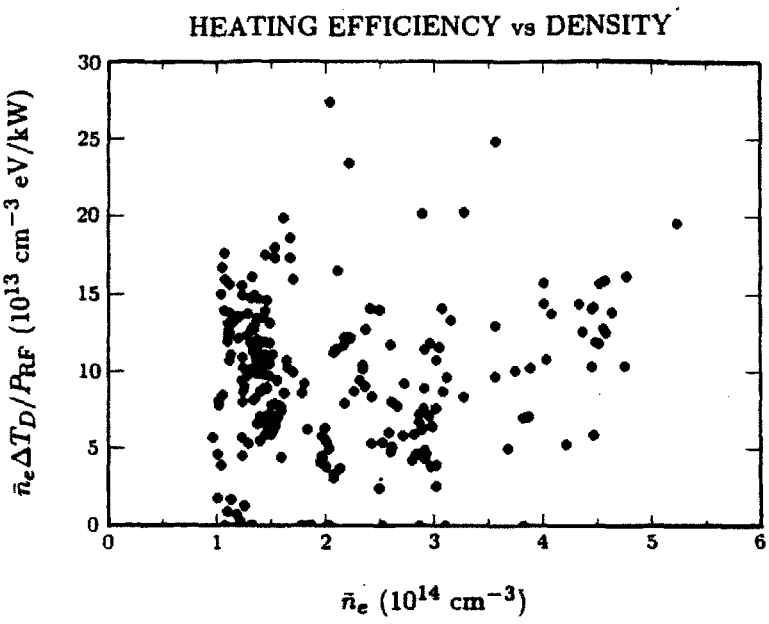

Figure 3.8.5: Deuterium Heating Efficiency versus Density—The figure-of-merit $\bar{n}_e \Delta T_D / P_{RF}$ shows no correlation with density.

From this plot one can see that, although the raw deuterium temperature data might at first sight appear to scale poorly with density, the deuterium energy increment per particle per kilowatt of RF power is independent of density. Although there is a great deal of scatter, the best efficiency that was observed was roughly the same at each density. However, the fact that the scatter is so severe suggests that this figure of merit is not a good parameter for characterizing the heating results. A slightly better figure of merit is the incremental confinement time, which is discussed below. In addition to deuterium temperature increase, the incremental confinement time calculation accounts for changes in density and electron temperature (in the rare cases when T_e changed). It also models the dependence of temperature profile shapes on plasma current.

The effect of the RF on energy confinement time is shown in Fig. 3.8.6, in which the global energy confinement time τ_E is plotted against density. The degradation in energy confinement time during the RF is fairly small, but this is simply because the RF power is also small. The net change in plasma thermal energy is always small, and therefore Fig. 3.8.6 would not look much different even if there were no heating at all during the RF. It is important to note that these energy confinement times were calculated assuming that the net forward RF power in the antenna feed line was equal to the net power deposited into the bulk plasma. If significant losses

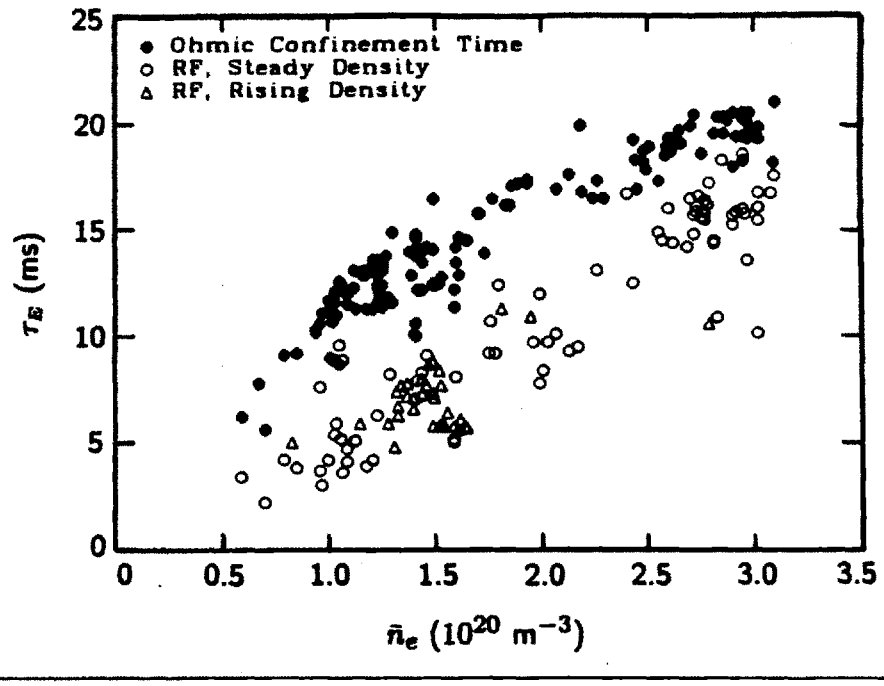

Figure 3.8.6: Energy Confinement Time versus Density—The degradation of the global energy confinement time was typically fairly small; however, the RF power was always smaller than the ohmic power.

are taken into account, then the calculated energy confinement time during the RF will be closer to the ohmic value.

Since detailed profile information was not available from experimental data, a simple model was used to estimate the temperature profile shapes in these energy content calculations. In order to do this analysis, what amounts to a 3-point fit was done by assuming that the temperature profiles of ions and electrons had the same shape, which was represented by a parabola raised to some power. The edge temperature was assumed to be zero and the central temperature was taken from the appropriate diagnostic measurement. The power to which the parabola was raised was determined by assuming classical resistivity to relate the electron temperature profile to the total measured plasma current, and determining the plasma current profile by assuming that the sawtooth instability requires that the central MHD safety factor q not differ very much from unity. It was also assumed that the temperature profiles were significantly more peaked than the density profile. This well-known procedure is described as follows.

The temperature and current profiles are assumed to have the following shapes:

$$T_e(r) = T_{e0}[1 - (r/a)^2]^{\alpha_T} \tag{3.8.1}$$

$$T_D(r) = T_{D0}[1 - (r/a)^2]^{\alpha_T} \tag{3.8.2}$$

$$J(r) = J_0[1 - (r/a)^2]^{\alpha_J} \tag{3.8.3}$$

The 3 parameters that will be adjusted to fit the electron temperature to measured data are α_T, J_0 (central toroidal current density), and T_{e0}. Assuming classical resistivity yields

$$J(r) = \sigma(r)E = \sigma_0 \left[\frac{T_e(r)}{T_{e0}}\right]^{3/2} E \tag{3.8.4}$$

from which it follows that

$$\alpha_J = \frac{3}{2}\alpha_T \tag{3.8.5}$$

Note that the electric field E was also assumed to be spatially uniform. Application of the Ampere equation then yields

$$B_P(r) = \frac{J_0}{r}\int_0^r [1 - (x/a)^2]^{\alpha_J} x\, dx = \frac{a^2 J_0}{2r}\frac{1 - [1 - (r/a)^2]^{\alpha_J+1}}{\alpha_J + 1} \tag{3.8.6}$$

Evaluating this expression at $r = a$ and again asymptotically in the limit as $r \to 0$, and using

$$q = \frac{rB_0}{RB_P} \tag{3.8.7}$$

yields

$$\alpha_J = \frac{q_a}{q_0} - 1 \tag{3.8.8}$$

If the density profile is sufficiently broad that $\alpha_n \ll \alpha_T$, then the volume-averaged thermal energy obeys the relation

$$\langle nT \rangle \approx \bar{n}\langle T \rangle = \bar{n}\frac{T}{1 + \alpha_T} \tag{3.8.9}$$

The plasma thermal energy content is then given by

$$W \approx \frac{3}{2}\bar{n}_e \frac{T_{e0} + T_{i0}}{1 + \alpha_T} 2\pi^2 a^2 R_0 \tag{3.8.10}$$

and the energy confinement time is

$$\tau_E = \frac{W}{P_{\mathrm{RF}} + P_{\mathrm{OH}}} \tag{3.8.11}$$

In the ONETWO transport code analysis in Chapter 4, a more sophisticated version of this fitting will be done. In that case, the electron temperature profile

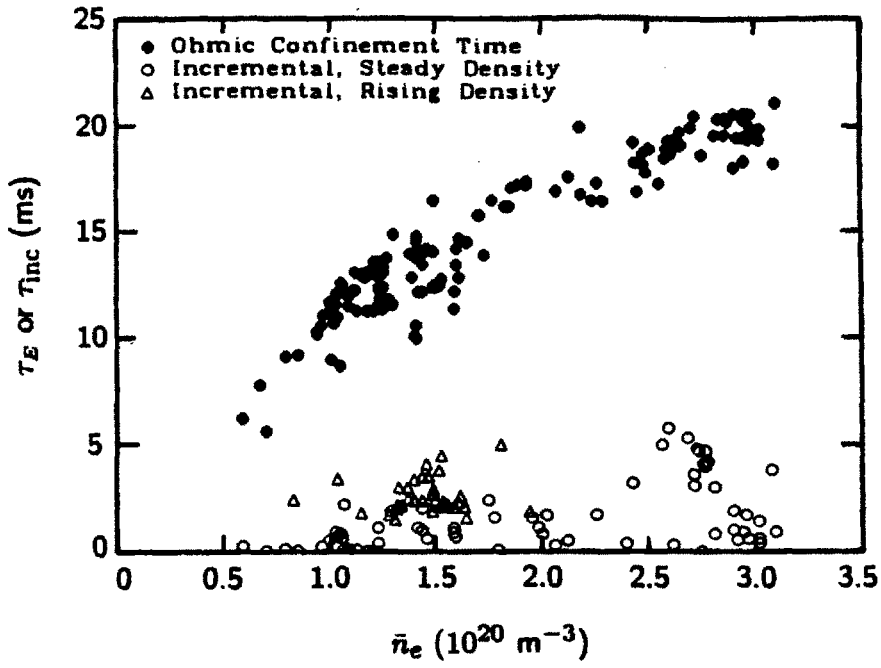

Figure 3.8.7: Incremental Energy Confinement Time versus Density— The incremental confinement time scales quite unfavorably with density, when compared with the ohmic confinement time. Incremental energy confinement time appears to be constant as a function of density.

will be treated the same way, but the ion temperature profile will be determined by assuming the ion thermal conductivity to be a constant multiple of the neoclassical thermal conductivity and adjusting the multiplier to match the measured central ion temperature. This will yield ion temperature profiles somewhat broader than the electron temperature profiles, with $\alpha_{T_i} \approx 0.635\alpha_{T_e}$. The density profile will be adjusted to match both the central density determined by the Thomson scattering diagnostic and the line-average density determined from the interferometer. This will verify the validity of the approximation $\alpha_n \ll \alpha_T$.

When the incremental plasma thermal energy is relatively small, a much more revealing measure of the RF heating efficiency is the incremental confinement time, defined as the ratio of the incremental thermal energy to the incremental heating power. Since the change in ohmic heating power during the RF is not negligible compared to the RF power, the change in ohmic heating power is included when calculating the incremental power. Otherwise, the RF heating efficiency would be exaggerated.

A comparison of the ohmic and incremental confinement times is shown in Fig. 3.8.7. The total energy confinement time, shown with solid circles, scales quite favorably with density. As density is increased, the ohmic confinement time initially

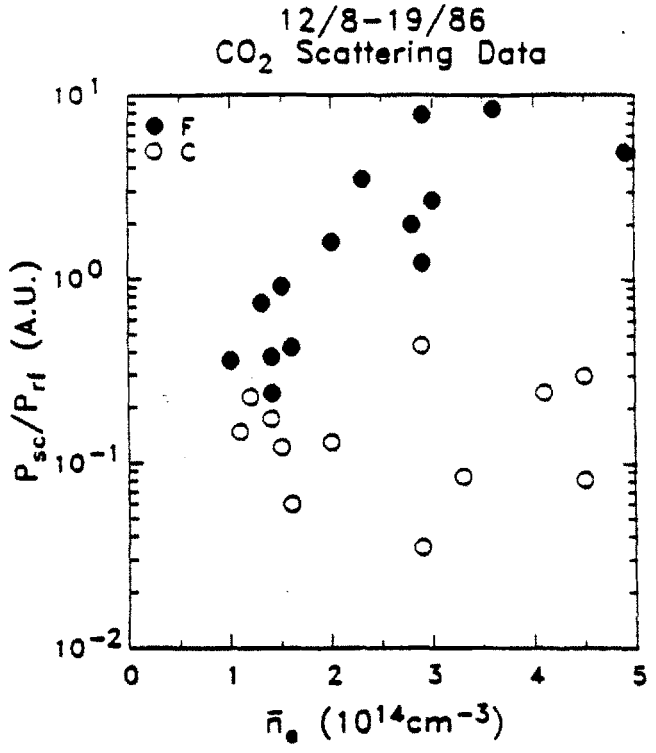

Figure 3.9.1: CO_2 Laser Scattering Data—Measurement of power scattered from the mode-converted ion Bernstein wave indicates that the wave is toroidally localized and that mode conversion increases with density.

exhibits neo-Alcator scaling ($\tau_E \propto n$), and then shows a tendency to saturate at higher densities. This tendency for the ohmic confinement time to saturate has been studied before, and has been attributed to a degradation of the ion energy confinement with increasing density. On the other hand, the incremental confinement time does not scale so favorably with density. Not only is the incremental confinement time much lower than the total confinement time, but its scaling with density is not much better than neutrally favorable.

3.9: Mode Conversion

Data obtained by Dr. Y. Takase from the CO_2 laser scattering diagnostic[121] are shown in Fig. 3.9.1. In this scan, the diagnostic was adjusted to detect density perturbations associated with the mode-converted ion Bernstein wave on the high-field side of the ICRF absorption layer. This diagnostic was very important for the IBW heating experiments performed by Moody, but is somewhat less useful for

the fast-wave experiments primarily because of the inability to obtain absolutely calibrated measurements of the IBW power. Precise interpretation of data from this diagnostic is complicated by the fact that the scattered power depends in a complicated way on the plasma density and the $N_{||}$ of the IBW.

The scattered power, which is a measure of the power carried in the mode-converted ion Bernstein wave, is plotted as a function of line-average electron density. For the ranges of $N_{||}$ predicted by the Brambilla code simulations in the next chapter, it is valid to conclude that the mode-converted power is increasing with density. Two ICRF fast-wave antennas were used in this scan, one installed on C-port and the other installed 180° away toroidally on F-port. The CO_2 laser was installed on F-port. Data taken when ICRF power was fed to the antenna on F-port are shown with solid circles, while data taken when ICRF power was fed to the antenna on C-port are shown with open circles. From these data, one can see that mode-conversion is a strong function of density, increasing significantly magnitude over the density range scanned. However, it is not valid to conclude that the IBW is either absorbed or toroidally localized from the behavior of the open circles, because of the possibility of large upshifts in the value of $N_{||}$ as the wave propagates in the toroidal direction. The fact that mode conversion increases with density is important supporting evidence for the results of the Brambilla code calculation in the next chapter.

3.10: Summary

Data taken during fast wave hydrogen minority regime heating experiments in Alcator C have been presented in this chapter. Significant deuterium heating was observed during the experiments, but electron heating was not observed and the hydrogen minority distribution function exhibited a suprathermal tail that was far too weak to account for the launched RF power. Because the hydrogen distribution function is truncated at relatively low energy, by an effect that has been attributed to toroidal field ripple trapping, the minority tail temperatures that were derived from the charge-exchange data may not accurately describe the actual distribution function at the centermost point of the viewing chord, as is customarily assumed. Thus, interpretation of the minority charge-exchange data is ambiguous.

Scaling of the heating efficiency with minority concentration has been found to be in contradiction with well-known theoretical results which predict an optimum minority concentration of a few percent. Instead, heating was found to improve as

concentration was lowered, and to continue this trend as concentration was scanned from 8% down to the lowest concentration obtainable. However, the theoretical result that there should be an optimum concentration at some non-trivial value is based on equating the collisional exchange power between hydrogen and deuterium with the RF power, without considering the possibility of other loss channels to which the power might flow.

Electron heating was not observed during the experiments. Although diagnostic data are not available from which the electron power balance can be studied, this result is not very mysterious. The source of electron heating power from the RF will be weak due to the truncation of the minority distribution function, but there might still be contributions to electron heating power from the mode-converted IBW and from a reduction in the electron-deuterium collisional exchange power as the deuterium heats up. However, the experiment was carried out in a high-Z-impurity environment. Based on an impurity radiation study carried out during earlier fast wave experiments on Alcator C, it seems reasonable to presume that it is radiation from high-Z impurities that is responsible for the lack of electron heating.

A simple type of power balance analysis was done, in which the thermal energy content and total power input to the plasma were estimated from experimental data. It was found that the incremental plasma heating was much less efficient than Ohmic heating, and that the scaling of the incremental heating with density was not favorable.

Because the hydrogen tail is so weak and the distribution function appears to be truncated at an energy consistent with previously studied results that have been attributed to toroidal field ripple trapping, it is hypothesized that the inefficient heating results are caused by severe losses associated with the hydrogen minority. The fact that energy losses from the hydrogen must be severe is clear, and it is obvious that some way must be found to estimate these losses in order to explain the heating results and to do any further analysis. However, it is also intuitively obvious that the losses from the minority alone cannot account for all the features observed in the data. This would not seem to explain the results from either the minority concentration scan or from the density scan. In either case, as minority concentration increases or as density increases, a less energetic hydrogen tail would be required in order to channel all the RF power to the deuterium. Thus, it would be expected that heating efficiency should improve at high minority concentration or majority density, in apparent contradiction with the experimental results. In fact, since this intuitive discussion suggests that ICRF power deposition should actually improve with increasing minority concentration and density, it is necessary to look for even more severe loss mechanisms whose scaling with concentration and density will dominate over the expected improved power deposition.

As has just been suggested, it is now necessary to embark on a study of the ICRF power deposition efficiency that takes into account, at least approximately, the effects discussed intuitively in the preceding paragraph. There is no adequate way to determine either the global RF power deposition or its profile from the available experimental data. In other experiments, RF power deposition on electrons is often studied by examining the sawtooth behavior of the electron temperature. However, in the present experiments, only the Thomson scattering diagnostic is available to study electron temperature, and this diagnostic does not have sufficient time resolution to resolve sawteeth. In analogy with the sawtooth technique, RF deposition on deuterium is sometimes studied by examining the slope of a T_D versus time plot. However, this method is too error prone to be used in the present study, and there is not sufficient profile information in the data either. Both of these methods involve the assumption that the slope of the temperature-versus-time plot can be measured over a time interval sufficiently short that none of the plasma properties vary significantly over the interval. It is possible to take the estimated power deposition to deuterium for the low-density case modeled in the next chapter and "work backwards" to figure out what the initial slope of the T_D versus time plot should be when the RF turns on. If this is superimposed on Fig. 3.3.1, it will be seen to be consistent with the measurement, but the uncertainty in starting from the plot and determining the slope will be obvious.

The one obvious exception to the statement that RF power deposition cannot be determined experimentally is the calculation done for the charge-exchange radial scan. The results from that one case are helpful in evaluating, at least qualitatively, the uncertainty in the model developed in the next chapter. Although the interpretation of the hydrogen charge-exchange diagnostic is ambiguous, the hydrogen temperatures from the radial scan happen coincidentally to be the same as the temperatures that would be obtained by my ad-hoc assumption $T_H = E_{\mathrm{tr}}$.

Thus, there is at least a limited amount of experimental data that can be compared with a theoretical RF deposition model. The development of such a model for Alcator C is the subject of the next chapter.

CHAPTER 4

Numerical Simulations and Analyses

4.1: Introduction

In this chapter, a theoretical model will be constructed in order to study the power balance in more detail than was done in Chapter 3. Up to this point, the power balance was studied by treating the plasma as a "black box". That is, the total amount of RF power launched into the plasma was compared to the total Ohmic heating power, and the heating efficiency was evaluated by comparing the total thermal energy content of the plasma before and during the RF. It was noted that a large fraction of the RF power was lost due to inadequate confinement of the hydrogen minority. It was also noted that there was no electron heating during the RF and that, while this fact was not very mysterious, there was insufficient experimental data available to study the electron power balance. Thus, when the thermal energy of the "black box" plasma increased during the RF, it was predominately the thermal energy of the deuterium that was increasing. The Ohmic input power is deposited directly on electrons, not ions. And the amount of Ohmic power that contributes to deuterium heating depends directly on the plasma density and the temperatures of the ions and the electrons. The temperature of the electrons is dependent on the electron confinement properties, Ohmic input power, and the electron radiation processes about which there are no experimental data. Thus the total Ohmic heating power is not a good measure of the amount of power input to the deuterium before the RF, nor is it a measure of the Ohmic contribution to the ion heating power during the RF. Also, the total launched RF power is not a good measure of the amount of RF power that is actually deposited to the deuterium. It is therefore not the least bit surprising that the power balance analysis performed in Chapter 3 cannot adequately explain the experimental results.

What is really needed is an analysis which concentrates more closely on the power sources and confinement of the deuterium, in isolation from the other plasma components. That is, it is desired to treat the hydrogen and electrons as known sources of collisional exchange power to the deuterium, add in the contribution from direct deuterium second harmonic absorption, and then model the various loss mechanisms from the deuterium. If some way can be found to model the various loss mechanisms associated with the hydrogen while at the same time calculating the collisional exchange power associated with the non-Maxwellian hydrogen distribution function, then the uncertainties associated with the electron power balance will have been effectively bypassed. This is possible because, even though data concerning the electron energy loss mechanisms are lacking, direct measurements of the electron temperature and density are available, and that is all one needs to

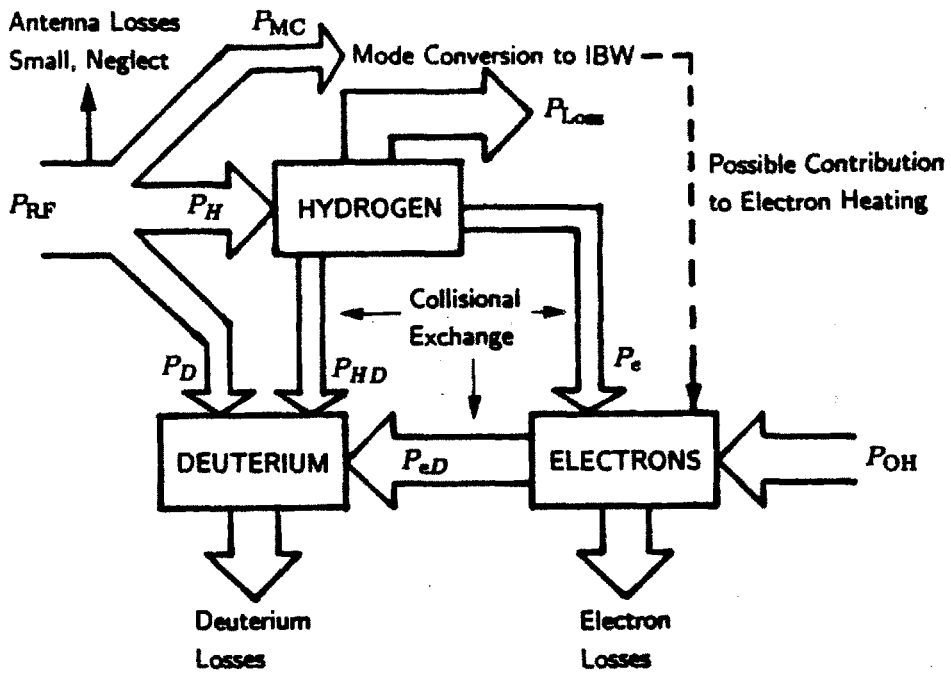

Figure 4.1.1: Power Balance—This block diagram shows the various power flows to and between the different species and defines the terminology that will be used in this chapter to refer to them.

know about the electrons in order to calculate the collisional exchange power from electrons to ions.

The procedure that has just been suggested is outlined in Fig. 4.1.1. This illustration also serves to define notation that will be used throughout this chapter to refer to the various power channels. The total RF power launched by the antenna is denoted by $P_{\rm RF}$. Resistive losses in the antenna system will be neglected, so $P_{\rm RF}$ will be taken to be the net forward power measured in the antenna feed line. This power will be distributed among three separate channels: mode conversion to the ion Bernstein wave ($P_{\rm MC}$), hydrogen fundamental cyclotron absorption (P_H), and deuterium second harmonic absorption (P_D). Although it is possible that the mode-converted power is deposited on the electrons via Landau damping, the computer programs to be used in this chapter do not model all the physics relevant to this process, so it will not be determined conclusively what happens to $P_{\rm MC}$. Since experimental data necessary to model the electrons are not available, there is absolutely nothing lost from the analysis by not knowing what happens to $P_{\rm MC}$. The power P_H absorbed by the hydrogen is then either collisionally deposited on deuterium (P_{HD}), or on electrons (P_e), or lost from the plasma ($P_{\rm Loss}$). The code FPPRF which will be used to model the hydrogen energy balance can calculate

components of $P_{\rm Loss}$ resulting from unconfined orbits, neoclassical transport, charge exchange, sawtooth transport, asymmetric drag, and toroidal field ripple diffusion. It cannot, however, calculate losses from toroidal field ripple trapping. Once this part of the model has been completed, the deuterium second harmonic absorption will be combined with the collisional exchange between hydrogen and deuterium to obtain an estimate of the net RF power $P_{\rm net} = P_H + P_{HD}$ deposited to deuterium. This power deposition profile $P_{\rm net}(r)$ will then be used as input to a transport code, along with data from experimental measurements. The transport code will then treat the electrons as a known source, by calculating $P_{eD}(r)$, along with the given power source $P_{\rm net}(r)$, and proceed to evaluate various loss mechanisms associated with deuterium. Then the heating efficiency (of deuterium only) resulting from $P_{\rm net} + P_{eD}$ during the RF will be compared with the heating efficiency of P_{eD} alone before the RF, and it will be found that both power sources are equally efficient at heating the deuterium. That is, no additional loss mechanisms or increased anomaly in known loss mechanisms is necessary in order to explain the experimental data.

It is important to realize that just because a great deal of simulations are going to be done using four highly sophisticated numerical codes, that does not necessarily mean that a highly accurate answer is going to be rigorously obtained. As far as the calculation of $P_{\rm net}$ is concerned, it must be emphasized that the treatment will be very ad-hoc in some respects. Of course, when running numerical codes, it is always important to understand what physical phenomena are modeled and what approximations are used in the codes, and any resulting limitations. But the authors of these codes did not necessarily have Alcator C in mind when the codes were developed, and Alcator C has some unique problems that were not considered when the codes were developed. One problem with Alcator C plasmas is that single-pass ICRF absorption is very weak. Because of this, codes were used to calculate the RF wave fields which self-consistently include the reflecting boundaries and antenna current source (assumed current distribution). However, the most serious problem encountered when modeling Alcator C with these codes is the presence of the ripple-trapping effect. It is clear that there are serious loss mechanisms associated with the hydrogen which must be modeled, and the Fokker-Planck code chosen to model the hydrogen treats most of them. Unfortunately, the code does not include the effect of ripple trapping. I am not aware of the existence of any code that includes ripple trapping while doing a Fokker-Planck calculation of the minority heating, with or without the other loss mechanisms. It turns out that the collisional power deposition from hydrogen to deuterium is dominated by contributions from suprathermal hydrogen ions which are not lost due to ripple trapping. That is, hydrogen ions with $E > E_{\rm tr}$ would tend to slow down on electrons rather than deuterium. Because of this, the inability to model ripple trapping will

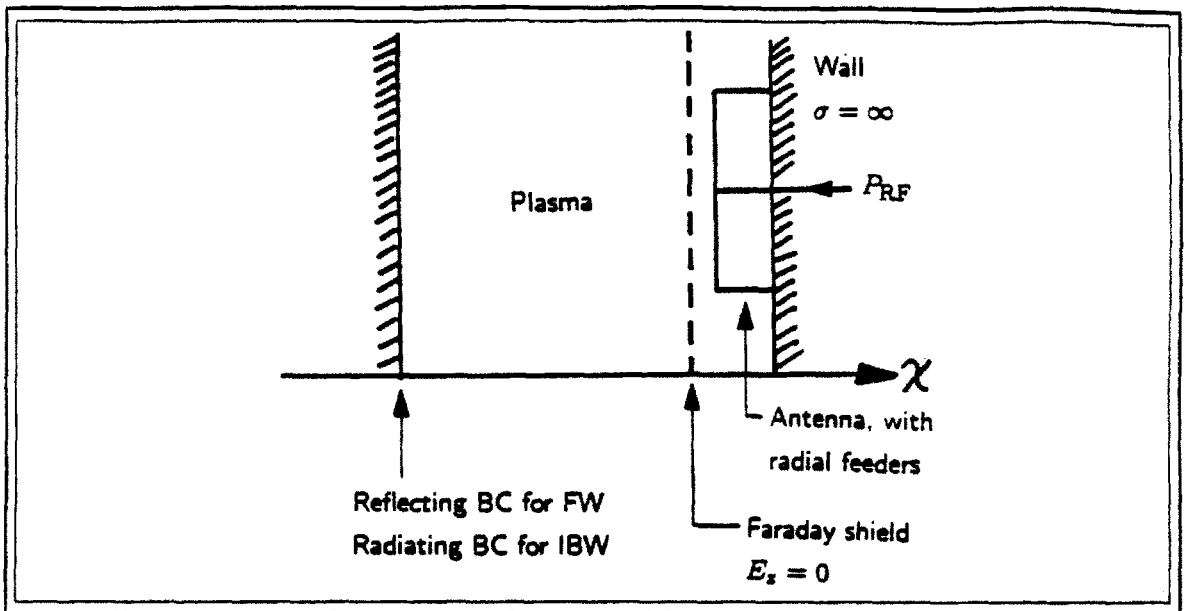

Figure 4.2.1: Slab Geometry for Brambilla Code—A plasma whose parameters are allowed to vary in an arbitrary manner in the x-direction exists between the Faraday shield and the far wall. The antenna was modeled as a toroidal (perpendicular to this page) array of two center-fed loops, driven in phase.

result in uncertainty in the distribution of power between P_{Loss} and P_e rather than uncertainty in the calculation of P_{HD}.

The interpretation and limitations of the codes will be discussed in further detail in the individual descriptions of each code that appear in the following sections.

4.2: Coupling, Absorption, and Mode-Conversion in Slab Geometry

A 1D, full-wave, hot-plasma code has recently been developed by Brambilla[122]. This code was developed for the purpose of modeling direct excitation of ion Bernstein waves by ICRF antennas, which is not the purpose for which it is being used here. However, this code is convenient because it provides a way to calculate cyclotron absorption and mode-conversion of the fast wave to the IBW using an $N_{||}$-spectrum determined self-consistently by including the antenna coupling problem as a boundary condition when solving the wave equations. It also allows a reflecting boundary condition to be imposed at the far wall without also requiring the IBW to be reflected. It is very important to emphasize that, since the code was written primarily to study phenomena which occur at the edge of the plasma, it omits some physics that can be important in the center. In particular, the code does not model magnetic pumping nor does it allow $N_{||}$ to evolve (due to non-zero poloidal field) as the IBW propagates. This will not be a drawback for the present application.

The geometry used by the Brambilla code is illustrated in Fig. 4.2.1. The plasma is assumed to be enclosed in a box of dimensions $2a + \delta$ in the x-direction, $2\pi a$ in the y-direction, and $2\pi R_0$ in the z-direction. Here δ is the distance from the limiter to the vacuum chamber wall. The hot-plasma wave equation is solved by the method of finite-elements (using cubic Hermite polynomial basis functions) in the x-direction, and Fourier series in the y and z-directions. Periodic boundary conditions are imposed in the y and z-directions and reflecting boundary conditions are imposed at both walls in the x-direction. An artificial damping term was added to the IBW to prevent reflection of the IBW at the far wall. This is necessary because the wave equation used is not valid for the IBW at the far edge of the plasma, where the IBW wavelength is so short that the FLR expansion used to derive the equation is not accurate. This has essentially the same effect as imposing a radiating boundary condition that affects only the IBW, somewhere on the high-field side of the absorption region. Within the limiter radius, the electron density profile was assumed to be a parabola and the electron and ion temperature profiles were assumed to be parabolas squared. In the scrape-off region between the limiter and the Faraday shield, the density and temperature profiles were assumed to be exponentials, using edge values and scrape-off lengths typical of measurements made by Wan in earlier experiments[123]. In the code, analytic vacuum solutions are used for the fields behind the Faraday shield, and these are matched to the numerical solutions at the location of the Faraday shield. The code allows arbitrary angles of orientation between the magnetic field, Faraday shield, and antenna, but in the results presented here, the Faraday shield was always assumed to be perpendicular to the antenna and parallel to the magnetic field.

Using notation similar to that in Ref. 122, the wave equation is approximated by the following 6th-order system:

$$-\left(\frac{\partial}{\partial x}+N_y\right)\left[\sigma\left(\frac{\partial}{\partial x}-N_y\right)(E_x+iE_y)\right]+(N_y^2+N_z^2-S)E_x + iN_y\frac{\partial E_y}{\partial x}+iDE_y-iN_z\frac{\partial E_z}{\partial x}=0 \tag{4.2.1}$$

$$i\left(\frac{\partial}{\partial x}+N_y\right)\left[\sigma\left(\frac{\partial}{\partial x}-N_y\right)(E_x+iE_y)\right]+iN_y\frac{\partial E_x}{\partial x}-iDE_x - \frac{\partial^2 E_y}{\partial x^2}+(N_z^2-S)E_y-N_yN_zE_z=0 \tag{4.2.2}$$

$$iN_z\frac{\partial E_x}{\partial x}-N_yN_zE_y-\frac{\partial^2 E_z}{\partial x^2}+(N_y^2-P)E_z=0 \tag{4.2.3}$$

where

$$L = 1 + \frac{\omega_{pe}^2}{\Omega_e^2}\left(1 - \frac{\Omega_e}{\omega}\right) - \sum_i \frac{\omega_{pi}^2}{\Omega_i^2} \underbrace{x_{0i} Z(x_{1i})}_{P_H} \tag{4.2.4}$$

$$R = 1 + \frac{\omega_{pe}^2}{\Omega_e^2}\left(1 + \frac{\Omega_e}{\omega}\right) - \sum_i \frac{\omega_{pi}^2}{\Omega_i^2} \frac{\omega}{\omega + \Omega_i} \tag{4.2.5}$$

$$P = 1 - \frac{\omega_{pe}^2}{\omega^2} \underbrace{x_{0e}^2 Z'(x_{0e})}_{\text{ELD}} \tag{4.2.6}$$

$$S = \frac{R+L}{2} \qquad D = \frac{R-L}{2} \tag{4.2.7}$$

$$\sigma = -\frac{1}{4} \sum_i \frac{\omega_{pi}^2}{\Omega_i^2} \underbrace{v_{thi}^2 x_{0i} Z(x_{2i})}_{\text{IBW}+P_D} \tag{4.2.8}$$

$$Z(x) = \frac{\text{Pv}}{\sqrt{\pi}} \int_{-\infty}^{\infty} \frac{e^{-u^2}}{u - x}\, du + i\sqrt{\pi} e^{-x^2} \tag{4.2.9}$$

$$x_{ni} = \frac{\omega - n\Omega_i}{k_z v_{thi}} \tag{4.2.10}$$

Included in these equations are the leading-order (in FLR expansion) contributions from fundamental cyclotron absorption by hydrogen (in L), second harmonic cyclotron absorption by deuterium (in σ), electron Landau damping (in P), and mode conversion (in σ). Once the wave fields are determined, the local power absorption is calculated from

$$P = \frac{1}{2}\left[\underbrace{-\text{Im}(\sigma)\left|\left(\frac{\partial}{\partial x} - N_y\right)(E_x + iE_y)\right|^2}_{P_D} + \underbrace{\text{Im}(L)|E_x + iE_y|^2}_{P_H} + \underbrace{\text{Im}(P)|E_z|^2}_{\text{ELD}}\right] \tag{4.2.11}$$

where the contributions from deuterium second harmonic cyclotron damping (P_D), hydrogen fundamental cyclotron damping (P_H), and electron Landau damping (ELD) are indicated.

The most important information to be gained by running the Brambilla code is the amount of power that is mode-converted to the IBW. By running a large number (350) of cases using simple (but reasonable) prototype plasma parameters, the behavior of the mode-converted power as a function of density, minority concentration, and minority temperature is determined. This information is important

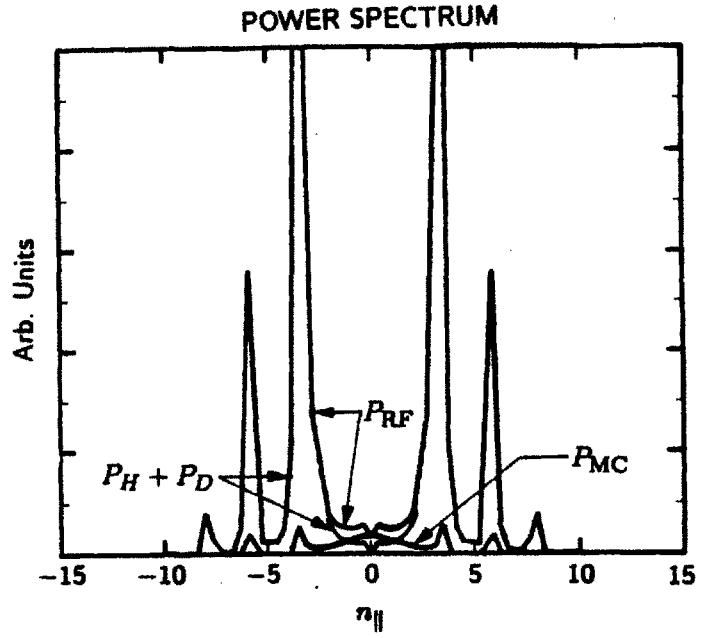

Figure 4.2.2: Absorbed Power Spectrum for Low-Density Case—The $N_\parallel$ spectrum of absorbed and mode-converted power is shown for the low-density case. The dominant contribution to absorbed power comes from components in the vicinity of $N_\parallel \sim 3.5$, and there is very little mode-conversion.

to resolve an ambiguity introduced because the 2D code SHOOT, described in the next section, cannot distinguish between mode conversion and deuterium second harmonic absorption.

Large scans of plasma parameters were done with the Brambilla code, SHOOT, and FPPRF. In addition to presenting the results of these scans, more detailed information will be shown for two prototype cases. These two prototype cases will be referred to hereafter as "the low-density case" and "the high-density case". The parameters assumed for the low-density case were $\bar{n}_e = 1 \times 10^{20}\,\mathrm{m}^{-3}$, $T_D = 1$ keV, $T_H = 10$ keV, $T_e = 2$ keV, $I_P = 160$ kA, $\eta_H = 0.5$ %, and $P_{\mathrm{RF}} = 220$ kW, and the parameters assumed for the high-density case were $\bar{n}_e = 4.5 \times 10^{20}\,\mathrm{m}^{-3}$, $T_D = 1$ keV, $T_H = 1$ keV, $T_e = 1.65$ keV, $I_P = 400$ kA, $\eta_H = 0.5$ %, and $P_{\mathrm{RF}} = 175$ kW.

The power spectrum determined by the Brambilla code for the low-density case is shown in Fig. 4.2.2. These powers are functions of the Fourier series variables $N_z = N_\parallel$ and N_y. In Fig. 4.2.2, the powers are summed over N_y and plotted as functions of N_z. The power launched by the antenna is found to go primarily to cyclotron damping on hydrogen and deuterium, with a small amount of mode conversion. Most of the power is found to be concentrated in peaks near $N_\parallel \sim 3.5$,

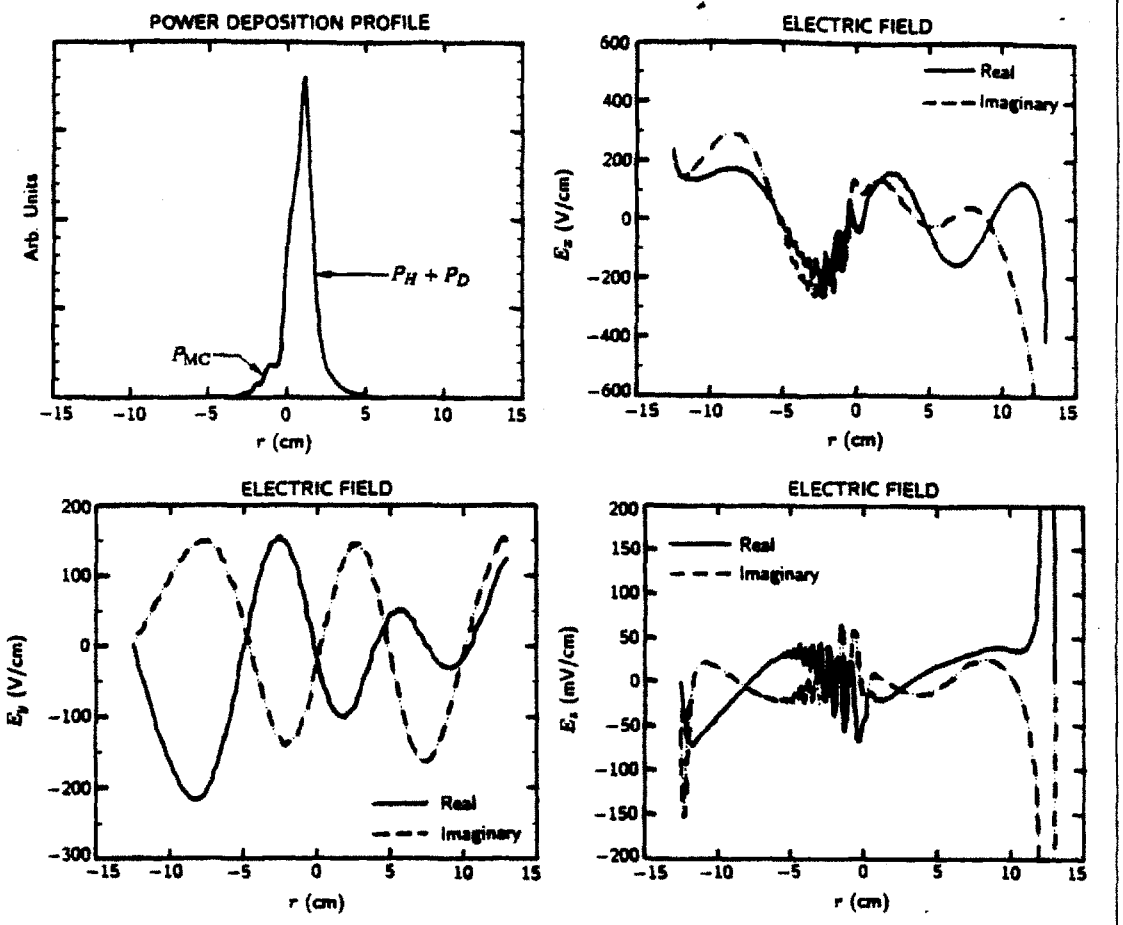

Figure 4.2.3: Electric Field Pattern and Power Deposition Profile in Slab Geometry for the Low-Density Case—The high-field side is on the left in these plots, and the antenna geometry is that of the two-element low-field-side launcher. The electric fields are calculated assuming 1 MW of launched ICRF power.

but one should realize that this result is somewhat dependent on the assumed geometry.

The power absorbed by electron Landau damping was found to be completely negligible for this case as well as for most other cases studied. This was checked by removing the artificial damping term on the IBW and imposing a true radiating boundary condition (for both waves) on the high-field side. However, this result is uncertain because the Brambilla code does not model all the relevant physics. The question of how much IBW power actually damps on electrons could be treated more carefully using a ray-tracing code. However, due to the experimentally measured lack of electron heating and the lack of diagnostic information regarding electron power loss, there is not much that could be done with the results of a ray tracing

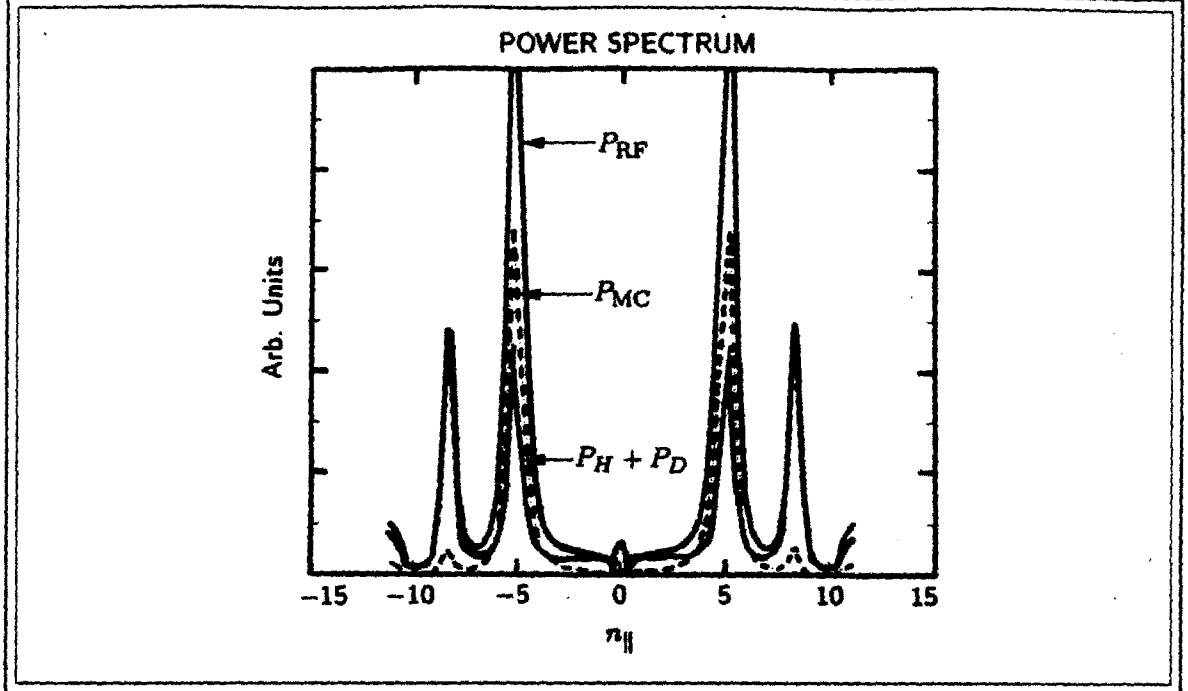

Figure 4.2.4: Absorbed Power Spectrum for High-Density Case—The spectrum peaks have shifted to $N_\parallel \sim 5$ and mode-conversion has become more significant.

analysis. As was mentioned previously, the approach to be taken in this work will be to treat the electrons as a known source of collisional-exchange power to the deuterium, and concentrate on analyzing the deuterium power balance. Therefore, this uncertainty about the fate of the mode-converted power is not a problem for the forthcoming analyses.

More Brambilla code output for the low-density case is shown in Fig. 4.2.3. Shown are the power deposition profiles and the real and imaginary parts of the three Cartesian components of the wave electric field. It will turn out that the fast wave is not focussed into a small spot at the plasma center in Alcator C. Because of this, Fig. 4.2.3 contains somewhat limited profile information, because the power deposition profile in two dimensions will actually have a large vertical extent. The shape of the part of the profile indicated as P_{MC} is determined by the strength of the imposed artificial damping and contains no physical information.

It can be seen that the fast wave contains primarily E_y and E_x components while the IBW contains primarily E_x and E_z components. The small-electron-mass effect $E_\parallel/E_\perp \sim O(m_e/m_i)$ is also apparent. The E_y field shows that the fast wave has a very high standing wave ratio (i.e., weak absorption), with only a small inward propagating component on the low-field side. This weak absorption was verified when running the Brambilla code in single-pass mode, with true radiating boundary conditions on the high-field side.

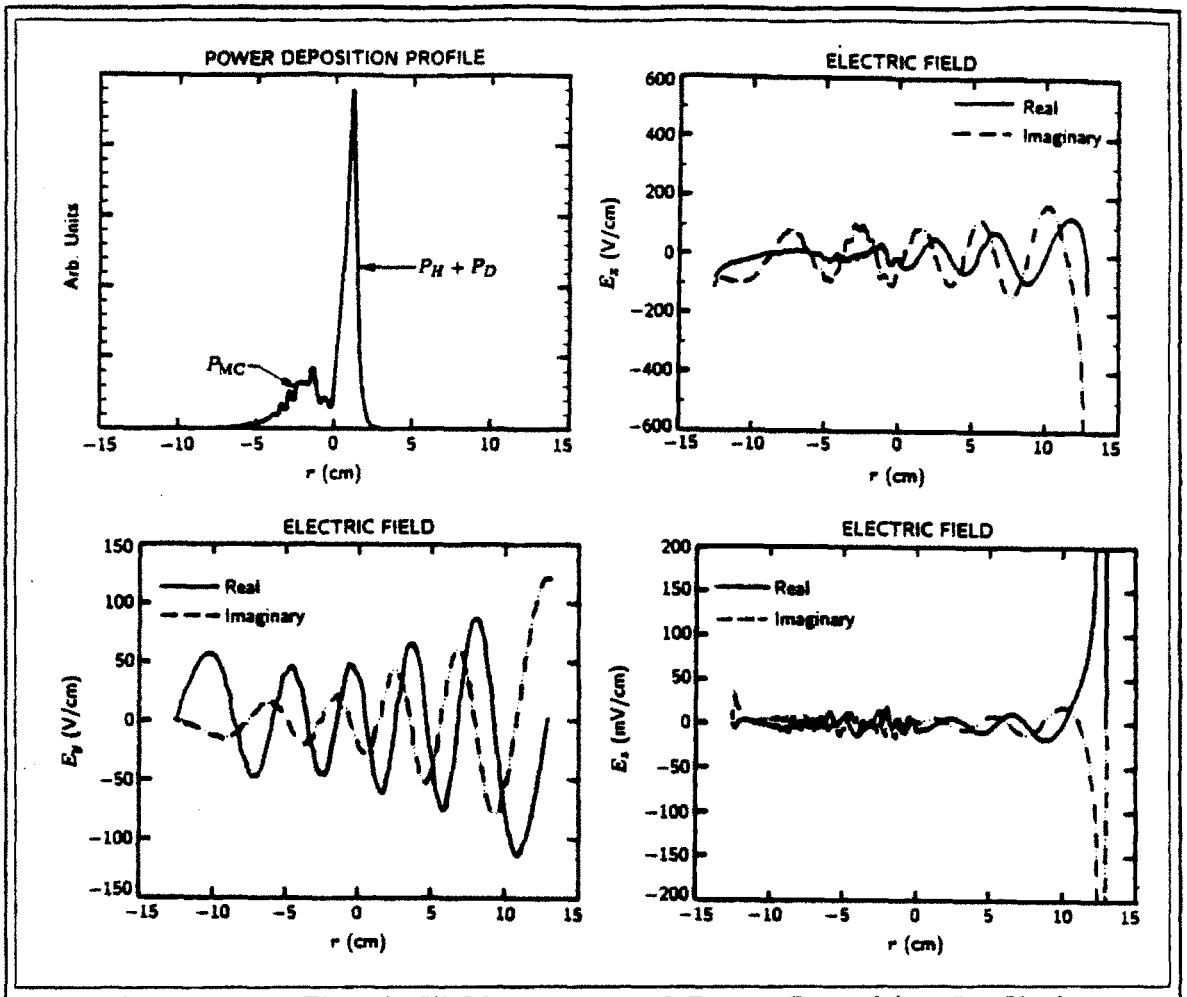

Figure 4.2.5: Electric Field Pattern and Power Deposition Profile in Slab Geometry for the High-Density Case—The width of the absorption region is narrower compared to the low-density case, due to the lower minority temperature, and the perpendicular wavelength of the fast wave is shorter as expected from cold-plasma theory.

The power spectrum for the high-density case is shown in Fig. 4.2.4. Significantly more mode conversion is evident here compared to the low-density case. Also evident is a shift of the spectrum peaks to higher values of $N_{\|}$.

The power deposition profile and electric field components for the high-density case are shown in Fig. 4.2.5. The power deposition profile is narrower compared to the low-density case, because the assumed minority temperature is lower, resulting in less Doppler broadening. The fast wave exhibits a shorter wavelength in the x direction, as expected from cold-plasma theory. The fast wave also shows a lower standing wave ratio than in the low-density case, indicative of stronger single-pass absorption. These results are comparable to the METS calculations shown in Sec. 1.5.

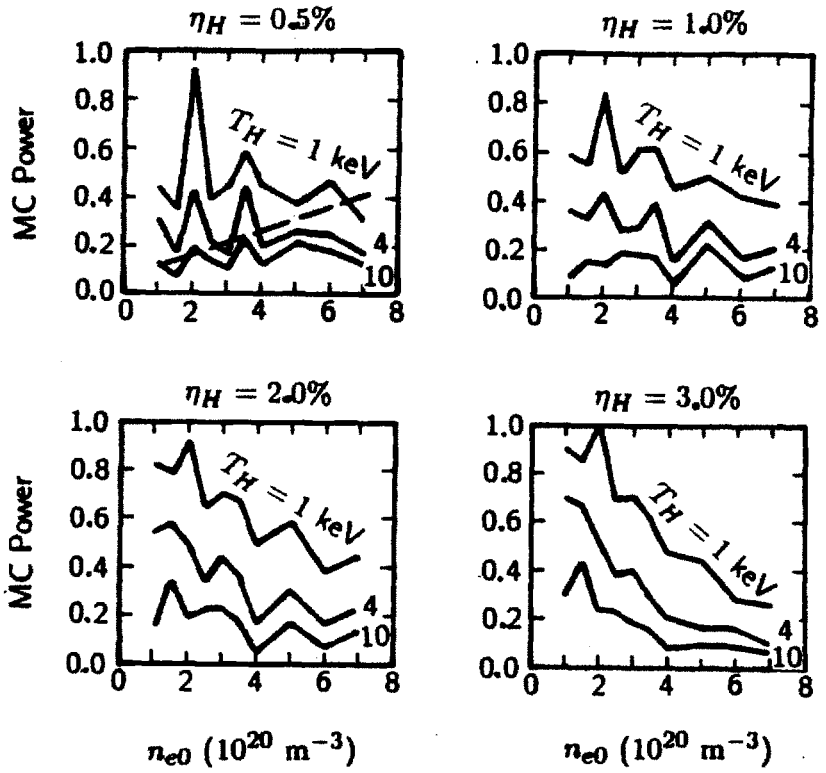

Figure 4.2.6: Mode-Conversion from Slab-Geometry Calculation—The fraction of power mode-converted is shown as a function of plasma density, minority temperature, and minority concentration. It is necessary to produce an elevated minority temperature in order to avoid significant mode-conversion. At high density and/or minority concentration, where it is not possible to produce an elevated T_H, a large fraction of the power can be mode-converted.

Results from a comprehensive Brambilla code scan are shown in Fig. 4.2.6. The fraction of power mode-converted is shown for all of the values of density, minority temperature, and concentration of interest to the experiment. Basically, it is found that it is necessary to have at least a modestly elevated tail temperature in order to avoid significant mode conversion.

In the experiment, data on minority tail temperature was very difficult to interpret, because of the TF ripple trapping effect previously discussed. There was also a great deal of scatter in the T_H data. Also, measurements of minority concentration were rare, due to the need to produce two similar shots in sequence in order to measure it. For most of the shots in the data base, when hydrogen was not being injected into the vacuum chamber, it is assumed, based on measurements of a small fraction of the shots, that the concentration was $\eta_H = 0.5$ %, with an uncertainty of $\pm 0.5\%$. For shots in which extra hydrogen was injected, more careful measurements were made, but these shots occurred only within a limited density range. Additional

uncertainty is introduced by the sharp peaks in the mode-converted power plotted in Fig. 4.2.6, which are a result of geometry-dependent wave coherence effects which occur because the wave phase fronts and the absorption layer are both planar in shape (in the assumed slab geometry). This would not be expected to occur in a more realistic geometry.

Because the measured minority distribution functions were truncated at $\sim$ 10 keV for low densities ($\bar{n}_e \lesssim 1 \times 10^{20}\,\mathrm{m}^{-3}$) and elevated minority temperatures were not observed for high densities ($\bar{n}_e \gtrsim 4 \times 10^{20}\,\mathrm{m}^{-3}$), and because of the uncertainties just discussed, it will be assumed that 10% of the RF power is mode converted at $n_{e0} = 1 \times 10^{20}\,\mathrm{m}^{-3}$, 40% is mode converted at $n_{e0} = 6 \times 10^{20}\,\mathrm{m}^{-3}$, and linear interpolation will be used for intermediate densities. This is indicated by the broken line in Fig. 4.2.6. The uncertainty in this ad-hoc assumption can be estimated in an equally ad-hoc manner from inspection of the $\eta_H = 0.5\%$ plot in Fig. 4.2.6. It should be noted that the uncertainty introduced by the sharp peaks is caused by the choice of boundary conditions, which is the most reasonable choice to use given slab geometry, and not by the code chosen. It is clear that if one is very concerned with accurately modeling mode conversion in a plasma with weak single-pass absorption, then a better way to treat this problem would be to modify the SHOOT code to allow P_D and P_{MC} to be determined separately. A few simple comparisons were made by using $P_D/P_H = \beta_D/\eta_H$ in combination with SHOOT in order to separate P_D from P_{MC}, and no serious discrepancies were found.

It will turn out that as far as the density scan is concerned, mode conversion is not the dominant effect and uncertainties in the amount of mode conversion will not alter the conclusion that will be reached. However, as one might guess from inspection of Fig. 4.2.6, this will not be the case for the concentration scan. Fortunately, careful minority concentration measurements were made when concentration was scanned in the experiment. Moreover, the magnitude of the sharp peaks in Fig. 4.2.6 is reduced as concentration is increased. In fact, the high-concentration, low-minority-temperature cases are where SHOOT encounters numerical difficulties, and thus these cases are the ones for which the Brambilla code is most useful. In the experimental data, the minority concentration was scanned at a density of $\bar{n}_e \sim 1.45 \times 10^{20}\,\mathrm{m}^{-3}$, and T_H decreased to values comparable to T_D (i.e., $\gtrsim 1$ keV) when η_H reached 3%.

In summary, from the Brambilla code it is learned that there is a significant increase in mode conversion as density is increased and a major increase in mode conversion as minority concentration is increased. This effect is caused by the inability to produce an elevated minority temperature at high density or high minority concentration.

4.3: Calculation of Power Deposition Profile in Cylindrical Geometry

The SHOOT code[124] was used to determine the profile of power absorption in cylindrical geometry, taking into consideration the vertical extent of the absorption region. The SHOOT code solves a fourth-order wave equation in two dimensions (the poloidal plane) by using an order-reduction technique, analogous to that used to obtain Eq. 1.5.47 from Eq. 1.5.46, to reduce the wave equation to second order. The zero electron mass approximation is used. To accomplish this mode reduction, Smithe *et al.* begin with a fourth order wave differential equation obtained from using an FLR expansion in the full integral wave equation. This equation is of the form

$$\nabla_\perp \times (\nabla_\perp \times \mathbf{E}) = \underbrace{\omega^2(\mathbf{K}^{(0)} - n_z^2\mathbf{I}) \cdot \mathbf{E}}_{P_H} - \underbrace{\mathbf{K}^{(1)} \cdot \nabla_\perp^2 \mathbf{E}}_{\text{IBW}+P_D} \tag{4.3.1}$$

where $\mathbf{K}^{(0)}$ contains the cold-plasma contributions and the leading-order terms describing hydrogen fundamental cyclotron absorption, and $\mathbf{K}^{(1)}$ contains the leading-order contributions from deuterium second harmonic cyclotron absorption and finite-temperature terms which describe propagation of the IBW and mode conversion of the fast wave to the IBW. The order reduction is accomplished by making the following substitution on the right-hand side of Eq. 4.3.1:

$$\nabla_\perp^2 \mathbf{E} \longrightarrow -\omega^2 \nu^2 \mathbf{E} \tag{4.3.2}$$

Here the quantity ν is the fast-wave root of the homogeneous hot-plasma dispersion relation. In this way, the IBW is treated as a dissipative load experienced by the fast wave, but the fields associated with the IBW are not actually generated when the wave equation is solved. It is therefore not necessary to resolve the fine detail of the short-wavelength IBW, and a major reduction in computing expense is realized. A "reduced" or "truncated" dielectric operator $\mathbf{K}_{\text{FW}}$ is then defined via

$$\mathbf{K}_{\text{FW}} = \underbrace{\mathbf{K}^{(0)} - n_z^2\mathbf{I}}_{P_H} + \underbrace{\nu^2 \mathbf{K}^{(1)}}_{P_D+P_{\text{MC}}} \tag{4.3.3}$$

leading to the following second order system:

$$\nabla_\perp \times (\nabla_\perp \times \mathbf{E}) = \omega^2 \mathbf{K}_{\text{FW}} \cdot \mathbf{E} \tag{4.3.4}$$

At the time of this writing, the validity of this order-reduction technique (in two dimensions) has not been rigorously proven. However, comparisons of SHOOT results

with other codes (including the Brambilla code) seem to give good agreement. It is emphasized that the total powers P_H, P_D, and P_{MC} are taken from the Brambilla code, while SHOOT is used only for the profile shape. This effectively side-steps any uncertainty in the validity of this order reduction technique.

The method used to solve this system is finite differencing (specifically, a predictor-corrector method) in the radial (r) direction combined with Fourier analysis in the tangential (θ) and axial (z) directions. Since the plasma properties ($\mathbf{K}$) are functions of θ as well as r, Fourier analysis in θ leads to a system of coupled equations, whose order is twice the number of poloidal modes used. This method is often called "poloidal mode expansion". In the solution technique, the antenna current is first Fourier expanded in θ and z. Then the finite difference algorithm is begun at $r = 0$, where a regularity condition is imposed, and stepped to the antenna location, where appropriate jump conditions are imposed on the various poloidal modes, and then stepped to the wall location, where perfect conductivity is assumed. There is no Faraday shield in the model.

Output from the SHOOT code is shown in Fig. 4.3.1 for the low-density case. Contours of E_y and power density (power per unit volume) are shown. (Negative values of E_y are shown by broken contours. The value on the outer contour is $\sim$15–20% of the maximum, depending on how the plot was auto-scaled.) The quantity called "radial power density" is power per unit length in the r direction, i.e., integrated over θ and z. Thus, the radial power density is always zero at $r = 0$ for SHOOT output. The profile is significantly broader than in the slab calculation due to the vertical extent of the absorption region.

The SHOOT calculation for the high-density case is shown in Fig. 4.3.2. The shorter fast-wave wavelength is apparent in part (a). In part (b), the blackened area indicates the area within the outer contour. The power-deposition profile is much narrower than for the low-density case, but the broadening effect from the vertical extent of the absorption region is quite significant.

In the next section, a Fokker-Planck code (FPPRF) will be used to determine the fate of the absorbed power. In those calculations, the inputs to the code will be adjusted so that the amount of power deposited to hydrogen is consistent with that determined by the Brambilla code, and the shape of the deposition profile will be that determined by the SHOOT code. The version of FPPRF used has SHOOT interfaced with it, in order to self-consistently determine the absorption and distortion of the distribution function. Therefore, the results of parameter scans using SHOOT will be presented in the next section, along with the FPPRF results.

There are some minor differences between this "standalone" version of SHOOT and the version of SHOOT which is interfaced with FPPRF. In FPPRF SHOOT, the

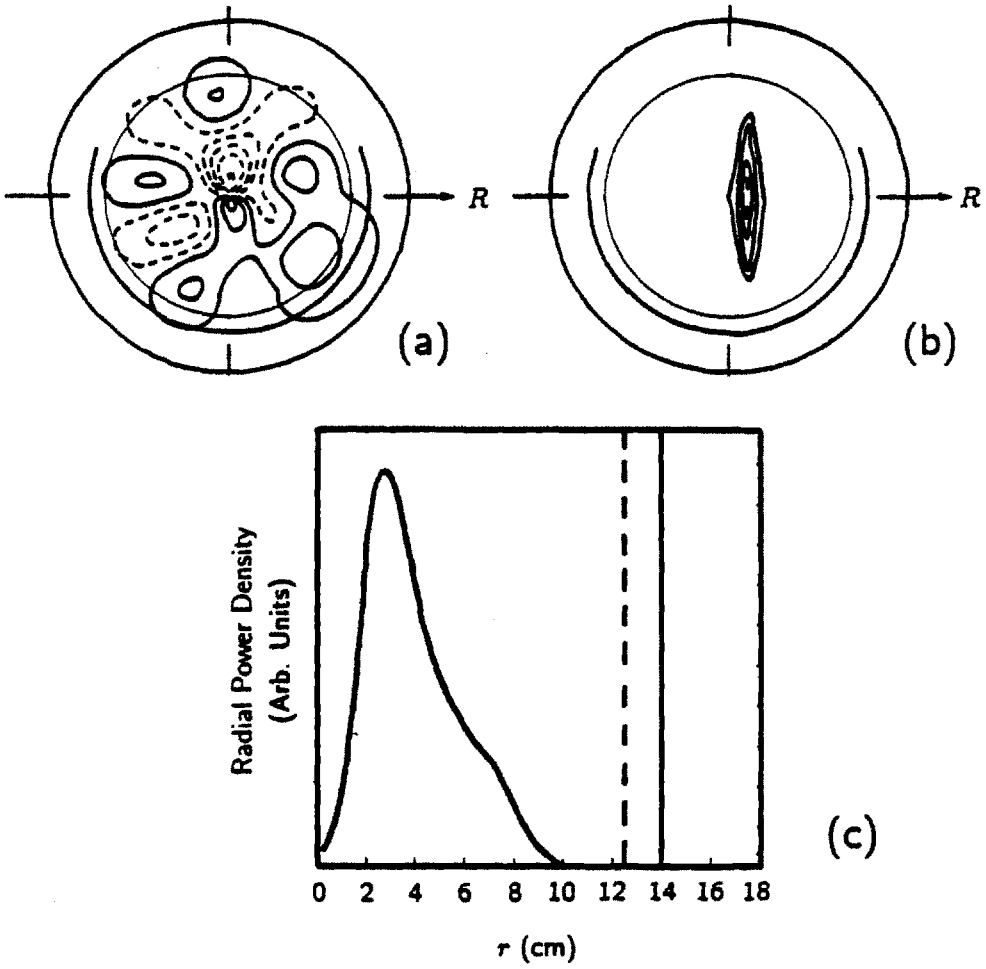

Figure 4.3.1: SHOOT Calculation for Low-Density Case—The electric field contours are shown in Part (a), and the power absorption contours are shown in Part (b). The resulting radial power deposition profile is shown in Part (c). The low-field-side is on the right in these plots, and the positions of the limiter, antenna, and wall are indicated. These results are for the two-side-launch antenna. For the low-field-side launch antenna, the field pattern is different, but the resulting deposition profile is similar.

antenna current is assumed to be independent of θ within $-\theta_0 < \theta < \theta_0$ and zero outside this range, whereas the actual antenna current is better approximated as sinusoidal in θ and centered about $\theta = 0$ for the outside-launch antenna and $\theta = -\pi/2$ for the two-side launch antenna. Standalone SHOOT was modified to include this more accurate model of the antenna current. The result is that FPPRF SHOOT produces slightly narrower absorption profiles than the standalone version, such that the peak power absorption densities are over-estimated by ~ 20 %. This is of

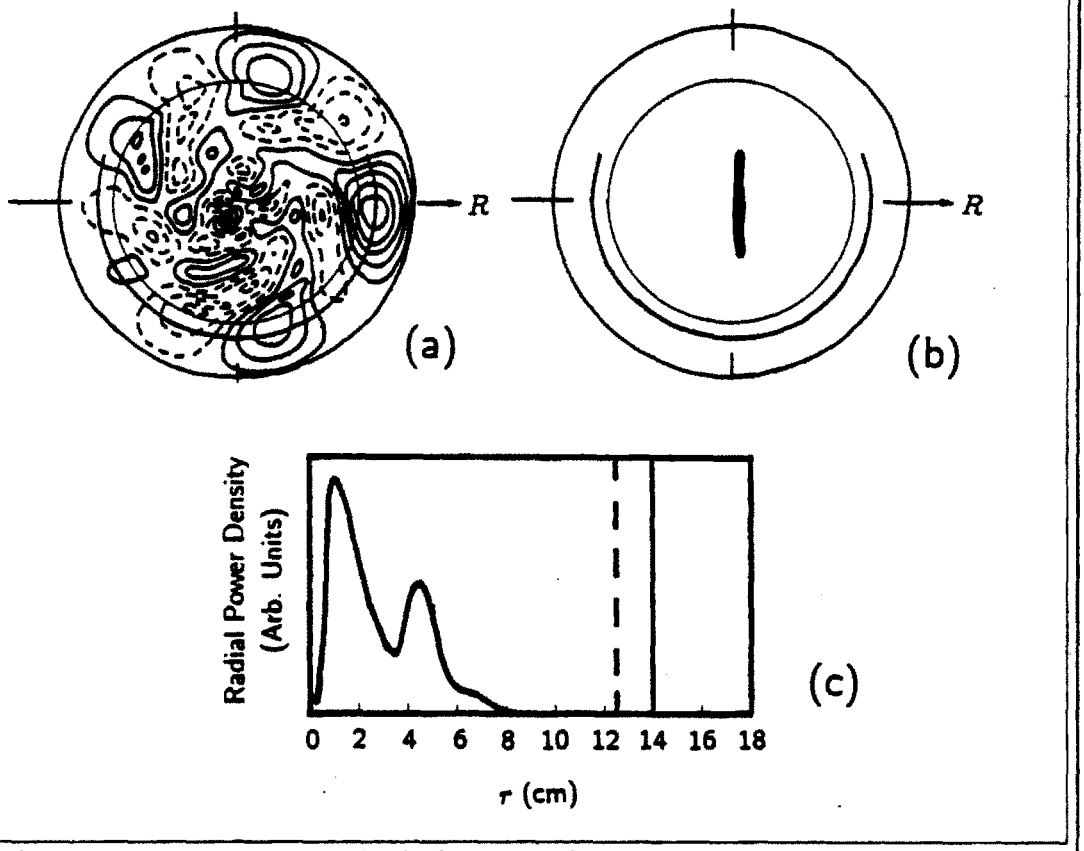

Figure 4.3.2: SHOOT Calculation for High-Density Case—The electric field pattern is finer than in the low-density case and the power deposition profile is narrower, although still broadened compared to the slab calculation due to the vertical extent of the absorption region.

no consequence for the calculation of P_H because the subsequent calculation of P_{HD} is dominated by broadening due to radial transport mechanisms, except for the two highest densities modeled. However, at high density, none of the loss mechanisms included in FPPRF are important, so it was a simple matter to replace FPPRF by an analytic calculation for these cases. Standalone SHOOT does not separate P_H from P_D, but FPPRF SHOOT does. The profile shapes used for $P_D(r)$ were obtained by applying $P_D/P_H = \beta_D/\eta_H$ to the $P_{\mathrm{RF}}(r)$ profiles determined by standalone SHOOT. This yields $P_D(r)$ profiles which are only slightly broader than those from FPPRF SHOOT, as was just mentioned. As discussed above, there is no way to determine the shape of the $P_{\mathrm{MC}}(r)$ profile using SHOOT, so this uncertainty is not resolved. However, in FPPRF, profiles can be calculated both for the target plasma and also for RF-heated plasmas in which the minority temperature is high enough to suppress most of the mode-conversion. No significant change in this profile shape is seen in the FPPRF calculation as the plasma heats up.

4.4: Fokker-Planck Calculations

Once the profiles of power absorption on hydrogen and deuterium have been calculated, it is necessary to determine how much of the power absorbed by hydrogen is collisionally transferred to deuterium and how much goes to other channels. This is accomplished using the bounce-averaged Fokker-Planck code FPPRF[120]. SHOOT is included as a subsystem in this code, and is used to determine the power absorbed by hydrogen. Once this power is known, a Fokker-Planck calculation is done to determine the evolution of the hydrogen distribution function and the amount of power collisionally transferred to the electrons and deuterium. The electron and deuterium temperature and density profiles are assumed fixed, i.e., transport and Fokker-Planck calculations are not carried out for them. Several other effects are also treated, including neoclassical transport of the hydrogen and losses caused by unconfined orbits, ripple diffusion, asymmetric drag, and charge exchange.

A simplified discussion of the theory on which FPPRF is based follows. The starting point is the drift kinetic equation:

$$\left[\frac{\partial}{\partial t}+\underbrace{\mathbf{v}_{D\perp}\cdot\frac{\partial}{\partial \mathbf{x}_\perp}}_{\equiv -Xf_0}+v_\parallel\frac{\partial}{\partial l}+\underbrace{\frac{q}{m}E_\parallel\left(1-\frac{Z}{Z_{\text{eff}}}\right)\frac{\partial}{\partial v_\parallel}}_{\equiv -Vf_0}\right]f_0=Cf_0+Qf_0+Sf_0 \quad (4.4.1)$$

where f_0 is the zero-order distribution function (no RF perturbations), $\mathbf{v}_{D\perp}$ is the particle guiding-center drift velocity, $v_\parallel$ is the velocity and l is the arc length along the guiding-center drift orbit, C is the Fokker-Planck collision operator, and Q is the resonant part of the RF quasilinear diffusion operator. The velocity coordinates are usually expressed in terms of the particle energy E and magnetic moment μ via

$$\frac{1}{2}mv_\parallel^2=E-\mu B \quad (4.4.2)$$

$$\mathbf{v}_{D\perp}=-v_\parallel\hat{\mathbf{b}}\times\nabla\frac{v_\parallel}{\Omega} \quad (4.4.3)$$

The term Sf_0 includes sources and sinks of particles (not necessarily all of which depend on f_0) such as charge-exchange, and an artificial source imposed to maintain the density at the specified value (i.e., a simple model of re-cycling). Neutral beam injection can also be included in S as an option. The second term on the left-hand side of Eq. 4.4.1 represents radial transport processes such as neoclassical transport and ripple diffusion and is denoted by X, as indicated. In the version of FPPRF described in Ref. 120, the term X was not included. In the present version of

FPPRF this term is included but is not derived rigorously by including it in the bounce averaging described below. Instead, random-walk test-particle arguments were used to obtain simple models for neoclassical diffusion, asymmetric drag, and ripple diffusion. The effect of a parallel Ohmic electric field is denoted by V. The next step is to perform a bounce-averaging operation on each term in Eq. 4.4.1. This operation is defined as $\langle\rangle \equiv \oint \frac{dl}{v_\parallel}$, and is an average over the particle guiding-center trajectory that is weighted by the amount of time the particle spends at each point. Performing the bounce averaging operation yields an equation of the form

$$\frac{\partial}{\partial t} f_0 = \langle C f_0 \rangle + \langle Q f_0 \rangle + \langle S f_0 \rangle + \langle V f_0 \rangle + \langle N f_0 \rangle + \langle R f_0 \rangle + \langle A f_0 \rangle \qquad (4.4.4)$$

For the first four terms, the bounce average in Ref. 120 is performed in the zero-banana-width limit, in which the integration is performed on the flux surface containing the banana tips, ignoring the fact that the particle actually drifts away from the flux surface during an orbit transit. Because of this, the asymmetric drag effect is not included in $\langle C f_0 \rangle$, and instead is represented by the additional term $\langle A f_0 \rangle$ on the right hand side. The terms $\langle N f_0 \rangle$, and $\langle R f_0 \rangle$ are intended to show that the X operator can be separated into a neoclassical diffusion operator N and a ripple diffusion operator R. In principle, these radial transport terms can be derived by performing the bounce average as suggested in Eq. 4.4.4. Such a derivation has recently been done by C. S. Chang, G. W. Hammett, and R. J. Goldston[125]. However, in the present version of FPPRF radial transport is modeled using random-walk test-particle arguments. The treatment of asymmetric drag and neoclassical transport in this manner can be found in Section 4 of Ref. 126, and the treatment of ripple diffusion can be found in Ref. 115.

Finite orbit width effects are not important in $\langle Q f_0 \rangle$ because absorption is localized at the banana tips, and they are not important for $\langle V f_0 \rangle$ because that term is quite small to begin with. The contributions from charge exchange in $\langle S f_0 \rangle$ are calculated in the zero-banana-width limit when solving Eq. 4.4.4, but finite-banana-width effects are included when simulating the charge-exchange spectrum. Terms describing direct RF-driven radial diffusion are not included in FPPRF. Derivations of these terms were done by Chen, *et al.*[126], and it was shown that these terms were generally negligible. Thus, flux surfaces are decoupled from each other when only the first four terms are retained, and radial transport is included in the last three terms. Eq. 4.4.4 is essentially the equation solved by FPPRF. It is two-dimensional in velocity space ($v_\perp^2$ and $v_\parallel$ or E and μ) and one-dimensional in physical space (r). Explicit expressions for the first four operators in Eq. 4.4.4 can be found in Ref. 120.

The non-ideal effects included are unconfined orbits, asymmetric drag, TF ripple diffusion, and charge-exchange losses. Unconfined-orbit loss occurs when a particle gains sufficient energy that its banana-orbit width increases to the point where the orbit intersects the limiter radius, at which point it is assumed to be lost from the plasma. This effect is included in the Fokker-Planck calculation by imposing the boundary condition $f(E_{\text{Loss}}) = 0$, where E_{Loss} is the energy at which the orbit becomes unconfined. Note that this boundary condition is a function of μ because the energy E_{Loss} is dependent on pitch angle. This pitch-angle dependence is included when the boundary condition is imposed. Asymmetric drag occurs when a banana orbit is large enough that the plasma parameters (density and temperature) vary significantly over the particle trajectory. For example, a particle initially banana-trapped at a small minor radius can absorb RF energy, causing the banana orbit to widen so that the particle travels through the outer portions of the plasma on the outside part of the orbit. In the outer part of the plasma, where the plasma is cooler and more collisional, the particle can lose significant energy so that its orbit becomes narrow again. Since the particle is at the outside part of the orbit when the banana width decreases, this causes the banana tips, and thus the flux surface about which the orbit is centered, to move outward. The TF ripple effect included in FPPRF is only the diffusion effect caused by non-closing of the drift orbits, and not the more severe ripple-trapping effect to which the truncation of the ion distribution function in Alcator C has been attributed.

In order to render the calculation computationally feasible, the following procedure is followed. The time span over which the simulation is to be performed is first divided into a number of intervals (typically 40 for the calculations described herein). Over each time interval, FPPRF first advances the distribution function by solving the equation

$$\frac{\partial}{\partial t} f_0 = \langle C f_0 \rangle + \langle Q f_0 \rangle + \langle S f_0 \rangle + \langle V f_0 \rangle \tag{4.4.5}$$

By keeping only these four terms, the flux surfaces are decoupled. The plasma is divided into a number of radial shells (typically 10) and Eq. 4.4.5 is solved separately on each shell. Then, starting with the value of f_0 determined from Eq. 4.4.5, another integration is performed over the same time interval using the equation

$$\frac{\partial}{\partial t} f_0 = N f_0 + R f_0 + A f_0 \tag{4.4.6}$$

(The bounce averaging operation $\langle\rangle$ is not shown in Eq. 4.4.6 to emphasize the fact that these operators were not really obtained from a rigorous bounce-averaging procedure.) The value of f_0 determined by Eq. 4.4.6 is then used as a starting value

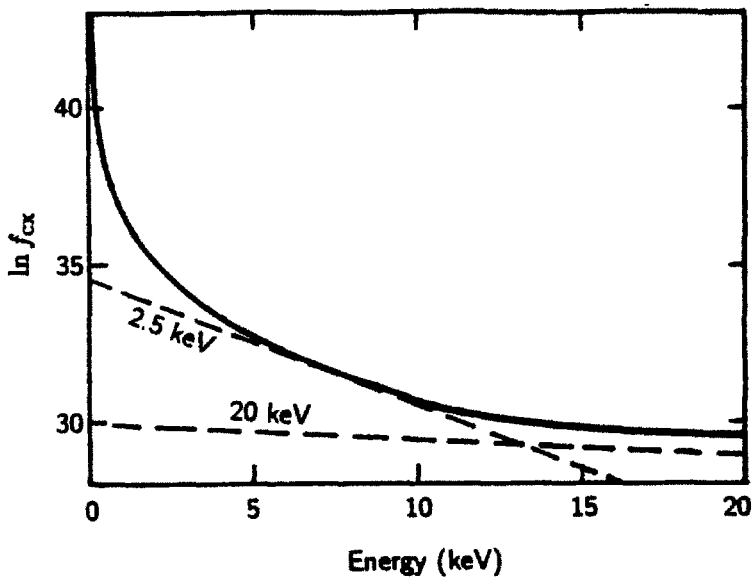

Figure 4.4.1: FPPRF CX Simulation for Low-Density Case—The charge-exchange neutral flux that would be seen by a perpendicularly viewing analyzer is shown as a function of energy for the low-density case. If ripple trapping is not accounted for, then the predicted tail temperature is $T(\infty) = 62$ keV. At $E = E_c \approx 20$ keV, the inferred T_{eff} would be 20 keV. For energies in the range $E \lesssim 10$ keV, which were seen in the experiment, the inferred T_{eff} is only 2.5 keV. In general, any time the actual central temperature is not much less than the energy at which the charge-exchange spectrum is fitted, the inferred temperature will not be an accurate indication of the real central temperature.

for the next time interval, and to infer a hydrogen tail temperature to be used in SHOOT to update Q for use in the next iteration of Eq. 4.4.5. This sequence is repeated for each time interval.

The fact that FPPRF does not properly treat the ripple trapping effect makes interpretation of the results somewhat complicated. Fortunately, while the omission of ripple trapping is expected to result in significant overestimation of the high-energy part of the distribution function, it appears that the calculation of P_{HD} is still approximately correct. To understand why this might be so, begin by considering the FPPRF charge-exchange simulation for the low-density case shown in Fig. 4.4.1. The quantity called f_{cx} is given by Eq. 1.4 in Ref. 120. The quantity $J_{cx} \equiv v f_{cx}$ is the velocity distribution of the neutral flux that would enter a charge-exchange detector and thus, except for an area element factor and an instrument calibration factor, is a simulation of the signal that would be produced by a charge-exchange neutral analyzer. In general, this signal contains contributions from all points along the detector sight line, although it is usually assumed that the high-energy part of the signal comes from an area localized at the part of the sight line nearest the plasma center.

The point to be made here is that this assumption is invalid for the measurements made during the Alcator C ICRF experiments. In order for this assumption to be true, it is generally necessary to look at high energies ~3–10 times the central ion temperature[120]. In the Alcator C experiments, the energy range for the fit was 4–8 keV while the inferred ion temperatures were in the range 2–10 keV, with a few cases that were significantly higher. Thus, even the *inferred* temperatures were too high for the range seen by the charge-exchange analyzer. In this case, the actual temperatures at the plasma center would have to be considerably higher than the inferred temperature, assuming that the distribution function is in fact Maxwellian. It is also true that, unless the actual hydrogen temperature is $\lesssim T_e$, the resulting distribution function is only Maxwellian in shape for energies in the range $E \gg E_c$, which does not include the energy range observed in the experiment. Thus, it is likely that the actual distribution function present at the plasma center is both distorted in shape and truncated due to ripple trapping.

The results of the FPPRF charge-exchange simulation are plotted in Fig. 4.4.1 for energies up to 20 keV, which is the energy E_c at which ion drag equals electron drag. The actual minority temperature at $r = 0$ determined by FPPRF for this case is 62 keV but, as was previously mentioned, it is necessary to fit to energies $E \gg E_c$ in order to measure it. For example, as shown in Fig. 4.4.1, a fit at $E = E_c \approx 20$ keV yields $T_H = 20$ keV and a fit in the same energy range used for the measurements in the experiments yields $T_H = 2.5$ keV.

Since the charge-exchange spectrum is probably not a good measure of the central minority temperature in this energy range, there are really only two conclusions that can be drawn from the charge exchange measurements: (a) there are probably high-energy ions up to $E = E_{\rm tr}$ (the estimated truncation), and (b) there are no high-energy ions at energies greater than $E = E_{\rm tr}$. A reasonable approximate model for the behavior of the distribution function would then be to assume a minority temperature $T_H = E_{\rm tr}$ for all cases where FPPRF predicts a minority temperature in excess of this value. The distribution function is then being approximated by a Maxwellian $f(E)$ whose value is down by $1/e$ times the peak value at $E = E_{\rm tr}$.

It is well-known that the Fokker-Planck drag force from slowing down of suprathermal ions on a background plasma composed of electrons and ions is as shown in Fig. 4.4.2. This result can be obtained analytically by assuming that the deuterium is cold ($T_D = 0$, use a delta function for $f_D(v)$) and that the electrons are hot ($v_{thH} \ll v_{the}$) and evaluating the drag terms in the Fokker-Planck collision operator. These approximations are well satisfied for the energy range of interest here. It turns out that $E_{\rm tr} \approx E_c$, with the approximation being pretty rough at low density, but improving at higher density. Thus, the suprathermal ions which

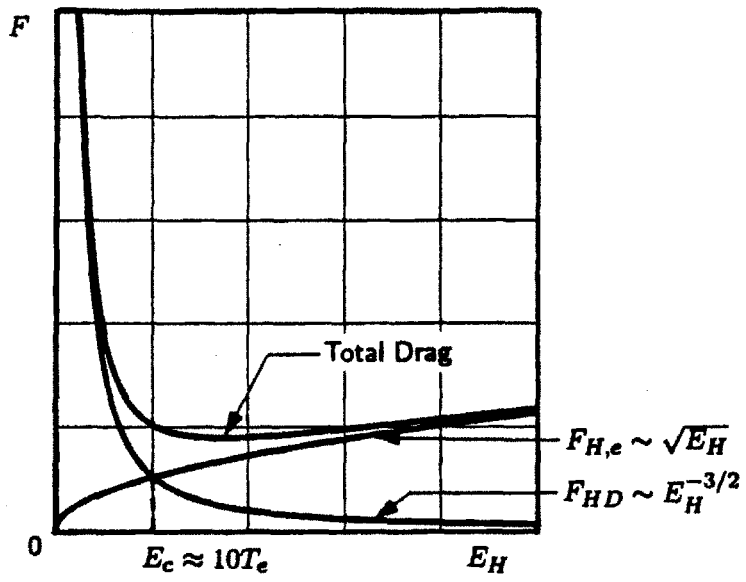

Figure 4.4.2: Kinetic Friction Drag Force for Fast Ions—This generic calculation comes from an analytic approximation in which the bulk ions are assumed to be "cold" and the fast "test particle" has a velocity significantly less than the electron thermal velocity.

produce the dominant contributions to P_{HD} are those that are least affected by ripple trapping. Moreover, the neoclassical transport and asymmetric drag effects treated by FPPRF cause higher-energy suprathermal ions to spread out to larger minor radii, so that the ultimate effect on deuterium heating from their contributions to P_{HD} is reduced. Also, when these higher-energy ions spread out to larger minor radii, the electron temperature and thus E_c is smaller there, so their contribution to ion heating is further reduced. Thus, it appears that the best way to run FPPRF for Alcator C is to simply forget about ripple trapping, and ignore the P_e calculated by the code, which is not needed anyway since the electron power balance is not being modeled.

It is possible to demonstrate this effect when running FPPRF by lowering the value of the plasma current to a level at which unconfined orbit loss occurs at the assumed ripple-trapping truncation energy. That is, the plasma current is selected by requiring that the width of a banana orbit at $E = E_{tr}$ be equal to the plasma minor radius. This is done using the equation on page 83 of Ref. 120. This equation does not depend on the large-aspect-ratio approximation often used in the calculation of the banana width, but instead uses the model for the plasma current profile discussed in Sec. 3.8. Before examining the results of this test, first consider the following simple isotropic analytic treatment. If each species is considered to have an isotropic Maxwellian distribution, then the collisional exchange power between

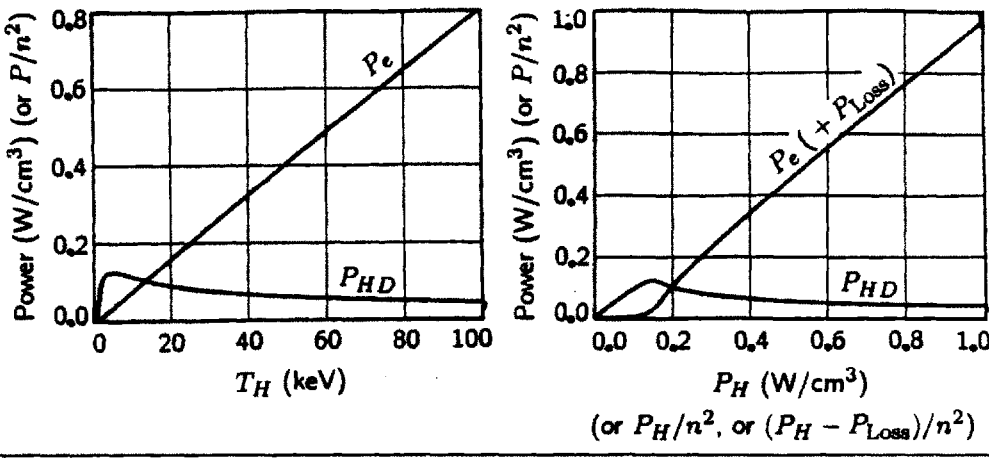

Figure 4.4.3: Simple Analytic Collisional-Exchange Model—Equations 4.4.8, 4.4.9, and 4.4.11 are evaluated using $n = 1$, $\eta_H = 0.5$, and $P_{\text{Loss}} = 0$.

two species (α and β) is given by

$$P_{\beta\alpha} = 4\sqrt{2\pi}\left(\frac{q_\alpha q_\beta}{4\pi\epsilon_0}\right)^2 \frac{\sqrt{m_\alpha m_\beta}(T_\beta - T_\alpha)}{(m_\alpha T_\beta + m_\beta T_\alpha)^{3/2}} \lambda_{\alpha\beta} n_\alpha n_\beta \tag{4.4.7}$$

Since the density dependence in Eq. 4.4.7 is very simple, it is helpful to express the ratio P/n^2 as a function only of T in practical units as follows:

$$\frac{P_{HD}}{n^2} = 2.4\eta_H \frac{T_H - T_D}{(T_D + 2T_H)^{3/2}} \tag{4.4.8}$$

$$\frac{P_e}{n^2} = \frac{\eta_H}{25.3} \frac{T_H - T_e}{(T_e + T_H/1836)^{3/2}} \tag{4.4.9}$$

where all powers are in W/cm^3, n is the local electron density in $10^{20}\,\text{m}^{-3}$, η_H is the hydrogen concentration in percent, and all temperatures are in keV. The type of power balance analysis that FPPRF does can then be modeled by

$$P_H = P_{HD} + P_e + P_{\text{Loss}} \tag{4.4.10}$$

or, equivalently,

$$\frac{P_H}{n^2} - \frac{P_{\text{Loss}}}{n^2} = \frac{P_{HD}}{n^2} + \frac{P_e}{n^2} \tag{4.4.11}$$

where one can model a variety of different density cases with a single calculation if the results are written in terms of P/n^2.

The results of this simple isotropic model are plotted in Fig. 4.4.3. They were calculated using $P_{\text{Loss}} = 0$, and $\bar{n}_e = 1 \times 10^{20}\,\text{m}^{-3}$. If variation of the electron

temperature with density is neglected, then other densities can be modeled by replacing any power quantity (P in W/cm^3) by P/n^2 with P in W/cm^3 and n in units of 10^{20} m^{-3}. From Eq. 4.4.3, one can see that P_{HD} is very weakly dependent on T_H or P_H and cannot exceed a certain limit under any circumstance. (Note, however, that this limit is directly proportional to η_H which is not known very accurately.) However, there is a significant peak in the P_{HD} curve for values of T_H in the vicinity of the assumed truncation energy. Thus, one might suspect that P_{HD} is underestimated by blindly taking the value as given by FPPRF. An analogous treatment with the isotropic approximation would be to use the second plot in Fig. 4.4.3 by assuming the electron power to be a measure of the quantity $P_e + P_{\text{Loss}}$ at some given P_H while P_{HD} is independent of P_{Loss} so long as P_H is held fixed. A more reasonable treatment would be to subtract P_{Loss} from P_H first, and then use the values of P_e and P_{HD} that correspond to this reduced value of P_H. That is, the difference between these two treatments is whether P_{Loss} is subtracted from P_e or P_H. These two treatments yield approximately the same results if $P_e \approx P_H$, which is true except at very low values of T_H.

One might try to argue that the uncertainty introduced is comparable to that resulting from the uncertainty in the measurement of η_H (a true statement), but it is actually possible to do better than this. In fact, an attempt to model this effect with FPPRF be reducing the plasma current suggests that the significant peak in P_{HD} in the isotropic approximation is not realistic. The reason for this is that the distribution function is highly anisotropic. In Fig. 4.4.4, the minority distribution function is calculated for the low-density case using the actual plasma current and several lower values. Although this technique does not exactly reproduce the desired correspondence between truncation energy and fitted temperature, it is possible to eliminate most of the electron power without seriously affecting the deuterium power.

In Fig. 4.4.4(a), using the full plasma current, the inferred values of $T_\perp$ and T_{peak} are well above the T_H corresponding to the peak P_{HD} in Fig. 4.4.3, but the inferred value of $T_\parallel$ is near the peak. When plasma current is lowered, $T_\perp$ decreases towards the value corresponding to the peak in Fig. 4.4.3 while $T_\parallel$ decreases away from it, and it turns out not to make much difference in the inferred value of P_{HD}. In Fig. 4.4.4(b), with $I_P = 45$ kA, the value of $T_\perp$ is equal to the ripple-truncation energy but the actual truncation from the artificially enhanced unconfined-orbit loss is somewhat higher. The value of P_{HD} increases only slightly from 17 to 19 kW while P_e is significantly reduced. In Fig. 4.4.4(c), with $I_P = 40$ kA, the value of T_{peak} is equal to the ripple-truncation energy, P_e is further reduced, and P_{HD} is unchanged. Intuitively, one can think of the calculations in the anisotropic case

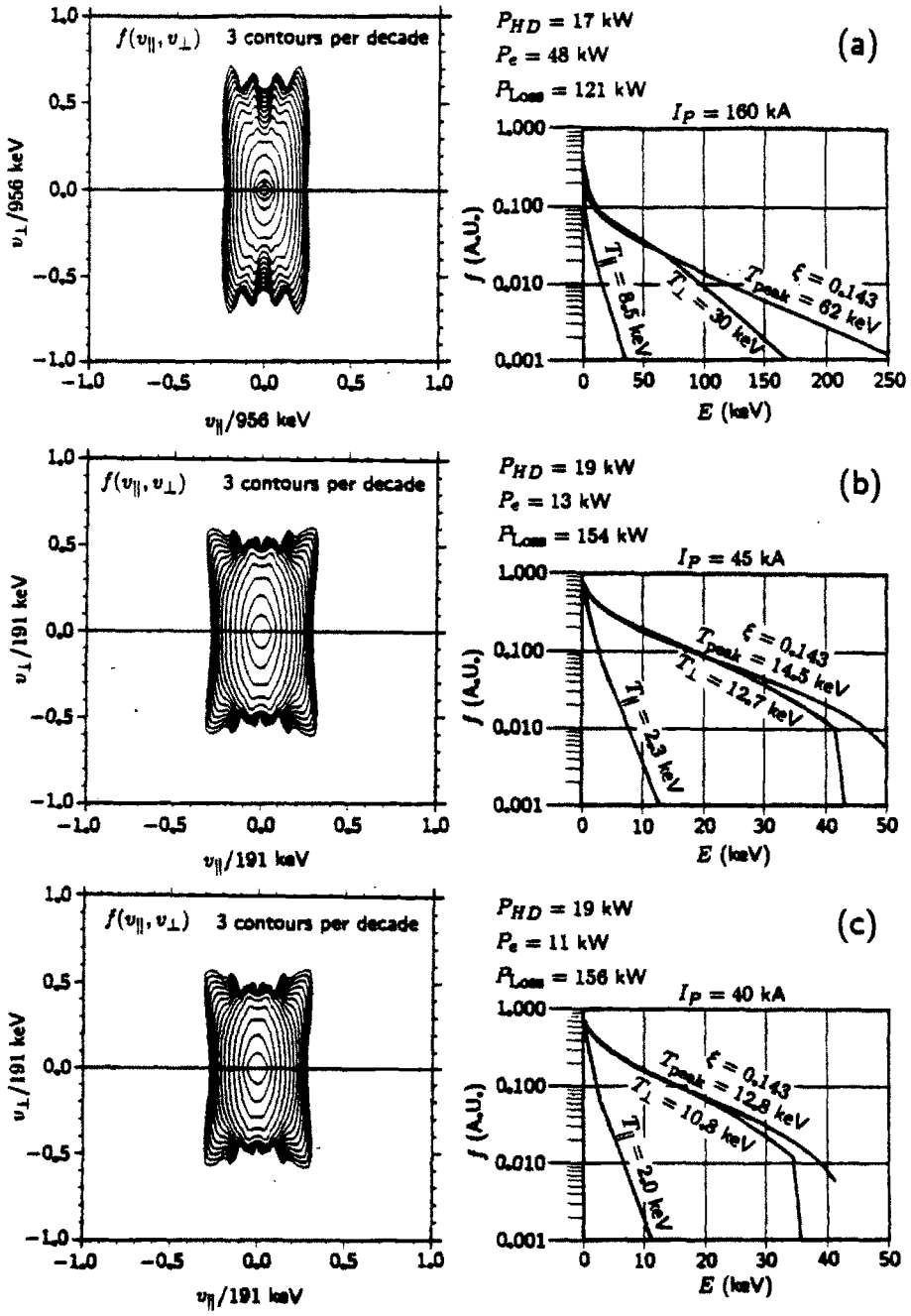

Figure 4.4.4: Truncation of Distribution Function by Reduced Plasma Current—The actual central distribution function (not CX simulation) is shown for the low-density case as calculated by FPPRF using the actual plasma current ($I_P = 160$ kA) and four lower values of I_P. The notation $v_\perp/956$ keV means that $v_\perp$ is normalized to the velocity given by $v = \sqrt{2E/m}$ where $E = 956$ keV is the highest energy considered in the calculation.

as averages over a range of energies of the calculations from the simple isotropic

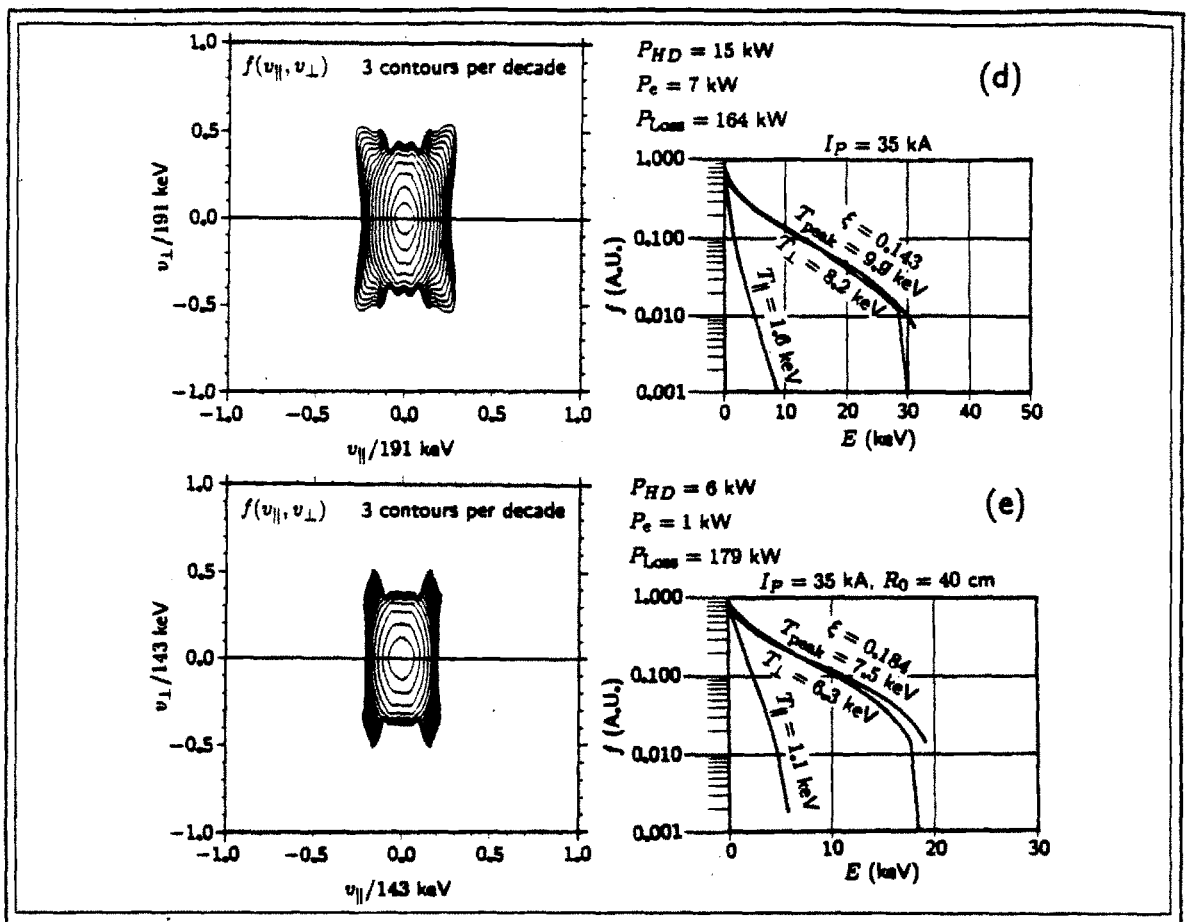

Figure 4.4.4: Truncation of Distribution Function (continued)—Radial "cross-sections" of the distribution function and corresponding temperature fits are given for the parallel direction, the perpendicular direction, and the direction for which the fitted temperature is maximum. The value $\xi = v_\parallel/v$ (the cosine of the pitch angle) which corresponds to this maximum is indicated.

approximation. Further increases in unconfined-orbit loss in Figs. 4.4.4(d) and (e) result in reduced values for P_{HD}. In Fig. 4.4.4(e), further truncation was obtained by reducing the major radius rather than plasma current. (This results in more banana-trapped particles, which have wider drift orbits.)

There was concern that this technique of reducing the plasma current would also significantly increase the neoclassical transport. This was easily investigated by turning off the neoclassical transport part of the calculation, which made only a ~ 1 kW difference in the inferred values of P_{HD} and P_e. Thus, the primary effect of ripple trapping appears to be a shift of power from P_e to P_{Loss}, with only a small change in P_{HD}. The profile shapes $P_{HD}(r)$ are also similar for the cases of full and reduced plasma current. Note that changing the plasma current this way will distort the shape of the drift orbits and change the orbit bounce and transit frequencies. Because of these considerations, it is felt that the best way to model

Alcator C with FPPRF is to use the actual plasma current in the simulation, and not worry about ripple trapping. One should keep in mind that when values for P_e are given in this chapter, those powers are likely to be predominately losses due to ripple trapping.

Finally, recall the estimate of P_{HD} directly from the charge-exchange data taken during the radial scan described in Sec. 3.4. From these data, it was estimated that the collisional exchange power P_{HD} for the inner portion of the plasma ($r \lesssim 7$ cm) was ~ 8 kW. This number is entirely consistent with the results of the FPPRF calculations. It is clear that FPPRF is not ideally suited for these calculations, because this code contains a great deal of computational overhead involved in determining the exact angular dependence of the distribution function while it lacks the ability to model the most important loss mechanism in Alcator C. The purpose for which FPPRF was originally developed was to explain the "negative-temperature" features seen in the PLT CX spectrum for certain tangential viewing angles[120]. For that purpose, an accurate calculation of the angular dependence is important. On the other hand, ripple-trapping is not important in PLT because the toroidal-field ripple magnitude is not strong enough in that machine to form local magnetic wells along the field lines. This suggests an idea for a new code with features specifically chosen for the purpose of analyzing experimental heating data. Rather than perform a full 2-velocity-dimentional Fokker-Planck calculation, the distrubution could be represented by a truncated spherical harmonic expansion, as was done in Ref. 88. Stix's treatment could be extended to include the same loss mechanisms that are included in FPPRF, including the ability to specify a truncation energy independent of any other input parameters (such as plasma current). For the treatment of high-density plasmas like Alcator C, CMOD, and CIT, an accurate calculation of the power deposition profile is essential. This could possibly be accomplished by solving the wave equation using the Hilbert-Schmidt technique suggested in Sec. 1.5 of this thesis and including an accurate antenna model in the calculation.

The simulation of ripple trapping also gives some assurance that the wave physics (SHOOT calculation) is not adversely affected by overestimating the minority temperature. The calculation of the wave fields is not expected to be erroneous because the cold-plasma screening of E_+ is insignificant regardless of whether the minority temperature is 10 keV or much higher. However, overestimation of T_H will probably result in an overly broad $P_H(r)$ profile. This is still not a problem, because the extra Doppler broadening of P_H is caused by suprathermal particles which slow down predominately on electrons (or, more likely, are lost), so that the resulting $P_{HD}(r)$ is still expected to be correct.

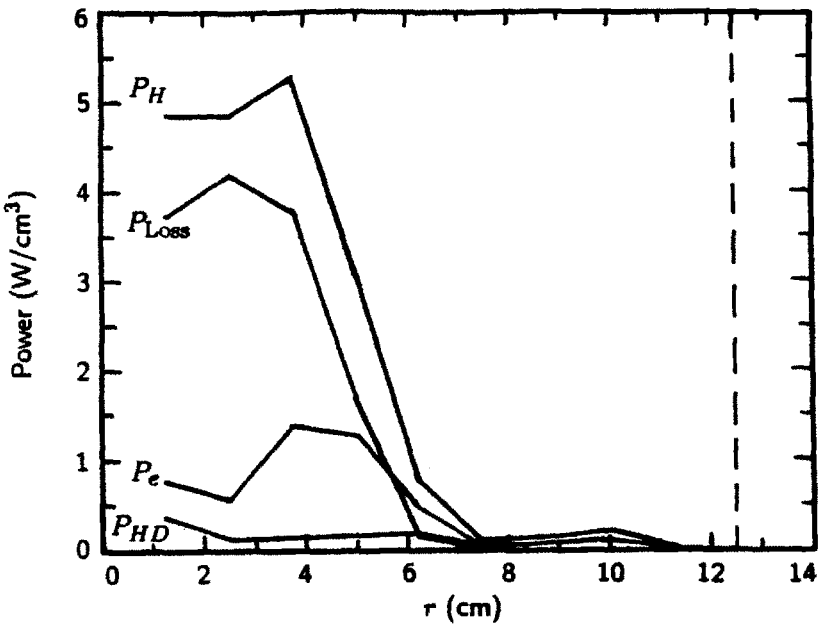

Figure 4.4.5: FPPRF Calculation for Low-Density Case—Hydrogen tail losses are extremely severe at low density. Only a small portion of the power absorbed by hydrogen is collisionally deposited on the deuterium. The resulting profile of $P_{HD}(r)$ is very broad. This calculation was done using $\bar{n}_e = 1 \times 10^{20}\,\mathrm{m}^{-3}$ and $P_{RF} = 220$ kW.

At high density, these considerations are much less important because then the tail temperatures determined by FPPRF are below the ripple-trapping truncation energy.

The FPPRF calculation for the low-density case is shown in Fig. 4.4.5. As expected, the loss mechanisms are extremely severe in this case, and only a small fraction of the power P_H absorbed by hydrogen is deposited on deuterium (P_{HD}). The deposited power P_{HD} has a very broad profile, comparable to the experimental results from the radial charge-exchange scan data, and is roughly uniform in r compared with the other power components. Note, incidentally, that the power P_e which is believed to be mostly lost due to ripple trapping, has a hollow profile, which is even more unfavorable. Even if this power were deposited on electrons, it would not be expected to have a large effect on the power balance. ($P_e \sim 60$ kW, hollow — $P_{OH} \sim 300$ kW, peaked)

The FPPRF calculation for the high-density case is shown in Fig. 4.4.6. The loss mechanisms are now much less severe, and P_{HD} is the largest component of P_H. The deposition profile is now much more centrally peaked, so much so that the coarseness of the radial grid is somewhat annoying. The power P_e, whose fate is not

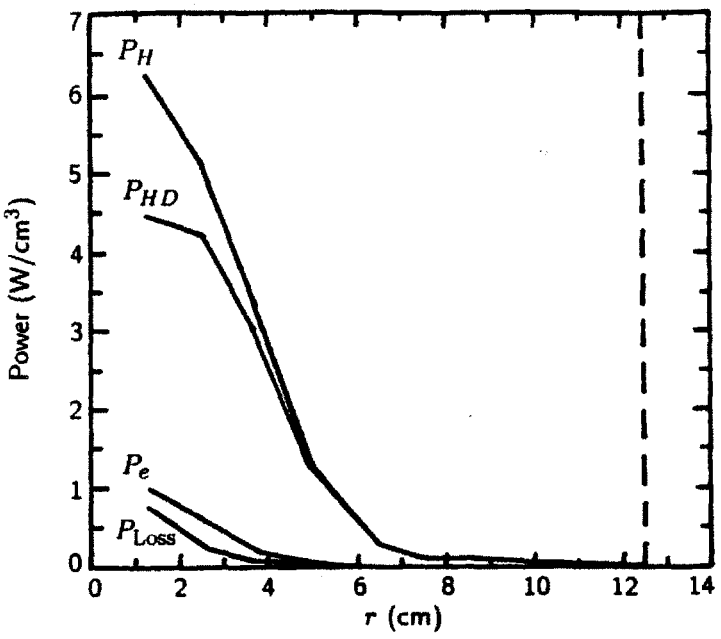

Figure 4.4.6: FPPRF Calculation for High-Density Case—Hydrogen tail losses are much less important at high density, compared to the low-density case. A majority of the power absorbed by hydrogen is deposited on the deuterium and $P_{HD}(r)$ is nicely peaked. This calculation was done using $\bar{n}_e = 4.5 \times 10^{20}\,\mathrm{m}^{-3}$ and $P_{RF} = 220$ kW even though the case of experimental interest has only $P_{RF} =$ 175 kW, to allow comparison with the calculation in Fig. 4.4.5. There is no significant difference in these profile shapes for 220 kW versus 175 kW.

conclusively resolved in these simulations, is negligible compared to the low-density case.

It is now possible to combine all the results from the Brambilla code, SHOOT, and FPPRF to construct estimates of the net power $P_{\mathrm{net}} = P_{HD} + P_D$ deposited on deuterium. Such results are shown in Fig. 4.4.7. It is interesting to note how large a part is played by the deuterium second harmonic absorption in both cases. For the low-density case, P_D is quite small compared to P_H (see Fig. 4.4.5), but, since the losses are so severe, P_D turns out to be comparable to P_{HD}. For the high-density case the losses are smaller, but P_D is larger, so P_D and P_{HD} still end up being comparable. The deposition is also much more favorably peaked at high density than at low density.

The power deposition profiles for a six-case density scan are shown in Fig. 4.4.8. The general trend is for P_D to be more sharply peaked than P_{HD} and for all profiles to become more peaked with increasing density, which is not surprising. These P_{net} profiles will be used for all $\eta_H = 0.5$ % shots to be analyzed with the ONETWO

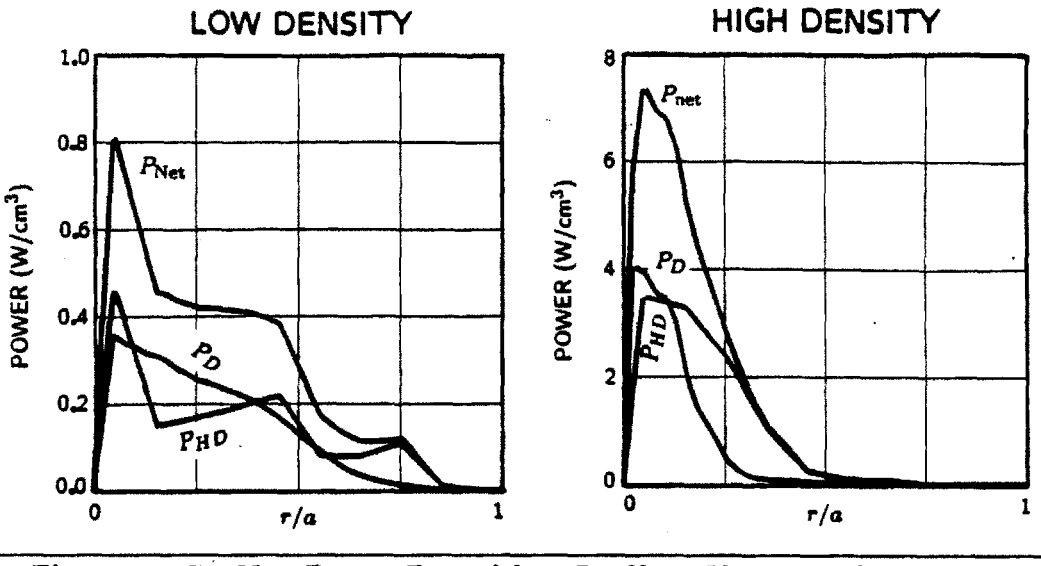

Figure 4.4.7: Net Power Deposition Profiles—The power deposition to deuterium, including contributions P_{HD} from collisional exchange with hydrogen and P_D from direct deuterium harmonic absorption is shown for both low and high-density cases. The contribution from P_D is significant in both cases. The reason for this, in the low-density case, where this would normally not be expected, is that most of the power absorbed by hydrogen is lost. The reason in the high-density case is because β is higher. These calculations were done using $\bar{n}_e = 1 \times 10^{20}\,\mathrm{m}^{-3}$ with $P_{RF} = 220$ kW for the low-density case, and $\bar{n}_e = 4.5 \times 10^{20}\,\mathrm{m}^{-3}$ with $P_{RF} = 175$ kW for the high-density case. The case for $P_{RF} = 220$ kW at high density is the $n_{e0} = 6 \times 10^{20}\,\mathrm{m}^{-3}$ case in the following illustration.

code in the next section. For shots with non-integral values of n_{e0} the assumed deposition profile will be obtained from an appropriate interpolation.

The entire process involved in constructing these power deposition estimates is summarized in Fig. 4.4.9. The ways in which the various power components add together to give the total power ($P_{RF} = P_D + P_H + P_{MC}$, $P_H = P_{HD} + P_e + P_{Loss}$, $P_{net} = P_D + P_{HD}$) are indicated. At low density, the losses are due primarily to unconfined orbits and ripple trapping, whereas at high density the losses are due primarily to mode conversion. As mentioned in Sec. 4.3, the highest two density points were calculated analytically, rather than using FPPRF. The reason for this is that the power density P_H/n^2 falls very close to the peak on Fig. 4.4.3. Because FPPRF SHOOT produces slightly narrower profiles than standalone SHOOT, a high-energy minority tail temperature of $\sim$ 15 keV was predicted. Standalone SHOOT, with the more accurate antenna current model, predicts a sufficiently lower power density that this tail would not be expected. It is felt that such a tail would be observable in the experiment if it had been present, but none was seen. Therefore, FPPRF, was replaced by the analytic calculation for these points, with the result

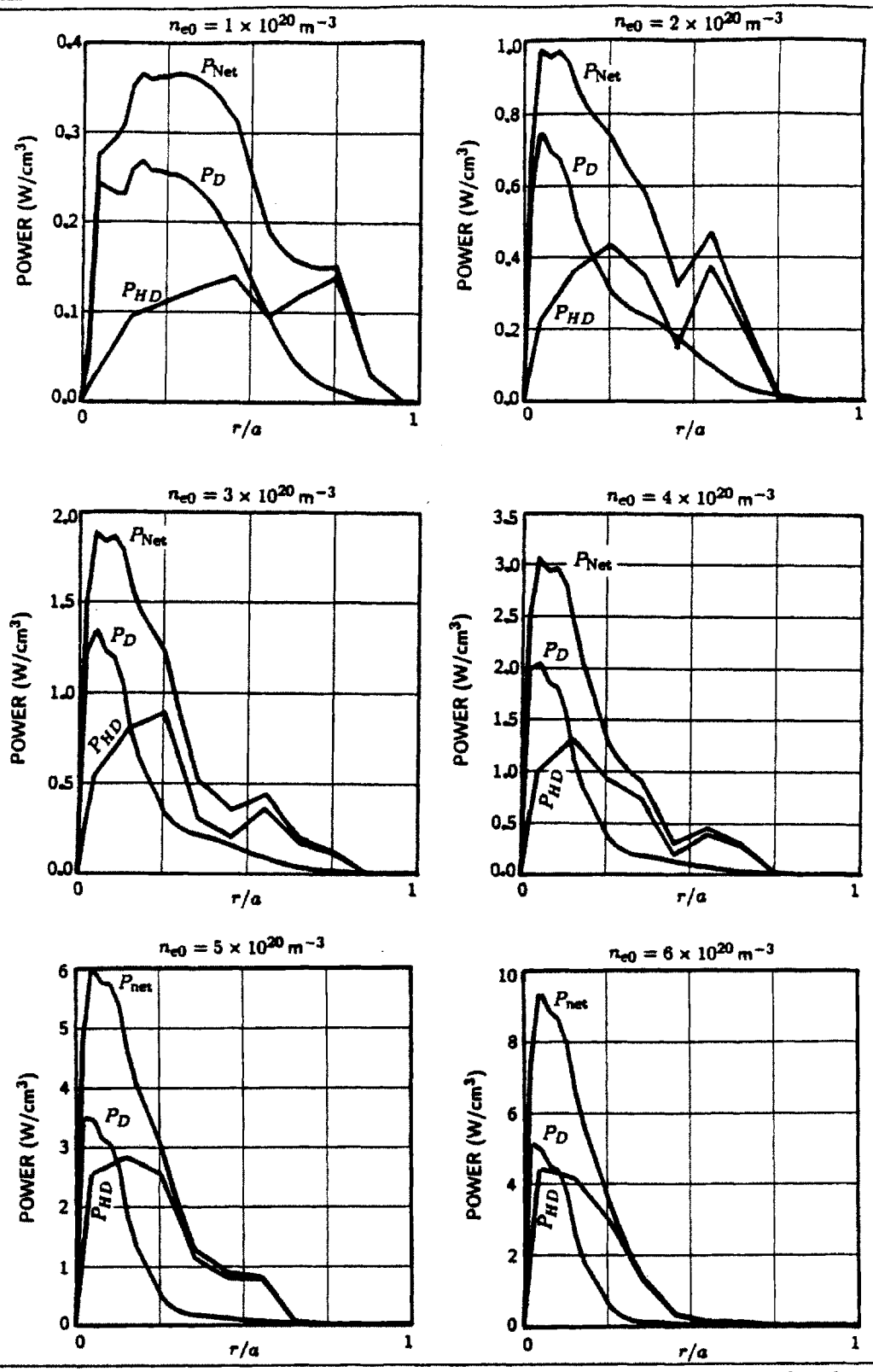

Figure 4.4.8: 1D Density Scan—Power deposition profiles are calculated at various densities assuming fixed launched RF power $P_{RF} = 220$ kW.

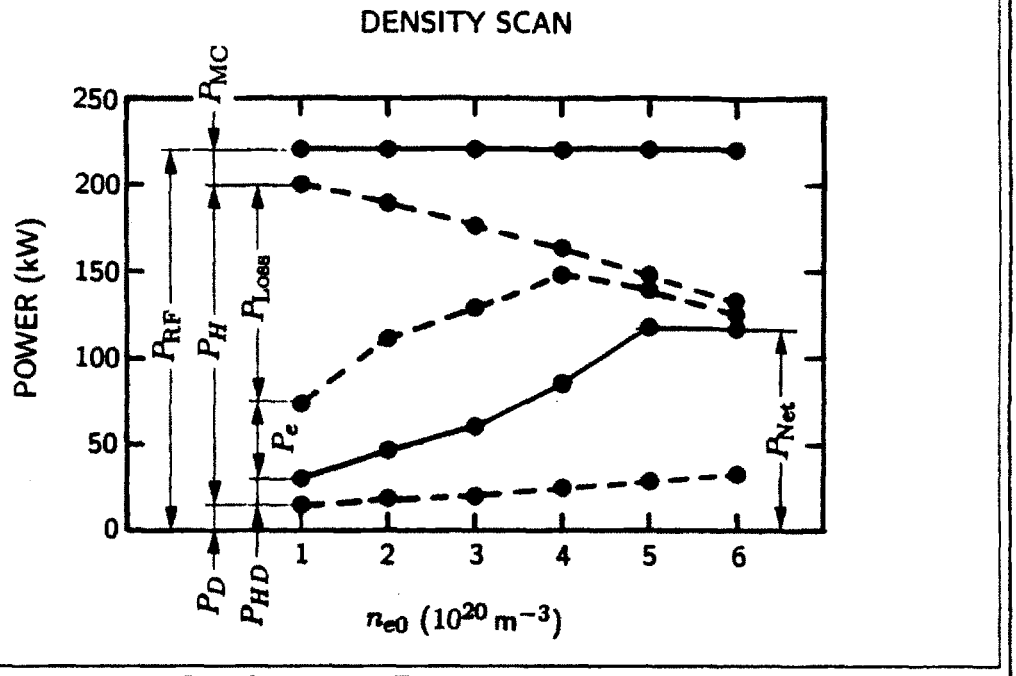

Figure 4.4.9: 0D Density Scan—The separation of the total RF power into the various channels is shown as a function of density.

that P_e and P_{Loss} are both reduced to negligible amounts at high density. However, if the RF power is increased by 20% above the value assumed here, then significant electron power P_e would be predicted by either FPPRF or the analytic model, and P_{HD} would not increase significantly for densities above 4×10^{20} m^{-3}.

After expending a major effort to come up with reasonable estimates of the power deposited to deuterium as a function of density, and modeling several different RF loss mechanisms, it is now clear that this in not going to explain the discouraging heating efficiencies observed at high density in the experiment. Although the loss mechanisms appear to be quite severe, their scaling with density is very favorable, and the profiles are nicely peaked at high density. In the ONETWO transport calculations to be done in the next section, it will be shown that there is an effect involving ion energy transport that scales unfavorably with density and is severe enough to account for the observed heating efficiency scaling in spite of the favorable scaling of the loss mechanisms.

Deposition profile calculations for a minority concentration scan are shown in Fig. 4.4.10. The parameters for this concentration scan were those of the low-density prototype case, in which only the minority concentration was varied. Numerical difficulties were encountered which made it impossible to run FPPRF for cases for which $\eta_H > 2$ %. The reason for these difficulties has to do with the way SHOOT and FPPRF calculate power deposition. SHOOT uses a dielectric tensor derived for

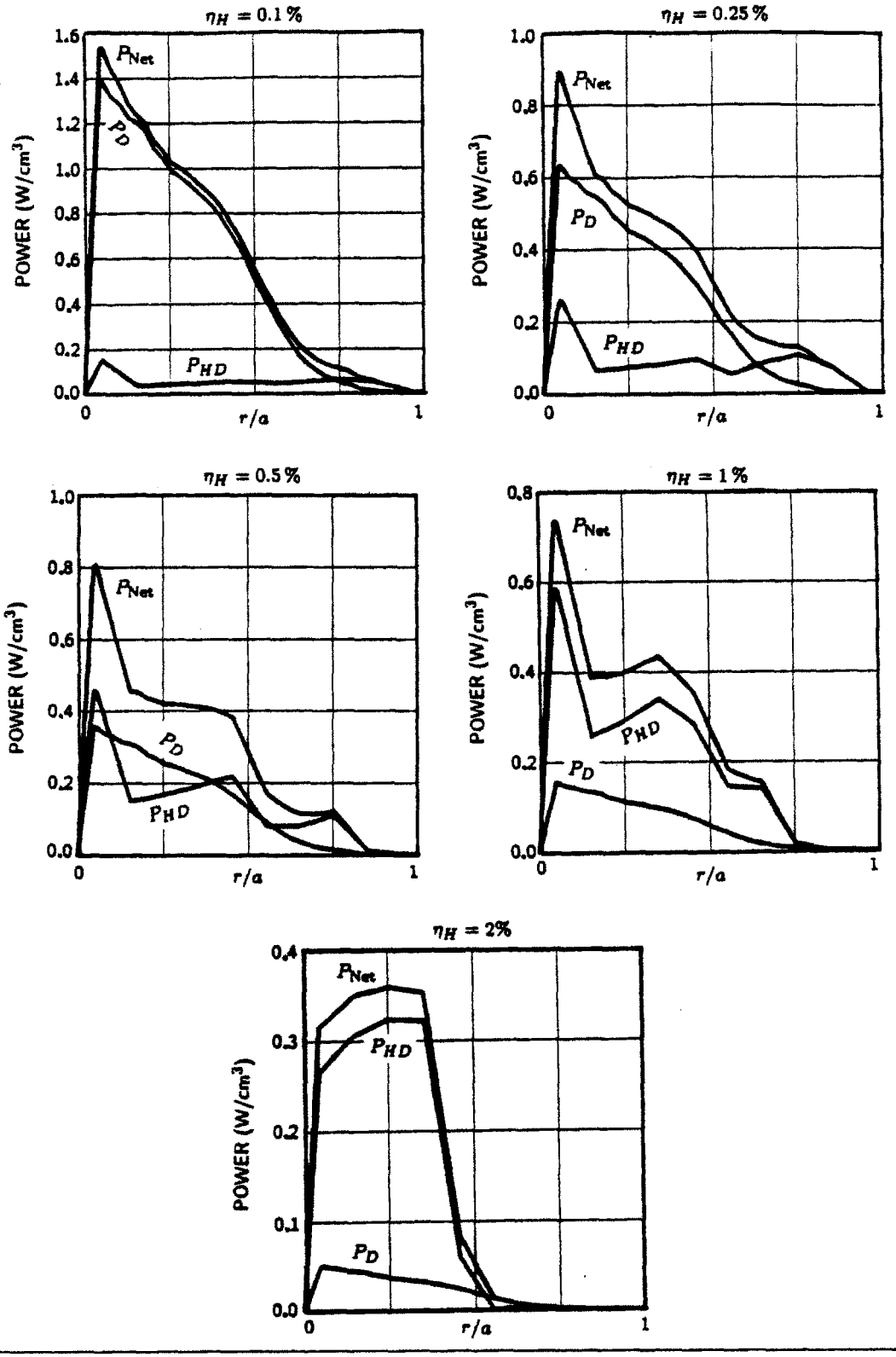

Figure 4.4.10: 1D Concentration Scan—These calculations were done for the low-density case at fixed RF power and density.

Maxwellian distribution functions and uses only leading order terms $\propto |E_+|^2$ to determine absorption. SHOOT first calculates the electric field components throughout the plasma based on the specified antenna current shape. Then P_H is calculated based only on E_+ and the electric field is scaled in magnitude in order to match the value of P_H specified as input to the program. On the other hand, FPPRF calculates absorption from the actual distribution function (initially a Maxwellian) but including terms from E_+ as well as supposedly smaller terms from E_-. As the minority concentration is increased, the magnitude of E_+ can become so small at the location of the cyclotron resonance that absorption is dominated by the E_- terms. Then SHOOT and FPPRF can disagree drastically about the amount of power that is being absorbed. FPPRF will then proceed to calculate a distribution function that is overly energetic. The contribution to absorption from E_+ may then begin to dominate, and it is possible for the algorithm to either converge to a steady state in which FPPRF and SHOOT power absorption calculations agree, or to converge to a steady state in which they disagree, or to diverge.

In spite of the inability to model all the cases that were attempted, enough seems to have been accomplished to offer an explanation as to why the heating efficiency in the experiment decreased monotonically with increasing minority concentration. From Fig. 4.4.10, one can see that as the concentration decreases to very low values, the loss mechanisms associated with hydrogen become increasingly severe, as one might expect. However, the contribution from deuterium second harmonic absorption increases to the point where it becomes dominant. Since the deuterium is not subject to such severe losses, the heating efficiency would be expected to increase.

As minority concentration is increased to higher values, one might expect that a less energetic minority tail would form, so that the losses would become less severe and the heating efficiency would increase. Inspection of the $\eta_H = 2$ % case in Fig. 4.4.10 shows this not to be the case. From Fig. 4.4.11, it is clear that the reason for this is that mode conversion increases drastically with minority concentration. Recall that the calculation of mode conversion is done using the Brambilla code, and that the interpretation of the results is least ambiguous at high minority concentration. This problem is obviously caused by the inability to produce an elevated minority temperature at high concentration. When this occurs, the E_+ shielding effect (from cold-plasma theory) is effective at the location of the cyclotron resonance, and there is not sufficient Doppler broadening to allow absorption at the hybrid resonance layer (where E_+ is enhanced). (The hybrid layer also moves farther away from the cyclotron resonance as concentration increases.) Thus, mode conversion will be favored.

The behavior of this power deposition model as a function of RF power is also of interest. The results of a power scan, using the parameters of the low-density

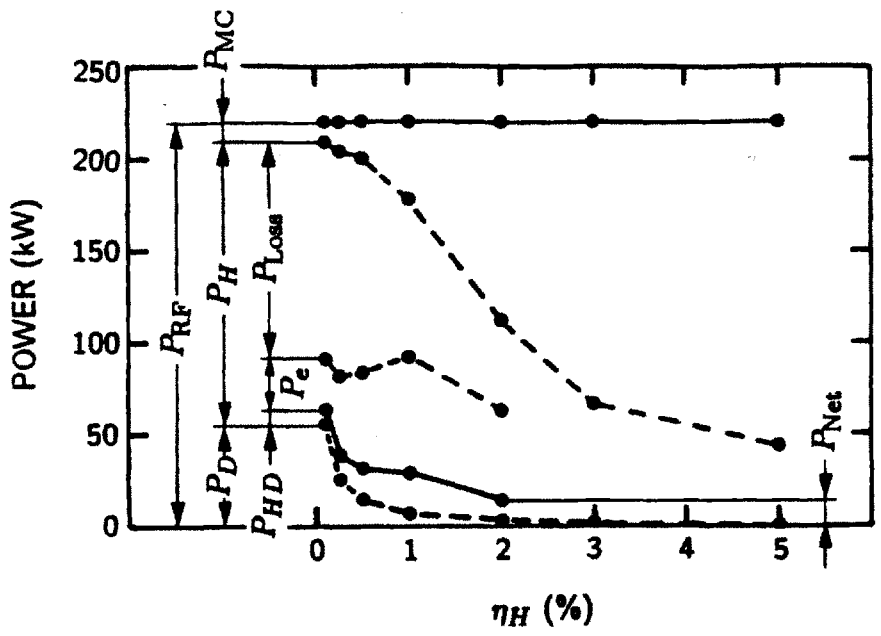

Figure 4.4.11: 0D Concentration Scan—The separation of the total RF power into the various channels is shown as a function of minority concentration. These calculations were done using fixed values $P_{RF} = 220$ kW and $\bar{n}_e = 1 \times 10^{20}\,m^{-3}$.

prototype case, are shown in Fig. 4.4.12. As one might expect, the loss mechanisms become more severe with increasing power. Note that an order-of-magnitude increase in launched RF power only increases the central power density by a factor of two. The deposition profile broadens significantly as power is increased, but the effect saturates as the losses become so severe that absorption is again dominated by deuterium second harmonic.

The effect in terms of bulk power quantities is shown in Fig. 4.4.13. This effect may explain some of the scatter in the experimental data. In the transport analysis to be done in the next section, most of the shots used will have P_{RF} between 200 and 300 kW, so this power dependent effect will not be very important.

4.5: Transport Analysis of Deuterium Heating

Having finally arrived at estimates for the RF deposition on deuterium P_{net}, it is now possible to analyze the deuterium power balance. This is done using the ONETWO transport code[127]. In this analysis, the electrons, hydrogen, and ICRF

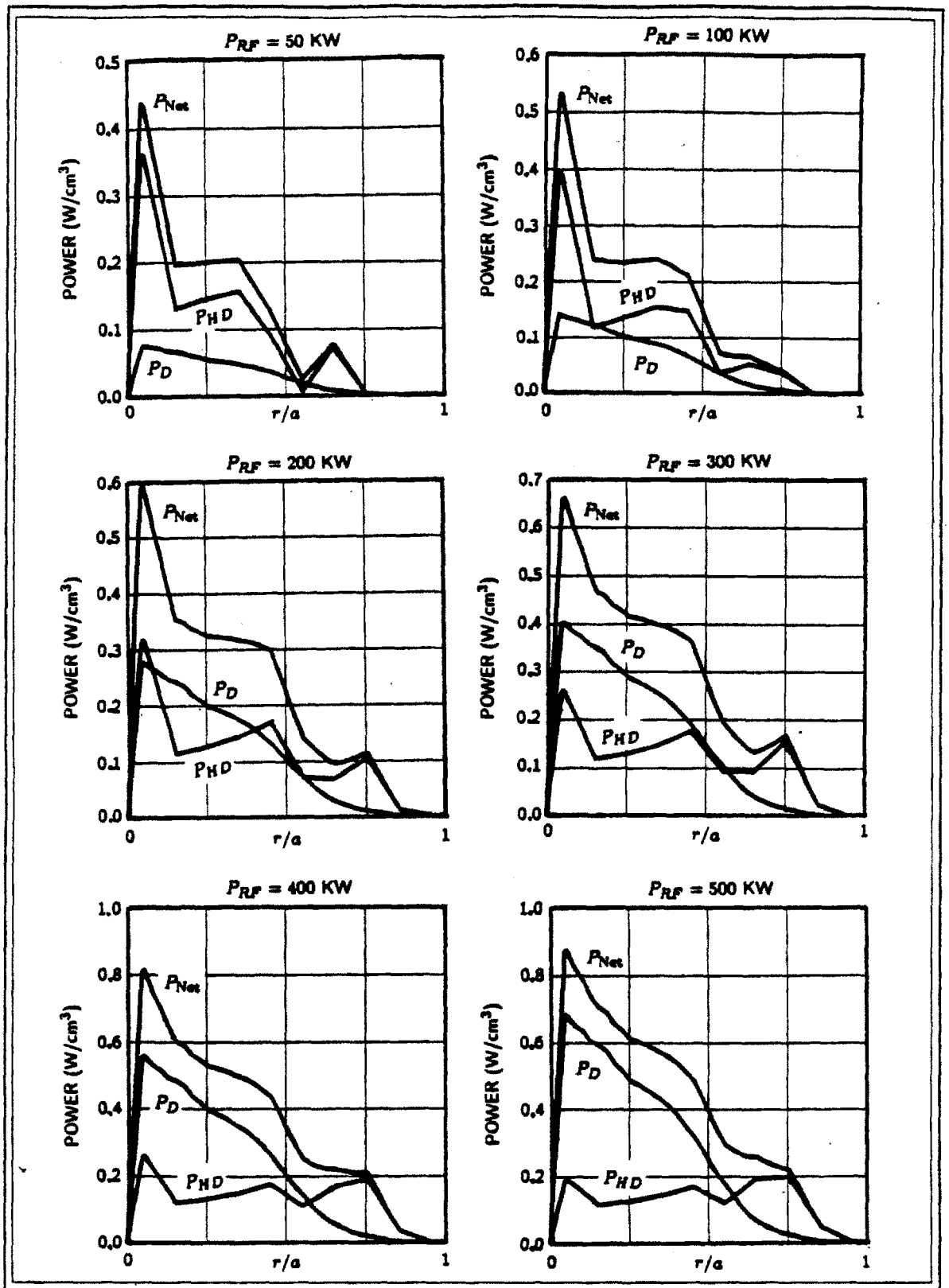

Figure 4.4.12: 1D Power Scan—These calculations were done for the low-density case at fixed density and minority concentration.

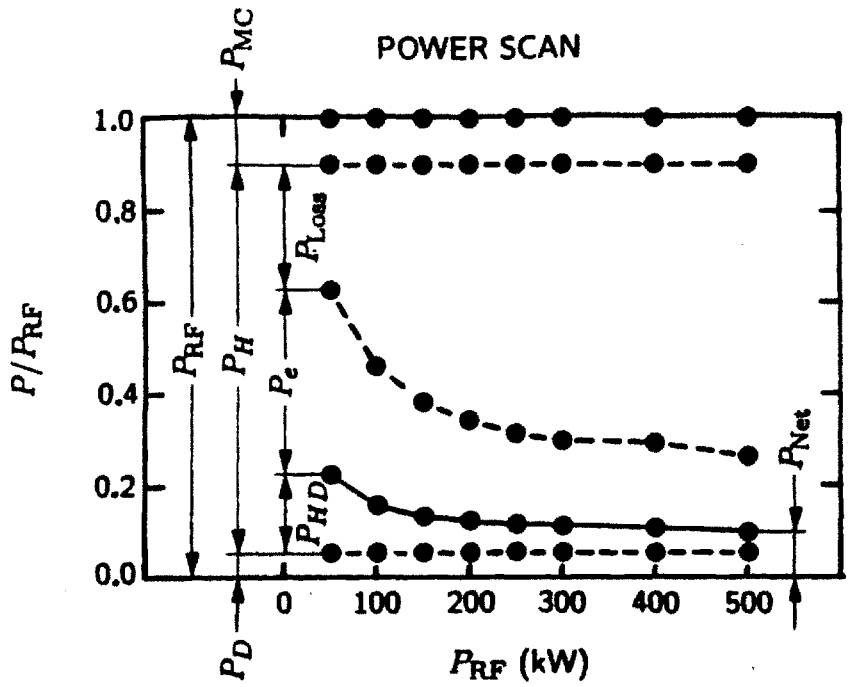

Figure 4.4.13: 0D Power Scan—The separation of the total RF power into the various channels is shown as a function of P_{RF}. These calculations were done using fixed values $\bar{n}_e = 1 \times 10^{20}\,\mathrm{m}^{-3}$ and $\eta_H = 0.5$ %.

will be treated as known sources of heating power for the deuterium (P_{eD}, P_{HD}, and P_D respectively). Then, several loss mechanisms associated with energy transport will be examined. The energy balance equation solved in these ONETWO runs is

$$\frac{3}{2}\frac{\partial}{\partial t}(n_D T_D) = \frac{1}{r}\frac{\partial}{\partial r}\left[r\left(n_D \chi_D \frac{\partial T_D}{\partial r} - \frac{5}{2} T_D \Gamma_D\right)\right] - \frac{\Gamma_e}{n_e}\frac{\partial}{\partial r}(n_D T_D) - P_{CX} + P_{eD} + P_{dep} \qquad (4.5.1)$$

The term on the left-hand side of Eq. 4.5.1 is the rate of increase of the thermal energy content of deuterium (i.e., the deuterium heating). The term containing χ_D is the heat transport due to thermal conduction, and the term containing Γ_D is the heat transport due to convection. The term containing Γ_e is the work done on the ions by the electrons as they flow against the ion pressure gradient. The loss due to charge exchange of deuterium ions with deuterium neutrals is denoted by P_{CX}, the heating source from collisions with electrons is P_{eD} and the net deposition of RF power on deuterium is P_{dep}. The electron flux Γ_e is determined from the equation

$$\frac{\partial n_e}{\partial t} + \frac{1}{r}\frac{\partial}{\partial r}(r\Gamma_e) = S_e \qquad (4.5.2)$$

where S_e includes the effects of ionization and recombination of impurities. The electron source rate S_e is calculated via a neutral transport package which is included as a subsystem of ONETWO. The boundary condition for this calculation is derived from an assumed global particle confinement time. The results of these analyses are insensitive to the exact choice of this parameter. A single impurity species is allowed in ONETWO, which was taken to be oxygen in the calculations to be presented in this chapter. Impurity transport is treated kinetically. The ion flux Γ_D is then determined from ambipolarity. All ion species, including impurities, are required to have the same temperature in ONETWO. This makes it impossible to include any realistic treatment of effects due to the presence of the minority species. This is not expected to be a problem since the minority concentration was small in all cases studied. For all of the cases analyzed, the conduction, electron collision, and RF deposition were the dominant terms. The convection, charge exchange, and work, though insignificant, were included in the calculations.

All the source and loss terms in Eq. 4.5.1 are evaluated according to appropriate models, using experimental data. For each experimental discharge that is analyzed, the evaluation is performed as a function of time, both during the Ohmic and RF heated portions of the shot, and the results are evaluated for consistency with and without RF. The experimental parameters used as input to the code are the electron temperature $T_e(r,t)$, electron density $n_e(r,t)$, toroidal field B_0, toroidal current $I_P(t)$, resistive loop voltage $V_R(t)$, fusion neutron production rate $R_f(t)$, and an assumed value of the central safety factor $q_0(t)$ (unity or slightly less depending on whether sawteeth were evident in the soft x-ray signal). The central electron temperature was taken from Thomson scattering data, and the profile shape was determined using the model discussed in Sec. 3.8. The electron density profile was determined by fitting a parabola raised to an adjustable power to the central density from Thomson scattering and the line-average density from the interferometer. The ion temperature and profile shape, and the current density profile shape were determined automatically and self-consistently by ONETWO. The Z_{eff} profile was fitted by a parabola raised to a power. The central and edge values of the profile were adjusted to match the specified resistive voltage and central safety factor, and the power to which the parabola was raised was chosen manually to be large enough to avoid values of Z_{eff} at the edge which would imply negative ion densities. The impurity charge state was determined from coronal equilibrium using the specified electron temperature, and the deuterium density was calculated from charge neutrality. Finally, both the central deuterium temperature and the deuterium temperature profile were determined by solving the ion heat transport equation (Eq. 4.5.1) assuming an ion thermal diffusivity of the form

$$\chi_D = W_{\text{neo}}\chi_D^{CH} + D_b f(q) \tag{4.5.3}$$

where χ_D^{CH} is the Chang-Hinton neoclassical diffusion coefficient[128, 129], which is multiplied by an adjustable scale factor W_{neo}, D_b is the Bohm diffusivity and

$$f(q) = \begin{cases} 1 - \frac{1}{1+(1/q-1)^2}, & q \le 1 \\ 0, & q > 1 \end{cases} \tag{4.5.4}$$

models the time-averaged effect of sawtooth activity. The contribution from D_b was found to be completely negligible in all cases studied. The neoclassical multiplier $W_{\text{neo}}(t)$ is adjusted dynamically so that a fusion neutron production rate calculation matches the experimental measurement. The electron-deuterium collisional exchange power was determined classically, from the expression

$$P_{eD} = \frac{3}{2} n_e \nu_{eD} (T_e - T_D) \tag{4.5.5}$$

where

$$\nu_{eD} = \frac{8\sqrt{\pi}}{3} \frac{m_e}{m_D} \left(\frac{e^2}{4\pi\epsilon_0} \right)^2 \frac{\lambda n_D}{\sqrt{m_e} T_e^{3/2}} \tag{4.5.6}$$

and the RF deposition to deuterium was calculated using the model developed in the preceeding sections of this chapter.

All of the parameter adjustments discussed in the preceeding paragraph are done by ONETWO using a PD (proportional-differential) feedback law in real time (i.e., transport time). The neoclassical multiplier W_{neo} is adjusted by comparing the calculated fusion neutron rate and its time derivative with the specified input value. The central and edge values of Z_{eff} are adjusted by comparing the values of resistive loop voltage and central safety factor and their time derivatives with the specified input values. The resistive loop voltage and central safety factor are determined from the current and resistivity profiles calculated in the code. The resistivity is calculated neoclassically, including corrections due to banana-trapped particles. Then the electric field and current profiles are determined from the magnetic diffusion equation.

It is possible for ONETWO to experience some difficulty when adjusting parameters dynamically to match input specifications, and one must watch out for cases where erroneous results are produced due to failure to converge on the specified parameters. This tended to occur often in the runs at the time when the RF turns on and parameters try to change quickly. This did not pose much of a problem,

however, because ONETWO always managed to converge on the specified parameters for most of the transport simulation time. In the analysis runs, parameters were specified at typically 9–15 time points, spaced approximately 20 ms apart. (The time points used were the times when the Thomson scattering diagnostic laser pulsed.) Because of this, and because of uncertainties in the timing of the Thomson data, there could easily be as much as a 20 ms discrepancy in the timing of the input data. This is likely to be the reason for the problems that occur when the RF turns on. This kind of timing error would result in temporary errors in the power balance which ONETWO would try to correct by making inappropriate adjustments in the neoclassical multiplier.

The ONETWO analysis was performed for 44 shots from the experimental database. The results for three representative shots are shown in Fig. 4.5.1. Case (a) is a relatively low-density shot in which the density increased during the RF. Case (b) is a medium-density shot in which the density decreased during the RF. And case (c) is a high-density shot in which the density was relatively constant during the RF. Values which have been determined to be erroneous due to failure of ONETWO to match the input value (usually of the fusion neutron rate) are shown with broken lines. The actual values of densities for these shots can be read from the next two illustrations. For these analyses, experimental data were used to evaluate the terms in Eq. 4.5.1, representing heating, convection, work, charge exchange, and collisional exchange from electrons. Since the convection, work, and charge exchange are small compared to the collisional exchange, it makes sense to use the adjustable parameter $W_{\rm neo}$ in the conduction term to achieve power balance. For each of the three shots in Fig. 4.5.1, the resulting value of $W_{\rm neo}$ is plotted as a function of time for three different values of the $P_{\rm dep}$ term in Eq. 4.5.1. Each case was run three times, assuming the power deposited to deuterium to be zero, $P_{\rm net}$ from the model developed in this chapter, and the total launched power $P_{\rm RF}$ respectively. For the $P_{\rm dep} = P_{\rm RF}$ cases, the RF power was assumed to be uniformly distributed for $r < a/2$, and zero for $r > a/2$.

When it is assumed that no RF power at all is deposited to deuterium, a noticeable drop in the calculated value of $W_{\rm neo}$ occurs during the RF. This behavior was observed for all 44 of the shots that were analyzed, regardless of whether or not there was any peaking of the density profile, and regardless of whether the density increased, decreased, or remained relatively constant during the RF. It therefore is reasonable to conclude that some amount of RF power must have been deposited on deuterium in order to produce the observed deuterium heating. If the RF power deposition model developed in this chapter is used, the resulting values of $W_{\rm neo}$ remain reasonably constant throughout the shot. If all of the RF power is assumed

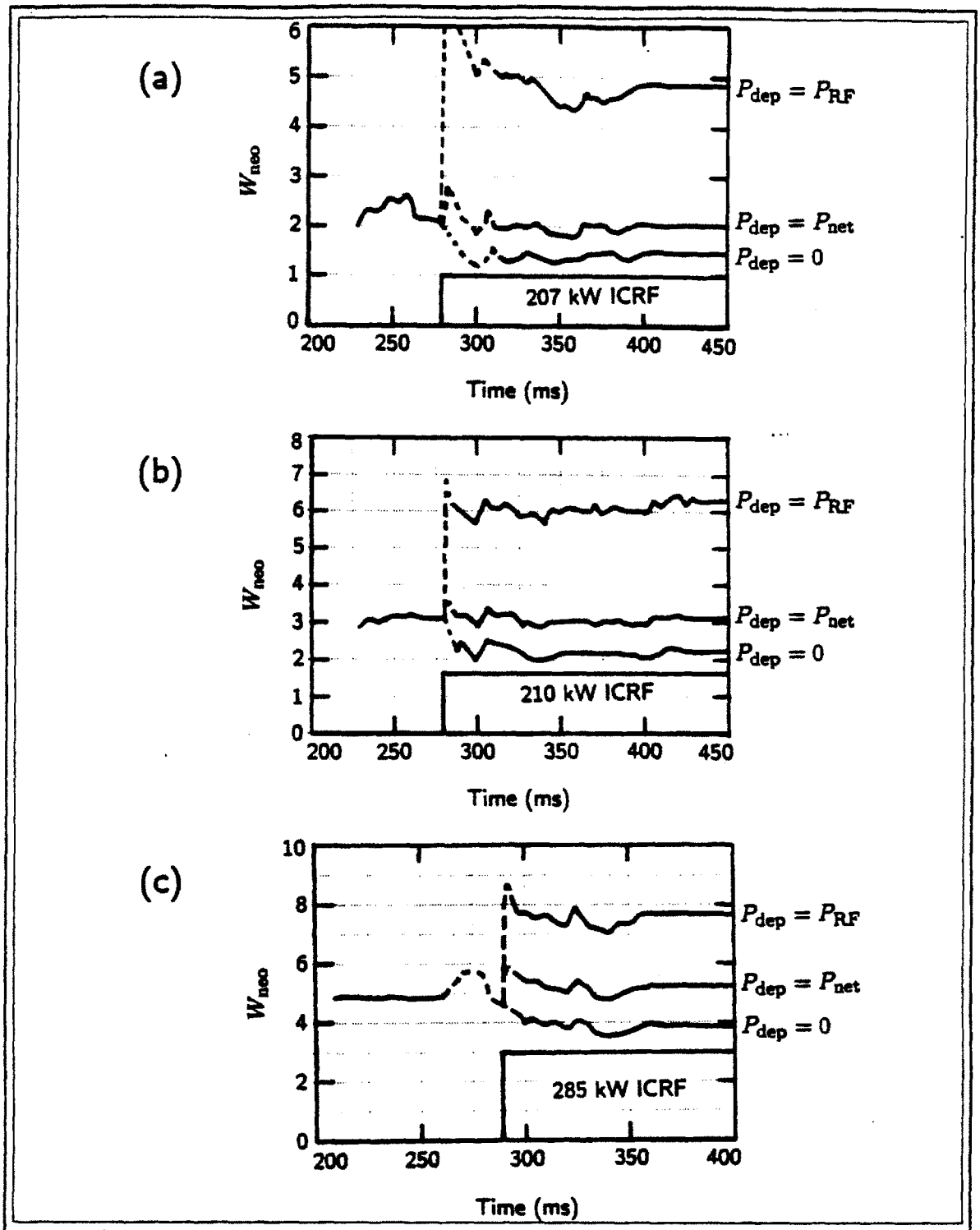

Figure 4.5.1: ONETWO Deuterium Transport Analysis—The neoclassical multiplier W_{neo} implied by the experimental data is shown for (a) a low-density, rising-density shot, (b) a medium-density, falling-density shot, and (c) a high-density shot. For each case, the calculation is shown assuming the net deposited RF power is either zero, P_{net} from the model developed in this chapter, or the total launched P_{RF} uniformly distributed within 1/2 the minor radius.

to be deposited on deuterium, then the inferred value of W_{neo} always increases significantly during the RF. This is strong evidence that the RF deposition estimates developed in this chapter are approximately correct.

It is important not to be misled about the meaning of the $P_{dep} = P_{RF}$ plots. Obviously, the purpose of those calculations is to get some idea of what might happen in an idealized case where the RF absorption was 100% efficient. However, if that were the case, then some of the RF power would be deposited on electrons. On the other hand, if impurity radiation were brought under control by eliminating high-Z impurities, and if ripple trapping and unconfined orbits were significantly reduced, so that a high-energy minority tail could be produced, then the electrons would be expected to heat, thereby depositing a significant amount of the power on deuterium. Also, if higher RF power was applied, so that a ~ 10 keV tail could be produced at low deuterium density with high minority concentration, or so that a ~ 20 keV tail could be produced at high deuterium density, (or if the target plasma was significantly hotter), then mode-conversion as well as minority slowing-down on electrons would be greatly reduced. Thus it is possible to conceive of a situation in which most of the RF power could indeed be deposited on deuterium. Since a model for electron heating by the RF has not been developed, and since experimental data related to the electron power balance are lacking, it is difficult to think of any more appropriate way to model an idealized "perfect absorption" case than the one shown here.

The behavior of the neoclassical multiplier W_{neo} is shown for all 44 of the shots that were analyzed in Figs. 4.5.2 and 4.5.3. These points were calculated using the value of $P_{dep} = P_{net}$ from the estimates developed in this chapter. An explanation for the unfavorable scaling of the RF heating efficiency with density now begins to appear. For the Ohmic target plasma, the deuterium thermal energy transport is not much worse than neoclassical at low density, but becomes increasingly anomalous with increasing density. Moreover, the observed deuterium heating is consistent with no significant change in the thermal transport properties during the RF, in spite of the fact that the net RF deposition from the estimates developed in this chapter increases significantly with density. In other words, after accounting for known RF loss mechanisms according to theoretical models, the net RF power deposited to deuterium heats with the same efficiency as the net ohmic power deposited via collisional exchange with electrons. It should be noted, however, that for these modest heating results the deuterium distribution function would not be expected to be distorted significantly from a Maxwellian (as was assumed when calculating the deposition).

It should be emphasized that the effect of increasingly anomalous ion conductivity is quite a significant effect compared to the neoclassical prediction. Numerical

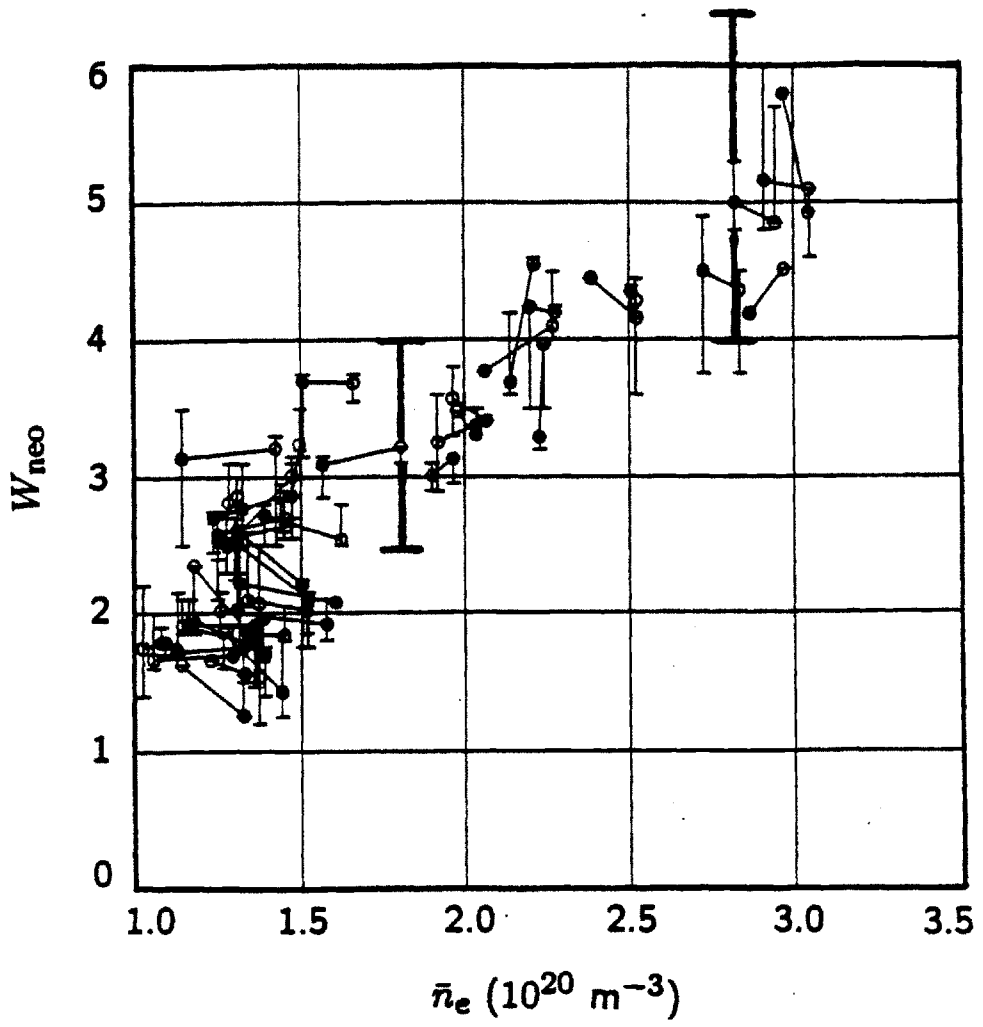

Figure 4.5.2: Neoclassical Multiplier—The inferred W_{neo} is shown for 44 shots as a function of line-average electron density. The values during the ohmic portion of the shot (excluding start-up) are shown with open circles and the values during the RF (after temperatures reached equilibrium) are shown with solid circles. Each ohmic point is connected to the corresponding RF point by a straight line. The small error bars indicate variations in the inferred W_{neo} during the relevant portion of the shot. The two bold error bars were calculated by varying the input data over the ranges of experimental uncertainty in the most unfavorable manner. These bold error bars correspond to cases (b) and (c) in Fig. 4.5.1.

values for the actual ion thermal conductivity and diffusivity and the Chang-Hinton neoclassical diffusivity (all taken from the ONETWO code results) for the three cases from Fig. 4.5.1 are shown in Table 4.5.1. Note that the neoclassical ion thermal diffusivity χ_i^{CH} is not strongly dependent on density. Thus, the neoclassical thermal conductivity $\kappa_i^{CH} = n_i \chi_i^{CH}$ increases linearly with density. From Fig. 4.5.2, one

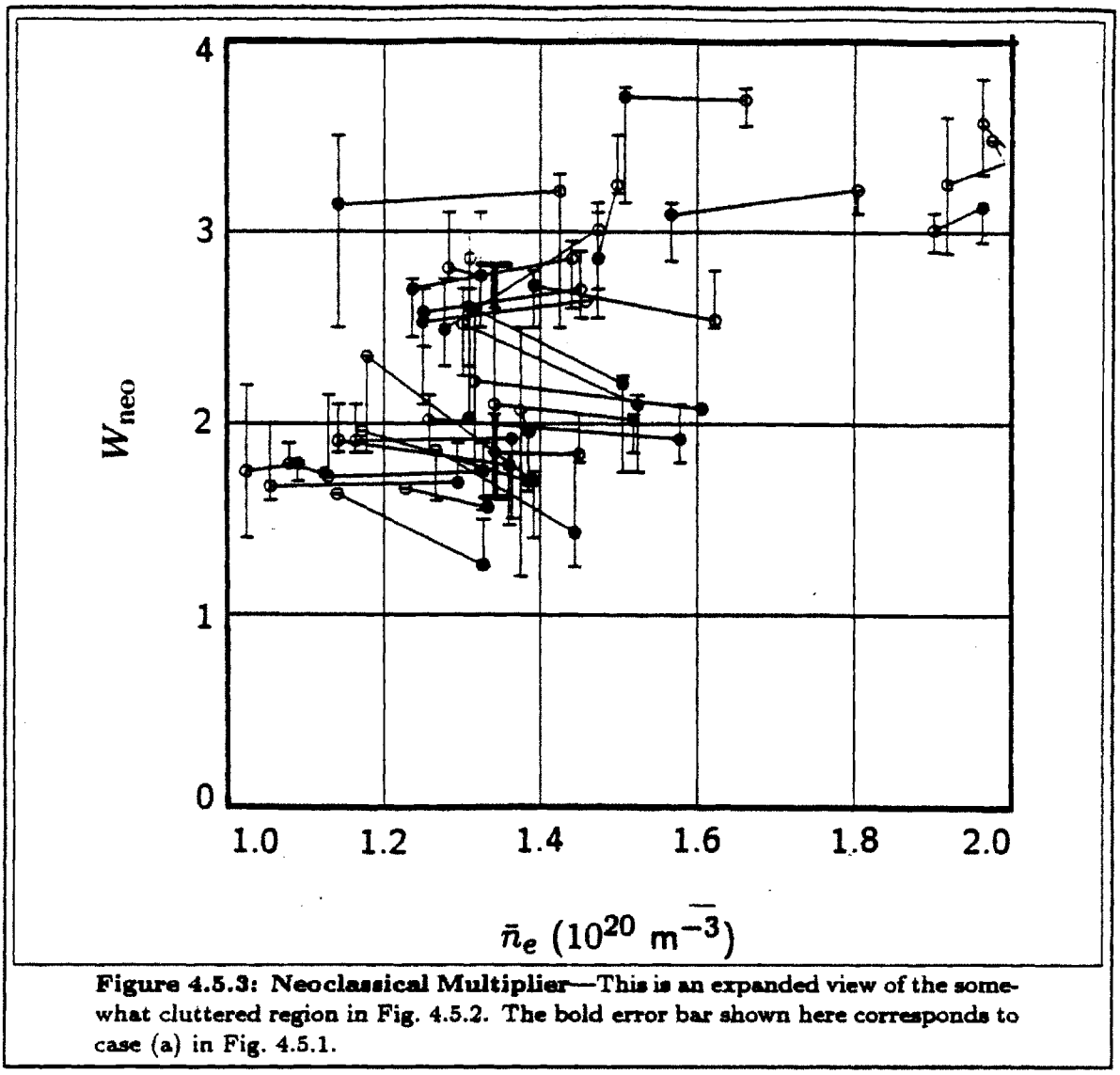

Figure 4.5.3: Neoclassical Multiplier—This is an expanded view of the somewhat cluttered region in Fig. 4.5.2. The bold error bar shown here corresponds to case (a) in Fig. 4.5.1.

can see that the anomalous behavior of $W_{\rm neo}$ is also proportional to n, resulting in an actual thermal conductivity for Alcator C which scales as the square of the density.

An expression for the neoclassical ion thermal diffusivity which can be found in Ref. 128 or Ref. 129 is

$$\chi_i^{CH} = K_2 \epsilon^{1/2} \frac{\rho_{i\theta}^2}{\tau_i} \tag{4.5.7}$$

where $\rho_{i\theta}$ is the "poloidal gyroradius"

$$\rho_{i\theta} \equiv \frac{2 m_i T_i}{Z_i^2 e^2 B_P^2} \tag{4.5.8}$$

Case	W_{neo}	$\kappa_i(0)$	$\kappa_i(r^*)$	r^*/a	$\chi_i(0)$	$\chi_i(r^*)$	$\chi_i^{CH}(0)$	$\chi_i^{CH}(r^*)$
(a)	2.0	0.87	0.30	0.4	0.37	0.18	0.18	0.089
(b)	3.1	1.08	0.45	0.4	0.47	0.26	0.15	0.085
(c)	5.3	3.01	1.24	0.5	0.80	0.43	0.15	0.082

Table 4.5.1: Thermal Conductivity and Diffusivity—Numerical values for κ_D and χ_D are shown for the shots in Fig. 4.5.1. These values were taken at the end of the RF pulse, but did not vary greatly during the shots. Values are given for the plasma center $r = 0$ and again at the point $r = r^*$, where r^* is chosen as the point where $T_e(r^*) = T_e(0)/2$. Thermal conductivities are given in units of $10^{20}/(\text{m-s})$ and thermal diffusivities are in units of m^2/s.

and

$$K_2 = K_2^0 \left[\frac{1}{1 + a_2 \nu_{i*}^{1/2} + b_2 \nu_{i*}} + \frac{\epsilon^{3/2}(c_2^2/b_2)\nu_{i*}\epsilon^{3/2}}{1 + c_2 \nu_{i*}\epsilon^{3/2}} \right] \tag{4.5.9}$$

where $K_2^0 = 0.66$, $a_2 = 1.03$, $b_2 = 0.31$, and $c_2 = 0.74$. The neoclassical collision parameter

$$\nu_{i*} = \frac{R_0 q}{v_{T_i} \tau_i \epsilon^{3/2}} \tag{4.5.10}$$

is essentially the ratio of the orbit transit time to the collision time, where the collision time is given by

$$\tau_i = \frac{3}{4\sqrt{\pi}} \left(\frac{4\pi\epsilon_0}{Z_i^2 e^2} \right)^2 \frac{\sqrt{m_i} T_i^{3/2}}{\lambda n_i} \tag{4.5.11}$$

The behavior of the neoclassical thermal diffusivity exhibited in Table 4.5.1 is characteristic of the plateau regime, for which $1 \ll \nu_{i*} \ll \epsilon^{-3/2}$. In this case, one has

$$K_2 \approx \frac{K_2^0}{b_2 \nu_{i*}} \tag{4.5.12}$$

In that case, the τ_i-dependence when Eq. 4.5.10 is substituted into Eq. 4.5.12 cancels the τ_i-dependence in Eq. 4.5.7, resulting in a thermal diffusivity which is independent of density. Near the magnetic axis, several of the quantities in Eq. 4.5.7 tend to zero or infinity, but if the limit is taken asymptotically, it can easily be shown that

$$\chi_i^{CH}(0) = q_0 \frac{K_2^0}{b_2} \frac{1}{\sqrt{2}\, R_0} \frac{v_{th_i}^3(0)}{\Omega_{i0}^2} \tag{4.5.13}$$

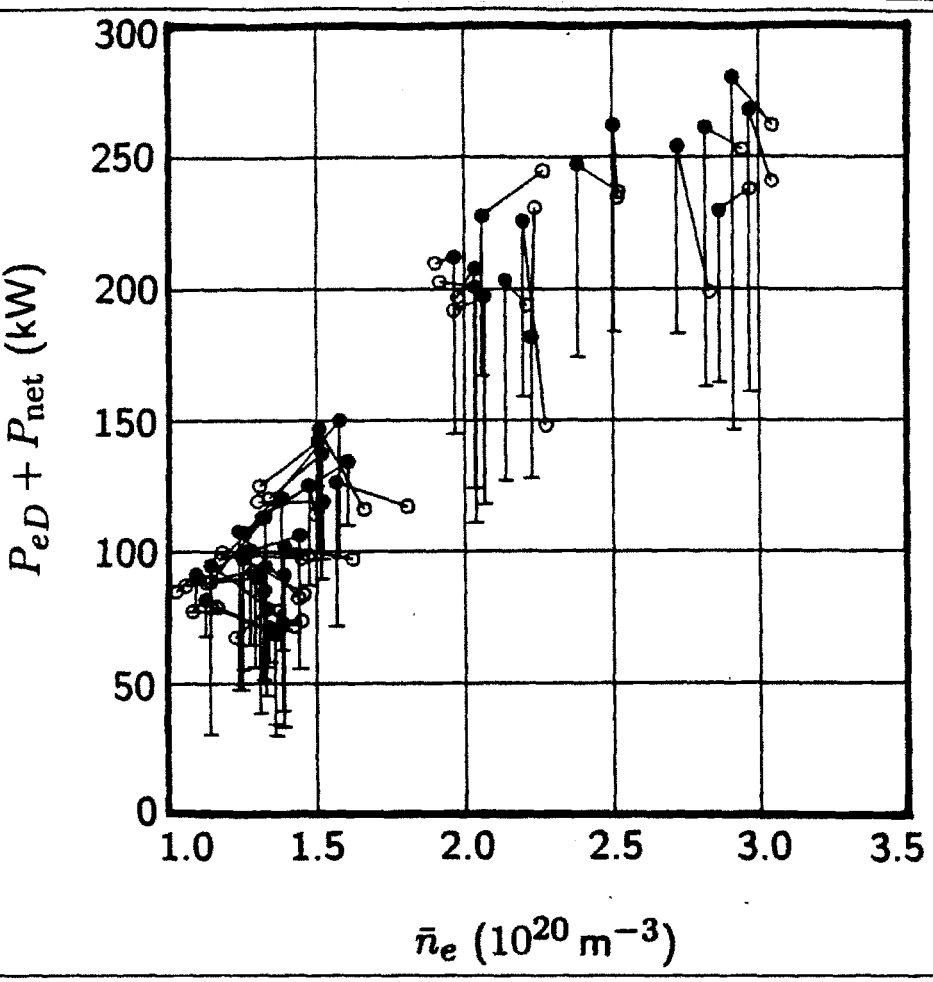

Figure 4.5.4: Ion Heating Power—The total ion heating power $P_{eD} + P_{\rm net}$ is shown as a function of density. The Ohmic points are shown with open circles and the RF points with solid circles. The vertical lines descending below each RF point are not error bars. Their function is to show the split between P_{eD} and $P_{\rm net}$. The length of each vertical line corresponds to $P_{\rm net}$, so the height of the short horizontal line at the bottom represents P_{eD}.

where Ω_{i0} is the ion cyclotron frequency in the toroidal field at the magnetic axis. Thus, in the plateau regime, the neoclassical thermal diffusivity is independent of density both in the bulk of the plasma and at the magnetic axis, confirming the thermal conductivity scaling discussed above. In the lower density ranges, the Alcator C discharges typically enter the banana regime, in which case an extra factor of n-dependence is introduced in the scaling. However, it is the plateau regime scaling that is of interest over most of the density range. Note that the effect of anomalous ion thermal conductivity in Alcator C is to produce banana-regime-like density scaling in plasma that is actually in the plateau regime.

Another way to compare the effectiveness of Ohmic and RF heating of the deu-

terium is to directly compare the net RF power deposited on deuterium with the collisional exchange power from electrons. Such a comparison is shown in Fig. 4.5.4. The total ion heating power is shown both before and during the RF. The split between collisional exchange and RF deposition is also shown during the RF. Changes in the convection, work, and charge exchange (which are small to begin with) are insignificant, but the collisional exchange power decreases significantly during the RF due to the decrease in temperature difference between electrons and deuterium as the deuterium heats up. However, the total ion heating power does not increase very much, and occasionally even decreases. Thus, the main effect on the deuterium of applying RF power to the Alcator C target plasmas is a replacement of collisional exchange power with RF power.

It is possible to run ONETWO to directly calculate the amount of deuterium heating that would be expected for a given Ohmic target plasma under the assumption that the transport properties, density, and electron temperature do not change during the RF. The results of such a calculation for the low and high-density cases are shown in Fig. 4.5.5. To obtain these results, ONETWO was first run in analysis mode, as has been done for the results presented so far in this section, using the Ohmic values (just one time point) assumed for these standard cases. This determines the value of $W_{\rm neo}$ which is consistent with the Ohmic target plasma. Then a second simulation-mode run is performed, in which $W_{\rm neo}$ is held fixed at the previously determined value, the RF power $P_{\rm net}$ is input to the code, and the resulting ion temperature is calculated. The electron temperature and density is held fixed. These results are comparable to the experimental data shown in Fig. 3.8.2. It is noted that the calculation of $W_{\rm neo}$ for the high-density case is very sensitive to the value assumed for the electron temperature. However, if the electron temperature is held fixed during the calculation, the resulting value of ΔT_D is only weakly dependent on the assumed electron temperature. But at high density, the electrons and ions are very strongly collisionally coupled and it is not necessarily reasonable to assume that the RF power will not affect the electron temperature. Thus, the simulation for the high-density case is considered to be only a rough estimate of the expected heating.

Finally, the calculation of $Z_{\rm eff}$ from the resistive loop voltage, as determined by ONETWO, is shown in Fig. 4.5.6. Normally, $Z_{\rm eff}$ for Alcator C is determined from a diagnostic which measures visible bremstrahlung radiation, but that diagnostic was seriously affected by RF interference during the experiments. Therefore, the measurement in Fig. 4.5.6 is the best $Z_{\rm eff}$ measurement available for these shots. A few comparisons were made with the visible bremstrahlung measurement, by looking at the value of $Z_{\rm eff}$ indicated immediately after the RF turned off, and no cause for concern was found. There is nothing surprising about the results shown

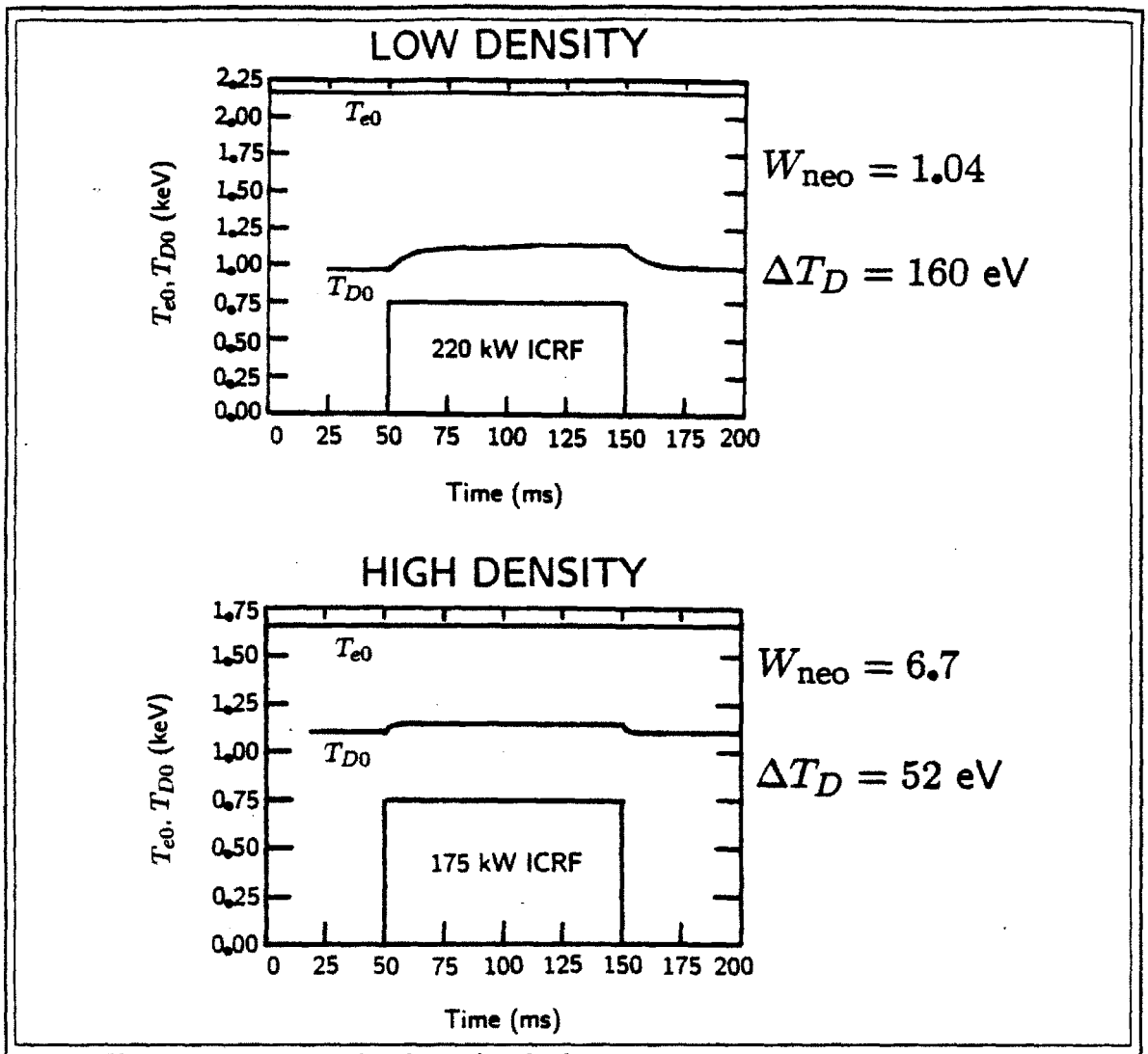

Figure 4.5.5: Ion Heating Simulations—ONETWO heating simulations are shown for the low-density case ($\bar{n}_e = 1 \times 10^{20}\,\mathrm{m}^{-3}$) and the high-density case ($\bar{n}_e = 4.5 \times 10^{20}\,\mathrm{m}^{-3}$). After running ONETWO in analysis mode to determine the value of W_{neo} during the Ohmic part of the discharge, a new simulation-mode run was set up, in which W_{neo} was held fixed at the Ohmic value and the deuterium heating was calculated for the given RF power input. These heating results are comparable to the steady-density experimental points in Fig. 3.8.2.

in Fig. 4.5.6. There is a tendency for Z_{eff} to increase significantly during the RF, and high-density shots are less susceptible to this effect.

The behavior of W_{neo} versus density found herein has been observed in previous non-ICRF Alcator C experiments and has been reported.[130–133] It has been blamed for the so-called saturated confinement regime in which energy confinement progressively degrades compared to neo-Alcator scaling ($\tau_E \propto \bar{n}_e$) with increasing density in the range $\bar{n}_e \gtrsim 3 \times 10^{20}\,\mathrm{m}^{-3}$[130].

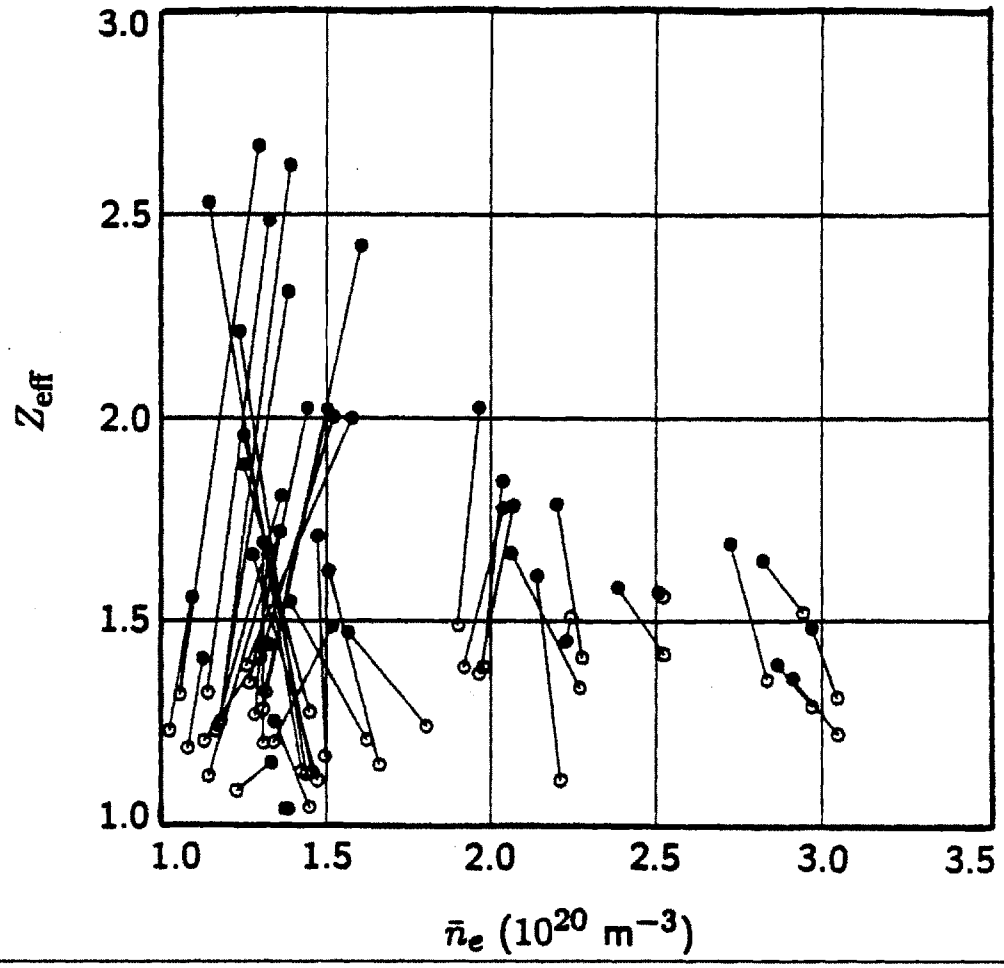

Figure 4.5.6: Z-Effective—The volume-average Z_{eff} determined by ONETWO from the resistive loop voltage measurements is shown using open circles for the Ohmic points and solid circles for the RF points.

During pellet injection experiments performed using high-density target plasmas in the saturated confinement regime[131], it was found that pellet injection resulted in a significant improvement in energy confinement time. The post-injection plasmas had energy confinement times consistent with a decrease in the ion thermal diffusivity to the neoclassical value ($W_{neo} = 1$). However, at those high densities the electrons and ions are so strongly collisionally coupled that it is not possible to determine unambiguously whether the improvement was a result of suppression of anomalous ion losses or of anomalous electron losses. To resolve this ambiguity, further experiments were performed at moderate density ($1 \times 10^{20}\,\mathrm{m}^{-3} \leq \bar{n}_e \leq 3 \times 10^{20}\,\mathrm{m}^{-3}$)[133]. For these densities, the electron and ion temperatures are sufficiently separated that the loss channels can be distinguished. Using the ONETWO code, Wolfe *et al.* determined unambiguously that the ion thermal diffusivity was reduced to the neoclassical value following pellet injection.

It was emphasized in Ref. 133 that, because of the ambiguity due to the strong collisional coupling in the saturated confinement regime, it was still conceivable that it could have been a suppression of anomalous electron losses that was responsible for the earlier pellet injection results. It could then be interpreted that the confinement saturation mechanism was analogous to the appearance of enhanced electron losses in L-mode neutral beam heated discharges, and that the improved confinement in pellet-fueled discharges might then be interpreted as a transition to H-mode resulting from a decrease in electron thermal conductivity.

While this possibility cannot be ruled out, I feel that the available evidence more strongly indicates that it is the ion transport that is dominating the results. The physical explanation for the confinement behavior would then be as follows: For low-density Alcator C discharges, the ion transport is neoclassical while the electron transport is strongly anomalous. Neo-Alcator scaling then implies the scaling κ_e independent of density so that $\chi_e \propto 1/\bar{n}_e$. As density increases, χ_e is decreasing while χ_i is continuously increasing. At the same time, the ions and electrons are becoming more strongly collisionally coupled. Eventually, a point is reached at which the ion loss dominates, and the saturated confinement regime begins. Thus, the saturated confinement regime is to be expected if the previously known behavior of the ion and electron transport is simply extrapolated into the regime where data interpretation is ambiguous. On the other hand, attributing this effect to the electrons requires a reversal in the previously observed trends.

In Ref. 133, it was found that the most apparent difference between pellet and gas-fueled discharges is that post-injection plasmas typically have more peaked density profiles. Density profile peaking and decreased fueling at the edge are indeed typical of H-mode discharges. However, as pointed out in Ref. 133, the result of their study was that this profile peaking was correlated with improvements in ion transport, and not electron transport — another feature that would have to "reverse" if the electrons were responsible for the high-density behavior. Wolfe *et al.* introduce the so-called ion mixing mode (or η_i-mode)[134–138] as an effect which is related to ion physics and could be responsible for the experimental results. The critical parameter for η_i-mode stability is given by

$$\eta_i \equiv \frac{d\ln T_i}{d\ln n_i} \tag{4.5.14}$$

i.e., the ratio of the ion density gradient scale length divided by the ion temperature gradient scale length. The η_i-mode becomes unstable when this parameter exceeds a critical value, given approximately by[137]

$$\eta_{\text{crit}} \approx \frac{1}{2}\left[1+\sqrt{1+113\left(\frac{r_n}{Rq}\right)^2}\right] \tag{4.5.15}$$

where r_n is the local density gradient scale length. Since peaking of the density profile reduces the local maximum value of the density gradient, it is reasonable that such an effect could stabilize the η_i-mode. Since profile data were not much more detailed in the experiments analyzed in Ref. 133 than in the present ICRF experiments, the determination of η_i from experimental data is very error prone. No experimental correlation between $\eta_i/\eta_{\text{crit}}$ and Wneo was found in Ref. 133; however, the calculated values of $\eta_i/\eta_{\text{crit}}$ were all close to unity. It would still be reasonable to blame the anomalous ion confinement on η_i-modes if the nonlinear saturation mechanism for the instability had the effect of driving the profile shape toward marginal stability. Such an effect is to be expected theoretically[138].

At any rate, whatever the cause of this anomalous ion confinement, the resulting values of W_{neo}, which are very similar in the present ICRF experiments to those found by Wolfe *et al.*, are responsible for the observed density scaling of the ICRF heating efficiency.

4.6: Summary

In this chapter, existing numerical models were used to treat the RF absorption, mode conversion, and collisional deposition in the presence of severe minority losses, in order to determine the net power deposited to deuterium. It was found that mode conversion plays a significant but not a dominant role in the scaling of deposited power with density. As expected, the deposition of power on deuterium becomes significantly more efficient at high density, offering no obvious explanation for the results from the experimental density scan. In particular, it is not necessary to generate an elevated minority tail in order to achieve efficient absorption at high density. However, the deposition calculations do offer an explanation for the results of the experimental minority concentration scan. It was found that mode conversion becomes dominant at high concentration, resulting in significantly reduced power deposited on deuterium. Since the target plasmas during the concentration scan were all similar, this was accepted as the explanation without performing analysis with the ONETWO code specifically for this purpose. This mode conversion behavior is attributed to the inability to produce an elevated minority tail at high minority concentration. Note, however, that the Brambilla code results predict that this

effect is less severe at high density. (No minority concentration scan was attempted at high density in the experiments.)

To further investigate the results of the experimental density scan, the deuterium power balance was studied in more detail using the ONETWO transport code. It was found that the dominant loss mechanism for the deuterium is conduction, and that the behavior of the conduction power becomes significantly anomalous at high density. After accounting for serious loss mechanisms associated with the minority, whose density scaling is quite favorable, it was found that the unfavorable density scaling observed in the experiment could quite reasonably be attributed to the behavior of the ion thermal conduction. Since the inferred ion thermal conduction during the Ohmic and RF heated parts of the discharge were in very good agreement, there is no need to postulate the existence of other loss mechanisms, such as a large increase in the previously insignificant convection power.

CHAPTER 5

Conclusion

5.1: Summary

The work described herein began with an effort to develop a more electrically robust ICRF antenna than was used in previous Alcator C fast wave heating experiments. These antennas allowed more reliable operation compared to the previous experiments, but did not result in improved heating efficiency. The feed-line standing wave ratio was greatly reduced by using a resonant antenna design, but an improved vacuum feedthrough (originally designed for experiments on the PLT tokamak) allowed reliable operation at high feed-line standing wave ratio with the non-resonant low-field-side launcher. There were no significant differences in the experimental heating results obtained with the two antennas.

Minority regime ICRF heating experiments were then carried out in a plasma composed of a deuterium majority and a hydrogen minority. Several plasma parameters were scanned during the experiments, but the main results analyzed in this thesis concern a density scan at (assumed) fixed minority concentration $\eta_H = 0.5\%$, and a minority concentration scan at fixed density $\bar{n}_e \approx 1.4 \times 10^{20}\,\mathrm{m}^{-3}$. Significant plasma heating was observed during the experiment, but the only significant contribution to the increase in thermal energy content (other than density changes) was an increase in deuterium temperature. The electrons were typically observed to neither heat nor cool during the RF; however, it should be noted that the absolute experimental uncertainty in the electron temperature measurement is higher than for the ion temperature measurement. Suprathermal hydrogen ions were observed, but they were not sufficiently energetic to collisionally deposit more than a small fraction of the total RF power onto the deuterium (or the electrons for that matter). Therefore, it was hypothesized that the hydrogen energy balance was dominated by losses.

The scaling of the heating efficiency, as quantified by the incremental energy confinement time, with density was not favorable. In contrast, the Ohmic energy confinement time was significantly higher than the incremental confinement time, and increased markedly with density. Since the losses associated with an energetic minority tail would be expected to scale quite favorably with density, this suggested that some other process was also involved. The scaling with minority concentration was also difficult to understand. Heating efficiency improved as minority concentration was lowered to extremely low values. In the presence of severe hydrogen losses, this could be understood if the contribution from deuterium second harmonic cyclotron absorption was dominating. However, as minority concentration was scanned upwards, heating efficiency continued to degrade even at concentrations for which the minority temperature was comparable to the majority temperature, at which point minority tail losses would be expected to be minimum.

Further progress in understanding the experimental results was gained through the coordinated application and careful interpretation of four sophisticated numerical codes. Three recently developed codes were used to model the RF wave physics and study the hydrogen minority energy balance. Using the RF deposition estimates obtained from these results, a well-established transport code was used to model the deuterium energy balance. It was found that the scaling of the heating efficiency with minority concentration could be understood as a result of greatly enhanced mode conversion at high minority concentrations. In turn, this mode conversion was a result of the inability to produce an elevated minority temperature at high concentration. A similar but less significant behavior of the mode conversion as a function of majority density was found, also a result of the inability to produce an elevated minority temperature. However, the density scaling was not dominated by this effect, and the net result of the deposition calculations was a very favorable scaling of RF absorption and deposition with increasing density. Therefore, more work needed to be done in order to understand the density scaling. By studying the power balance of the deuterium, it was found that the density scaling result could be attributed to an increasingly anomalous ion thermal confinement at high density. This ion confinement anomaly is a well-known property of Alcator C plasmas and has previously been invoked to explain the high-density saturated-confinement regime.

Before concluding, it is acknowledged that it cannot be conclusively proven that the preceding explanation of the experimental results is correct. Note that the entire analysis presented in Chapter 4 is dependent on the assumption that all of the RF power is absorbed either by fundamental or second harmonic cyclotron absorption on the hydrogen or deuterium respectively, or mode converted to the ion Bernstein wave. One might also attempt to explain the results by postulating that some kind of loss mechanisms prevent the RF power from ever reaching the interior of the plasma. Possible candidates for such loss mechanisms could be resistive losses or electrical breakdown in the antenna, or nonlinear absorption mechanisms (such as parametric decay) in the plasma edge. The significant increase in antenna loading by the plasma compared to the loading seen during vacuum conditioning or bench tests suggests that resistive losses in the antenna are not important. Intermittent electrical breakdown in the antenna was observed during the experiments, and usually resulted in tripping of the RF fault detection apparatus and/or disruption of the plasma current. Although one cannot rule out the possibility of some kind of steady breakdown phenomenon during the RF which might well depend on plasma density, it seems unlikely that such a phenomenon would depend on minority concentration. Parametric decay has been seen during other ICRF heating experiments

(e.g., ASDEX[139]) and it has been suggested that it might result in direct RF absorption in the edge. Attempts to detect evidence of parametric decay during the ICRF experiments on Alcator C were inconclusive.

Nevertheless, the explanation that has been put forth in this thesis is based on predictions consistent with contemporary theory, and offers plausible explanations both for the amount of heating observed and for the density and concentration scaling behaviors. Moreover, the effect attributed to the density scaling behavior is a well-known property of Alcator C plasmas. Thus it appears that the explanation for the Alcator C fast wave ICRF heating results can be summarized by the following statement: Heating efficiency was limited by poor confinement of the minority species at low density, and of the majority species at high density.

5.2: Prospects for Future High-Density Experiments

If very efficient RF heating had been observed during the Alcator C experiments, then evaluation of the prospects for future high-density experiments, such at CIT, would be easy. Lacking that, it is worth considering the various mechanisms that seem to be responsible for the Alcator C results, and speculating on how important they may be for future devices.

Consider first the electron losses. It was not possible to study them during the present experiments, but they were studied in earlier Alcator C experiments and in experiments carried out on other tokamaks. It is well established that the key to eliminating impurity radiation is to operate in a low-Z environment, for example by using graphite limiters and Faraday shields and using wall carbonization. This is well-known to result in higher values of $Z_{\rm eff}$ which increases losses due to bremstrahlung radiation and displaces a significant fraction of the "reactant" ions — an effect which, for a given $Z_{\rm eff}$, is worse for low-Z impurities than for high-Z impurities. This also reduces the fusion reaction rate. Although the net result of carbonization has been favorable in experiments to date, large values of $Z_{\rm eff}$ must be avoided in an ignition experiment. This impurity problem is not unique to high-density plasmas, and may even be less severe at high density. (See Fig. 4.5.6 in this thesis.)

Next consider the minority losses. There is no question that toroidal-field ripple-trapping must be avoided in an ignition experiment because, even if RF heating is not used in the experiment, it will be necessary to confine high-energy fusion reaction products. This requires that the toroidal field ripple be reduced to a

sufficiently low but nonzero value. This is an engineering task and is more difficult (but, in principle, not impossible) to achieve with compact high-field devices than with low-field large devices. All the other significant hydrogen tail losses that were considered in this thesis are finite-banana-width effects that can be minimized by operating at lower q (higher plasma current), and/or at high density. Since high-energy fusion reaction products are susceptible to these same loss mechanisms, they must be avoided in any fusion device, regardless of the auxiliary heating method. Consider the simulation results shown in Figs. 4.4.8 and 4.4.9 in this thesis. If ripple trapping can be avoided, then the total loss associated with the hydrogen minority is $P_{\rm Loss}$ in Fig. 4.4.9. Note that this quantity becomes quite small at high density in Alcator C. Thus, if electron losses as well as ripple trapping were brought under control, then the results in Fig. 4.4.9 would imply very efficient RF absorption and deposition. Of course, this does neglect possible RF losses in the antenna and the edge plasma. It also has not been shown how the absorbed power density in Alcator C compares with what would be needed in an ignition experiment, so the ratio $P_{\rm Loss}/P_{\rm RF}$ may not be the same in an ignition experiment as in Alcator C. Nevertheless, the fact that the very favorable RF deposition scaling shown in Figs. 4.4.8 and 4.4.9 are theoretical predictions which also agree with experimental results is quite encouraging.

Thus, it appears that the anomalous ion thermal conductivity is the only serious disadvantage for high-density operation. The key to successful ICRF heating of high-density plasmas would then be to find a way to eliminate this anomaly. When this effect was studied previously on Alcator C, it was suggested that it could be a result of ion-temperature-gradient-driven instabilities (so-called η_i-modes). It was also found that pellet injection experiments resulted in improved energy confinement, that might have been caused by altering the density profile in a manner that stabilized the η_i-modes. This suggests that one should plan on performing pellet injection experiments using ICRF heated target plasmas in the C-MOD and CIT tokamaks. If the anomalous ion confinement is indeed caused by η_i-modes, then there might be other ways to alter the profile in order to stabilize them. For example, flattening of the temperature profile should provide another way to reduce the quantity η_i. This might be possible by heating the plasma edge, perhaps using ECRH. Of course, the net effect of non-central heating for this purpose might be energetically unfavorable, i.e., it might use up more power than it saves. The density profiles obtained using a diverted instead of a limited plasma might be more favorable towards η_i-modes. It is also conceivable that this anomalous ion confinement may not occur in high-density H-mode plasmas. Better yet, if the high density results were caused by an electron-related effect analogous to L-mode scaling, then the achievement of H-mode in a high-field compact device might still

eliminate the effect. These possibilities should be investigated theoretically and/or experimentally.

Thus, as for any research project, there are both compelling motivations for attempting an ICRF-heated compact high-field ignition experiment, and uncertainties about its prospect for success. I conclude that it should be attempted.

References

1. J. D. LAWSON, *Some Criteria for a Power Producing Thermonuclear Reactor*, *Proc. Phys. Soc. London* **B**:70 (1957) 6

2. G. BATEMAN, *MHD Instabilities*, M.I.T. Press, Cambridge, MA, (1978)

3. J. P. FREIDBERG, *Ideal Magnetohydrodynamics*, Plenum Press, (1987)

4. L. SPITZER, JR., R. HÄRM, *Transport Phenomena in a Completely Ionized Gas*, *Phys. Rev.* **89**:5 (1953) 977

5. EQUIPE TFR, *ICRF Heating and Antenna Coupling Studies in TFR*, *Proceedings of the 3rd Joint Varenna-Grenoble International Symposium — Heating in Toroidal Plasmas*, (Grenoble, France 22–26 March 1982) **I** 225

6. TFR GROUP, *Non-Thermal Electron Cyclotron Emission During ICRF Heating in the TFR Tokamak*, *Proceedings of the 3rd Joint Varenna-Grenoble International Symposium — Heating in Toroidal Plasmas*, (Grenoble, France 22–26 March 1982) **I** 423

7. EQUIPE TFR, *ICRF Heating in TFR and the Problem of Impurity Release*, *11th European Conference on Controlled Fusion and Plasma Physics* (Aachen, 5–9 September 1983)

8. TFR GROUP, F. SAND, *ICRF Heating Experiments in TFR Using a Low-Field-Side Antenna*, *Nucl. Fusion* **25**:12 (1985) 1719

9. V. K. TRIPATHI, C. S. LIU, *Tentative Interpretation of Some Results on Parametric Instability in ICRF Heating of TFR*, *Nucl. Fusion* **26**:7 (1986) 963

10. TFR GROUP, *Influence of Partially Stripped Impurity Ions on the Cyclotron Absorption of the Fast Magnetosonic Wave in TFR Plasmas*, *Nucl. Fusion* **26**:7 (1986) 873

11. F. WESNER, *et al.*, *ICRH for ASDEX and W VII*, *Proceedings of the 3rd Joint Varenna-Grenoble International Symposium — Heating in Toroidal Plasmas*, (Grenoble, France 22–26 March 1982) **I** 429

12. K. STEINMETZ, *et al.*, *High Power ICRF Heating on the Divertor Tokamak ASDEX*, *12th European Conference on Controlled Fusion and Plasma Physics* (Budapest, 2–6 September 1985)

13. K. STEINMETZ, *et al.*, *Ion Cyclotron Resonance Heating in the Divertor Tokamak ASDEX*, *31st National Symposium of the American Vacuum Society* (Houston, TX 18–22 November 1985)

14. G. JANESCHITZ, *et al.*, *Impurity Production During ICRF Heating, 13th European Conference on Controlled Fusion and Plasma Heating* (Schliersee, 14–18 April 1986)

15. K. STEINMETZ, *et al.*, *ICRF H-Mode and $2\Omega_{cH}/D(H)$-Minority Heating on ASDEX, 13th European Conference on Controlled Fusion and Plasma Heating* (Schliersee, 14–18 April 1986)

16. J.-M. NOTERDAME, *et al.*, *The Role of the Faraday Screen in ICRF Antennae: Comparison of an Optically Open and Optically Closed Screen in ASDEX, 13th European Conference on Controlled Fusion and Plasma Heating* (Schliersee, 14–18 April 1986)

17. K. STEINMETZ, *et al.*, *Ion Cyclotron Resonance Heating in the Divertor Tokamak ASDEX, J. Vac. Sci. Technol. A* **4**:3 (1986) 1088

18. M. KEILHACKER, *et al.*, *Confinement in ASDEX with Neutral Beam and RF Heating, Plasma Phys.* **28**:1A (1986) 29

19. K. STEINMETZ, *et al.*, *High Power ICRF Heating in the Divertor Tokamak ASDEX, Plasma Phys.* **28**:1A (1986) 235

20. F. WAGNER, *et al.*, *Combined Application of Neutral Injection, Lower Hybrid, and Ion Cyclotron Resonance Heating in ASDEX and Synergetic Effects, Plasma Phys.* **28**:9A (1986) 1225

21. K. STEINMETZ, *et al.*, *Observation of a High-Confinement Regime in a Tokamak Plasma with Ion Cyclotron-Resonance Heating, Phys. Rev. Lett.* **58**:2 (1987) 124

22. S.-I. ITOH, *et al.*, *ICRF Heating Analysis on ASDEX Plasmas, Max-Planck-Institut für Plasmaphysik* Report IPP III/115 (1987)

23. J. HOSEA, *et al.*, *Fast-Wave Heating of Two-Ion Plasmas in the Princeton Large Torus through Minority-Cyclotron-Resonance Damping, Phys. Rev. Lett.* **43**:24 (1979) 1802

24. P. L. COLESTOCK, *et al.*, *Modeling of ICRF Heating in PLT, Proceedings of the 2nd Joint Varenna-Grenoble International Symposium — Heating in Toroidal Plasmas*, (Como, Italy 3–12 September 1980) **I** 471

25. J. HOSEA, *et al.*, *High Power ICRF Heating on PLT and Extrapolation to Future Devices, Proceedings of the 3rd Joint Varenna-Grenoble International Symposium — Heating in Toroidal Plasmas*, (Grenoble, France 22–26 March 1982) **I** 213

26. D. Q. HWANG, G. GROTZ, J. C. HOSEA, *Surface Physics Problems During ICRF Heating of Tokamak Plasmas*, *J. Vac. Sci. Technol.* **20**:4 (1982) 1273

27. J. HOSEA, *et al.*, *PLT Ion Cyclotron Range of Frequencies Heating Program*, *Plasma Physics Laboratory, Princeton University* Report PPPL-2117 (1984)

28. B. C. STRATTON, *et al.*, *Changes in Impurity Radiation During ICRF Heating of PLT Tokamak Plasmas*, *Nucl. Fusion* **24**:6 (1984) 767

29. S. A. COHEN, *et al.*, *Measurements of Low-Energy Neutral Hydrogen Efflux During ICRF Heating*, *Plasma Physics Laboratory, Princeton University* Report PPPL-2133 (1984)

30. S. A. COHEN, *et al.*, *Measurements of Low-Energy Neutral Hydrogen Efflux During ICRF Heating*, *Nucl. Fusion* **24**:11 (1984) 1490

31. E. MAZZUCATO, *et al.*, *Ion Cyclotron Heating Experiments in PLT*, *10th International Conference on Plasma Physics and Controlled Nuclear Fusion Research* (London, UK, 12–19 September 1984)

32. P. L. COLESTOCK, *et al.*, *The Effects of ICRF Heating on Plasma Edge Conditions in PLT*, *J. Vac. Sci. Technol. A* **3**:3 (1985) 1211

33. J. HOSEA, *et al.*, *RF Experiments on PLT*, *Plasma Phys.* **28**:9A (1986) 1241

34. M. ICHIMURA, *et al.*, *ICRF Heating Experiments on JIPP T-II*, *Nucl. Fusion* **24**:6 (1984) 709

35. N. NODA, *et al.*, *Impurity Origin During ICRF Heating in JIPP T-IIU Tokamak*, Report IPPJ-682 (1984)

36. R. ANDO, *et al.*, *ICRF Current Drive Experiment on JIPP T-IIU*, *Nucl. Fusion* **26**:12 (1986) 1619

37. R. J. TAYLOR, G. J. MORALES, *ICRF Heating in Microtor/Macrotor*, *Proceedings of the 2nd Joint Grenoble-Varenna International Symposium — Heating in Toroidal Plasmas*, (Como, Italy 3–12 September 1980) **I** 509

38. R. J. TAYLOR, *et al.*, *Observation of Short ICRF Waves in Microtor/Macrotor*, *Proceedings of the 3rd Joint Varenna-Grenoble International Symposium — Heating in Toroidal Plasmas*, (Grenoble, France 22–26 March 1982) **I** 309

39. JFT-2 GROUP, *ICRF Heating Experiment in JFT-2*, *Proceedings of the 3rd Joint Varenna-Grenoble International Symposium — Heating in Toroidal Plasmas*, (Grenoble, France 22–26 March 1982) **I** 213

40. M. MORI, *et al.*, *High Power ICRF Heating Experiments in the JFT-2M Tokamak*, *10th International Conference on Plasma Physics and Controlled Nuclear Fusion Research* (London, UK 12–19 September 1984)

41. K. ODAJIMA, *et al.*, *Scaling of Incremental Energy Confinement Time in the JFT-2M Tokamak*, *Phys. Rev. Lett.* **57**:22 (1986) 2814

42. Y. SHIMOMURA, K. ODAJIMA, *Scaling of Incremental Energy Confinement Time of L-Mode Plasma and Comments on Improved Confinement in Tokamaks*, *Japan Atomic Energy Research Institute* Report JAERI-M 86-128 (1986)

43. H. TAMAI, *et al.*, *Impurity Reduction During ICRF Heating in JFT-2M Tokamak*, *Nucl. Fusion* **26**:3 (1986) 365

44. J. SCHARER, J. JACQUINOT, *et al.*, *Fokker-Planck Calculations for JET ICRF Heating Scenarios*, *Nucl. Fusion* **25**:4 (1985) 435

45. J. JACQUINOT, *et al.*, *Preliminary ICRF Results from JET*, *Plasma Phys.* **27**:12A (1985) 1379

46. J. JACQUINOT, *et al.*, *ICRF Studies on JET*, *12th European Conference on Controlled Fusion and Plasma Physics* (Budapest, 2–6 September 1985)

47. J. JACQUINOT, *et al.*, *ICRF Studies on JET*, *Plasma Phys.* **28**:1A (1986) 1

48. R. J. BICKERTON, *et al.*, *Confinement and Heating of Plasmas in the JET Tokamak*, *Plasma Phys.* **28**:12B (1986) 1943

49. THE JET TEAM, *Plasma Heating in JET*, *Plasma Phys.* **28**:9A (1986) 1211

50. THE JET TEAM, *RF Heating on JET*, *Proceedings of 11th IAEA Conference on Plasma Physics and Controlled Fusion Research* (Kyoto, Japan, November 1986)

51. G. A. COTTRELL, R. O. DENDY, *Superthermal Radiation from Fusion Products in JET*, *Phys. Rev. Lett.* **60**:1 (1988) 33

52. M. BUREŠ, *et al.*, *The Modification of the Plasma Edge and Impurity Production by Antenna Phasing During ICRF Heating on JET*, *Plasma Phys.* **30**:2 (1988) 149

53. R. R. WEYNANTS, *et al.*, *Ion Cyclotron Heating on TEXTOR*, *6th Topical Conference on Radio Frequency Plasma Heating AIP*, (Callaway Gardens, GA 1985)

54. A. M. MESSIAEN, *et al.*, *Ion Cyclotron Resonance Heating on TEXTOR*, *12th European Conference on Controlled Fusion and Plasma Physics* (Budapest, 2–6 September 1985)

55. A. M. MESSIAEN, *et al.*, *Ion Cyclotron Resonance Heating on TEXTOR*, *Plasma Phys.* **28**:1A (1986) 71

56. G. H. WOLF, *et al.*, *Properties, Control and ICR-Heating of the Plasma in TEXTOR*, *Plasma Phys.* **28**:9A (1986) 1413

57. U. SAMM, *et al.*, *Plasma Edge Research on TEXTOR*, *Plasma Phys.* **29**:10A (1987) 1321

58. M. P. J. GAUDREAU, *et al.*, *Medium Power ICRF Results on the Alcator A Tokamak*, *Proceedings of the 4th Topical Conference on Radio Frequency Plasma Heating* (Austin, TX 9–10 February 1981)

59. H. L. MANNING, *et al.*, *Impurity Generation During ICRF Heating Experiments on Alcator C*, *Nucl. Fusion* **26**:12 (1986) 1665

60. H. L. MANNING, *VUV Study of Impurity Generation during ICRF Heating Experiments on the Alcator C Tokamak*, *MIT Plasma Fusion Center* Report PFC/RR-86-14

61. J. D. MOODY, *Ion Bernstein Wave Heating Experiments on the Alcator C Tokamak*, Ph.D. Thesis, Massachusetts Institute of Technology (1988)

62. I. B. BERNSTEIN, *Waves in a Plasma in a Magnetic Field*, *Phys. Rev.* **109**:1 (1958) 10

63. T. H. STIX, *The Theory of Plasma Waves*, McGraw-Hill, New York, NY (1962)

64. G. W. HAMMETT, *Fast Ion Studies of Ion Cyclotron Heating in the PLT Tokamak*, Ph.D. Thesis, Princeton University (1986)

65. K. G. BUDDEN, *Radio Waves in the Ionosphere*, Cambridge University Press, (1966)

66. C. F. KENNEL, F. ENGELMANN, *Velocity Space Diffusion from Weak Plasma Turbulence in a Magnetic Field*, *Phys. Fluids* **9**:12 (1966) 2377

67. D. SMITHE, *et al.*, *Effect of Parallel Magnetic Field Gradients on Absorption and Mode Conversion in the Ion-Cyclotron Range of Frequencies*, *Phys. Rev. Lett.* **60**:9 (1988) 801

68. P. L. COLESTOCK, R. J. KASHUBA, *The Theory of Mode Conversion and Wave Damping Near the Ion Cyclotron Frequency*, *Nucl. Fusion* **23**:6 (1983) 763

69. H. L. BERK, R. R. DOMINGUEZ, *J. Plasma Phys.* **18** (1977) 31

70. A. K. RAM, A. BERS, *Electron Heating by Mode-Converted Ion-Bernstein Waves in ICRF Heating of Tokamak Plasmas*, *Proc. 7th Topical Conference on Applications of RF Power to Plasmas* (May 4–6, 1987, Kissimmee, FL) AIP Conference Proc. 159 (S. Bernabei, R. W. Motley Ed.) (1987)

71. D. G. SWANSON, *Mode Conversion of Toroidal Alfvén Waves*, *Phys. Fluids* **18**:10 (1975) 1269

72. D. G. SWANSON, *Mode Conversion and Tunneling at the Two-Ion Hybrid Resonance*, *Phys. Rev. Lett.* **36**:6 (1976) 316

73. Y. C. NGAN, D. G. SWANSON, *Mode Conversion and Tunneling in an Inhomogeneous Plasma*, *Phys. Fluids* **20**:11 (1977) 1920

74. F. W. PERKINS, *Heating Tokamaks via The Ion-Cyclotron and Ion-Ion Hybrid Resonances*, *Nucl. Fusion* **17**:6 (1977) 1197

75. D. G. SWANSON, *Cyclotron Harmonic Absorption via the Green's Function for the Mode Conversion-Tunneling Equation*, *Phys. Fluids* **21**:6 (1978) 926

76. D. G. SWANSON, *The Effects of Localized Absorption on the Mode Conversion Process in the RF Heating of Plasmas*, *Nucl. Fusion* **20**:8 (1980) 949

77. D. G. SWANSON, *Derivation of the Mode Conversion-Tunneling Equation from the Vlasov Equation*, *Phys. Fluids* **24**:11 (1981) 2035

78. F. W. PERKINS, *ICRF Heating Theory*, *IEEE Trans. Plasma Sci.* **PS-12**:2 (1984) 53

79. D. J. GAMBIER, D. G. SWANSON, *An Algorithm to Solve the Linear Mode Conversion Problem in a Weakly Inhomogeneous Plasma*, *Phys. Fluids* **28**:1 (1985) 145

80. D. G. SWANSON, *Radio Frequency Heating in the Ion-Cyclotron Range of Frequencies*, *Phys. Fluids* **28**:9 (1985) 2645

81. R. A. CAIRNS, C. N. LASHMORE-DAVIES, *The Absorption Mechanism of the Ordinary Mode Propagating Perpendicularly to the Magnetic Field at the Electron Cyclotron Frequency*, *Phys. Fluids* **25**:5 (1982) 1605

82. R. A. CAIRNS, C. N. LASHMORE-DAVIES, *A Unified Theory of a Class of Mode Conversion Problems*, *Phys. Fluids* **26**:5 (1983) 1268

83. V. FUCHS, A. BERS, L. HARTEN, *On the Theory of Pairwise Coupling Embedded in More General Local Dispersion Relations*, *Phys. Fluids* **28**:1 (1985) 177

84. C. N. LASHMORE-DAVIES, V. FUCHS, R. A. CAIRNS, *Ion-Cyclotron Resonance Heating by Means of the Fast Wave in a Longitudinally Inhomogeneous Magnetic Field*, *Phys. Fluids* **28**:6 (1985) 1791

85. C. N. LASHMORE-DAVIES, *et al.*, *A Theory of Fast Wave Absorption, Transmission and Reflection in the Ion Cyclotron Range of Frequencies*, *Plasma Fusion Center, M.I.T.* Report PFC/JA-87-35 (1987)

86. V. FUCHS, A. BERS, *On Dissipative Mode-Coupling in ICRF Minority Heating*, *Plasma Fusion Center, M.I.T.* Report PFC/JA-88-19 (1988)

87. D. G. SWANSON, *Exact Order Reduction in Mode Conversion Problems*, *Proc. 7th Topical Conference on Applications of RF Power to Plasmas* (May 4–6, 1987, Kissimmee, FL) AIP Conference Proc. 159 (S. Bernabei, R. W. Motley Ed.) (1987)

88. T. H. STIX, *Fast-Wave Heating of a Two-Component Plasma*, *Nucl. Fusion* **15** (1975) 737

89. D. ANDERSON, L.-G. ERIKSSON, M. LISAK, *Analytical Treatment of the Distortion of Velocity Distributions in the Presence of ICRH*, *Nucl. Fusion* **25**:12 (1985) 1751

90. D. ANDERSON, M. LISAK, L.-O. PEKKARI, *Effects of Particle Trapping on Ion-Cyclotron Resonance Heating in a Toroidal Plasma*, *Phys. Fluids* **28**:12 (1985) 3590

91. D. ANDERSON, *et al.*, *Distortion of Ion Velocity Distributions in the Presence of ICRH — A Semi-Analytical Analysis*, *JET Joint Undertaking* Report JET-R(86)09 (1986)

92. D. ANDERSON, L.-G. ERIKSSON, M. LISAK, *Anisotropic Analysis of Ion Distributions Distorted by ICRH in a Tokamak Plasma*, *Plasma Phys.* **29**:7 (1987) 891

93. D. ANDERSON, *et al.*, *Distortion of Ion Velocity Distributions in the Presence of ICRH: A Semi-Analytical Analysis*, *Nucl. Fusion* **27**:6 (1987) 911

94. T. MORISHITA, *et al.*, *Analysis of Minority Velocity Distribution and Power Deposition Profile in ICRF Heating in a Tokamak*, *Nucl. Fusion* **27**:8 (1987) 1291

95. F. YASSEEN, J. VACLAVIK, *Quasilinear Theory of Uniformly Magnetized Inhomogeneous Plasmas: Electromagnetic Fluctuations*, *Phys. Fluids* **29**:2 (1986) 450

96. D. W. FAULCONER, *Adverse Magnetic Shielding and High Ohmic Loss Introduced by Antenna Shields Employed in RF Heating, Proceedings of the 3rd Joint Varenna-Grenoble International Symposium — Heating in Toroidal Plasmas*, (Grenoble, France 22–26 March 1982) **I** (1982) 347

97. C. M. FORTGANG, D. Q. HWANG, *Measurements of the Electrostatic and Electromagnetic Fields of Faraday-Shielded Half-Turn Loop-Type ICRF Antennae, Plasma Physics Laboratory, Princeton University* Report PPPL-2183 (1984)

98. C. M. FORTGANG, D. Q. HWANG, *Measurements of the Electrostatic and Electromagnetic Fields of Faraday-Shielded Half-Turn Loop-Type ICRF Antennae, IEEE Trans. Plasma Sci.* **PS-13**:6 (1985) 569

99. S. L. DAVIS, D. MUELLER, C. J. KEANE, *Rev. Sci. Instrum.* **54**(1983) 315

100. S. M. WOLFE, *et al.*, *Applied Optics* **15**(1976) 2645

101. R. WATTERSON, *et al.*, *Bull. Am. Phys. Soc.* **30**(1985) 1497

102. H. L. BERK, A. A. GALEEV, *Velocity Space Instabilities in a Toroidal Geometry, Phys. Fluids* **10**:2 (1967) 441

103. A. GIBSON, D. W. MASON, *Binary Collision Losses in Stellarators, Plasma Phys.* **11**(1969) 121

104. A. A. GALEEV, *et al.*, *Plasma Diffusion in a Toroidal Stellarator, Phys. Rev. Lett.* **22**:11 (1969) 511

105. E. A. FRIEMAN, *Collisional Diffusion in Nonaxisymmetric Toroidal Systems, Phys. Fluids* **13**:2 (1970) 490

106. O. A. ANDERSON, H. P. FURTH, *Imperfect Axisymmetry in the Tokamak Configuration, Nucl. Fusion* **12**(1972) 207

107. T. E. STRINGER, *Effect of the Magnetic Field Ripple on Diffusion in Tokamaks, Nucl. Fusion* **12**(1972) 689

108. J. W. CONNOR, R. J. HASTIE, *Neoclassical Diffusion Arising from Magnetic-Field Ripples in Tokamaks, Nucl. Fusion* **13**(1973) 221

109. Y. N. DNESTROVSKII, *et al.*, *Energy Balance in Tokamak Devices with Allowance for Magnetic-Field Ripple, Nucl. Fusion* **13**(1973) 1185

110. D. L. JASSBY, H. H. TOWNER, R. J. GOLDSTON, *Reduced Fusion-Neutron Production in Non-Axisymmetric Tokamak Devices, Nucl. Fusion* **18**:6 (1978) 825

111. J. J. SCHUSS, *et al.*, *Lower-Hybrid-Wave Heating in the Alcator A Tokamak*, *Phys. Rev. Lett.* **43**:4 (1979) 274

112. R. J. GOLDSTON, H. H. TOWNER, *Generalization of Connor and Hastie's Ripple-Trapping Coefficient, $G(\alpha)$*, *Nucl. Fusion* **20**:6 (1980) 781

113. A. H. BOOZER, *Enhanced Transport in Tokamaks due to Toroidal Ripple*, *Phys. Fluids* **23**:11 (1980) 2283

114. M. GREENWALD, J. J. SCHUSS, D. COPE, *Depletion of Ripple-Trapped Particles in the Alcator Tokamaks*, *Nucl. Fusion* **20**:6 (1980) 783

115. R. J. GOLDSTON, H. H. TOWNER, *Effects of Toroidal Field Ripple on Suprathermal Ions in Tokamak Plasmas*, *J. Plasma Phys.* **26**:2 (1981) 283

116. K. C. SHAING, J. D. CALLEN, *Boundary Layer Corrections to Neoclassical Ripple Transport in Tokamaks*, *Phys. Fluids* **25**:6 (1982) 1012

117. K. C. SHAING, J. D. CALLEN, *Neoclassical Ripple-Transport in Tokamaks*, *Nucl. Fusion* **22**:8 (1982) 1061

118. D. P. SCHISSEL, *High Energy Ion Depletion in the Charge Exchange Spectrum of Alcator C*, *Plasma Fusion Center, M.I.T.* Report PFC/RR-82-21 (1982)

119. S. D. SCOTT, *et al.*, *Measurements of Periodic Ripple Transport in the ISX-B Tokamak*, *Nucl. Fusion* **25**:3 (1985) 359

120. G. W. HAMMETT, *Fast Ion Studies of Ion Cyclotron Heating in the PLT Tokamak*, *Princeton University* Ph.D. Thesis (1986)

121. Y. TAKASE, *Plasma Fusion Center, M.I.T.* Report PFC/RR-83-29 (1983)

122. M. BRAMBILLA, *Theory of Bernstein Wave Coupling with Loop Antennas*, *Nucl. Fusion* **28**:4 (1988) 549

123. A. S. WAN, *Ion and Electron Parameters in the Alcator C Tokamak Scrape-Off Region*, *Plasma Fusion Center, M.I.T.* Report PFC/RR-86-13 (1986)

124. D. N. SMITHE, *et al.*, *An Algorithm for the Calculation of Three-Dimensional ICRF Fields in Tokamak Geometry*, *Nucl. Fusion* **27**:8 (1987) 1319

125. C. S. CHANG, G. W. HAMMETT, R. J. GOLDSTON, To be presented at 1988 meeting of American Physical Society, Division of Plasma Physics.

126. L. CHEN, J. VACLAVIK, G. W. HAMMETT, *Ion Radial Transport Induced by ICRF Waves in Tokamaks*, *Nucl. Fusion* **28**:3 (1988) 389

127. W. W. PFEIFFER, *et al.*, *ONETWO: A Computer Code for Modeling Plasma Transport in Tokamaks*, *GA Technologies Inc.* Report GA-A16178 (1980)

128. C. S. CHANG, F. L. HINTON, *Phys. Fluids* **25** (1982) 1493

129. F. L. HINTON, R. D. HAZELTINE, *Theory of Plasma Transport in Toroidal Confinement Systems*, *Rev. Mod. Phys.* **48**:2 (1976) 239

130. ALCATOR GROUP, *Alcator C Status and Program Plan*, *Plasma Fusion Center, M.I.T.* Report PFC/IR-82-3 (1982)

131. M. GREENWALD, *et al.*, *Phys. Rev. Lett.* **53** (1984) 352

132. R. R. PARKER, *et al.*, *Progress in Tokamak Research at MIT*, *Nucl. Fusion* **25**:9 (1985) 1127

133. S. M. WOLFE, *et al.*, *Effect of Pellet Fueling on Energy Transport in Ohmically Heated Alcator C Plasmas*, *Nucl. Fusion* **26**:3 (1986) 329

134. M. PORKOLAB, *Phys. Lett.* **22** (1966) 427

135. B. COPPI, M. N. ROSENBLUTH, R. Z. SAGDEEV, *Instabilities due to Temperature Gradients in Complex Magnetic Field Configurations*, *Phys. Fluids* **10**:3 (1967) 582

136. M. PORKOLAB, *Nucl. Fusion* **8** (1968) 29

137. T. ANTONSEN, B. COPPI, R. ENGLADE, *Nucl. Fusion* **19** (1979) 641

138. H. BIGLARI, P. H. DIAMOND, P. W. TERRY, *Nonlinear Ion-Temperature-Gradient-Driven Instability in Low-Collisionality Plasmas*, *Phys. Rev. Lett.* **60**:3 (1988) 200

139. R. VAN NIEUWENHOVE, *et al.*, *Parametric Decay in the Edge Plasma of ASDEX During Fast Wave Heating in the Ion Cyclotron Frequency Range*, Submitted to Nuclear Fusion.